A Study of Brightest Cluster Galaxies Over the Last Five Billion Years

TIMOTHY STEPHEN GREEN

A Study of Brightest Cluster Galaxies Over the Last Five Billion Years

Timothy Stephen Green

A Thesis presented for the degree of
Doctor of Philosophy

Centre for Extragalactic Astronomy
Department of Physics
University of Durham
United Kingdom

June 2017

Preface

Charles Dickens could almost have been describing the Ph.D. process when he penned his famous description of 18th Century England and France:

> *"It was the best of times, it was the worst of times, it was the age of wisdom, it was the age of foolishness, it was the epoch of belief, it was the epoch of incredulity, it was the season of Light, it was the season of Darkness, it was the spring of hope, it was the winter of despair, we had everything before us, we had nothing before us, we were all going direct to Heaven, we were all going direct the other way – in short, the period was so far like the present period, that some of its noisiest authorities insisted on its being received, for good or for evil, in the superlative degree of comparison only."*
>
> - Charles Dickens, *A Tale of Two Cities*, 1859

Dedicated to

My beautiful Bengali and soon to be wife, Shuprova.

Thanks for being you.

A Study of Brightest Cluster Galaxies Over the Last Five Billion Years

Timothy S. Green

Submitted for the degree of Doctor of Philosophy
June 2017

Abstract

The location of Brightest Cluster Galaxies (BCGs), at the centre of the clusters of galaxies, suggests a strong link between the formation and evolution of the BCG and that of the host cluster; with their unique environment distinguishing BCG evolution from that of massive field ellipticals. In this thesis I explore some of the contributing factors to the unique evolution of BCGs. In particular, I investigate the interaction of gas cooling from the intracluster medium (ICM) and the BCG, in fuelling star formation and AGN activity in BCGs, as well as the properties of the multi-phase gas itself. I also investigate the stellar mass growth of BCGs through galaxy–galaxy mergers.

I attempt to constrain the prevalence of BCGs undergoing star formation and/or AGN activity by conducting a multi-wavelength photometric census of 981 BCGs, from an X-ray selected sample of clusters at $z < 0.5$. It is found that at least 14 per cent of the BCGs have colours which deviate from those expected for a passively evolving galaxy. A strong association is discovered between BCG colours and optical line emission, indicating the presence of multi-phase gas and a strong association is also discovered between BCG colour and the X-ray luminosity of the host cluster, with implications regarding the proportion of active BCGs and the selection of a particular sample of clusters. These results demonstrate that a significant fraction of BCGs are in fact active, contrary to their "red and dead" reputation.

The theme of AGN activity in BCGs is continued via an investigation searching for clusters around some 3500 *ROSAT* selected AGN. The aim is to address the

ambiguity that exists between clusters and AGN in low resolution X-ray imaging, which disfavours the detection of the inherently rare systems where a strong AGN is hosted by a BCG. I identify 22 candidate systems with significant overdensities of red galaxies, with several being independent rediscoveries of such systems. Six best candidate systems are found where the cluster and AGN X-ray emission are likely to be comparable. Identification of such systems will ultimately aid in our understanding of the role of AGN feedback in this unique environment.

The stellar mass assembly of BCGs at $z < 0.25$ is also explored, targeting 23 merger–like BCGs, drawn from a large parent cluster sample, with wide-field integral field spectroscopy. The stellar kinematics are used to determine a bound probability for companion cluster galaxies and average merger timescales are estimated. Due to selection effects the average BCG stellar mass growth cannot be constrained tighter than between 9 ± 3 and 57^{+20}_{-17} per cent, with typical values in the literature of 10–20 per cent. Nevertheless, the techniques utilised in this analysis should help lay the groundwork for subsequent studies; demonstrating the power of using a statistically significant number of IFU observations to study BCG mergers.

Spatially resolved optical line emission is also explored in ten cluster cores. A variety of morphologies and kinematic profiles are discovered, and the properties of each individual system are discussed in turn. The most striking results relate to two systems where the ionised gas lies offset from the BCG. An X-ray observation of A2566 confirms the X-ray peak is offset from the BCG and coincident with the offset line emission, which, along with previous observations, suggest cooling of the ICM can occur in isolation of, and away from, the BCG – likely related to sloshing of the ICM. A 40 kpc filament is discovered in A2533, offset from the BCG and spatially coincident with star formation and dust lane features in the continuum. An ALMA observation also finds cold molecular gas, which almost perfectly traces the warm ionised gas. Without a high resolution X-ray observation a definitive link between the offset emission and the ICM cannot be established for this system, however, we predict the X-ray peak will be offset, analogous to A2566. Such systems allow the rare opportunity of studying cooling flows in isolation of the role of AGN feedback within BCGs.

Declaration

The work in this thesis is based on research carried out between 2013 and 2017, under the supervision of Professor Alastair Edge, at the Centre for Extragalactic Astronomy, Department of Physics, University of Durham, United Kingdom. No part of this thesis has been submitted elsewhere for any other degree or qualification and it is all my own work unless referenced to the contrary in the text.

Sections of this thesis appear, or will appear, in the following publications:

- **"A Multiwavelength Photometric Census of AGN and Star Formation Activity in the Brightest Cluster Galaxies of X-ray Selected Clusters"**
  Green, T. S.; Edge, A. C.; Stott, J. P.; Ebeling, H.; Burgett, W. S.; Chambers, K. C.; Draper, P. W.; Metcalfe, N.; Kaiser, N.; Wainscoat, R. J.; Waters, C.; **2016**, *Monthly Notices of the Royal Astronomical Society*, Volume 461, Issue 1, p.560-577

- **"Hiding in Plain Sight - Recovering Clusters of Galaxies With the Strongest AGN in Their Cores"**
  Green, T. S.; Edge, A. C.; Ebeling, H.; Burgett, W. S.; Draper, P. W.; Kaiser, N.; Kudritzki, R.-P.; Magnier, E. A.; Metcalfe, N.; Wainscoat, R. J.; Waters, C.; **2017**, *Monthly Notices of the Royal Astronomical Society*, Volume 465, Issue 4, p.4872-4885

- **"Witnessing the Assembly of Brightest Cluster Galaxies with MUSE - An Investigation into the Kinematics of Merging BCGs "**
  Green, T. S. *et al.* in prep.

- **"Spatially Resolved Optical Line Emission in the Cores of Clusters of Galaxies"**

  Green, T. S. *et al.* in prep.

Acknowledgements

First and foremost, I would like to direct my thanks towards Alastair Edge, without whom this thesis would not have been possible. His supervision, guidance, advice, patience and support has been invaluable throughout the duration of my PhD. He provided a comfortable working environment, productive yet relaxed, focused yet flexible. Alastair's enthusiasm for his research is infectious and I am still in awe of his knowledge and his brain, which is essentially an encyclopedia of galaxy clusters – show him an image of a cluster and he'll likely be able to tell you its Abell number, RA and DEC and describe the X-ray and radio properties associated with the BCG. It has been a genuine pleasure working with you the last few years Alastair, thank you. I look forward to our continued friendship.

A great deal of thanks are also owed to all the wonderful people I have been lucky enough to call friends during my time in Durham. Thank you to Andrew Robertson, Helen Johnson and Paddy Alton – house-mates extraordinaire – who have provided a suitable mix of intellectually stimulating discussion and ridiculous antics. A special thanks to all the people I have shared an office with over the years, most notably Steph Bartle and Helen Johnson, who were in it for the long-haul, but also Alice Mills and Chris Harrison, who provided invaluable help in those crucial early stages, and James Trayford, whom provided a much welcomed source of distraction in those busy final few months. And of course a thanks to all the other great friends, from both Durham past and present, including Saavi Perera, Sownak Bose, Greg Ashworth, and Charles Finn. You have all made the last few years the great experience that it has been.

I would also like to thank John Lucey, Mark Swinbank and Russell Smith for always being happy to oblige whenever I wanted to pick their brains for some of their

vast expertise. I should also thank the support staff, such as Alan Lotts, Lindsay Borrero and Sabine Schindler, the often unsung heroes, without whom the Durham astronomy group would collapse into disarray.

I'd especially like to thank my family for all of their love and support over the last twenty-seven years. You have always been an inspiration to me and demonstrated such strength. Thank you for providing me with all the opportunities that have enabled me to reach this stage. I hope I can continue to make you proud.

Lastly, but most certainly not least, I would like to thank my future wife, Shuprova. You have quite literally changed my life over the last seven years. You have introduced me to a whole other world and culture, and much of the person I am now is down to your influence. Despite living five thousand miles apart for the last three years, our bond has only gone from strength to strength. You are my partner and my best friend. I can't wait to start the next chapter of our lives together. I love you.

I would just like to finish with an homage to the City of Durham – a place I will dearly miss – with its peaceful riverside and woodland walks, local shops and markets, Gala Theatre, friendly people and beautiful historic bridges and buildings:

"Grey towers of Durham
Yet well I love thy mixed and massive piles
Half church of God, half castle gainst the Scot
And long to roam these venerable aisles
With records stored of deeds long since forgot."

- Sir Walter Scott, 1817

Contents

List of Figures

List of Tables

Chapter 1

Introduction

As far back as historical records exist for human civilisation, astronomical records have been found, making astronomy the oldest of all the natural sciences. Astronomy has always been a significant aspect of society and, up until the last few centuries, the study of celestial phenomena was intricately linked to a variety of mythological, philosophical, religious and astrological believes. Astronomical observations were also instrumental in measuring the passage of time, with the majority of historical and contemporary calendars based on cycles of either the Sun or Moon.

It was not until the 17th Century however that physics and astronomy were combined to lay the foundation for modern astrophysics. It was just after the turn of the century, in 1608 and 1609, that the first telescopes were invented, with Galileo Galilei the most famous of these early pioneers. This significantly advanced our ability to observe the cosmos. It was however Johannes Kepler who first used a mathematical description, based on fundamental principles derived from terrestrial physics, to predict the motion of celestial bodies. These would later become Kepler's three laws of planetary motion. Isaac Newton then developed these ideas further, creating the law of universal gravitational attraction, presented in his 1687 *Philosophiae Naturalis Principia Mathematica* (although, controversially, a number of these ideas were first proposed by Robert Hooke in 1660 and 1667).

The subsequent couple of centuries were largely spent accurately measuring the motion of celestial bodies, providing observational evidence to support the physical predictions by these 17th Century pioneers. However, in the 19th Century another

significant discovery was made. In 1814, Fraunhofer discovered that the stellar spectrum of the Sun contained dark and bright lines. These were later matched up with the spectral properties observed in known elements in laboratory experiments by Kirchhoff and Bunsen in the 1860's, indicating that the same chemicals must be present in both the Sun and on the Earth. Different stars were shown to exhibit differing spectral properties and by the end of the 19th Century a catalogue of some 10,000 stars had been compiled with classifications based on these spectral properties.

It was however over the previous century that the majority of the advances in our understanding of the cosmos have been made. A fundamental shift in our cosmic perception occurred in the early 20th Century, with the pioneering work of Edwin Hubble. The prevailing view at the time was that the Universe was confined to the Milky Way. However, in 1925 Hubble noted that, by using Cepheid variable stars as cosmic standard candles, some 'nebulae' were too distant to be part of the Milky Way; and thus the existence of galaxies outside of our own was discovered and our perception of the scale of the Universe increased enormously. This raised questions about how these galaxies compare to what we know of the Milky Way and hence the field of extra-galactic astrophysics was born. Then in 1929 Hubble, using the concept of Doppler shifting of light, (first proposed in the mid-19th Century), measured the velocities of these galaxies and discovered they are moving away from us, with velocities proportional to their distance. This was the first observational evidence for the expansion of the Universe, which had been suggested by Alexander Friedmann in 1922 and and Georges Lemaitre in 1927 from studies into Einstein's 1917 theory of General Relativity. And thus, observational cosmology was born.

The numerous advances made over the last several decades are to many to list. Suffice to say that we are now in an era of precision cosmology, where the parameters that go into the models, which very accurately describe the evolution of the Universe, right back to fractions of a second after the Big Bang, are measured to within a few per cent. That is not to say that significant questions do not remain unanswered; most notably the nature of the dark matter and dark energy, which constitute the majority of the energy density of the Universe. Great advances have been made

into the astrophysics related to baryons, with our understanding of galaxy evolution being broadly understood. However, the "devil is in the detail" and a great amount of the astrophysics of galaxies is still a matter of mystery and debate. It is some of these problems that will be explored in this thesis.

1.1 Cosmic Structure Formation

In the standard ΛCDM model of cosmology, the favoured paradigm of cosmology today, structure in the Universe formed and is still growing via hierarchical growth (White & Rees, 1978). The redshift distribution of observed galaxies shows that galaxies are not uniformly distributed, but tend to group together into a web-like structure, known as the cosmic web. Figure 1.1 illustrates the distribution of some 200,000 galaxies, up to $z = 0.2$, from the 2dF Galaxy Redshift Survey (Colless et al., 2001) and clearly shows some regions have higher number densities of galaxies than others. This tendency for structure to cluster together is a natural consequence of the mutual gravitational attraction that is felt by matter in the cosmos. The cosmic web has been demonstratively recreated in modern large-scale cosmological simulations such as in the Millennium (Springel et al., 2005), Illustris (Vogelsberger et al., 2014) and EAGLE simulations (Schaye et al., 2015).

In the ΛCDM paradigm a period of rapid expansion shortly after the Big Bang, known as inflation, amplified primordial overdensities. Over time, the enhanced gravitational pull of these overdense regions drew in matter, leading to the accumulation and collapse of cold dark matter, into what are called dark matter halos. As these halos draw in more matter from the surrounding areas their mass and resulting gravitational potential increases and, as a result, yet more material is accreted. This growth via gravitational attraction is the primary principle behind the hierarchical formation and growth scenario – in which the more massive dark matter halos accrete smaller dark matter halos and baryons, in the form of gas and dust, leading to the formation of galaxies in these halos. This accretion occurs along filaments, with the biggest halos forming at the point where many of these filaments meet. It is at the most overdense nodes of this cosmic web that galaxies begin to accumulate into

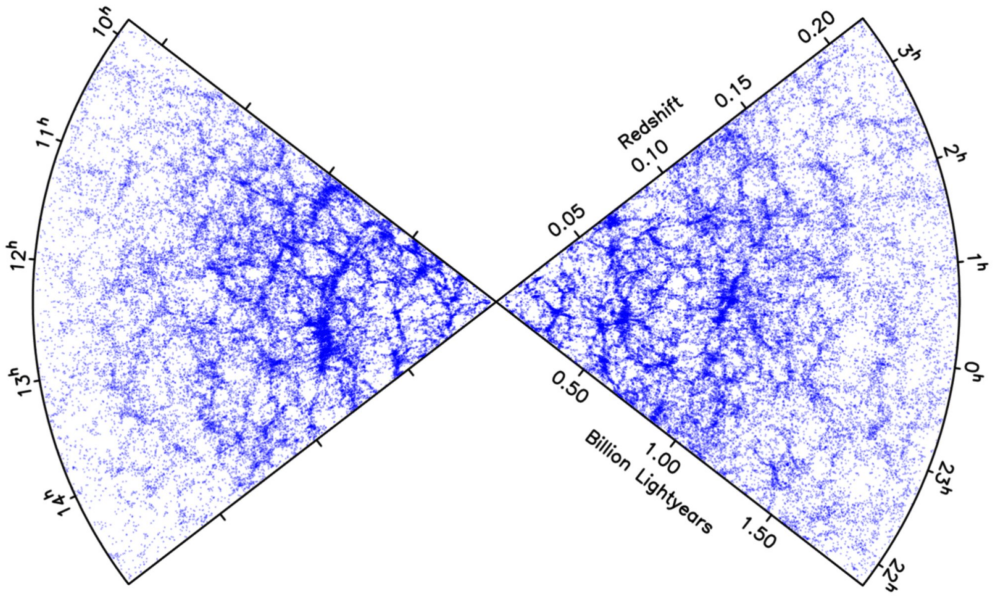

Figure 1.1: The distribution of galaxies observed in the 2dF Galaxy Redshift Survey. Image taken from Colless et al. (2001).

groups and clusters.

1.2 Clusters of Galaxies

Clusters of galaxies are the most massive gravitationally bound systems in the Universe, lying at the intersection of filaments of the large scale structure of the Universe. They have typical masses of $10^{14} - 10^{15}\,\mathrm{M}_{\odot}$ and spatial extents of several Mpc (with typical virial radii of 1–3 Mpc). With the dark matter content accounting for $\sim 85\%$ of the cluster mass, they are dark matter dominated systems, with the remaining mass in the form of baryons. The galactic component of clusters typically consist of a few tens of massive early type galaxies and hundreds, if not thousands, of smaller dwarf galaxies. However, the baryonic composition is greatly dominated by a diffuse hot plasma, known as the Intracluster Medium (ICM).

As the most mature manifestation of primordial overdensities, they are useful probes of cosmology and the formation of large scale structure. Since clusters have gravitational potentials sufficiently high to effectively capture all the matter that was present during their collapse, their compositions are thought to reflect that of

the Universe at large and, as they are essentially closed systems in terms of their gas, they provide a record of nucleosynthesis in the Universe. Clusters are also invaluable laboratories in the study of dark matter, with cluster–cluster collisions, such as in the Bullet Cluster, providing insight into the collisional properties of dark matter particles. Indeed, it was observations of clusters which first led to the proposition of the existence of dark matter by Zwicky (1933). These make galaxy clusters powerful tools in constraining cosmological parameters (see Allen et al. 2011 for a review on cluster cosmology).

The complex mix of baryons in clusters also provide a whole suite of astrophysical processes to understand. With a high number of galaxies, the many processes involved in galaxy evolution can be studied. The formation history and evolution of giant early type galaxies can be traced from observations of the mature, passively evolving galaxies in the core (§ 1.2.1). Whereas, in the cluster periphery, quenching processes, such as ram pressure stripping, are revealed as infalling late type galaxies pass through the dense ICM. The ICM itself provides a laboratory of plasma physics, which is dominated by thermal processes, but with a number of non-thermal ones too. Gas cooling and feedback, which play such a vital role in the star formation history of galaxies, leaves their traces in the ICM also. Clusters also act as cosmological telescopes, magnifying distant galaxies through gravitational lensing. Therefore, galaxy clusters, representing the intersection of cosmology and astrophysics, have been a very lucrative field of research for the best part of the last century.

1.2.1 The Galaxies in a Cluster Core

Although now known to be a minority contributor to the overall mass of a cluster, it is observations of the constituent galaxies which first led to the discovery of clusters. Optical images of local clusters, such as Abell 1689 given in Figure 1.2, reveal a high density of giant early type galaxies near the cluster centre. Often clusters exhibit one clearly distinct galaxy at the centre of the galactic distribution, which is typically much more extended and brighter than the other giant ellipticals. This particular class of galaxy is called a Brightest Cluster Galaxy, or BCG, and will be the focus

Figure 1.2: Galaxy cluster A1689. Image taken from NASA.

of this thesis. But for now I will address the general properties of cluster galaxies.

A notable feature of images like Fig. 1.2 is that the cluster galaxies are, generally speaking, the same colour. The red (as opposed to blue) colour of these galaxies is indicative of the fact that the stellar populations of these galaxies are old. In essentially all local massive clusters a linear relationship is found between magnitude and colour, for a significant fraction of the cluster member galaxies, and is called the cluster red-sequence. A study by Bower et al. (1992) demonstrated that the red sequence relation in both the Virgo and Coma clusters had the same form, suggesting they are homogeneous. Further work has revealed that across all clusters red sequence galaxies form a roughly homogeneous population. The evidence – such as the over density of red galaxies found in proto-clusters (the progenitors of virialised local clusters; Kodama et al. 2007; Zirm et al. 2008) and the already well established red sequences of clusters at high redshift (e.g. Stanford et al. 2012; Cooke et al. 2016a) – suggest that the stellar populations of these early-type galaxies, which dominate the galaxy population toward the centre of clusters, have been, for the most part, passively evolving since forming in an essentially instantaneous burst of star formation at high redshift ($z > 2$) (e.g. Aragon-Salamanca et al. 1993; Stanford et al. 1998; Andreon 2003; Thomas et al. 2005; Mei et al. 2006; van Dokkum & van der Marel 2007).

The colour–magnitude relation in clusters follows a trend such that the galaxies at the brighter end of the red sequence are redder than that of the faint end. This is generally understood as a mass–metallicity relation (Kodama & Arimoto 1997; Kodama et al. 1998), in which the deeper potential wells of more massive (luminous) galaxies are more effective at retaining the metals released by supernovae and stellar winds. The slope of the red sequence is also expected to depend on differences between the ages of red sequence galaxies, although it is disputed to what extent this contributes (e.g. Kodama et al. 1998; Kaviraj et al. 2005). Over time, hierarchical growth suggests that there should be a build up of the red sequence, primarily via two possible channels: 1) through the transition of blue galaxies onto the red sequence, through quenching of their star formation, or, 2) the growth of already red galaxies via mergers. Understanding how the properties of the red sequence, such as slope, zero-point and scatter, have evolved over time can inform us about the evolution of these galaxies. A number of studies indicate an evolution in the observed slope of the red sequence between $z = 0$ and $z \sim 1$ (e.g. López-Cruz et al. 2004; Kaviraj et al. 2005; Stott et al. 2009), which could result from the build of the red sequence, (or may just reflect the changing rest frame wavelengths in the colour regime). However, other studies suggest no significant evolution of these properties up to $z \sim 1.3$ (e.g. Menci et al. 2008; Mei et al. 2009). I will address the slope of the red sequence further in Chapter 2.

1.3 Brightest Cluster Galaxies

At the brightest end of the luminosity distribution of cluster galaxies is a class of galaxy called Brightest Cluster Galaxies (BCGs). BCGs are the most massive and luminous stellar systems in the Universe and tend to reside in the very core of a cluster. They are typically located at the centre of the cluster potential (characterised by a close proximity to the peak of the cluster X-ray emission; see § 1.5). They appear to have a distinct luminosity function, with respect to other cluster ellipticals, or bright field galaxies. The properties of BCGs generally correlate with those of their host cluster; such as between BCG stellar mass and cluster mass, and they

exhibit small velocity offsets with respect to the host cluster. These observations, as well as others, indicate the evolution of BCGs is intrinsically linked to that of the cluster and distinct from that of other galaxies. So the study of BCGs is recognised as a worthy area of research in its own right.

1.3.1 The Formation and Growth of BCGs

Historically, the unique properties of BCGs were proposed to have arisen by a few potential mechanisms. One was that their formation and evolution was the result of cooling flows (Fabian & Nulsen 1977; Fabian 1994), in which runaway cooling of ambient gas in the cluster core leads to a flow of cool gas toward the cluster centre. However, as will be described in § 1.5.1, this scenario has since been discredited, with perhaps only 1% of typical BCG mass being attributable to this (Liu et al., 2012).

Another early prediction was that BCGs form from galactic cannibalism, as a result of dynamical friction (White 1976; Ostriker & Hausman 1977). Dynamical friction is a process in which, as galaxies move through a cluster, their gravitational attraction leaves a higher density of dark matter/baryonic particles in their wake, building up mass behind the galaxy and creating a gravitational drag, opposing its direction of motion. As more massive galaxies provide a greater potential, the effects of dynamical friction are felt more strongly the more massive a galaxy is. This formation scenario assumes that as massive galaxies are accreted by a cluster they gradually sink toward to the centre, with one settling at the centre. This subsequently grows by merging with more of these infalling galaxies. However, this mechanism was shown to be unsuitable, in isolation, as the estimated dynamical friction timescales are too long to explain the existence of well established, dominant central galaxies in the observations (Merritt 1985).

The CDM model of hierarchical formation is now widely favoured. Early simulations of hierarchical cluster formation, such as Dubinski (1998), found that it was natural for a series of mergers at high redshift ($z > 3$) to lead to a massive galaxy, which settles in the cluster centre. These have been further refined and the current school of thought is that BCG formation and growth follows a two–phase

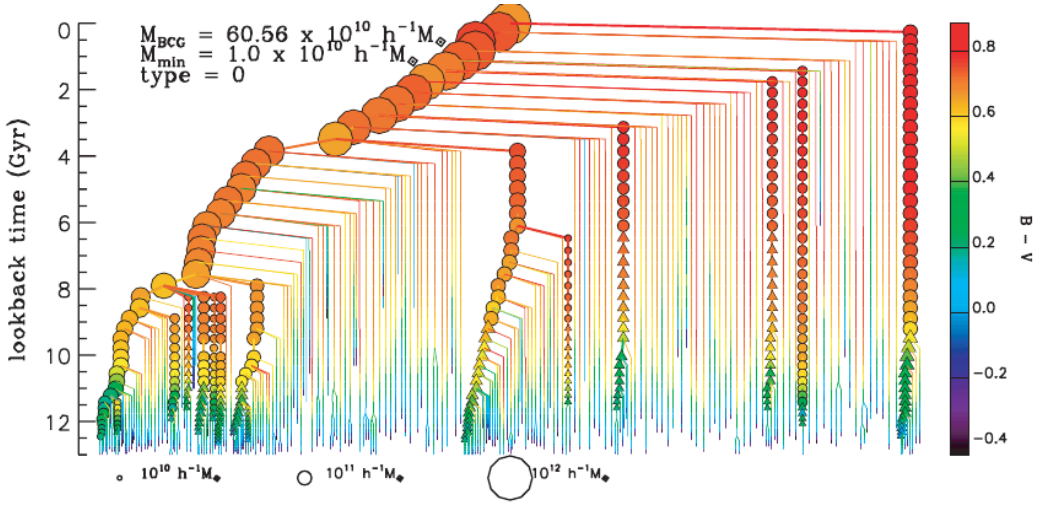

Figure 1.3: An example merger tree for a BCG, schematically demonstrating how the BCG has grown via a hierarchical process of merging, where each branch represents an accreted galaxy. Image taken from De Lucia & Blaizot (2007).

hierarchical formation scenario (e.g. De Lucia & Blaizot 2007; Laporte et al. 2013). The first stage involves rapid cooling and in-situ star formation at high redshifts ($z \gtrsim 2$), building up a number of small galaxies. It is at this stage that the majority of the stellar populations of later galaxies are thought to have formed, with the semi-analytic models by De Lucia & Blaizot (2007) finding that as much as 80% of the stars in the $z = 0$ BCGs have already formed by $z \sim 3$. This is then followed by subsequent growth through repeated dissipation-less dry (meaning a lack of gas) galaxy–galaxy mergers at $z < 2$. An illustrative BCG merger tree is presented in Figure 1.3.

A number of observations confirm the existence of BCGs in a state of ongoing or recent merger activity. At low and intermediate redshifts, a number have been found which exhibit close companion galaxies (e.g. Lauer 1988; Rines et al. 2007; Tran et al. 2008; Rasmussen et al. 2010; Brough et al. 2011; Jimmy et al. 2013) . Some of which exhibit not only multiple components, but also asymmetrically extended envelopes, associated with the BCG, which could be the result of a recent major mergers (such as CL0958+4702 as observed by Rines et al. 2007) or streams between the components (Lauer, 1988). The model of De Lucia & Blaizot (2007) predicted that this growth would be dominated by minor mergers (i.e. mergers

between galaxies with a large mass ratio), whereas observationally the evidence suggests that growth is dominated by major mergers (e.g. Lidman et al. 2013; Liu et al. 2009, 2015).

The hierarchical growth model is supported by the correlation between BCG mass and cluster mass (Edge 1991; Stott et al. 2010, 2012; Lidman et al. 2012; Green et al. 2016), which suggests that the growth of BCGs must, to some degree, mirror the hierarchical growth of the cluster, with more galaxies drawn into the cluster leading to more migration of galaxies toward the cluster core. Additionally it is the process of accreting galaxies which is thought to have expanded the outskirts of the central galaxy (Laporte et al., 2013; Cooper et al., 2015), leading to the very extended size which is so characteristic of BCGs, (with estimates of $\sim 60\%$ of local BCGs classed as cD galaxies; Zhao et al. 2015).

Whilst BCGs have been observed to be undergoing mergers, the extent to which BCGs continue to merge and grow in mass over time is less well understood. De Lucia & Blaizot (2007) found that only 20–30% of the stellar mass of the BCGs have assembled by $z \sim 1$, suggesting significant growth by a factor of ~ 4 via mergers between $z = 1$ and $z = 0$. However, a number of observations suggest more modest mass growth factors of ~ 2 over the same redshift interval (e.g. Lidman et al. 2012, 2013; Burke & Collins 2013), which are more consistent with later models (e.g. Tonini et al. 2012; Laporte et al. 2013; Shankar et al. 2015). However, there are also a number of observational studies which find no evidence for significant mass growth over this time (e.g. Whiley et al. 2008; Collins et al. 2009; Stott et al. 2008, 2010).

The observational studies investigating the mass growth of BCGs can be broadly categorised into three techniques. The first is to compare the stellar mass of BCGs at high and at low redshift (e.g. derived from BCG luminosity; Aragon-Salamanca et al. 1998; Whiley et al. 2008; Collins et al. 2009; Stott et al. 2008, 2010; Lidman et al. 2012, or SEDs; Oliva-Altamirano et al. 2014). The premise is that if there has been significant mass growth of BCGs over time then there should be a measurable difference in luminosity/mass between the two sets of observations. However, although this technique is conceptually simple, disassociating the results from se-

lection effects is difficult. It is known that the mass of BCGs correlates with the mass of their host cluster (Edge, 1991), so early studies matched cluster masses in their high and low redshift samples. However, this does not account for the mass growth of a high redshift cluster down to $z = 0$, making the progenitor more massive at $z = 0$ than the mass–matched local comparison clusters. Lidman et al. (2012) suggest that this is responsible for the apparent lack of BCG mass growth in Collins et al. (2009) and Stott et al. (2008, 2010). An additional complication is that in De Lucia & Blaizot (2007) it was found that the main progenitor of a local BCG is not necessarily the most massive cluster galaxy in past epochs, so even after matching the evolving mass of the cluster, the high redshift BCGs may not be true progenitors. Therefore careful consideration of selecting true progenitors at high redshift has to be made, with a number of studies attempting to address this (Lidman et al. 2012; Shankar et al. 2015; Zhao et al. 2017).

The second method has been to use the pair fraction as a merger proxy and derive mass growth estimates from a statistical analysis of the number of close companions to BCGs in imaging. First, the fraction of BCGs with nearby companions, that could soon merge, are determined. Then, using close companions as a merger tracer and assuming merger timescales based on projected separation, the average merger rate and corresponding mass growth rate can be estimated (e.g. Edwards & Patton 2012; Burke & Collins 2013; Liu et al. 2009, 2015; Groenewald et al. 2017). The uncertainty associated with this technique stems largely from assumptions made. Firstly an assumption has to be made that the close companion galaxies are indeed likely to merge. However, projection effects mean that galaxies which appear close together on the sky may in fact have large physical separations. The corresponding level of contamination is uncertain, with studies often assuming some contamination fraction based on simulations (Edwards & Patton, 2012). Further to this, even if physically close, the companion may have a significant velocity relative to the BCG, in which case it is likely to pass by without interacting. Studies on the trajectory of galaxy infalls indicate that it is common to have a number of fly-bys in the core before any settling and merging are possible (Nipoti, 2017). Assumptions also have to be made about the merger timescales, which are difficult to estimate. Finally

the fraction of BCGs with close companions in the observations is assumed to be representative of a snap-shot in time and that the average merger rates they provide can be extrapolated over a suitable period of lookback time (redshift), which may not be valid.

The third technique has been to use spectroscopy to measure the kinematics of likely BCG–companion mergers and determine whether they are likely to merge. The uncertainty due to projection effects is reduced significantly, with the line-of-sight velocity of close companion galaxies allowing an estimation of the likelihood of that companion being dynamically bound to the BCG. This technique has become more viable in recent years with advances the instrumentation of integral field spectroscopy (see Chapter 5). A number of such studies have been applied to a handful of individual systems, (e.g. Rasmussen et al. 2010; Brough et al. 2011; Jimmy et al. 2013; Edwards et al. 2016), confirming the dynamically linked companion galaxies and estimates of corresponding merger timescales and mass contributions. However, no such study using a statistically significant of clusters has been conducted as of yet.

In Chapter 6 of this thesis therefore I will combine the latter two techniques, constraining the stellar mass growth rate of BCGs by investigating the full stellar kinematics of a sample of 23 cluster cores selected as containing BCGs which are likely to undergo mergers, based on optical imaging of several hundred X-ray selected clusters. There is some observational evidence suggesting that the stellar mass growth of BCGs has flattened out since $z \sim 0.5$ (Lin et al., 2013; Oliva-Altamirano et al., 2014; Inagaki et al., 2015; Shankar et al., 2015), which will be explored further in Chapter 6.

An important additional consideration, in investigating the stellar assembly of BCGs, is the Intra-Cluster Light (ICL). This is the diffuse light in clusters arising from stars which are bound by the cluster potential, but, are not associated with a galaxy. The main formation channels of the ICL are understood to be via tidal stripping of galaxies and/or relaxation following mergers with the BCG. Simulations by Murante et al. (2007) suggest that galaxy interactions with the BCG are the primary build up mechanism of the ICL and that a significant fraction of the mass

of a companion galaxy is dispersed into the ICL when merging with a BCG (e.g. 80% in the semi-analytic models of Conroy et al. 2007 and 45% in Puchwein et al. 2010). Observations of CLASH clusters, by Burke et al. (2015), suggest the build up of the ICL mostly occurs at low redshift. So for studies estimating growth rates from predicted mergers of close companions, assumptions have to be made about what fraction of the mass of the companion galaxy contributes to the stellar mass growth of the BCG and what fraction contributes to the ICL (e.g. Burke & Collins 2013; Groenewald et al. 2017).

Note that there are indications that the group environment plays a crucial role in the growth and merger histories of these galaxies also. For example, Tran et al. (2008) find merging Brightest Group Galaxies (BGGs) in a set of groups, with the groups themselves likely to, at some point, merge and form a massive cluster. This is supplemented by observations of dry mergers in BGGs in Mulchaey et al. (2006) and Jeltema et al. (2007) in intermediate-redshift groups. The lower velocity dispersions of groups are more conducive to mergers (McIntosh et al., 2008), suggesting the group environment may be critical for the process of galaxy assembly via major dry merging, which could later be accreted into a galaxy cluster environment (Martel et al., 2014).

1.4 The Detection of Galaxy Clusters

Clusters can be detected in a number of ways, each with their own advantages and limitations. The original technique, in which clusters were first identified, was via optical selection – which involves searching for regions of overdensities of galaxies in imaging. The first significant catalogue of galaxy clusters was compiled by George Abell in 1958 (Abell, 1958), which contained some $\sim$ 2000 systems, via visual inspection of photographic plates. Later significant contributions were similarly compiled by Zwicky et al. (1961) and Abell et al. (1989). This method of looking for overdensities is however subject to significant contamination from projection effects. Modern techniques therefore utilise additional colour information, benefiting from the existence of the red sequence galaxies observed in clusters (e.g.

the Red-Sequence Cluster Survey (RCS) algorithm; Gladders & Yee 2000, and the redMaPPer red sequence cluster finder algorithm; Rykoff et al. 2014).

Another method of detection is via the SunyaevZel'dovich (S-Z) effect (Sunyaev & Zeldovich 1972; Birkinshaw 1999), in which photons of the Cosmic Microwave Background (CMB) undergo inverse Compton scattering as they pass through dense clusters of galaxies. High energy electrons in the Intracluster Medium (ICM) provide an energy boost to these CMB photons, betraying the presence of the cluster in measurements of the CMB. The key advantage of S-Z detection is that is almost independent of redshift, and as such, a significant number of high redshift ($z > 1$) clusters have been discovered this way.

The third main cluster detection technique is X-ray selection, and is the method used to identify the cluster sample studied throughout this thesis. X-ray selection relies on the emission of X-ray photons from the hot diffuse plasma of the ICM (see § 1.5). The first X-ray detection of a galaxy cluster, Virgo, was in the 1960's by Byram et al. (1966). Then, by the end of the first X-ray satellite mission, *UHURU*, there were 52 confirmed X-ray clusters (Forman et al., 1978). The *Einstein* mission was the next significant contributor, with the quantity of X-ray detected clusters numbering some ~ 300 by the early 1980's, and, by the end of the *ROSAT* mission, which operated throughout the 1990's, the number of galaxy clusters was ~ 4000 (Edge, 2004). Since the turn of the millennium, significant advances in the imaging capability of X-ray satellites, with *XMM-Newton* and *Chandra*, have transformed our understanding of cluster physics (see § 1.5), but have made few advances in the growth of the number of X-ray detected clusters, relative to the *ROSAT* era.

1.5 The Intracluster Medium

The intracluster medium (ICM) is the name for the hot diffuse plasma (although it is commonly interchangeably referred to as a gas, as will occur throughout this thesis) which is distributed throughout clusters of galaxies. Outweighing the constituent galaxies by a factor of 10 in rich clusters (Lin et al., 2003), the ICM represents the dominant baryonic content of clusters. The primary composition of this gas is

electrons and protons, mostly from ionised hydrogen, and some helium nuclei, with typical particle densities ranging from $10^{-2} - 10^{-4}\,\mathrm{cm}^3$ (several orders of magnitude higher than the mean cosmic baryon density $\sim 10^{-8}\,\mathrm{cm}^3$). The ICM also contains trace amounts of heavier elements, such as iron and silicon (with typical abundance $\sim 1/3$ Solar), visible in emission lines in X-ray spectroscopy (see Werner et al. 2008 for a review on metals in the ICM). The exact origins of ICM remain uncertain, but it is likely a combination of warm baryons pulled in by collapsing dark matter and gas that has been processed in the stars of the cluster galaxies (hence the metal abundances observed).

In order to maintain virial equilibrium, the typical virial temperature of the gas ($kT \propto GM/R$) is of the order $T \sim 10^{7-8}\,\mathrm{K}$, reflecting the immense depth of the cluster potential. The gas is believed to have been heated through a process of adiabatic compression and shocks due to gravitational infall. The gas temperature is sufficiently high that X-ray photons are produced, in abundance, through thermal bremsstrahlung – a process in which photons are produced by the deceleration of electrons as they approach the nucleus of ions. As such, clusters are the second brightest sources in the X-ray sky (after quasars), with typical X-ray luminosities of $L_{\mathrm{X}} \sim 10^{43-45}\,\mathrm{ergs}^{-1}$. The temperature of the ICM is dependent on the potential depth of the cluster, so X-ray observations of the ICM can be used to measure the mass of clusters. This is demonstrated in the correlation that exists between gas temperature and cluster velocity dispersion (e.g. Edge & Stewart 1991).

It is interesting to note that a number of non-thermal processes are known to take place in the ICM, such as interactions with magnetic fields. These are observed in the form of diffuse radio emission, due to synchrotron radiation, known as radio halos, relics and mini-halos (see Feretti et al. 2012 for a review). However the energy density of these non-thermal processes is $\leq 1\%$ that of the thermal component in the ICM.

Clusters can be broadly categorised into two dynamical states; relaxed systems, where the density profile of the ICM (as traced by the X-ray emission) is symmetric and approximately in hydrostatic equilibrium, or unrelaxed/disturbed systems, where the X-ray profile shows elongation in one direction and exhibits features like

shocks and cold fronts (see review by Markevitch & Vikhlinin 2007). Dynamically disturbed systems are believed to result from a recent cluster–cluster scale interaction, which acts to skew the ICM distribution along the axis of the interaction and leads to discontinuities in the gas temperature. Relaxed systems conversely appear to be clusters which have not undergone a major merger is recent history.

For a cluster in hydrostatic equilibrium, you expect the pressure distribution of the gas to trace the gravitational potential of the cluster. So as the X-ray surface brightness is proportional to the gas density squared (i.e. $L_{\rm X} \propto n_e^2$), the X-ray surface brightness profiles decrease radially away from the more dense cluster core. Some clusters have a particularly strong peak in their X-ray surface brightness profiles (e.g. Figure 1.4), reflecting the particularly high gas density in their cores. The high X-ray emission nature of these cores means a substantial amount of energy gets radiated away and so the gas radiatively cools. Since the cooling-time scales as $t_{cool} \propto T^{1/2}/n_e$, where T is the temperature and n_e is electron density, and the density of the gas increases as it cools, sufficiently high density cores can have central cooling timescales shorter than the age of the Universe. Therefore you expect to find cool gas in the cores of such clusters, earning them the name cool core clusters.

Cool core clusters are found to be dynamically relaxed systems and it is understood that the cool core nature represents the natural relaxation state of a cluster. Non cool core clusters on the other-hand are more likely to exhibit disturbed, irregular morphologies. Hence the presence of a cool core is thought to indicate a lack of any recent major mergers for the cluster, which would have disturbed the existence of any cool core in the process (Burns et al. 2008; Rasia et al. 2015). The cool core and non cool core nature of a cluster thus represents a temporary state, with clusters able to transition from one to the other given enough time.

1.5.1 Cool Cores and the Cooling Flow Problem

Cool core clusters, which have gas densities in their cores sometimes as high as $n_e \sim 0.1\,\mathrm{cm}^3$, have central cooling timescales shorter than a Hubble time and are characterised by peaky X-ray surface brightness profiles (e.g. A478 in Figure 1.4). As many cool core clusters have central cooling timescales $\lesssim$ 1Gyr, we anticipate

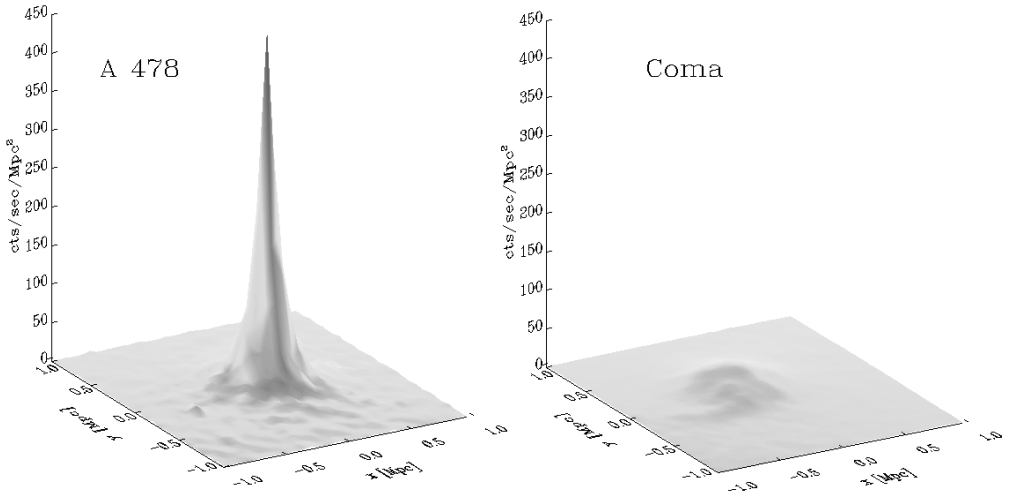

Figure 1.4: A comparison of the X-ray surface brightness profiles of a typical cool core cluster and non-cool core cluster. Image taken from Fabian & Sanders (2009)

the presence of multi-phase gas as it cools through intermediate temperatures and a reservoir of cold gas in the centre of such clusters. When centrally located, we would also expect star formation in the BCG, fuelled by this external source of cool gas. Early models predicted that as the gas cools the pressure would drop and the weight of the overlying hot gas would cause it to flow in and replace the compressed gas, with estimated mass deposition rates of $100\text{s}-1000\text{s}\,M_{\odot}\text{yr}^{-1}$ (Fabian, 1994). However, X-ray observations, with *XMM-Newton* and *Chandra*, of cool core clusters reveal that this "cooling flow" scenario is not the case, at least not to the extent initially thought – flows do not occur on the scale estimated, observed temperatures of the cool cores are rarely lower than 1/3 of the virial temperature and evidence suggests only $1-10\%$ of the predicted mass of cooling gas goes on to form stars (O'Dea et al. 2008). This discrepancy existed for a number of years and came to be known as the cooling flow problem, however it is now widely understood that a heating mechanism exists, offsetting the cooling rate.

The primary source of this heating is thought to be feedback from Active Galactic Nuclei (AGN; McNamara & Nulsen 2007, 2012; Fabian 2012). The scenario which has emerged is that a self-regulated cycle exists, where gas cools, condenses into filaments (e.g. Fabian et al. 2008; Tremblay et al. 2012; McDonald et al. 2014), leading to star formation in the BCG (Cavagnolo et al. 2008; Donahue et al. 2010;

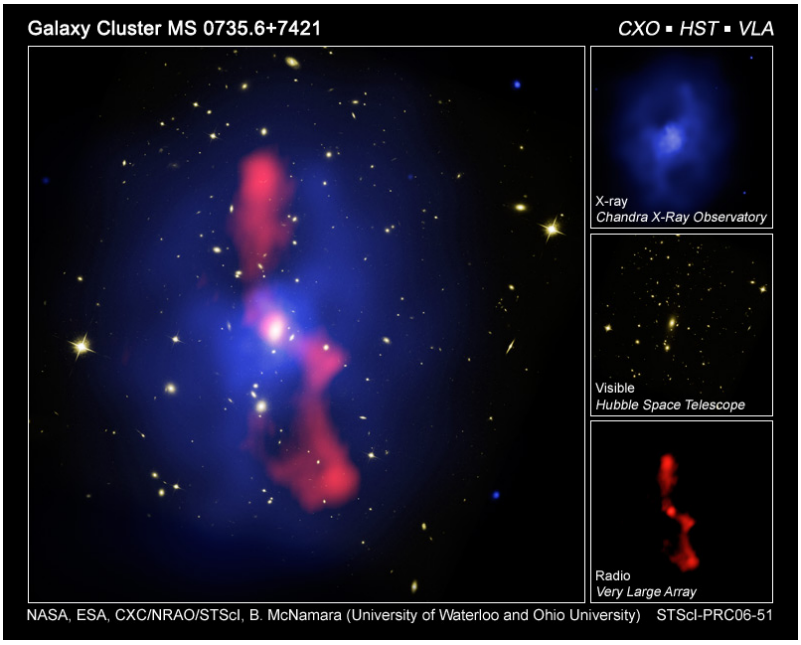

Figure 1.5: X-ray, optical and radio composite image of MS0735.6+7421, illustrating the cospatial nature of cavities in the X-rays and the radio emission from the nucleus of the BCG.

Rawle et al. 2012; Hoffer et al. 2012; Fogarty et al. 2015; Green et al. 2016) and accretion onto the supermassive black hole of the BCG. Then, as the central black hole accretes matter, energy gets ejected back out into the system, heating the gas and halting the supply of gas for subsequent accretion and star formation. As the AGN 'switches off', the process of radiative cooling takes over again and the cycle repeats.

The evidence for this scenario relies on observation that the majority of cool core clusters have a central radio galaxy (Burns 1990; Hogan et al. 2015a), suggesting past AGN activity. Heating via this AGN activity is supported by observations of co-located X-ray cavities and radio lobes around radio bright BCGs (e.g. Boehringer et al. 1993; McNamara et al. 2000; Hlavacek-Larrondo et al. 2015). An illustrative example of this is given in Figure 1.5, showing a composite image of the X-ray, optical and radio emission in the core of MS 0735.6+7421. Cavities, resulting from the displacement of the X-ray emitting ICM, by jet driven outflowing plasma, are seen in $\geq 70\%$ of cool core clusters (Dunn & Fabian 2006; Hlavacek-Larrondo et al. 2012). The AGN power, estimated by measuring the mechanical power necessary to

create the cavities, is generally sufficient to balance the energy loss through radiative cooling in most cool core clusters (Bîrzan et al. 2004; Rafferty et al. 2006; McNamara & Nulsen 2007). Although it should be noted that the high variability of AGN power (Hogan et al. 2015b) introduces a further challenge when comparing AGN power with cooling rates. Further evidence comes from the fact that not only is AGN power sufficient to offset cooling, but, a correlation is found between the X-ray cooling luminosity and AGN power, such that more powerful AGN are found in the cores of the most rapidly cooling cores (Pfrommer et al. 2012). This is consistent with a causal connection between cooling and AGN accretion, as needed for true self regulation. However, the precise nature of how energy is transferred, between the sub-parsec scales of accretion and the cooling scale of tens of kiloparsec, is still a topic of uncertainty and debate (e.g Pizzolato & Soker 2005; Voit et al. 2008; Li & Bryan 2014; Voit & Donahue 2015; Prasad et al. 2015; and reviews; McNamara & Nulsen 2007, 2012; Fabian 2012).

A key challenge in understanding this AGN feedback is that BCGs which exhibit signs of an ongoing strong AGN outburst are rare, because of the short AGN duty cycle. This is despite the fact it is common to see radio emission from BCGs (Burns 1990; Hogan et al. 2015a) and that evidence suggests that the AGN often play an important role over time-scales of at least 1 Gyr. Hence, in order to constrain the prevalence of ongoing AGN in BCGs, over a wide range of AGN power, a large sample of BCGs is necessary. The questions related to AGN feedback and the inherent rarity of catching still active AGN is a key motivation for Chapter 4 of this thesis, which attempts to identify clusters around X-ray selected AGN.

1.6 Star Formation and AGN Activity in BCGs

Feedback from AGN activity in galaxies plays a crucial role in galaxy evolution, truncating star formation in massive galaxies (Bower et al., 2006). As has just been discussed, in the case of BCGs their unique environment, at the centre of clusters of galaxies, leads to an interplay between AGN activity and the wider external environment of the galaxy, affecting the evolution of both the host galaxy and

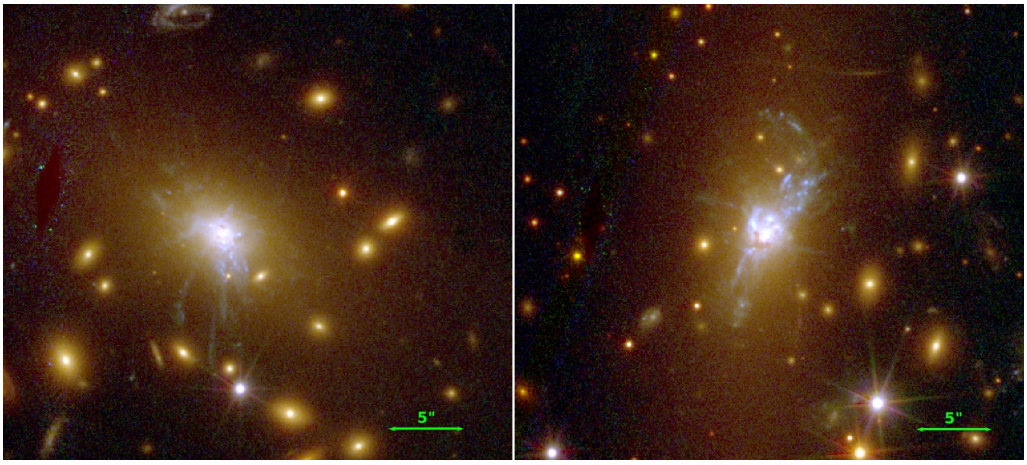

Figure 1.6: *Hubble Space Telescope* images of the star formation in the BCGs of RXJ1532.9+3021 ($z = 0.363$) and MACS1931.8-2653 ($z = 0.352$). Image taken from Fogarty et al. (2015).

the surrounding intracluster medium (ICM). The visible effects of AGN feedback, which are imprinted on the ICM, provide a valuable observational window into how the energy from accretion onto a black hole, at sub-parsec scales, can affect their surroundings on kiloparsec scales. This is otherwise difficult to observe in the low density intergalactic medium around isolated galaxies, making observations of BCGs vital in the quest to understand feedback more broadly.

Although the star formation rates in BCGs are lower than pure cooling models would predict, an enhanced star formation is observed in the BCGs of many clusters (e.g. Egami et al. 2006a; Donahue et al. 2010; Hicks et al. 2010; Liu et al. 2012; Fogarty et al. 2015; see Figure 1.6), which correlates with the gas properties of the host cluster. For example, Wang et al. (2010) find that when comparing optically, and X-ray, selected BCGs, along with non-BCGs, that only X-ray selected BCGs show an enhanced star formation, particularly in cool cores, suggesting that the thermodynamic state of gas is important in BCG activity. Infrared (IR) emission in BCGs is seen to anti-correlate with the X-ray cooling time in the cluster core, both in the far-IR (Rawle et al., 2012), and the Mid-IR (O'Dea et al., 2008), such that more IR luminous BCGs are found in clusters with shorter cooling times .

From X-ray observations the gas entropy of the ICM can be determined, typically defined as $K = Tn_e^{-2/3}$ (e.g. Ponman et al. 1999; Lloyd-Davies et al. 2000; Cavagnolo

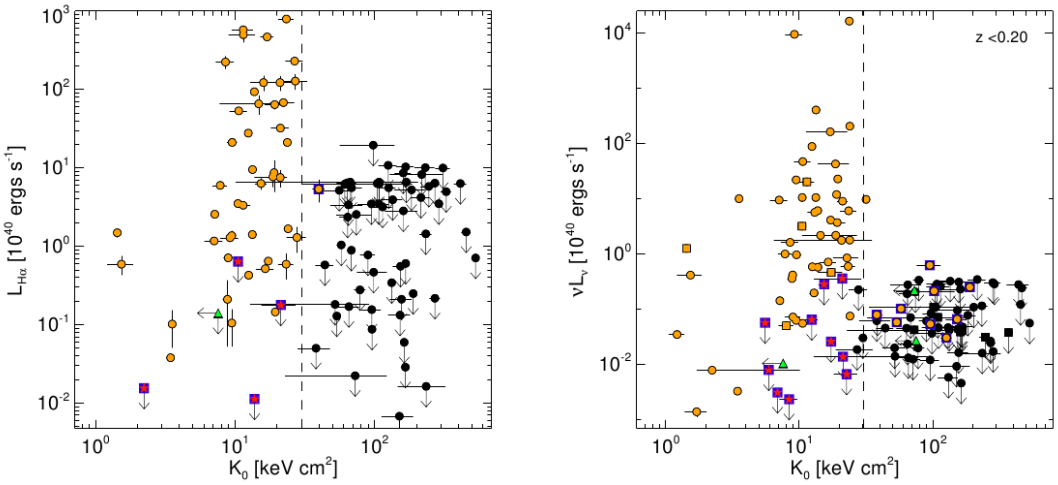

Figure 1.7: *Left*: Central gas entropy of cluster against BCG Hα luminosity. *Right*: Central gas entropy of cluster against BCG radio power. The black dashed lines indicate the apparent entropy threshold for BCG activity of $K_0 \lesssim 30\,keV\,cm^2$. Arrowed points indicate upper limits. Image taken from Cavagnolo et al. (2008).

et al. 2008). This specific entropy term is commonly used in the context of galaxy clusters as it is more strongly associated with the thermodynamic history of clusters than is the temperature. The specific entropy increases when thermal energy is added or decreases when it is radiated away, whereas the gas temperature is also altered when thermal energy is converted into potential energy (Voit et al., 2002, 2005). The gas entropy term is related to the traditional thermodynamic entropy, s, as $s = \ln K^{3/2} + \text{constant}$ (Voit et al., 2005). As the gas entropy is dependent on both temperature and density it provides a good measure of the thermodynamic state of the gas, with cool and dense gas having a low entropy. A number of observational studies suggest the existence of a critical entropy threshold. Cavagnolo et al. (2008) find that strong Hα and radio emission is only present in BCGs below an entropy $K_0 \leq 30\,\mathrm{keVcm}^2$ (see Fig. 1.7). Similarly, Rafferty et al. (2008) find that optically blue cores are found only in clusters with $K_0 \leq 30\,\mathrm{keVcm}^2$, and Hoffer et al. (2012) find BCGs are more likely to show an UV excess and enhanced Mid-IR emission below the same entropy. This apparent critical entropy threshold, equivalent to an approximate cooling timescale of 0.8 Gyr, below which star formation and AGN activity in BCGs is observed, supports the notion that they both result from the

same source, specifically cooled intracluster gas.

For the majority of the examples from the literature given above however the BCGs are rarely drawn from a representative sample of clusters. They are often systems that have had dedicated observation time, across various wavelengths, because they are known to be particularly interesting systems (often cool cores). As a result, few constraints exist on how common BCGs which exhibit signs of star formation or AGN activity are if drawn from a broader cluster sample. In Chapter 3 of this thesis I will investigate the photometric colours of several hundred BCGs in an attempt to address this.

The location of the BCG relative to the X-ray emission also appears to be important in terms of BCG activity, where throughout this thesis I will commonly use the term "activity" to refer to either, or both, star formation and AGN activity, unless otherwise noted. In Stott et al. (2012) for example, a correlation between the radio loud fraction of BCGs and proximity to X-ray centroid is seen. Crawford et al. (1999) find that BCGs with emission lines have smaller separations between their position and the X-ray centroid than BCGs without lines. Similarly Sanderson et al. (2009) find that all the LoCUSS BCGs with optical emission-lines are within 15 kpc of the X-ray centroid and a close correspondence between Hα and radio emission and BCG/X-ray offset exists. These observations hint toward a strong association between activity in the BCG and its proximity to the centre of the cluster potential.

1.7 Gaseous Line Emission in and Around BCGs

Predictions about radiative cooling of the ICM (Fabian & Nulsen 1977; Fabian 1994) suggest that as the gas cools, from the cluster virial temperature, it should lead to the presence of multi-phase gas of decreasing temperature. This should then be traceable through line emission at different wavelength regimes, determined by the temperature of the gas. As we have just discussed, the amount of this multi-phase gas is substantially less than initially predicted, but the existence of this gas has been observed in the majority cool core clusters. For example, lines have been observed at temperatures of $\sim 10^{5.5}$ K, traceable from the O VI line in the UV (Bregman

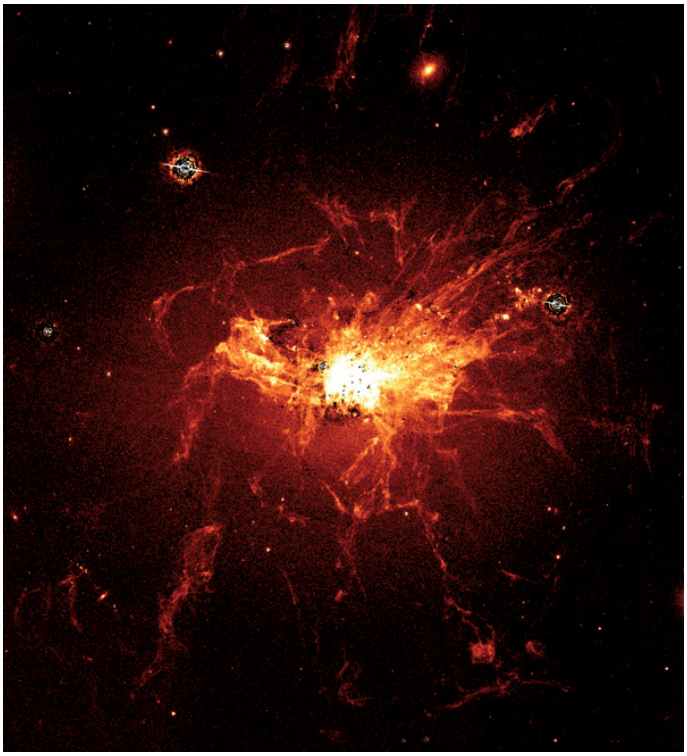

Figure 1.8: An image showing the Hα filaments in NGC1275, the BCG of the cool core Perseus Cluster. Image taken from Fabian et al. (2008).

et al., 2006), 10^4 K, from Hα in the optical (Crawford et al. 1999; Wilman et al. 2006; McDonald et al. 2012b; Hamer et al. 2016), 10^3 K, from warm molecular H_2 gas (Jaffe & Bremer, 1997; Edge et al., 2002; Egami et al., 2006b; Donahue et al., 2011), $\sim 10^1 - 10^2$ K, from C II in cold atomic gas in the FIR (Edge et al. 2010; Mittal et al. 2012), to $\sim 10^1$ K, from CO measurements of cold molecular gas (Edge, 2001; Salomé & Combes, 2003; Russell et al., 2016, 2017).

For a long time it has been observed that there is a strong link between the presence of emission lines in BCGs and cool core clusters (e.g. Heckman 1981; Hu et al. 1985; Johnstone et al. 1987; Heckman et al. 1989; Cavagnolo et al. 2008). A significant fraction of BCGs exhibit some form of optical line emission in their spectra. Crawford et al. (1999), for example, found that of the $\sim$ 200 BCS (Ebeling et al., 1998) X-ray selected clusters 32% had line emission in their BCG, with 27% exhibiting Hα. Of the BCGs with line emission in Crawford et al. (1999), $\sim$ 80% had line intensity ratios consistent with that of nebulae in cool core clusters.

The line emission found in cluster cores is generally found in a filamentary struc-

ture with a radial extent from the core of the central galaxy (e.g. Fabian et al. 2008; McDonald 2011) and is understood to originate from cooling of the ICM (Fabian & Nulsen 1977; Heckman et al. 1989; McDonald et al. 2010). An example illustrating the Hα filaments in NGC1275 is presented in Figure 1.8. The molecular and ionised gas also tend to trace one another in this structure (Jaffe et al. 2005; Salomé et al. 2006; Werner et al. 2014; Tremblay et al. 2016), along with co-spatial dust lanes (McNamara et al. 1996; Edge et al. 1999; Fabian et al. 2016), indicative that the source of the ionisation and warming of gas are coupled. It is possible that the ionised nebulae we see are actually the ionised skin of molecular clouds (Fabian et al., 2011).

There are a number of possible sources of the ionisation. Most notably, (1) AGN, (2) stellar photoionisation, (3) heat conduction between the hot ICM and the cool gas, (4) photoionisation from ICM X-rays, (5) cosmic rays or (6) shocks and turbulent heating. McDonald et al. (2012b) investigate the line intensity ratios of optical line emitting filaments in BCGs and suggest their results rule out (1), (4) and (5) as significant sources. Whilst inconsistent in isolation, photoionisation from young stars and X-rays from the ICM are thought to play some role. But the favoured source of ionisation is composite of star formation and shocks.

The formation origins of the filamentary structure of this cool gas are attributable to three primary potential mechanisms. One is radial gravitational infall, whereby the cooled ICM gas, external to the galaxy, is in gravitational free-fall into the BCG. Alternatively, a number of recent observations reveal that these filaments often trace the shape of radio bubbles/X-ray cavities (e.g. Russell et al. 2017), which suggest that perhaps the cool gas gets buoyantly lifted with the plasma. The third mechanism is the cool gas gets entrained within the radio jets and uplifted that way. Or, it is possible that all three play an active role.

A rare but interesting phenomena is that a handful of clusters have been observed where the line emission in the cluster core is physically offset from the BCG. These include A1991 and A3444 where the line emission is offset in both by $9 - 13$kpc (Hamer et al., 2012), Ophiuchus (offset by 2.2kpc) (Edwards et al., 2009; Hamer et al., 2012) and A2146 (Canning et al., 2012). For all four of these systems the

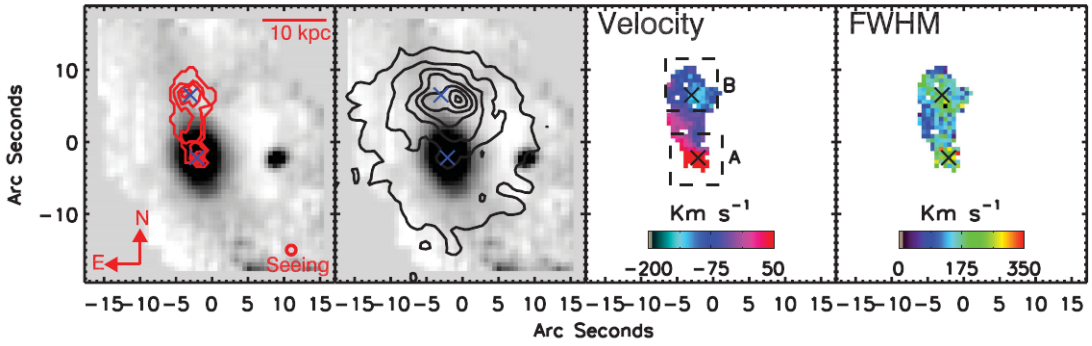

Figure 1.9: This figure illustrates the offset optical line emission observed in A1991. *Left*: Hα contours in red overlaid onto the stellar continuum. *Centre–left*: X-ray contours in black overlaid onto the stellar continuum. *Centre–right*: Hα velocity and *Right*: Hα velocity dispersion. Image taken from Hamer et al. 2012.

peak in X-ray surface brightness is offset from the BCG, but is cospatial with the offset optical line emission. An example of the Hα and X-ray distribution of the core of A1991 are given in Fig. 1.9 from Hamer et al. (2012). It is understood therefore that these represent systems where the ICM is radiatively cooling, leading to a cooling flow, but where the X-ray peak has been perturbed away from the central galaxy, in a process known as sloshing of the ICM (Ascasibar & Markevitch 2006; ZuHone et al. 2010, 2011).

Gas sloshing is thought to arise when the potential of a passing/infalling subcluster pulls on the dark matter and gas of the main cluster. Whereas the dark matter is collisionless, the gas is subjected to ram pressure, causing the gas to separate from the dark matter potential. The gas then sloshes back and forth within the cluster potential, often leading to a set of spiral shaped cold fronts (see Markevitch & Vikhlinin 2007 for a review). If the main cluster is a cool core cluster than the low entropy gas gets entrained in this sloshing motion. However, the BCG in this scenario retains its position at the centre of the dark matter potential, meaning the cool core and BCG can decouple, leading to the offset between the BCG and the X-ray peak.

As well as the cospatial X-ray and line emission peaks, the X-ray contours of these systems show elongation in the direction of the offset line emission indicative

of their disturbed nature. The deep *Chandra* observation by Werner et al. (2016) of the Ophiuchus cluster, which has offset line emission (Edwards et al., 2009; Hamer et al., 2012), demonstrates clear signs of dynamical disturbance in its core, such as a truncated cool core. There also exist multiple cold fronts and the likely existence of a subcluster. All of which point toward a recent cluster scale interaction.

In addition to the optical line emission, Hamer et al. (2012) find $\sim 10^9\,M_\odot$ of molecular gas in observations of CO in A1991, spatially coincident with the offset Hα nebulae. They conclude that the presence of a substantial mass of molecular gas, offset from the galaxy, is indicative that the gas cooling in a cool core can occur in isolation from the BCG. The close association normally found between cooling ICM and line emission in BCGs is therefore likely just a reflection of the close proximity that BCGs usually have with the ICM density peak. The study of offset line emission could thus reveal properties of cooling flows, without the feedback effects introduced by the nucleus of the BCG.

In Chapter 7 of this thesis I will explore the optical line emission of several BCGs. The kinematics of the line emitting nebulae will be presented, as well an investigation into the source of the ionised gas. Newly identified examples of offset line emission will be presented.

1.8 The Aims and Structure of This Thesis

This thesis aims to explore the properties of BCGs in relation to some of the outstanding problems discussed in this introduction.

Chapter 2 will describe the cluster sample, which forms the foundation of this thesis. A description of the optical photometry based on Pan-STARRS imaging will be given, as well as a description of the red sequence selection. The first results highlighting properties of the red sequences of these clusters will be explored.

In Chapter 3 BCG colours, ranging from the UV to the mid-IR, will be explored as tracers of star formation and AGN activity in BCGs. This chapter aims to constrain the prevalence of active BCGs in a representative cluster sample. The relationship between BCG colours and the presence of optical line emission will be

explored, as well as with the X-ray luminosity of the host cluster.

Chapter 4 involves a systematic investigation of X-ray selected AGN, looking for signs of an otherwise undetected cluster. This Chapter aims to address the ambiguity between AGN and clusters in low spatial resolution X-ray data, which introduces a selection effect against the identification of AGN in BCGs. As discussed above, these systems are inherently rare, yet provide vital insight into AGN feedback.

Chapter 5 will introduce the concept of integral field spectroscopy and a description of the MUSE instrument. The target selection and spectroscopic methodology for both stellar and gaseous kinematics will be reported.

In Chapter 6 the stellar kinematics of 23 BCGs, selected to have close companion galaxies, will be explored with integral field spectroscopy. The aim is to constrain the stellar mass growth of BCGs at $z < 0.25$.

Chapter 7 will explore the properties of optical line emitting nebulae in cluster cores, including new examples of line emission offset from the BCG. The kinematics and source of ionisation for these nebulae will be reported.

Finally, in Chapter 8 the main results will be summarised as well as a description on how these can be developed further. Then some concluding remarks will be made.

1.9 Afterword

Throughout this thesis we adopt AB magnitudes, except for the presentation of *WISE* data which uses Vega, and assume a standard cosmology of $H_0 = 72\,\mathrm{km\,s^{-1}\,Mpc^{-1}}$, $\Omega_M = 0.27$ and $\Omega_\Lambda = 0.73$.

Chapter 2

The Cluster Sample and Optical Data and Techniques

2.1 Overview

All of the following science Chapters in this thesis are, at least to some extent, reliant on the cluster sample introduced in this Chapter, as well as analysis of Pan-STARRS imaging described. The following Chapter will outline the composition of the cluster sample, as well as details regarding the computation and distribution of X-ray luminosities for these clusters. A description of the photometry, performed on Pan-STARRS PS1 3π optical imaging, will be given, as well as a description of the red sequence selection algorithm developed and applied to this imaging. Resulting properties of the red sequence; colour, richness and slope will also be presented.

2.2 The Cluster Sample

The research in this thesis utilises a large sample of *ROSAT* All-Sky Survey (RASS) X-ray selected clusters, drawn together by years of work by Alastair Edge and Harald Ebeling from their own analysis and from the literature. The subset of this cluster sample, used throughout this thesis, consists of 981 clusters within the Pan-STARRS-1 (PS1) 3π survey footprint and within the redshift interval $0.03 < z < 0.5$. The sample is drawn from a systematic investigation into the RASS Bright Source

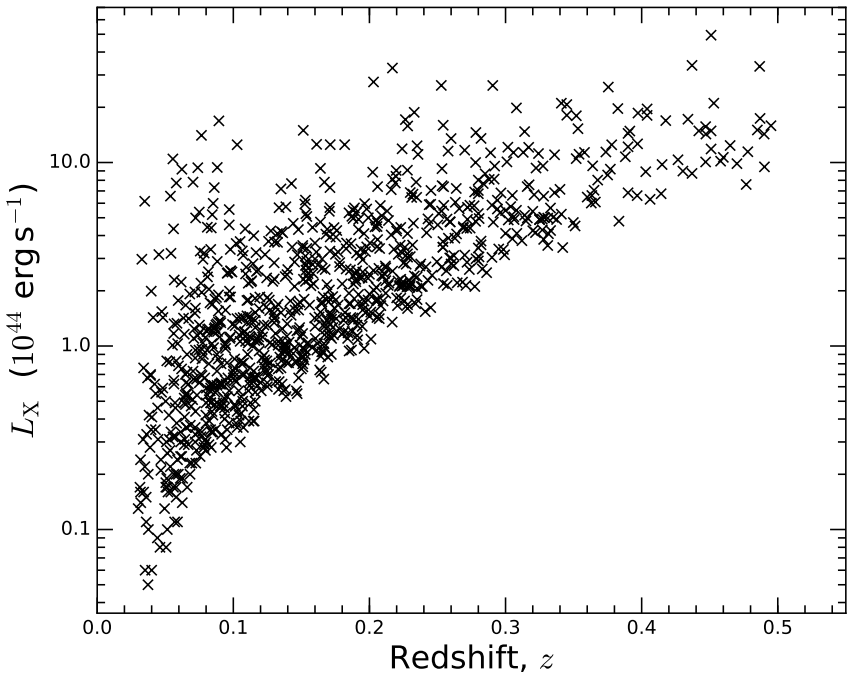

Figure 2.1: The RASS 0.1–2.4 keV X-ray luminosity and redshift for each of the 981 clusters in this sample.

Catalogue, BSC (Voges et al., 1999). Included in this are all published samples within the PS1 3π footprint, namely the Brightest Cluster Sample, BCS, (Ebeling et al., 1998), the extended Brightest Cluster Sample, eBCS, (Ebeling et al., 2000), the *ROSAT* ESO Flux Limited X-ray survey, REFLEX (Böhringer et al., 2004), the Northern *ROSAT* All-Sky Galaxy Cluster Survey, NORAS, (Böhringer et al., 2000) and the Massive Cluster Survey, MACS, (Ebeling et al. 2001, 2007, 2010). It also includes all cluster identifications of RASS Bright Source Catalogue sources below the flux limits of these published surveys. The sky coverage of these additional clusters is not uniform, due to variation in the exposure time and Galactic column density, but this spatial incompleteness does not affect any particular class of cluster more than another. Therefore, while the fainter clusters are incomplete and do not constitute a flux–limited sample, these clusters can still be used as a representative sample of the overall population. In Chapter 3 we investigate BCG activity – however the duty cycle of an AGN, or a burst of star-formation activity, is relatively short – so in order to capture a meaningful number of these rare events we need to maximise the parent sample we study.

With X-ray luminosities ranging over two dex, but with a median luminosity, $L_{\rm X} \sim 2 \times 10^{44}\,{\rm erg\,s^{-1}}$, the sample covers a broad range of cluster mass, whilst still including only massive clusters (i.e. not groups). The redshift and X-ray luminosity distribution of our sample is given in Figure 2.1. The X-ray luminosities are all drawn from the RASS, corrected for Galactic absorption and are quoted in the band 0.1–2.4 keV. We stress that from Fig. 2.1 it is evident that only the highest X-ray luminosity clusters in our sample cover the full redshift range.

The cluster redshifts come from a combination of different papers, primarily the three main ROSAT Surveys, BCS, eBCS and REFLEX, with additional information from large redshift surveys, e.g. the Sloan Digital Sky Survey (York et al., 2000) and the 6dF Galaxy Redshift Survey (Jones et al., 2004), and long slit spectroscopy by Harald Ebeling and Alastair Edge using UH2.2m, Keck and NTT. All clusters have at least one spectroscopic redshift, with typically 5–10 redshifts for all $z < 0.25$ clusters in the SDSS footprint and in many cases > 100 for the richest $z < 0.1$ systems. Note that not all BCGs have a spectrum that covers Hα, so the spectral completeness for lines is less that 100 per cent (see Chapter 3).

2.2.1 X-ray Photometry: RASS

Declaration: The data analysis described in this section (§ 2.2.1) was performed by Alastair Edge/Harald Ebeling.

The count rates were recorded by the PSPC in channels 11–235 ("broad-band") during the RASS. These were then converted to unabsorbed X-ray fluxes in the 0.1–2.4 keV band by convolving the cluster X-ray emission with the PSPC detector response function. In this process, the cluster emission is modelled as a hot thermal plasma, characterised by metallicity (frozen at 0.3 Solar) and an intra-cluster gas temperature kT. Since the latter has not been measured for the vast majority of the clusters in our sample, it was estimated iteratively, from the observed redshift and the inferred bolometric X-ray luminosity in the cluster rest-frame, using the $L_{\rm X}$-kT relation of White et al. (1997). In order to correct for absorption by Galactic gas the $n_{\rm H}$ column densities compiled by Dickey & Lockman (1990) were adopted. In practice, this process for translating counts to fluxes was performed as an interpo-

lation in three dimensions ($n_{\rm H}$, kT, z).

This sample included all cluster identifications of RASS Bright Source Catalogue (Voges et al., 1999) sources below the flux limits of the published RASS cluster catalogues. However, as the RASS Bright Source Catalogue source detection was optimised for point sources, the count rate estimates from it may underestimate the counts from extended sources. The magnitude of this effect was investigated by Ebeling et al. (1998) as a function of extent and found to be significant (a factor of > 1.3) in only the most extended sources. A statistical correction for the missing extended flux from the unpublished clusters was therefore made by determining the ratio of count rates for the brightest clusters (the ratio of BCS and eBCS rates to the BSC rates) as a function of redshift. Above the redshift lower limit of $z = 0.03$ this ratio is at most a factor of 2.5, with an average of 1.2 for $z > 0.05$. The X-ray morphology of each individual cluster however is not accounted for in this correction, hence the flux of a few of the most nearby, most extended systems is likely underestimated.

2.3 Pan-STARRS 3π Survey

The Pan-STARRS, PS1 3π survey (Tonry et al., 2012) is a wide-field photometric survey in the optical g, r, i, z and y bands. Covering the entire sky north of a Declination of $-30°$, the survey is conducted with the 1.8 m PS1 telescope in Hawaii, with an imaging pixel resolution of 0.25 arcsec per pixel. Images are made by the stacking of multiple exposures, with typical total exposure times of $\sim 800 - 1000$ seconds, achieving typical depths of ~ 22 mag in the i-band.

2.3.1 Optical Photometry

Using postage stamps from the PV3 data release, we performed aperture photometry on the *griz* bands using Source Extractor (SExtractor) (Bertin & Arnouts, 1996). SExtractor was run in dual mode, using the i-band as the detection image, due to red-sensitive nature of the instrument. The inbuilt CLASS_STAR function was used for star-galaxy separation with a very conservative cut of < 0.95 applied,

(where 1 is a star and 0 is not), as the misidentification of faint galaxies as stars was more problematic than stellar contamination in this work. Magnitudes are given by the MAG_AUTO parameter, which measures the flux within a flexible elliptical aperture with a Kron–like radius (Kron, 1980), and colours are derived from the MAG_APER parameter, with a fixed circular aperture.

An aperture diameter of 4 arcsec was used to measure colours. This is intentionally small, minimising contamination from source blending in the dense cluster environment. This is supported by a χ^2 test which revealed apertures of this size minimised the scatter in the colour-magnitude relation. Metallicity (or age) induced colour gradients across galaxies are known to exist (Cardiel et al., 1998), so in order to quantify the effect of aperture size on colours, the 40 lowest redshift BCGs (median $z = 0.035$), which generally have the largest angular size on the sky and hence should represent the most extreme cases, were measured at aperture diameters of 4, 15, and 30 arcsec. In the case of the most extreme difference, that is between the (g–r) colour measured in a 30 arcsec and 4 arcsec apertures, (corresponding to median angular diameters of 20.5 kpc and 2.7kpc respectively), a median/mean colour difference of only $0.04^{+0.05}_{-0.04}$ mag was measured, which has a negligible effect on our analysis.

Throughout this thesis optical Galactic reddening corrections are made using the Galactic Extinction calculator available through the NED[1], based on the Schlafly & Finkbeiner (2011) extinction maps. And, where needed, K-corrections are made assuming a simple stellar population model, (Bruzual & Charlot, 2003), with solar metallicity, a Chabrier Initial Mass Function, formation at $z = 3$ and subsequent passive evolution.

2.4 Identifying the BCG

The identification of the BCGs was made via a visual inspection in the Pan-STARRS 3π imaging. The selection was primarily based on their morphology and centrality, looking for the visually most extended galaxy - often with a cD-like profile - at

[1] http://ned.ipac.caltech.edu/forms/calculator.html

the centre of the galactic distribution. As such, the BCG need not necessarily be photometrically the brightest galaxy. For the most part, selection of the BCG was obvious, however, when the choice of galaxy was ambiguous (as was the case for approximately 5% of the BCGs), the candidate best aligned with the X-ray emission was selected. Visual identification, although time consuming, is probably still the most reliable method, minimising issues with projection. Visually inspecting each image also aided in the identification of misclassified X-ray point sources in the sample, since these generally lack the visually obvious galactic overdensities characteristic of clusters. Additionally, as in Chapter 3 the colours of BCGs are investigated, an automated BCG selection, which often relies on the application of colour cuts, would not have been appropriate.

Lauer et al. (2014) find that if taking the literal definition of a BCG as the brightest galaxy, then 12% of local clusters have a BCG $>$ 500 kpc from the X-ray centre. They conclude these are likely drawn into a cluster from recent merger events, as modelled by Martel et al. (2014). However, as we are interested in the interplay between the BCG and its traditionally-central environment, we redefine our BCGs as the brightest, most extended, central galaxy.

2.5 Cluster Red Sequence

The cluster red sequence, the observed linear relationship between magnitude and colour for cluster galaxies (§ 1.2.1), was selected using a multi-colour band approach. First, a conservative colour cut was applied around the expected red sequence colour, given its redshift. Then, in order to capture the non-zero slope, the magnitudes were binned and the median colour selected for each bin. A further colour cut was then applied around each of these median colours and a linear fit was made to the remaining sources, constituting the initial red sequence fit. The colour index spanning the rest-frame 4000Å break and the adjacent redder-colour index were then cross-matched, with only sources that fit the initial red sequence in both colour bands classified as red sequence galaxies. Because cluster early type galaxies are the reddest, brightest galaxies at a given redshift, this stage reduces contamination

of the red sequence, as spanning the 4000Å break provides the most significant contrast with field galaxies. The linear fit and colour cross-matching process was then repeated iteratively, decreasing the width of the colour clipping each time, until a final clip of ± 0.1 mags around the red sequence best fit was made and defined as the cluster red sequence. The analysis of the colour-magnitude relation was restricted to a radius of 0.5 Mpc around the BCG position, corresponding to an angular radius of 856 and 83 arcsec at $z = 0.03$ and $z = 0.5$ respectively.

In order to better illustrate the selection process, and the logic behind some of the selection criteria, examples of colour magnitude diagrams for some of the clusters in this sample are provided in Figs. 2.2 – 2.5. These represent some typical red sequences at different redshifts. Fig. 2.2 shows a typical red sequence for a reasonably rich cluster, whereas Fig. 2.3 shows that of a poorer cluster at similar redshift. This property of red sequence richness will be explored in § 2.5.3. Note that at these redshifts, the 4000Å break resides in g–r, so red sequence is made in g–r and r–i. A1201, shown in Fig. 2.4, is an unusual case where there is a structure at $z = 0.068$, foreground to the $z = 0.169$ cluster, leading to two distinct red sequences in the g–r colour magnitude diagram. A *Chandra* observation reveals that the X-ray contribution from the foreground structure is negligible. But, this example illustrates the advantage of using a colour regime which spans the 4000Å break, leading to the distinct distributions in g–r, which is less evident in r–i and i–z. It also illustrates the benefit of selecting red sequence galaxies which lie near the best fit line in two separate colour regimes. If the red sequence selection had been made in r–i or i–z in isolation, without the constraint from g–r, the apparent red sequence for this cluster would be strongly contaminated by foreground galaxies. Fig 2.5, of MACSJ1006.9+3200 at $z = 0.403$, illustrates how the red sequence selection becomes more uncertain at higher redshift. At high redshift, ($z \gtrsim 0.3$), only the very brightest few red sequence galaxies are detected, giving few points on which to select and extrapolate the red sequence. This leads to uncertainty in the red sequence slope (§ 2.5.1) and resulting colours (§ 2.5.2). Note that by this redshift, the 4000Å break has transitioned into r–i, so the red sequence selection is made on the r–i, i–z colours, as the red sequence in g–r becomes far less pronounced.

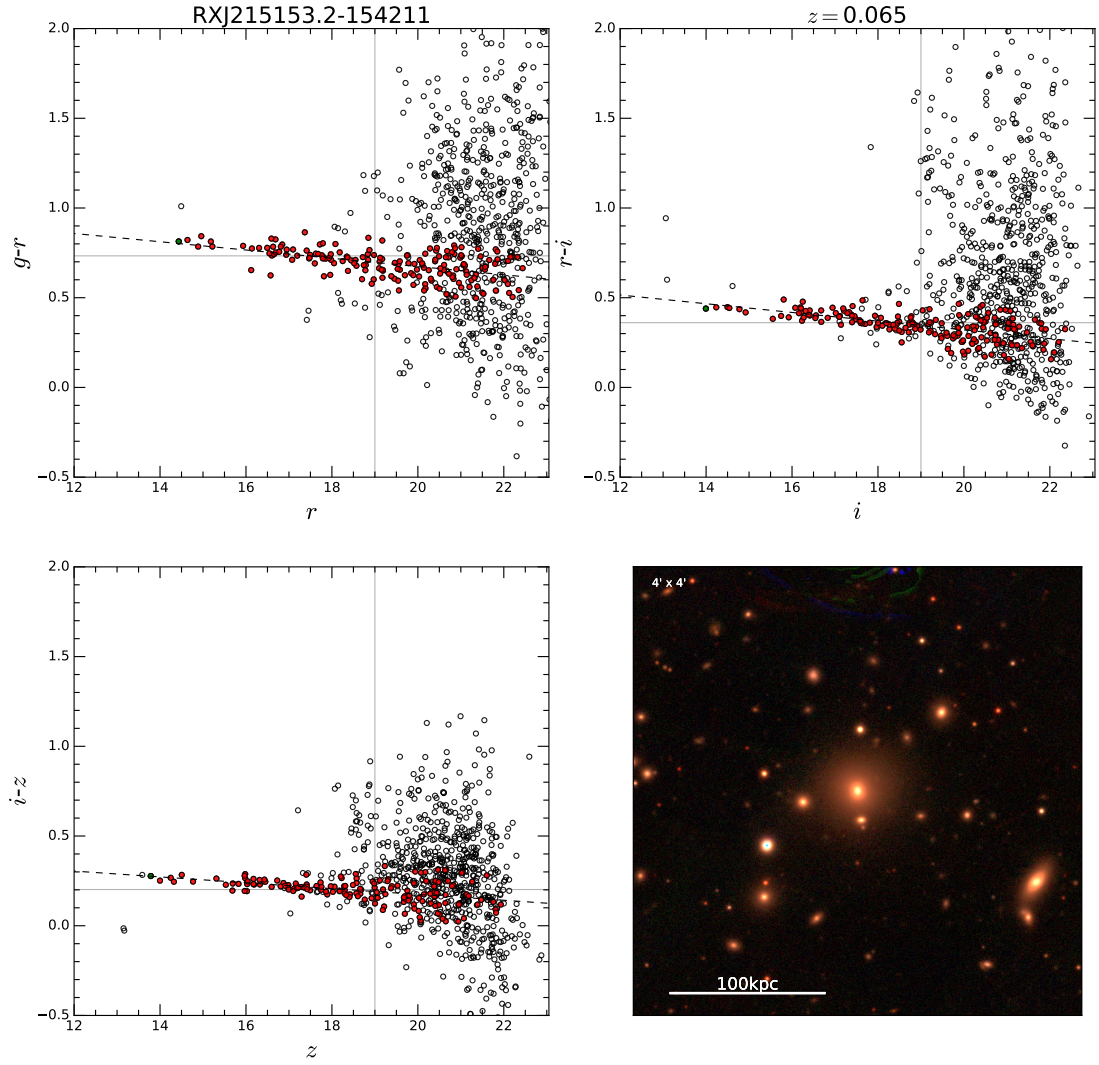

Figure 2.2: Colour magnitude diagrams and a *gri* colour composite image for cluster RXJ215153.2-154211. In the colour magnitude diagrams the black empty circles represent all sources detected within 0.5 Mpc of the BCG. The filled red circles represent those sources which are selected as red sequence galaxies. The green filled circle in each panel indicates the BCG. The black dashed lines are the best fitting lines to the red sequences, and the points at which the solid grey lines intersect indicates the expected red sequence colours at a flux of 19th mag (derived from the best fitting trends in Fig. 2.7).

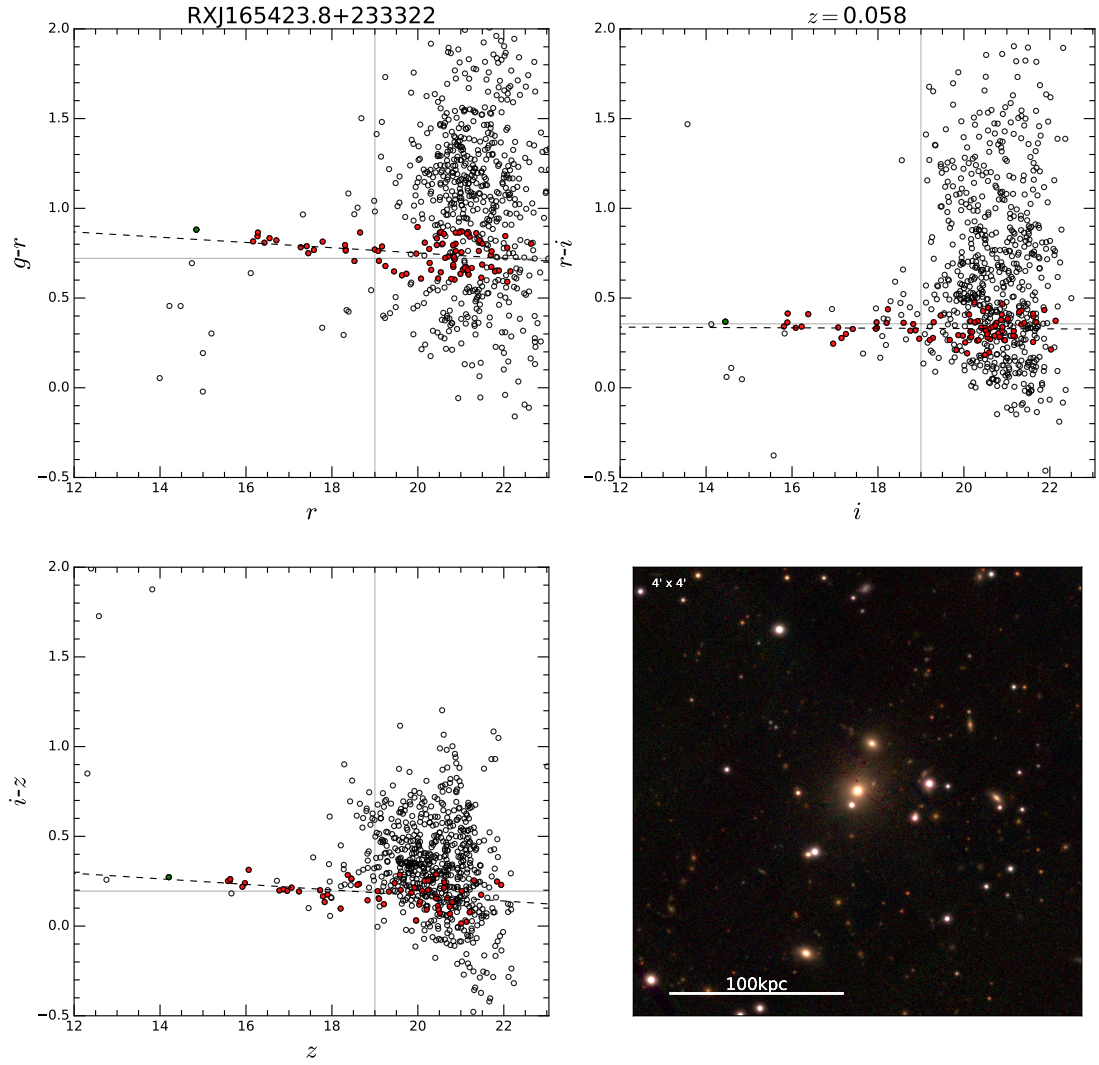

Figure 2.3: Similar to Fig. 2.2 but for cluster RXJ165423.8+233322.

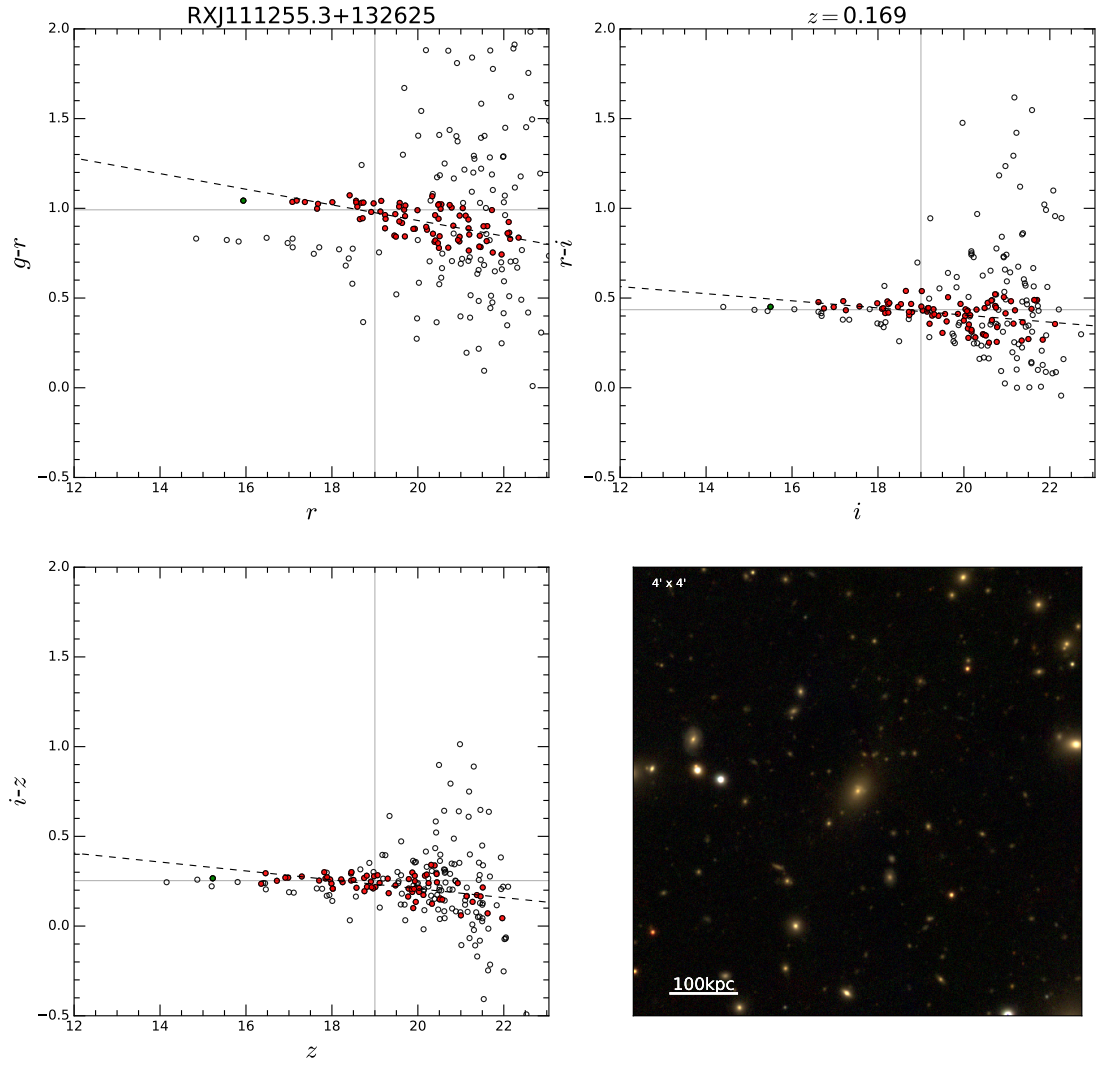

Figure 2.4: Similar to Fig. 2.2 but for cluster RXJ111255.3+132625, a.k.a A1201.

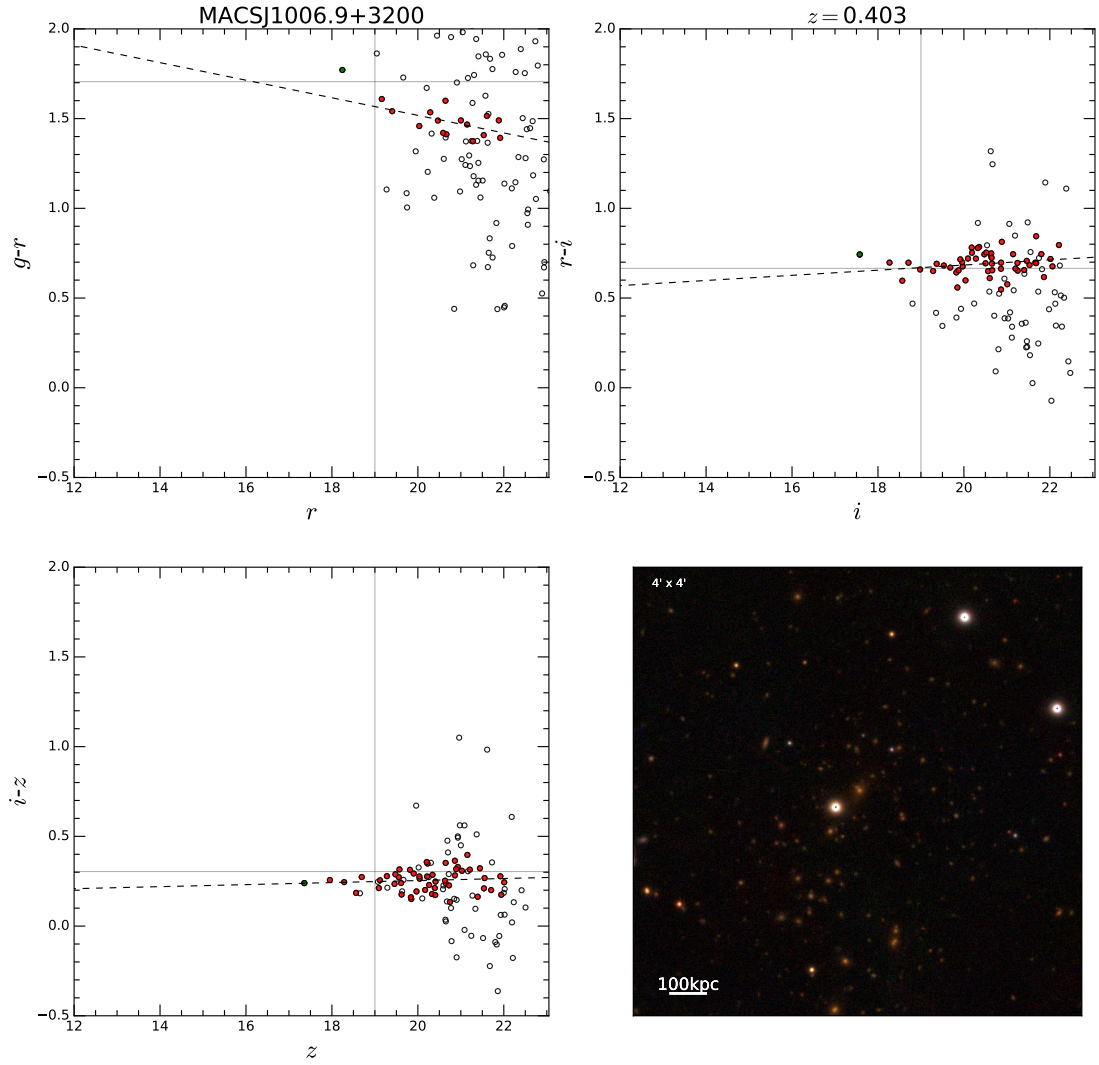

Figure 2.5: Similar to Fig. 2.2 but for cluster MACSJ1006.9+3200.

2.5.1 Red Sequence Slope

The observed slope of the red sequence is expected to steepen negatively with respect to an increasing redshift. Semi-analytic models by Kaviraj et al. (2005) find a steepening slope with respect to redshift, consistent with hierarchical formation models. This has been observed in literature, although the steepening is generally slight (e.g. López-Cruz et al. 2004; Stott et al. 2009). We determine the slope of the red sequence in g–r as displayed in Figure 2.6. Although the distribution for an individual cluster is varied, particularly at high redshift, we do see a weak trend of steepening of the red sequence with respect to redshift. That is, the slope gets increasingly more negatively sloped at higher redshifts. The cause of this trend is debated in the literature however, López-Cruz et al. (2004) for example attribute the variation in slope as the sampling of bluer rest–frame wavelengths at higher redshift, and claim when correcting for this the slope is indeed uniform, whereas Stott et al. (2009) attributes it to the build up of the red sequence over time.

A point to note is that this trend is contrary to an expected observational effect resulting from the use of fixed apertures to measure colour. As galaxies have an inverted colour gradient, such that they are increasingly redder towards the centre, colours are measured over a varying fraction of their effective radius for different sized galaxies, and at different epochs. At low redshift, particularly for the most massive end of the red sequence, we are measuring only a relatively small fraction of the galaxy, (with an aperture size equivalent to 2.3 kpc at $z = 0.03$ for example). As a fraction of the effective radius a galaxy, this is much higher for the low mass galaxies, than the high mass ones. Hence this would be expected to emphasise the slope of the red sequence between low and high mass galaxies. Whereas at higher redshift, a higher fraction of the effective radius of a galaxy is included in the same fixed aperture, (with an aperture size equivalent to 24 kpc at $z = 0.5$), reducing any aperture contributions to the relative colour difference between the low and high mass ends of the red sequence. So aperture effects alone are expected to contribute towards a shallower gradient at high redshift, contrary to the observed trend.

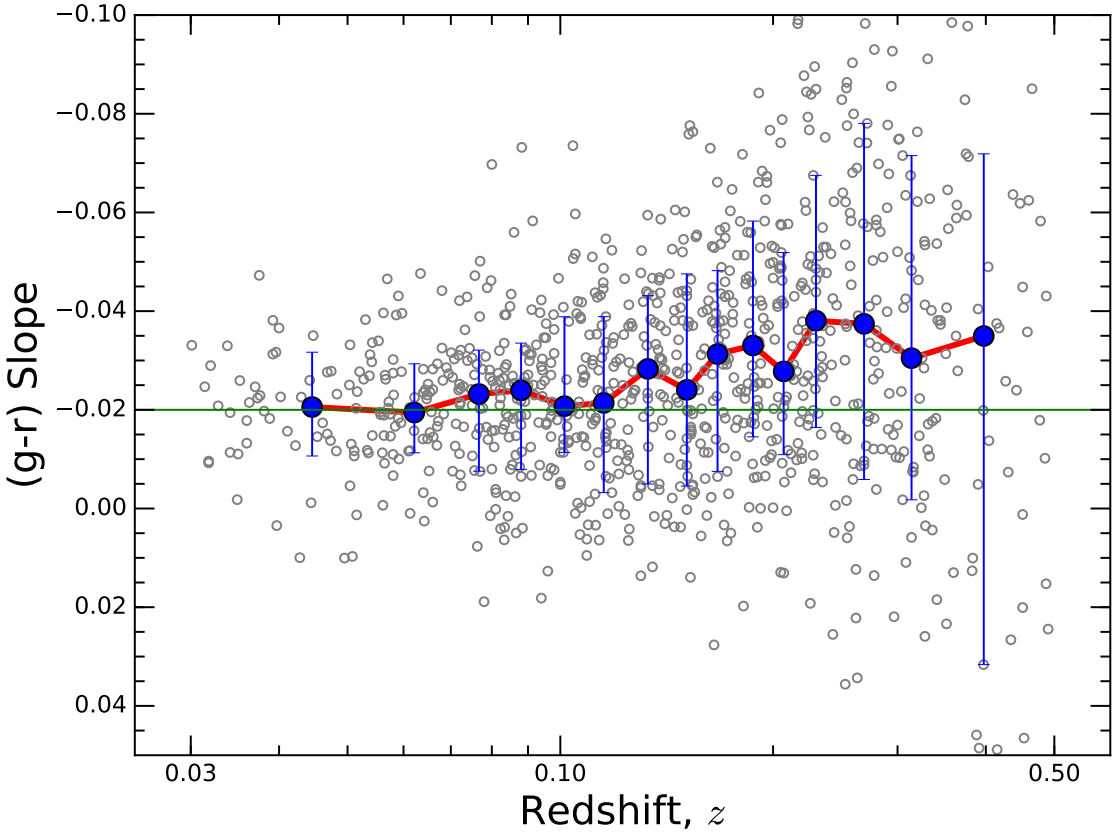

Figure 2.6: Slope of the red sequence in g–r, against redshift. The empty grey data points correspond to the slope for an individual cluster red sequence. The filled blue circles indicate the median slope and redshift value after binning the data into 15 equal sized bins (each containing 66 clusters). The error bars represent the 16th and 84th percentage quartiles of the distribution in slope in each bin. The green solid line is a straight line at $y = -0.02$ to guide the eye to the changing nature of the median slope over redshift.

2.5.2 Red Sequence Colour

In Fig. 2.7 we explore the PS1 g–r, r–i and i–z colours of the red sequence, measured at a fixed flux of 19th magnitude, and how this relates to redshift. We measure this at magnitude 19 as the red sequence generally pivots about this value, thus minimising the colour error due to the uncertainty of the red sequence slope. The small level of scatter of this distribution illustrates the homogeneity of the cluster red sequence population, despite the different cluster environments and masses in our sample (Andreon, 2003). The observed evolution with z is dominated by the transition of the 4000Å break through the photometric bands (i.e. the redshift evolution that one would K-correct for), and also the relative change in position of 19th magnitude along the red sequence gradient (which typically goes redder at the bright end).

The tight relationship in red sequence colour with redshift means the colour of a cluster's red sequence can provide an estimate for its redshift. In Fig. 2.8 we test this by comparing the redshift predicted by its red sequence g–r colour, against the actual redshift, for our cluster sample. We find that the predicted and actual redshift agree to within 0.025 at $1\,\sigma$. The spectrum were rechecked for clusters in which the predicted redshift significantly deviated from their catalogued redshift, in order to verify the correct redshift had been catalogued, and was amended where necessary. We are confident therefore that deviations in the predicted redshift are due to uncertainties in the red sequence colour. The increased scatter at higher z is due to the increased difficulty in reliably selecting the red sequence. At high redshift, ($z > 0.3$), only the very brightest few red sequence galaxies are detected, giving few points on which to select and extrapolate the red sequence. The largest source of uncertainty is correctly sampling the red sequence slope. Poor selection of the red sequence at high z accounts for those clusters with significant redshift residuals.

The colour of the cluster red sequence provides a standard for the colour one would expect for a passively evolving galaxy on the red sequence. The equivalent colour of the BCG can thus be compared to this and hence used to determine whether deviations from passivity exist for these galaxies, which is explored in Chapter 3. In addition to this, analysis of the red sequence is a useful tool in identifying and

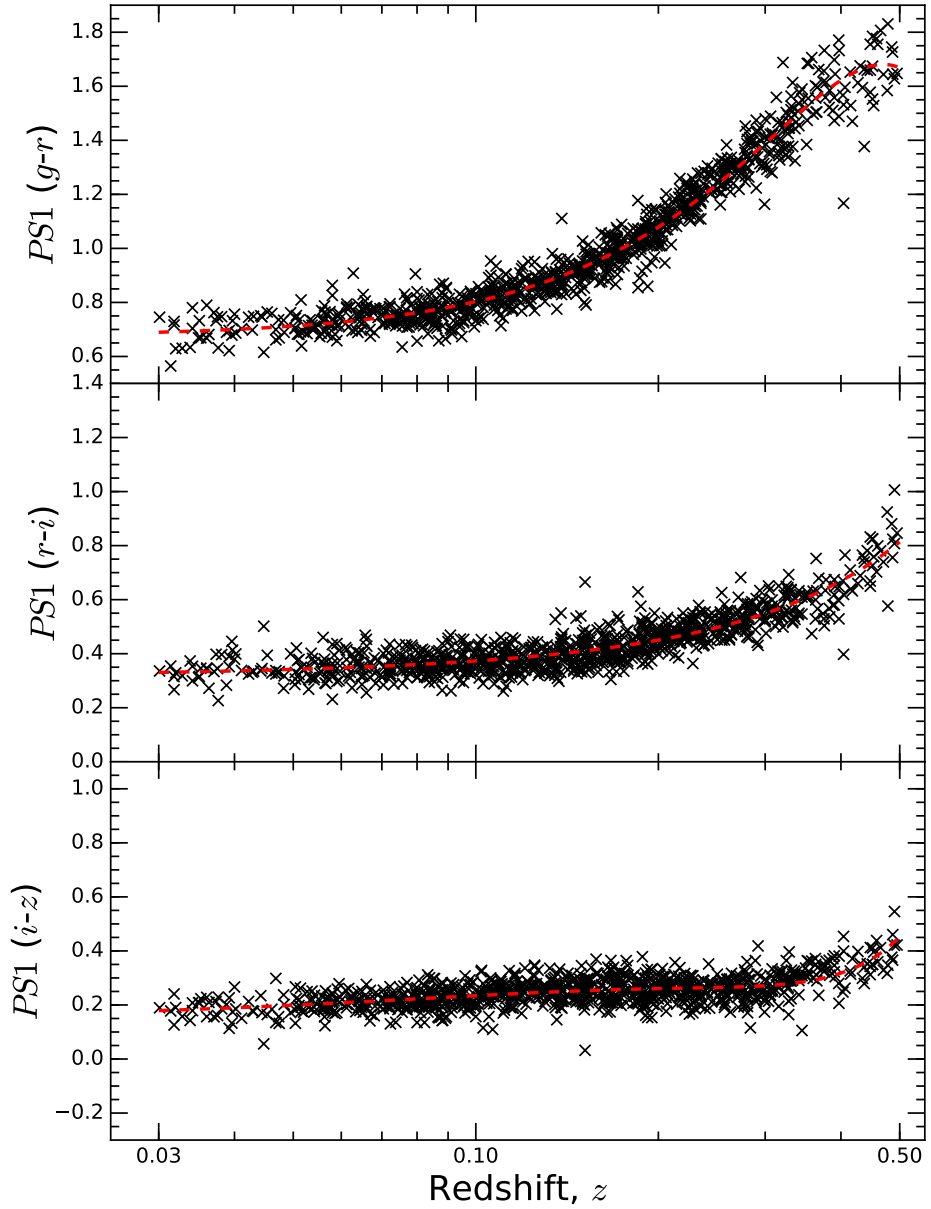

Figure 2.7: PS1 g–r (top panel), r–i (middle panel) and i–z (bottom panel) colours of the cluster red sequence, against redshift. The red sequence colour is measured at a flux of 19th magnitude for each cluster. The (red) dashed line in each panel show the best fitting trend.

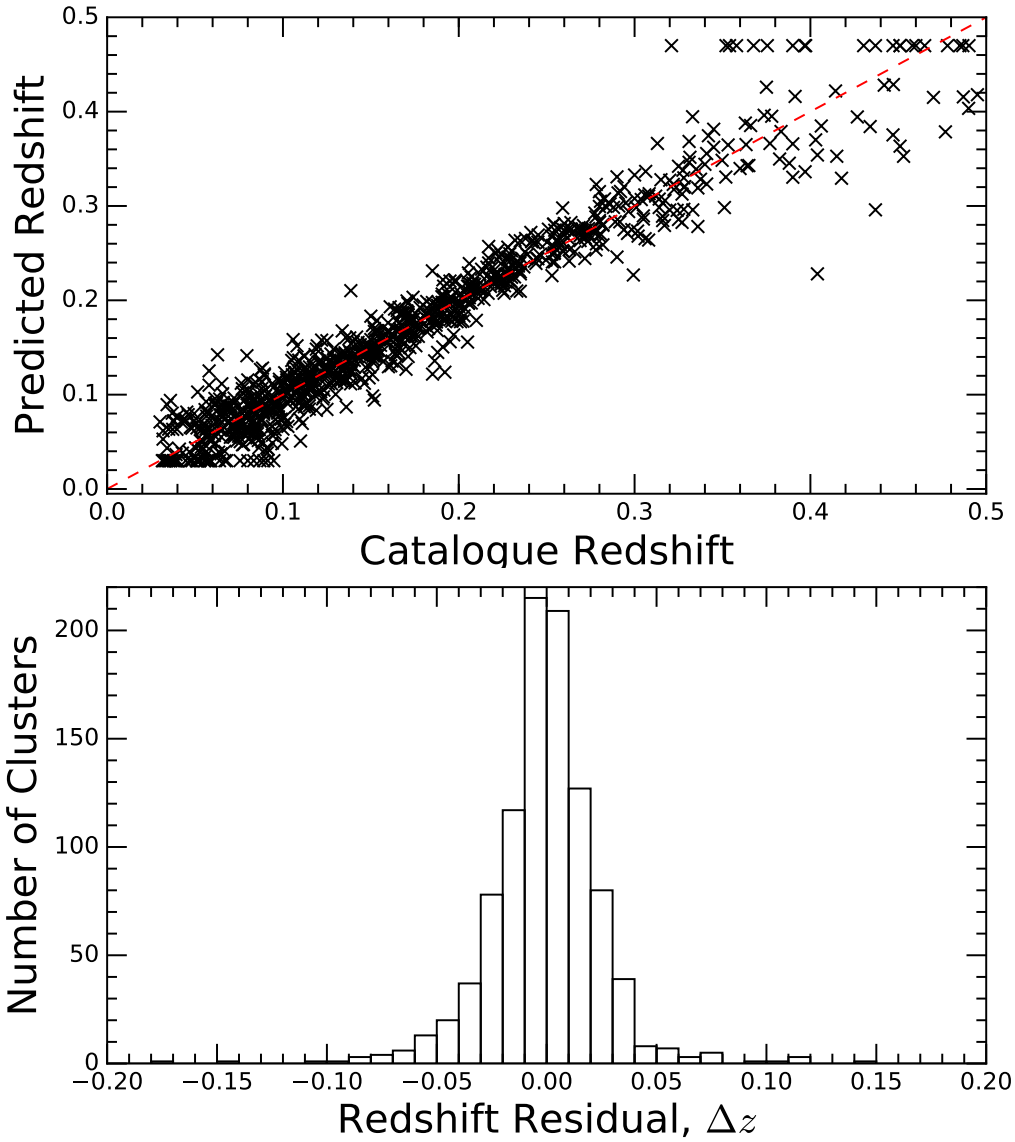

Figure 2.8: Top: The predicted redshift, derived from the g–r colour of the red sequence, against the catalogued redshift for each cluster. Bottom: The redshift residuals between the predicted and actual redshifts. The distribution has a mean at zero and standard deviation of 0.025 . At higher redshifts there are sometimes very few red sequence galaxies above the PS1 flux depth, and as a result the true red sequence is difficult to select correctly; this explains those cases where the predicted redshift and actual redshift significantly deviate. Also, any red sequence colour above our peak in the curve results in a predicted redshift corresponding to the sample maximum at ~ 0.46.

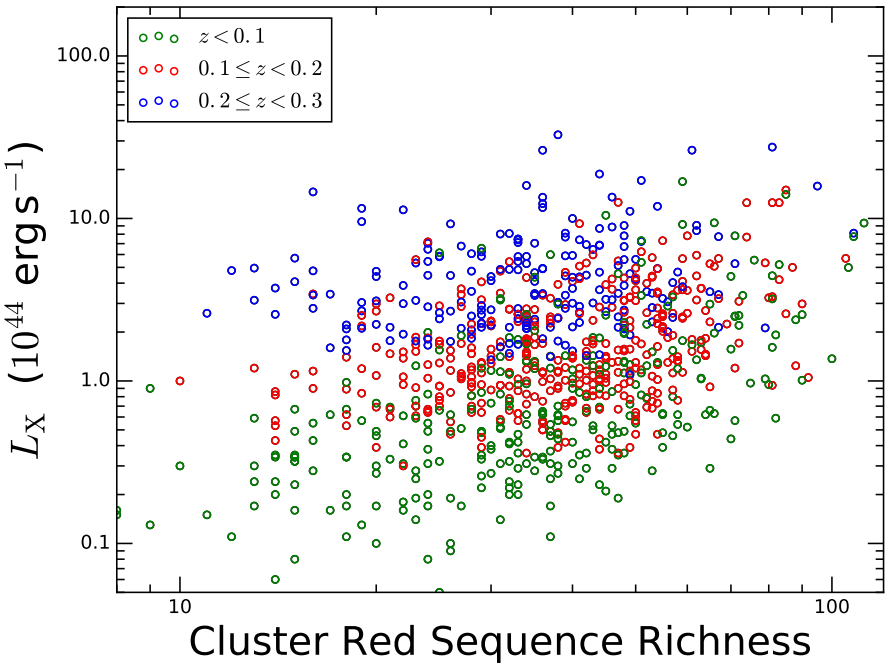

Figure 2.9: *ROSAT* All Sky-Survey X-ray luminosity against red sequence richness (number of red sequence galaxies above i-band luminosity of -19 mag).

removing any misclassified source in the X-ray catalogue. For example, a number of sources ($\sim$ 20) in the initial sample were misidentified as clusters, but were in fact found to be point sources, such as AGN and white dwarfs. The lack of red sequence in such cases made identification, and thus removal, of these simple. This ambiguity between AGN and clusters in low spatial resolution X-ray data will be explored further in Chapter 4.

2.5.3 Red Sequence Richness

In the hierarchical growth scenario galaxy clusters grow a through a process of smooth accretion and mergers, both of which contribute new galaxies and mass to the cluster. So you would expect to find an observational connection between the richness of a cluster, that is the number of galaxies in it, to scale with the cluster mass, which has been observationally confirmed (e.g. Hall et al. 1997; Johnston et al. 2007; Andreon & Hurn 2010). Hence we expect that the richness of the cluster red sequence – that is, the number of galaxies selected on the cluster red sequence – should scale with the X-ray luminosity of the cluster, (since L_X traces cluster

mass). We define richness of the red sequence as the number of galaxies on the red sequence above an i–band luminosity of -19 mag. We find in Figure 2.9 a weak correlation between $L_{\rm X}$ and red sequence richness for the cluster sample, but with considerable scatter. A source of scatter in the richness is that we perform our optical photometry within a fixed 0.5 Mpc aperture around the central galaxy. Hence, richness is actually a measure of galaxy density, so diffuse clusters, which tend to be unrelaxed systems that are currently undergoing, or have recently undergone, mergers will be measured with lower richness. Note that richness measurements are restricted to the 867 clusters at $z < 0.3$. This is because an absolute magnitude of -19 mag corresponds to an apparent magnitude of ~ 22 mag at $z \sim 0.3$, which is the typical flux depth of the i–band in PS1 3π. The rationale behind choosing a luminosity cut of -19 mag was a compromise between the flux depth of the imaging and achieving a reasonable dynamical range in magnitude for the colour–magnitude relation, such that the measured values for richness are meaningful. In order to investigate whether a relationship exists between the richness–$L_{\rm X}$ distribution and redshift, the data in Figure 2.9 is colour coded by bins of redshift. No correlation appears to exist for richness, with respect to redshift, the only association seen is that of the underlying relationship which exists between redshift and the X-ray luminosity, due to the flux limited nature of the cluster sample.

Chapter 3

A Photometric Census of Brightest Cluster Galaxies

The work in this chapter is adapted from the following publication:

Green et al. (2016), MNRAS, 461, 560.

3.1 Overview

Despite their reputation as being "red and dead", the unique environment inhabited by Brightest Cluster Galaxies (BCGs) can often lead to a self-regulated feedback cycle between radiatively cooling intracluster gas and star formation and AGN activity in the BCG. However the prevalence of "active" BCGs, and details of the feedback involved, are still uncertain. We have performed an optical, UV and Mid-IR photometric analysis of the BCGs in 981 clusters at $0.03 < z < 0.5$, selected from the *ROSAT* All Sky Survey. Using Pan-STARRS PS1 3π, *GALEX* and *WISE* survey data we look for BCGs with photometric colours which deviate from that of the bulk population of passive BCGs - indicative of AGN and/or star formation activity within the BCG. We find that whilst the majority of BCGs are consistent with being passive, at least 14% of our BCGs show a significant colour offset from passivity in at least one colour index. And, where available, supplementary spectroscopy reveals the majority of these particular BCGs show strong optical emission lines. On comparing BCG "activity" with the X-ray luminosity of the host cluster, we find that

BCGs showing a colour offset are preferentially found in the more X-ray luminous clusters, indicative of the connection between BCG "activity" and the intracluster medium.

3.2 Introduction

As discussed in Chapter 1, the evolution of BCGs is affected by the ICM and, in turn, feedback effects from AGN and star formation activity in the BCG affects the evolution of the ICM. A self-regulated cycle of radiative cooling and AGN heating is widely acknowledged, however, the physics of this heating mechanism are not well understood (McNamara & Nulsen 2012; Fabian 2012). With photometric surveys becoming ever wider and deeper, identification of active BCG candidates through photometry is crucial in our attempts to understand the important role that feedback plays in galaxy evolution.

The primary goal of this Chapter is to use optical, Mid-IR and UV survey data to investigate what extent correlations exist between BCG photometric colours and BCG activity, where throughout this Chapter we use the term "activity" to refer to either, or both, star formation and AGN activity, unless otherwise noted. This correlation may manifest as colour deviations from those of the bulk population of passive BCGs. With the advantage of a large sample of $\sim$ 1000 clusters, the aim is to investigate what proportion of BCGs, selected on host cluster X-ray emission alone, show signs of activity and determine how effectively we can detect active BCGs through photometry. In addition, we explore how, if at all, this relates to the overall X-ray properties of the cluster.

3.3 The Data

A description of the cluster sample, the BCG selection and optical photometry used throughout this Chapter are given in Chapter 2.

3.3.1 Spectroscopic Data

The optical spectroscopy for the BCGs in the sample are drawn from a wide range of sources. The bulk of this comes from the nearly complete follow-up of the BCG sample by Crawford et al. (1999), the large spectroscopic surveys by the Sloan Digital Sky Survey (York et al., 2000) and the 6dF Galaxy Redshift Survey (Jones et al., 2004), a VLT FORS survey of BCGs in REFLEX (Edge et al., in prep) and any other spectra in the literature. In total, we have reliable spectra, sufficient to detect optical emission lines, for 73% of the sample.

Note that there is a slight observational effect in which a higher fraction of the BCGs with line emission are likely to have targeted spectroscopy than for the non-line emitting BCGs. This however has no bearing on the conclusions to this work as the results are presented as a fraction of active BCGs within subsamples based on line emitting status.

3.3.2 Mid-IR Photometry: *WISE*

The *Wide-field Infrared Survey Explorer* (*WISE*) (Wright et al., 2010) covered the whole sky in the Mid-IR at 3.4, 4.6, 12 and 22 μm. From the AllWISE Source Catalogue we extract photometry for our BCG sample in the $W1$, $W2$ and $W3$ bands at 3.4, 4.6 and 12 μm respectively. The *WISE* source closest to the BCG position is selected, which is within 1 arcsec for 79% of BCGs, 2 arcsec for 94% of BCGs and within 6 arcsec for all BCGs. We do not perform any Galactic extinction corrections as this is negligible for Mid-IR observations (Cardelli et al., 1989).

The full BCG sample is well detected in $W1$ and $W2$, with a Signal to Noise, $S/N > 3$ for all observations. At 12 μm ($W3$) however some sources are not detected due to the flux limit of *WISE*. We thus restrict our $W3$ analysis to detections with $S/N > 3$ and find that the number of robustly detected BCGs in $W3$ is 552 (56% of total sample size). As the $W1$ and $W2$ observations are complete they are free from any observational bias. However, as $W3$ is flux limited we preferentially detect BCGs with an excess in $W3$. Hence, in order to avoid this observational effect biasing our results, the number of BCGs with a $W3$ excess in the subsequent analysis are given

as a fraction of the total BCG sample, not just those with $W3$ detections.

3.3.3 UV Photometry: *GALEX*

The *Galaxy Evolution Explorer* (*GALEX*) (Martin et al., 2005) was a space based observatory imaging in two ultraviolet bands, the Far-UV (FUV) at 1350–1780Å and the Near-UV (NUV) at 1770–2730Å. We used the aperture photometry available from the *GALEX* catalogue[1] and extracted any source within six arcsec of our BCG position. If multiple observations were returned, we attempted to maximise the signal to noise by taking the observation with the longest exposure time - unless the next longest exposure was more central within the *GALEX* field-of-view and within 2/3 of the highest exposure time, since the PSF is poorer with radius from the centre of the *GALEX* field of view. We correct for Galactic extinction assuming $A_{\rm FUV} = 2.5\,A_V$ and $A_{\rm NUV} = 3.25\,A_V$ (Hoffer et al., 2012).

The *GALEX* catalogue is compiled of observations from numerous nested *GALEX* surveys, which vary in sky coverage and depth, none of which are full sky and hence our sample is far from complete in the UV. The widest survey, the All-sky Imaging (AIS), (which despite the name covers only 26,000 square degrees of the sky) has typical exposure times of only 100s, which are insufficient for a robust detection of passive galaxies for most of our redshift range. Hence, despite the catalogue returning a detection for 541 of our BCGs within 6 arcsec, when we restrict our analysis to detections with $S/N > 3$, the number of galaxies reduces to 245 BCGs ($\sim 25\%$ of the total sample).

The *GALEX* observations are spatially incomplete, which does not favour one class of clusters over another, however, the variable limiting flux depth means BCGs with a UV excess were preferentially detected. Hence later results are given as lower limits, where the fraction of BCGs with a UV excess are quoted relative to the total BCG sample.

[1] http://galex.stsci.edu/GalexView/

3.3.4 Radio: NVSS

The NRAO VLA Sky Survey (NVSS) (Condon et al., 1998), operating at 1.4, GHz, covered the entire sky north of a Declination of $-40°$ and thus provides observations of our entire sample. We use the NVSS Source catalogue[2] to extract the photometry for the nearest detection within 45 arcsec of the BCG position. Whilst the spatial resolution of NVSS does not permit us to attribute a radio detection to the BCG with certainty, BCGs are the most likely cluster galaxy to host a radio-loud AGN (Burns et al. 1981; Valentijn & Bijleveld 1983; Burns 1990; Best et al. 2007) and hence we assume any radio detection to be associated with the BCG. We find 512 BCGs with an associated radio detection, corresponding to a radio detection rate of 52%, this is comparable to the $\sim$ 60% detection rate of Hogan et al. (2015a), but logically less, given our sample goes to higher redshift and uses shallower survey data. The NVSS data are spatially complete, but are flux limited. This favours the detection of radio loud BCGs over radio quiet BCGs. However this effect has no bearing on our conclusions.

3.4 Optical Analysis and Results

3.4.1 BCG Luminosity

We begin our optical analysis by comparing the properties of the BCG with those of the host cluster, as seen in Fig. 3.1. We find that the BCG i-band luminosity is weakly correlated with the host cluster X-ray luminosity, such that, whilst for any individual BCG the scatter is significant, we do see a general trend in which the brighter BCGs tend to reside in the more X-ray luminous clusters. This reinforces previous results showing a correlation between optical BCG luminosity and cluster X-ray luminosity (e.g. Edge 1991; Stott et al. 2012). We conclude that, given that optical luminosity traces stellar mass and cluster X-ray luminosity traces the cluster mass, the most massive BCGs tend to belong to more massive clusters. This interpretation is supported by the results of Stott et al. (2010) and Lidman et al. (2012)

[2] www.mrao.cam.ac.uk/projects/surveys/nrao/NVSS/NVSS.html

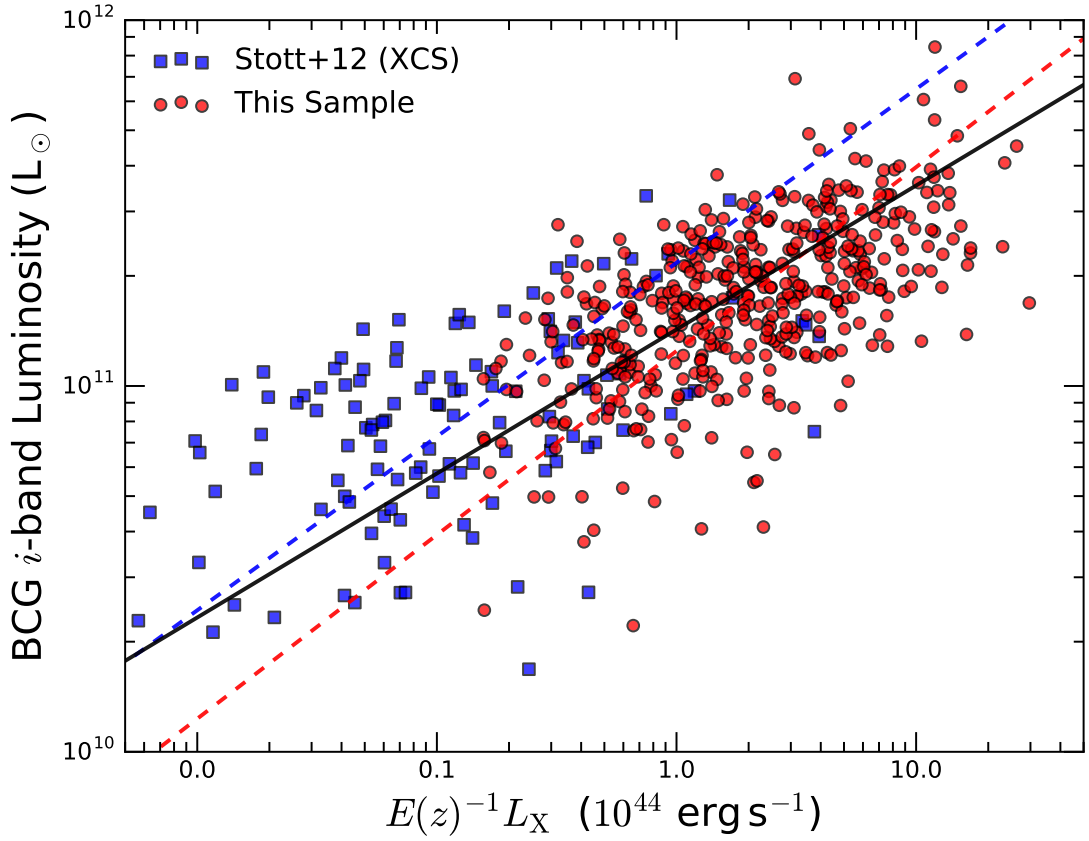

Figure 3.1: The i-band luminosity of BCGs, against the 0.1–2.4 keV X-ray luminosity of the host cluster. The (red) circles represent our cluster sample and the (blue) squares represent the groups/clusters from Stott et al. (2012) - corrected to have optical and X-ray measurements comparable to our own. The dashed lines represent the BCES bisector best fits to the sample of corresponding colour and the solid black line represents a BCES bisector fit to the combined data sets.

who derive BCG stellar masses and cluster masses from BCG Near-IR luminosities and cluster X-ray temperatures respectively, (which are both more reliable tracers of mass). Additionally, a positive correlation between BCG luminosity and the cluster velocity dispersion – another tracer of cluster mass – has also been observed (Whiley et al. 2008; Lauer et al. 2014).

In Fig. 3.1 we plot the corrected values of L_X and L_i from Stott et al. (2012) (hereafter S12) alongside our own for comparison. The S12 L_i values are derived from SDSS model magnitudes, which have systematically brighter fluxes than measured through our own PS1 photometry by a few tenths of a magnitude. Since this offset

in BCG flux is uniform with redshift we apply a correction of the median value of 0.4 mag to the S12 values. Additionally we apply a correction in the S12 $L_{\rm X}$ values, (taken from the XCS; Mehrtens et al. 2012), from bolometric values to that of 0.1–2.4 keV. This is achieved using the ratio of 0.1–2.4 keV flux to bolometric flux, as a function of temperature, and the XCS temperature values from S12. Applying a linear regression BCES bisector fit (Isobe et al., 1990) to the points we find,

$$\log_{10}(L_i) = \alpha \log_{10}(E(z)^{-1} L_{\rm X}) + \beta, \tag{3.4.1}$$

where L_i is the BCG i-band luminosity (L$\odot$), $L_{\rm X}$ is the 0.1–2.4 keV X-ray luminosity ($10^{44}\,{\rm erg\,s^{-1}}$) and $E(z) = [\Omega_m(1+z)^3 + \Omega_\Lambda]^{1/2}$ with $\alpha = 0.48 \pm 0.08$ and $\beta = 11.34 \pm 0.08$ for the S12 sample, $\alpha = 0.50 \pm 0.04$ and $\beta = 11.09 \pm 0.02$ our sample and $\alpha = 0.39 \pm 0.04$ and $\beta = 11.15 \pm 0.09$ for the combined samples. We adopt the parameter, $E(z)$, in order to be quantitatively consistent with S12. This expansion term gives the Hubble constant as a function of redshift, $H(z) = H_0 E(z)$, but in the redshift interval relevant for this sample the $E(z)$ factor has an effect of only a few per cent (with a mean value of $E(z) = 1.07$ for this data). Hence we find, when comparing the best fitting lines to this sample and the S12 sample, that the slopes are consistent but there is an offset in the normalisation. The interpretation is that this reflects the differing sample selection – specifically that the XCS sample is dominated by low mass galaxy groups/clusters and our sample is dominated by massive clusters. We find the slope for the combined samples is flatter than either separate sample, suggesting a possible flattening of the relation in low mass haloes. This is perhaps driven by a lower prevalence of AGN feedback in low mass haloes. Hence the stellar mass growth of their central galaxies is not as effectively truncated.

3.4.2 BCG Colour

The cluster red sequence for each cluster is selected using the red sequence algorithm described in Chapter 2 and colours measured at a fixed flux of 19th magnitude. In Fig. 3.2 we explore the PS1 g–r, r–i and i–z colours of the red sequence, and how this relates to redshift. After taking into account the relative position of a galaxy along the red sequence slope, the colour of the cluster red sequence can provide

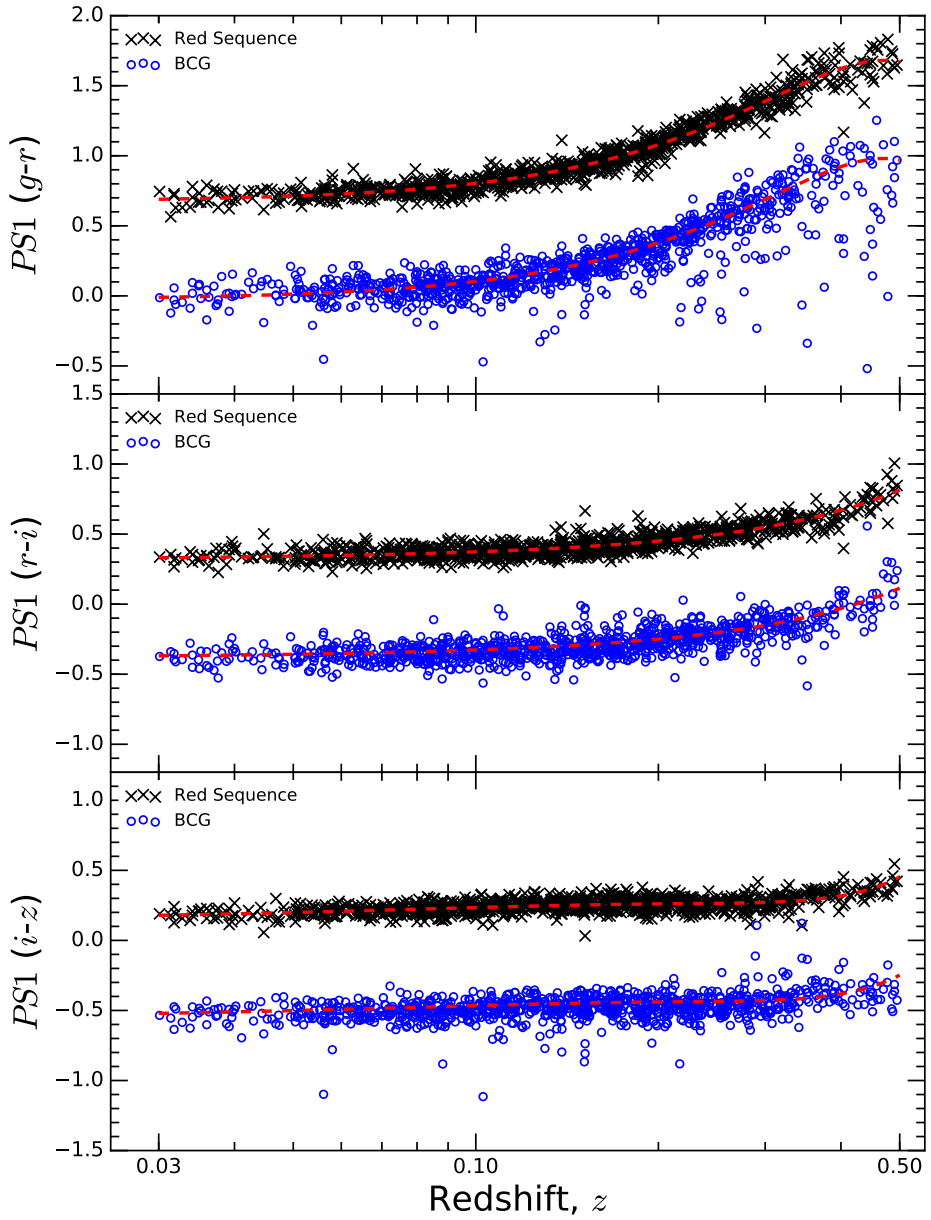

Figure 3.2: PS1 g–r (top panel), r–i (middle panel) and i–z (bottom panel) colours, against redshift. The (black) crosses show the colour of the cluster red sequence, measured at a flux of 19th magnitude for each cluster. The (blue) open circles show the colour of the BCG for each cluster, but corrected to be at a flux of 19th magnitude also. The BCGs (open circles) have been artificially offset by -0.7 mag for visual clarity. The upper (red) dashed line in each panel shows a best fit to the red sequence. These exact same lines are offset by -0.7 mag also, forming the lower dashed lines, this is to show the reader that the bulk population of BCGs lie on the cluster red sequence as expected for a passive galaxy.

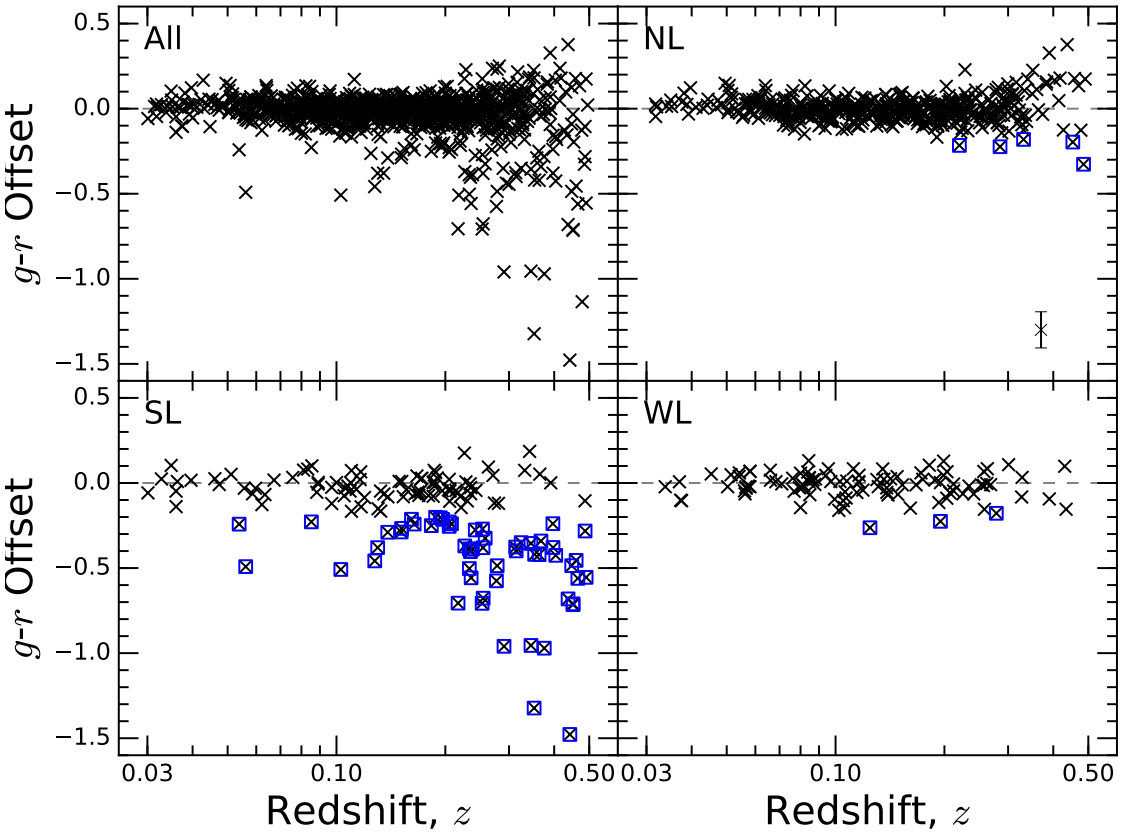

Figure 3.3: Each panel shows the BCG g–r colour offset – defined as the difference between the BCG and red sequence colour – against redshift. The panel is split into: full sample (top left), non line emitters (top right), strong line emitters (bottom left) and weak line emitters (bottom right.) The (blue) squares indicate those BCGs with colour offsets in excess of $> 2.5\sigma_p$ from zero, where σ_p is the scatter of the non-line emitters. The 1σ representative error on the colour is given in the bottom right of the non line emitters panel.

a standard for the colour one would expect for a passively evolving galaxy on the red sequence. Thus we investigate the equivalent colour of the BCG in order to determine whether deviations from passivity exist for these galaxies.

In Fig. 3.2 we also display the PS1 g–r, r–i and i–z colours of the BCG in each cluster, corrected to be at the same flux as the red sequence (although artificially offset in colour for visual clarity). We see that the BCG colour evolution generally follows the same trend with redshift as the red sequence, indicating that most BCGs lie on the red sequence. As with the red sequence colours, the BCGs form a fairly tight relation suggesting BCGs are generally a fairly homogeneous galaxy population. This is to be expected if you consider BCGs to be quiescent galaxies that formed their stellar populations at $z > 2$, like the other cluster members. However, we see also a significant number of BCGs with optical colours that differ from that of the bulk, passive population, particularly in g–r.

In Fig. 3.3 we show the g–r colour offset, defined as the colour difference between the BCG and the red sequence at the same flux. There are a number of BCGs which have g–r colours significantly bluer than the red sequence galaxies, which could be indicative of star formation and/or AGN activity. To explore this further we split our BCG sample by emission line status as both star formation and AGN activity lead to optical emission lines in galaxies. We divide our BCGs into: those with strong emission lines (Hα slit flux $\gtrsim 10^{-15}$ erg cm^{-2}s^{-1}), those with weak emission lines ($\lesssim 10^{-15}$ erg cm^{-2}s^{-1}), those with no lines, and those without any spectral data available. Note that these flux cuts are only approximate, illustrative values. The distinction between strong and weak is only used in order to crudely differentiate between systems with significant line emission and systems with weaker lines, which are diluted in a bright, lower redshift BCG. More thorough cuts using emission line luminosities are therefore not necessary, particularly given the inherent uncertainty in using a slit flux for determining line strength.

We see from Fig. 3.3 there is a clear connection between g–r colour offset and line status with most blue BCGs also showing strong emission lines. This is in stark contrast to BCGs without emission lines, which have a mean g–r offset of zero, as expected for passive galaxies. If we thus assume the non line-emitting BCGs

are representative of the quiescent population, we can use these to estimate the general scatter in colour and hence quantify what constitutes a significant deviation in colour from passivity. We find a standard deviation of $\sigma_p = 0.07$ mag for the non line-emitting ("passive") BCGs.

Defining our threshold for BCG activity as a colour offset in excess of $2.5\,\sigma_p$, we find that 8% of BCGs exhibit significantly blue colours and as such are classed as "active". Of the strong line emitting subsample, 39% of BCGs show a g–r offset $> 2.5\,\sigma_p$ and the mean offset is -0.19 mag. In fact, all the BCGs with g–r offsets < -0.5 mag are either strong line emitters or have no available spectra (and are likely strong line emitters themselves). The strong connection between optical colour and line status is indicative that these BCGs are optically blue because of activity in the BCG. Note that we have manually investigated the colour magnitude diagrams of all apparently blue BCGs to rule out incorrect selection of the red sequence as an origin for the offset in g–r, in addition to double checking our BCG selection was correct. A summary of the fraction of optically blue BCGs as related to line status is provided in Table 3.1. By assuming that the BCGs without any optical emission lines are representative of the quiescent BCG population, which is reasonable given the common presence of line emission in star formation and AGN activity, then the fraction of non line emitting BCGs with significant colour offsets provides a measure of the level of general scatter in BCG colour and the uncertainty in the active BCG fraction. Using this argument we find the fraction of significantly blue BCGs to be 8 ± 1 per cent.

It is interesting to note that whilst optical emission lines are indicative of activity, $\sim 60\%$ of those BCGs with emission lines do not show up as optically blue. In most cases this is likely a result of the fact that obscured SF and/or AGN activity can lead to ionisation of the gas, visible as strong emission lines, whilst having minimal influence on the continuum emission, and hence colour, of the overall galaxy. Additionally, the optical line emission associated with the BCG may result, not from ionising stars or AGN, but from ionisation at the hot/cold interface between clouds of cold molecular gas and the surrounding hot ICM in the cores of cool core clusters (Ferland et al. 2009; Fabian et al. 2011; Hamer et al. 2016). Aperture effects may

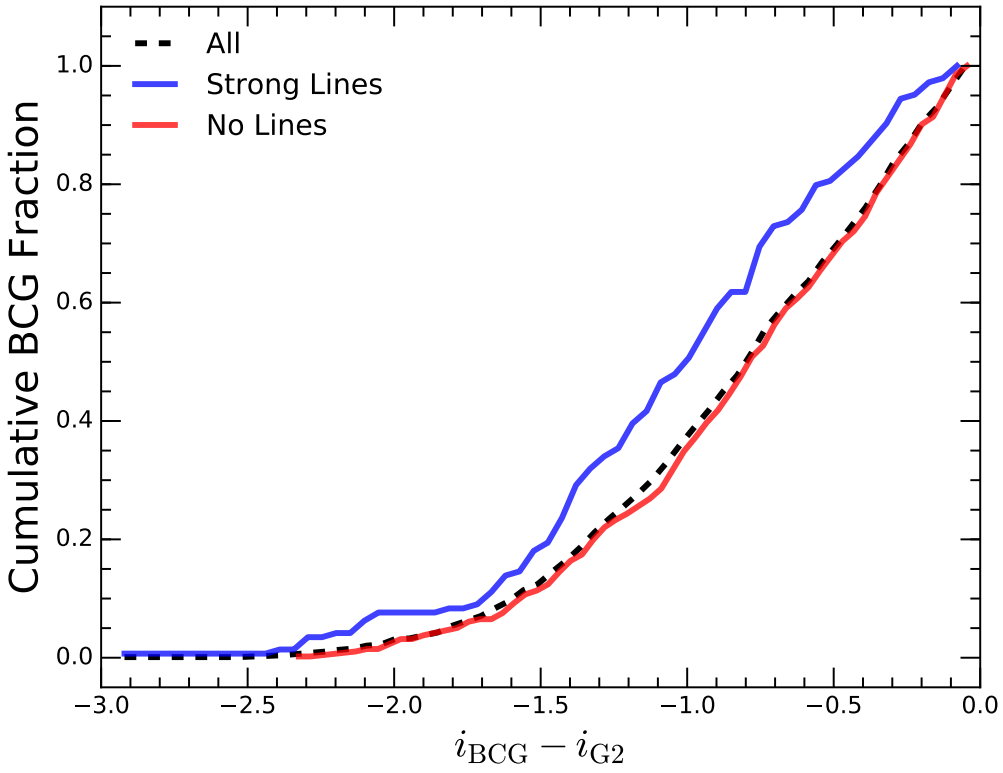

Figure 3.4: The cumulative fraction of clusters as a function of the i–band magnitude difference between the BCG and *G2*, the 2nd ranked cluster red sequence galaxy.

also be a contributing factor, whereby the photometry and spectroscopy are probing different regions of the BCG. As an aside, it should be noted that the fact some BCGs are optically blue has implications regarding optical cluster algorithms, which often select the BCG assuming a BCG colour on the red sequence.

3.4.3 BCG Dominance

Next we investigate the connection between the emission line status of the BCG, and its dominance relative to its companions in the cluster. In Fig. 3.4 we show the cumulative fraction of BCGs, as a function of the magnitude difference between the BCG and the 2nd ranked galaxy on the red sequence, $G2$. A connection appears to exist between the luminosity dominance of the BCG and its emission line status, with a higher fraction of strong line emitting BCGs showing a large magnitude separation between itself and $G2$ compared to those with no lines. This observation is consistent

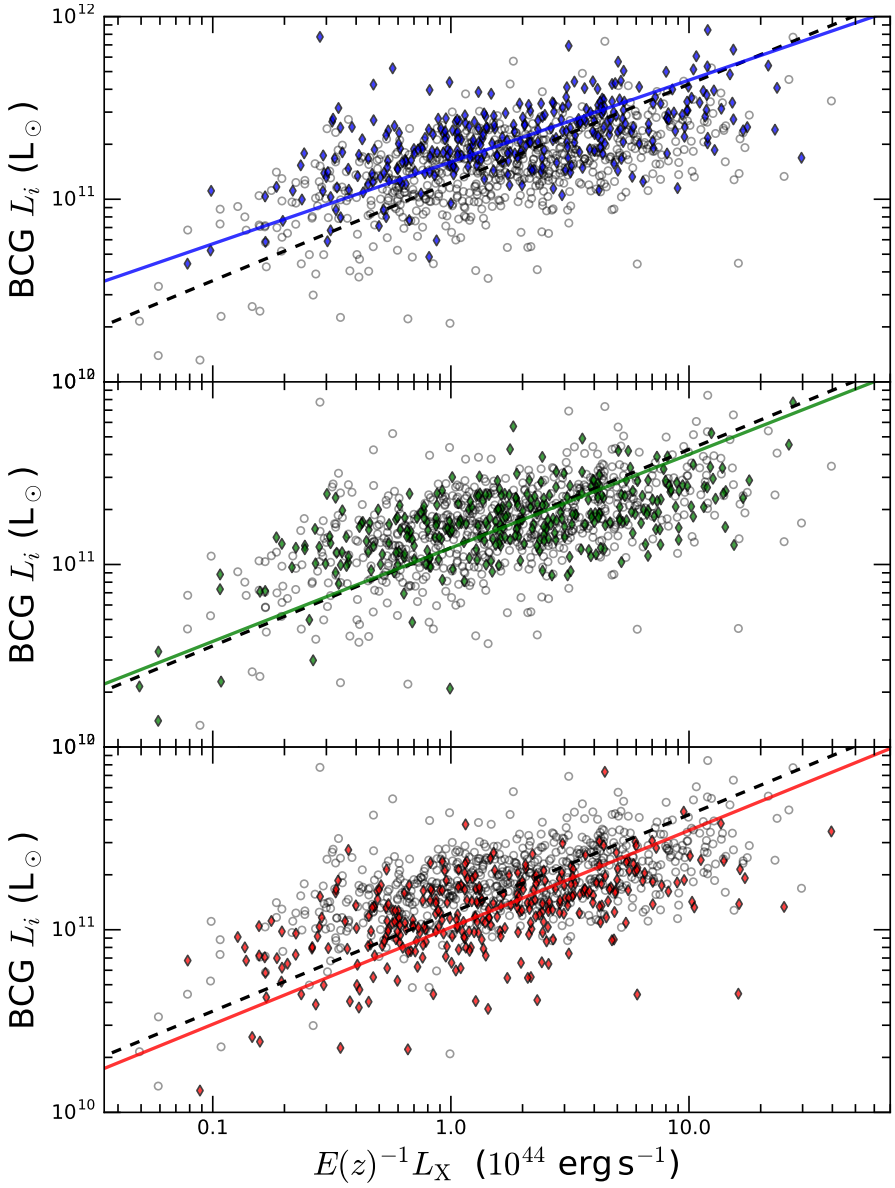

Figure 3.5: The PS1 i–band luminosity of the BCG, against the 0.1–2.4 keV X-ray luminosity of the host cluster. The sample is split equally into three based on BCG dominance, described by the difference in magnitude between the BCG and the 2nd ranked galaxy. The filled diamonds in the top panel correspond to BCGs in the top tier – that is, the BCGs with the biggest magnitude difference – the filled diamonds in the second panel correspond to the middle tier and the filled diamonds in the bottom panel correspond to the bottom tier. The open circles show the full sample to aid visual comparison. The dashed line indicates the best fit, made using a BCES bisector fit, to the full sample, the solid line in each panel indicates a best fit to the filled diamonds of that panel.

with implications from the literature, that is, that BCGs with emission lines trace cool core clusters (Heckman 1981; Hu et al. 1985; Johnstone et al. 1987; Heckman et al. 1989; Crawford et al. 1999; McDonald 2011), thus tend to be located at the very centre of the cluster potential (Sanderson et al., 2009) and the observation that BCGs are more likely to be cD galaxies when in close proximity to the cluster centre (Lauer et al., 2014). This also agrees with Smith et al. (2010) which demonstrated a direct association between the BCG dominance and the central gas density profile of the cluster, specifically that clusters hosting a high luminosity gap also host strong cool cores.

BCG dominance is also explored in Fig. 3.5 - here we divide the full sample into three based on the magnitude difference between themselves and $G2$ and find that the most dominant BCGs are systematically more luminous than other BCGs in clusters of similar X-ray luminosity, with the converse being true for the least dominant BCGs. This supports the notion that the magnitude difference is dominated by the brightness of BCGs themselves and not just reflective of a deficit in the brightness of $G2$ in these particular systems. In principle, the apparent correlation between BCG $L_{\rm i}$ and cluster $L_{\rm X}$ that is seen could be explained by the association between cool core clusters and an enhanced BCG dominance - whereby the cool core nature of a cluster leads to an enhancement in both the i–band and X-ray brightness. However the existence of this correlation in all three subsamples, even in the lowest third by luminosity gap, supports the interpretation that this is not a significant factor here.

3.5 Mid-IR Analysis and Results

3.5.1 BCG Luminosity

In Fig. 3.6, we find that the BCG *WISE* $W1$–band luminosity correlates with the X-ray luminosity of the host cluster. This reinforces the results from our optical analysis (Fig. 3.1), but with less scatter in the Mid-IR. The interpretation is that BCGs with higher stellar mass tend to reside in more massive clusters, as suggested from Near-IR observations also (e.g. Lin & Mohr 2004; Stott et al. 2008, 2010;

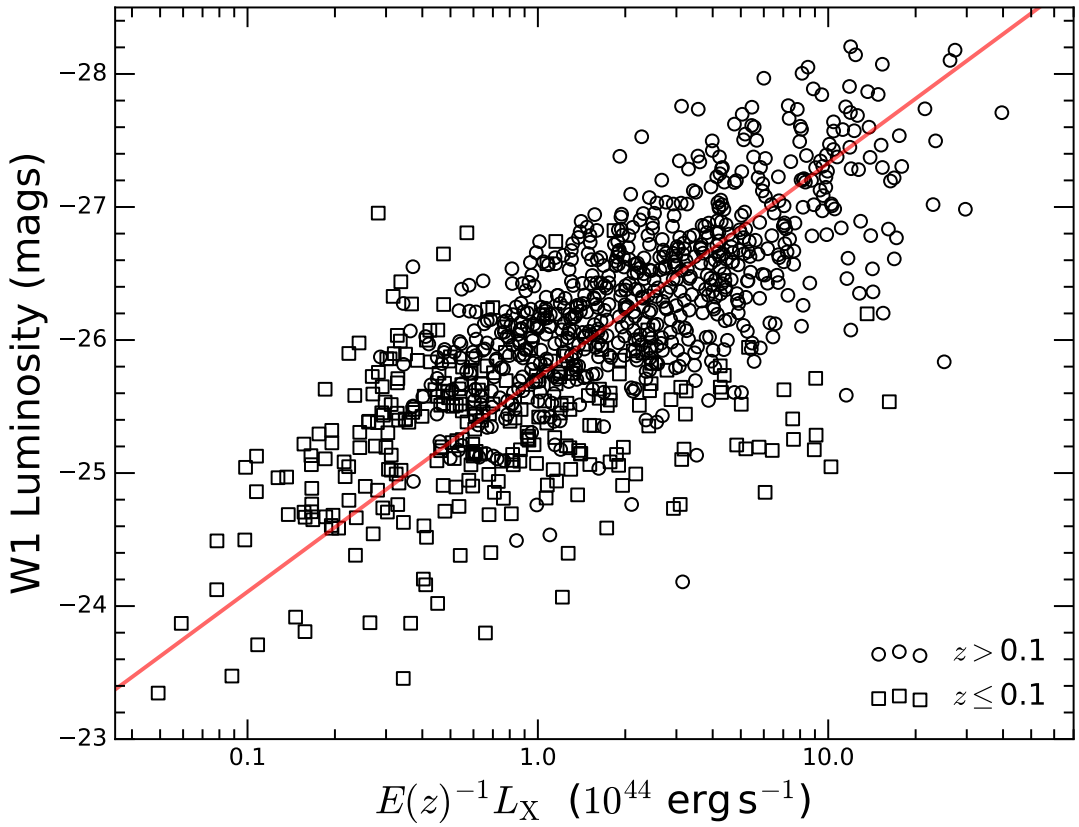

Figure 3.6: The *WISE* $W1$ (3.4μm) luminosity of the BCG against the 0.1–2.4 keV X-ray luminosity of the host cluster. The (red) dashed line indicates our best fit, made using a BCES bisector fit.

.

Lidman et al. 2012). Applying a linear regression BCES bisector fit (Isobe et al., 1990) we find,

$$L_{W1} = (-1.61 \pm 0.02)\log_{10}(E(z)^{-1}L_{\rm X}) - (2.57 \pm 0.02), \tag{3.5.2}$$

where L_{W1} is the BCG $W1$-band luminosity (mag), $L_{\rm X}$ is the X-ray luminosity ($10^{44}\,{\rm erg\,s^{-1}}$) and $E(z) = [\Omega_m(1+z)^3 + \Omega_\Lambda]^{1/2}$.

3.5.2 BCG Colours

In the IR the contribution from stellar mass decreases with wavelength, becoming more strongly dependent on dust emission at longer wavelengths. Hence in the Mid-IR, particularly at 12μm, we are sensitive to reprocessed emission from dust. An active BCG, with recent star formation and/or AGN activity, is consequently expected to show an excess in Mid-IR emission as the dust gets heated by the hot young stars and/or AGN. The colour of an active galaxy would as a result be redder than that of a passive galaxy, because the dust contribution is more significant in the redder band. As AGN output can heat dust to $T > 80K$, the most extreme cases of Mid-IR excess are likely due to AGN contribution.

All BCGs are well detected in $W1$ and $W2$, but only 552 BCGs are robustly detected (i.e. $S/N > 3$) in $W3$, due to the declining continuum in the SEDs of passive galaxies with respect to wavelength in the IR. In Fig. 3.7 we show the $W1$, $W2$ and $W3$ flux against redshift, with arrows indicating upper limits (i.e. where $S/N < 3$). The proportion of BCGs detected in $W3$ is clearly a function of redshift and beyond $z \sim 0.15$ the quiescent BCG population is not well sampled. Fortunately BCGs with a clear $W3$ excess continue to have robust detections across the redshift range and hence we expect this to have minimal effect on the detection of active BCGs. In order to define a $W3$ excess however this does require an extrapolation of the $W3$ flux-redshift relation for the bulk population of passive BCGs. Firstly a best fit is made to the bulk population for $W1$ and $W2$, ignoring those with a clear excess (i.e. with flux values deviating from the best fitting flux–redshift relation for $W1$ and $W2$ in excess of $2.5\,\sigma$). From the Figure we see the relation between these two is very similar and the relation for $W3$ is expected to be similar also.

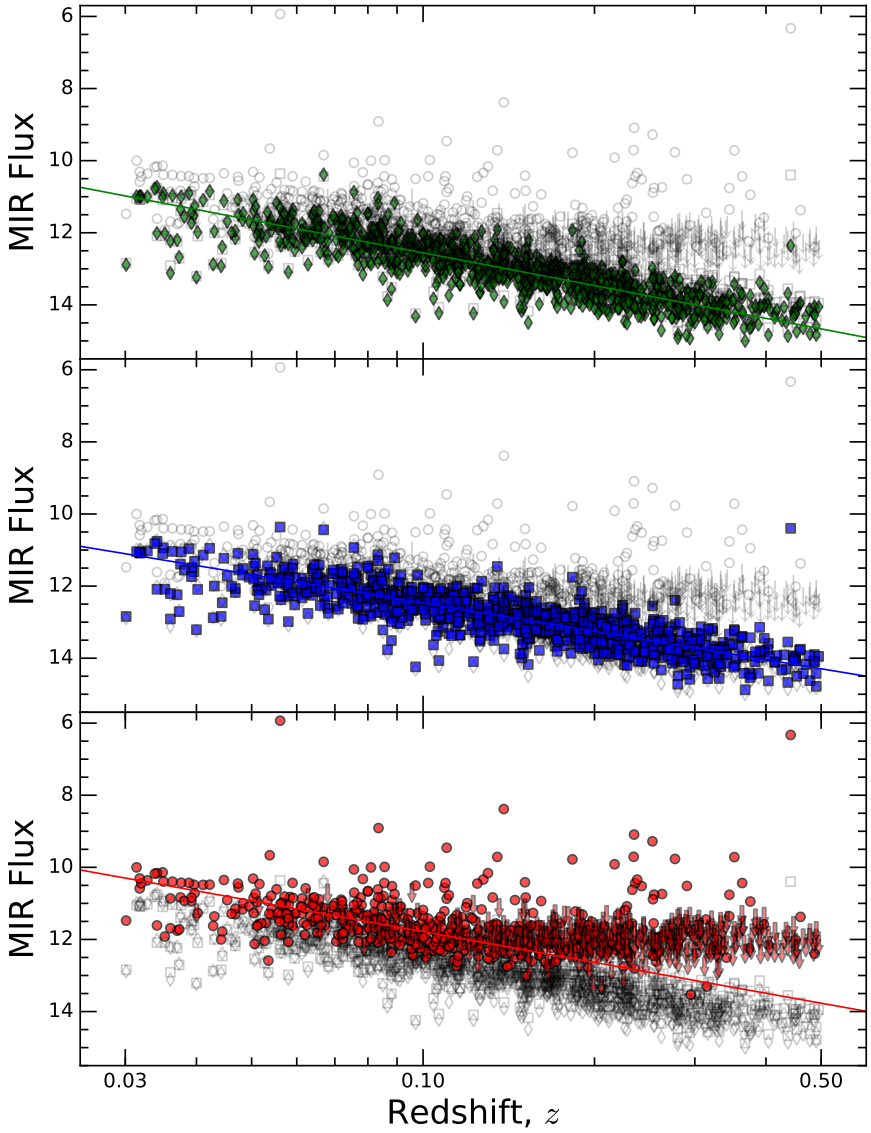

Figure 3.7: The *WISE* fluxes of our BCGs against redshift. The $W1$ (3.4μm) fluxes are given by the (green) diamonds in the top panel, the $W2$ (4.6μm) fluxes by the (blue) squares in the middle panel and the $W3$ (12μm) fluxes by the (red) circles in the bottom panel. The grey points correspond to the values of the other bands with their respective symbols. Any points given as arrows indicate limiting magnitudes with poor signal to noise (S/N <3). Clearly from this figure the depth of $W3$ is insufficient to probe the quiescent galaxy population beyond $z \sim 0.15$, but crucially for our study, those with a strong $W3$ excess continue to show up at least until $z = 0.5$. The solid lines show the respective best fit trends to the bulk quiescent population of BCGs, in the case of $W3$, this is extrapolated from $z \leq 0.15$.

Hence using the $W2$-z relation as a template, we iteratively determine the best fit to those BCGs with $S/N > 3$ and $z < 0.15$, again ignoring the BCGs with a clear $W3$ excess (i.e $W3$ flux values which deviate in excess of $2.5\,\sigma$ from the best fit), and extrapolate this relation to the higher z, where our bulk quiescent population is lost to the flux limit.

We can also deduce from Fig. 3.7 that *WISE* can measure BCG fluxes beyond $z > 0.5$. In $W1$ and $W2$ it appears we can continue detecting the bulk population further, but crucially for studies of activity, we expect to be able to measure excesses even further. This will be a useful factor when comparing BCG properties of the low-z Universe to those at higher z. For instance, the most extreme systems at $z > 0.5$, such as the Phoenix cluster ($z = 0.598$, McDonald et al. 2012a), that is an AGN-dominated BCG with $W3$ magnitude of 7.93 mag, would be detectable with *WISE* to at least $z = 1.5$. So, while the less active AGN are lost at $z > 0.3$, we can still identify the most active systems in any sample, such as the XCS (Romer et al., 2001) in the X-ray, or MaDCoWS (Stanford et al., 2014) in the Mid-IR.

In order to test for a Mid-IR excess we explore the Mid-IR colours, $W1{-}W2$ and $W2{-}W3$. In Fig. 3.8 the $W1{-}W2$ ($3.6 - 4.6\mu$m) colour against redshift shows that the passive BCG population undergoes a peaked evolution with redshift - due to the redshift of a continuum break in the SED here. This effect has sometimes been ignored in the literature, where conclusions are drawn from raw colours only (e.g. Fraser-McKelvie et al. 2014; Quillen et al. 2008). Fig. 3.8 illustrates that if using just raw colours, $W2$ excesses at redshifts below the peak are lost to the redshift relation and hence some star forming galaxies would be missed. This illustrates why one should consider a colour offset (as used here) or a normalised flux ratio (such as in Hoffer et al. 2012). Having already established most BCGs are indeed passive we can hence determine a $W1{-}W2$ colour offset by collapsing along the best fit line to the bulk passive trend in Fig. 3.8, with the offset defined as the difference in the measured colour and that predicted by this best fit.

The $W1{-}W2$ offset shown in Fig. 3.9 show that there are a number of BCGs which exhibit a significant offset and that these correlate with the optical emission line status. For the non-line emitting BCGs, i.e. passive BCGs, we measure a scatter

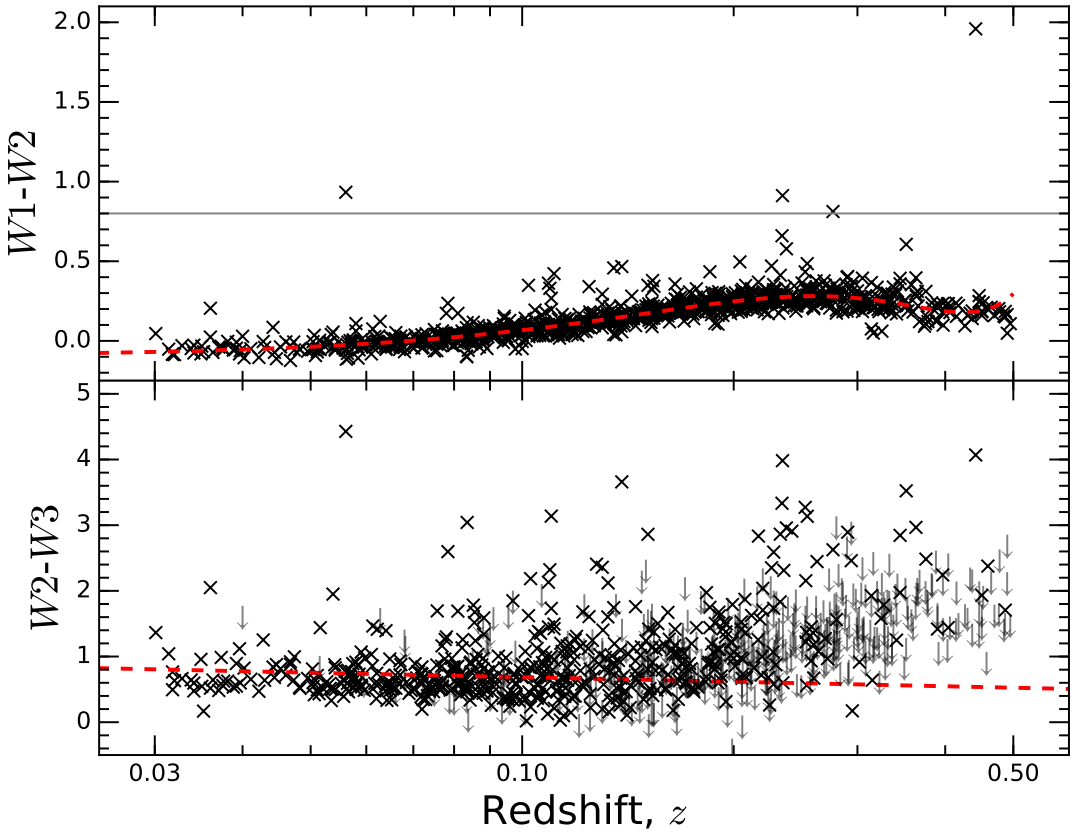

Figure 3.8: The $W1$-$W2$ ($3.4-4.6\mu$m) and $W2$-$W3$ ($4.6-12\mu$m) colour evolution of the BCGs, with respect to redshift. The grey arrows indicate sources where $W3$ S/N <3 and the red dashed lines indicate the assumed best fit for a passively evolving galaxy (see main text). The solid grey line in the top panel indicates the selection criteria of $W1{-}W2 > 0.8$ mag for strong AGN.

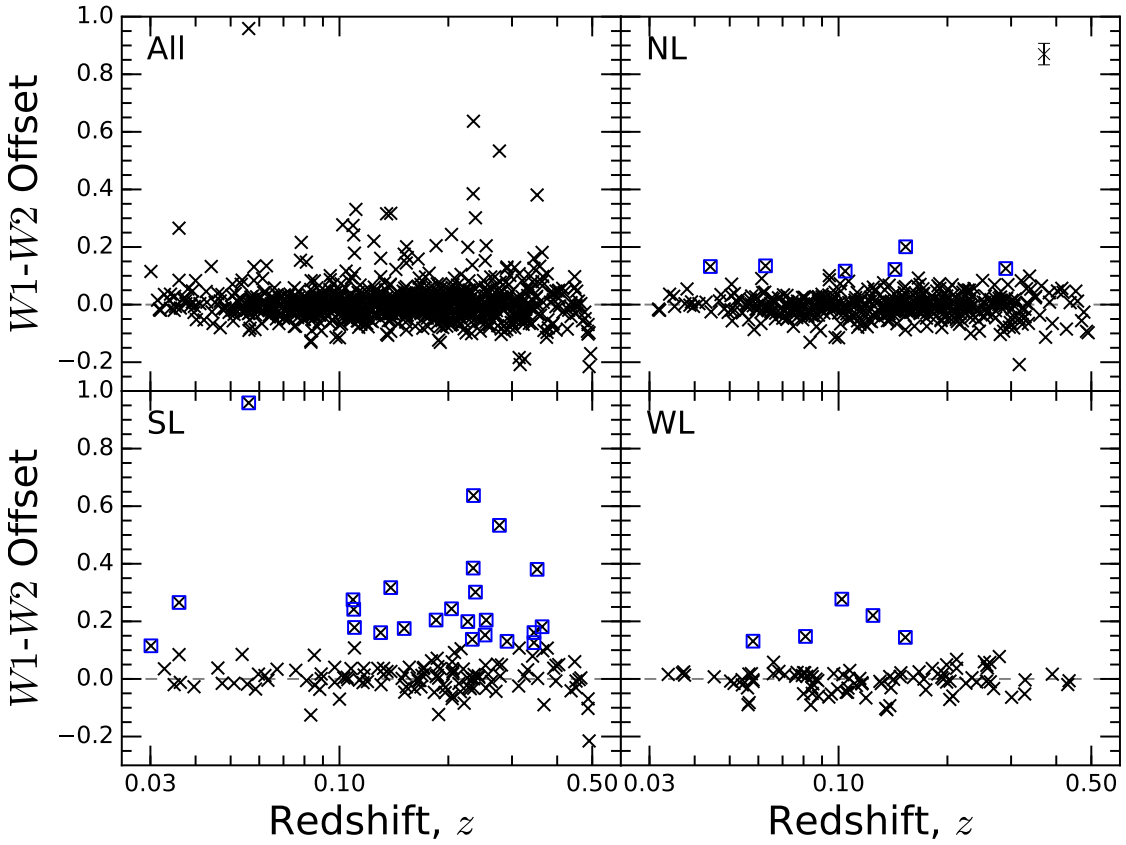

Figure 3.9: The *WISE* $W1$–$W2$ ($3.4 - 4.6\mu$m) BCG colour offset against redshift. The panel is split into: full sample (top left), non line emitters (top right), strong line emitters (bottom left) and weak line emitters (bottom right.) The (blue) squares indicate those BCGs with colour offsets in excess of $> 2.5\sigma_p$ from zero, where σ_p is the scatter of the non-line emitters. Note there is another point with a $W1$–$W2$ offset of 1.78, corresponding to MACSJ0913.7+4056, which is omitted here for the sake of visual clarity. The 1σ representative error on the colour is given in the top right of the figure.

with a standard deviation, $\sigma_p = 0.04$ mag and a mean of zero. If we then define a $W2$ excess as an $W1{-}W2$ offset $> 2.5\sigma_p$, we find 5% of the total show an excess, increasing to 17% for the subsample of strong line emitters.

Enhanced $W2$ emission is often used as an indicator of AGN activity in a galaxy (resulting from the nature of the power spectrum of AGN (O'Dea et al., 2008)). Using the basic AGN selection criteria of $W1{-}W2 > 0.8$ from Assef et al. (2013) we recover four BCGs hosting a strong AGN. These four are the BCGs of Zw 2089 (Russell et al., 2013), Cygnus-A (Russell et al., 2013), MACSJ0913.7+4056 (Hlavacek-Larrondo et al., 2013), and PKS2338+000. Note that *Chandra* observations of Zw 2089, Cygnus-A and MACSJ0913.7+4056 confirm the presence of an AGN, but that the AGN does not dominate the X-ray emission (see Chapter 4 for an investigation into AGN within BCGs). This basic colour cut allows us to determine a conservative lower limit of four BCGs hosting strong AGN in our sample ($< 1\%$). However the reliability and completeness of a simple colour AGN selection method assumes highly luminous AGN only, and are calibrated on 'typical' AGN host galaxies. BCGs are anything but typical and hence it is inevitable that the host BCG has a significant contribution to the $W1$ flux, diluting the relative $W2$ excess. Hence we are almost certainly underestimating the overall AGN fraction with other AGN host galaxies just falling short of this formal selection cut. Nonetheless, this result shows that whilst ongoing strong AGN are extremely rare, the AGN duty cycle is non-zero in these galaxies.

Fig. 3.10 shows the $W2{-}W3$ ($4.6 - 12\mu$m) colour offset. This is the difference between the measured $W2{-}W3$ and the estimated best fit for $W2{-}W3$, given by the $W2$ best fit minus the expected $W3$ best fit. Once again we see that non-line emitting BCGs do not generally show any Mid-IR excess, with a mean offset of zero, consistent with passivity. With a scatter of $\sigma_p = 0.35$ mag in the non-line emitters we find at least 8% of total BCGs show a significant colour offset (i.e. an offset $> 2.5\sigma_p$). This fraction is increased to 35% for the strong line emitting BCGs. As expected weak line emitters behave somewhere in between, with most near zero but with a handful showing a significant offset (6%). The reader should note that the apparent deficit of non-offset galaxies at high redshift is a result of the passive

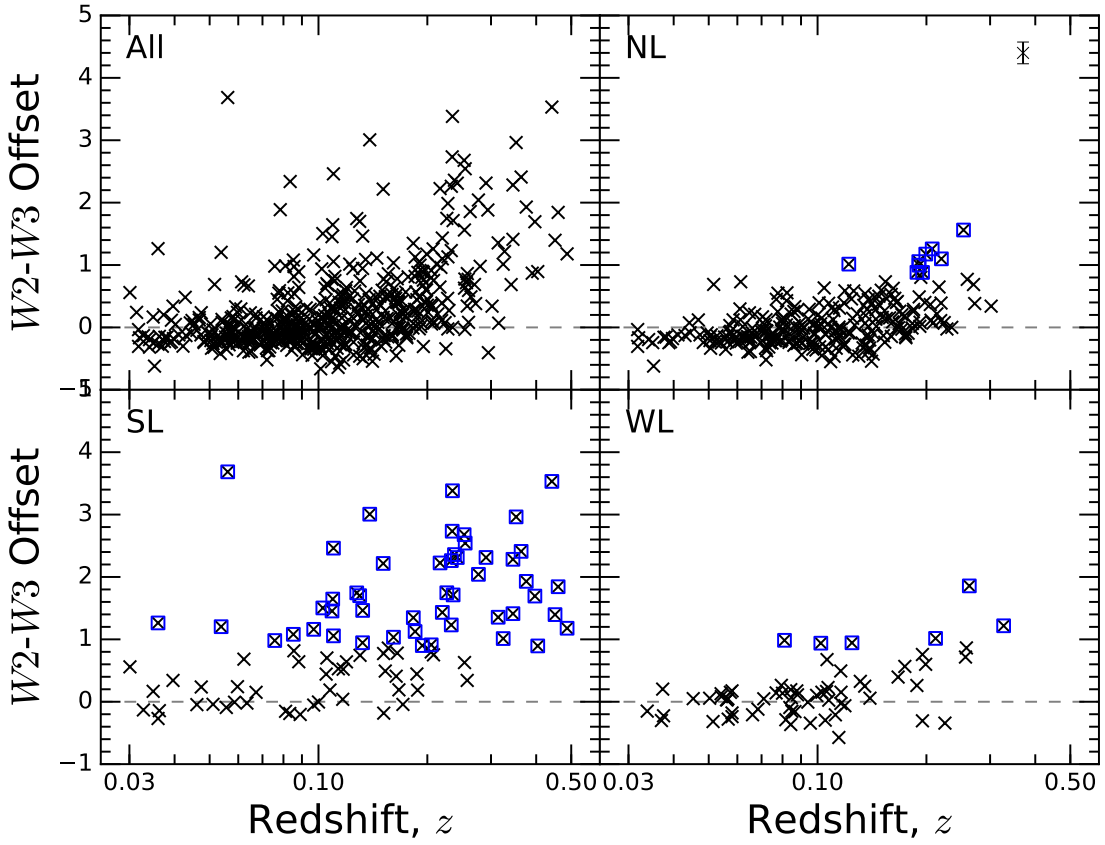

Figure 3.10: The *WISE* $W2$–$W3$ (4.6 − 12μm) colour offset against redshift for BCGs with a $W3$ S/N>3 (552 BCGs). The panel is split into: full sample (top left), non line emitters (top right), strong line emitters (bottom left) and weak line emitters (bottom right.) The (blue) squares indicate those BCGs with colour offsets in excess of $> 2.5\sigma_p$ from zero, where σ_p is the scatter of the non-line emitters. The 1σ representative error on the colour is given in the top right of the figure.

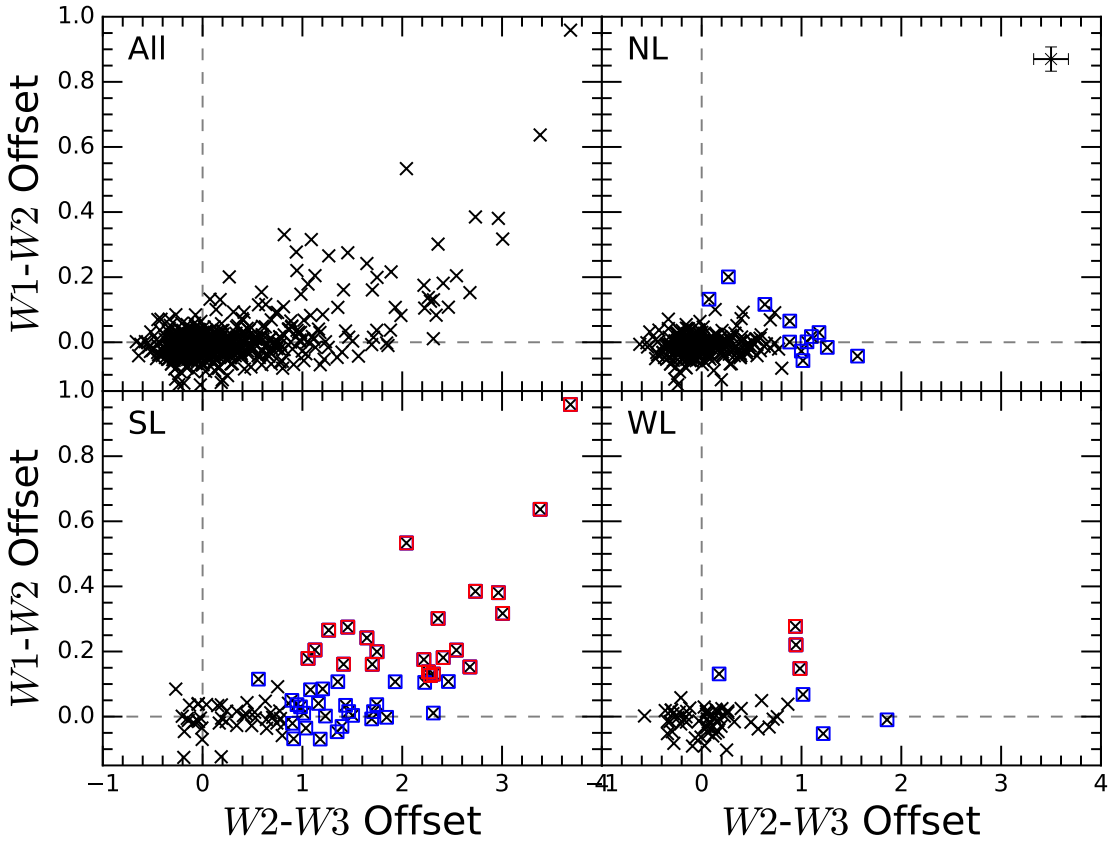

Figure 3.11: The $W1{-}W2$ offset against $W2{-}W3$ offset for BCGs. The panel is split into: full sample (top left), non line emitters (top right), strong line emitters (bottom left) and weak line emitters (bottom right.) The (blue) squares indicate those BCGs with colour offsets in excess of $> 2.5\sigma_p$ from zero, where σ_p is the scatter of the non-line emitters. The red squares correspond to galaxies significantly offset in both colours and thus likely indicate BCGs hosting AGN. Note there is another point with $W1{-}W2$ and $W2{-}W3$ offsets of 1.78 and 3.52 respectively, corresponding to MACSJ0913.7+4056, which is omitted here for the sake of visual clarity. The 1σ representative error on the colours are given in the top right of the figure.

BCG population lacking robust detections in $W3$ at $z \gtrsim 0.15$. The trend in the non-line emitting panel appears not to be flat because of this limiting depth of $W3$; which causes the dimmer BCGs in $W3$ (i.e. the more blue BCGs in $W2$–$W3$) to be undetected in $W3$ at lower redshifts than the more $W3$ bright ($W2$–$W3$ redder) BCGs at the same redshift, leading to an apparent slope in the trend at higher redshift. One should also note that the fraction of BCGs said to show a significant offset are evaluated as a proportion of the total sample, under the assumption that the undetected BCGs are exclusively passive. This means that the fractions are in fact lower limits, since although most BCGs with Mid-IR excess are still detected, there could be some BCGs with a modest, but still significant offset, where robust detections are not possible in $W3$.

In Fig. 3.11 we plot the $W1$–$W2$ and $W2$–$W3$ colour offsets against each other for BCGs with $S/N > 3$. There is clearly a correlation between a $W1$–$W2$ offset and $W2$–$W3$ offset, with the most extreme offsets in one corresponding to the most extreme offset in the other. As discussed above, the BCGs with the largest offsets in both the Mid-IR colours are likely to be a result of AGN contribution within the BCG. Whereas the BCGs with a significant offset in $W2$–$W3$, but which do not show a significant $W2$ excess are likely to be dominated by star formation (Donahue et al., 2011). Overall, we find at least 9 ± 3 per cent of our BCGs show an excess in either $W2$ or $W3$, increasing to 36 ± 3 per cent for the strong line emitting subsample (see Table 3.1). Note that the uncertainties are measured from the fraction of non line emitting BCGs with significant colour offsets.

3.6 UV Analysis and Results

In the UV wavelength regime we are particularly sensitive to emission from young O and B type stars, hence recent star formation is characterised by an enhanced UV emission. We investigate the BCG NUV–i colour against redshift, (Fig. 3.12), in order to test for enhanced UV emission in our BCG sample. We use the i band photometry because at these redshifts it is unaffected by the shift of the 4000Å break. There appears to be no significant redshift evolution in the NUV–i colour

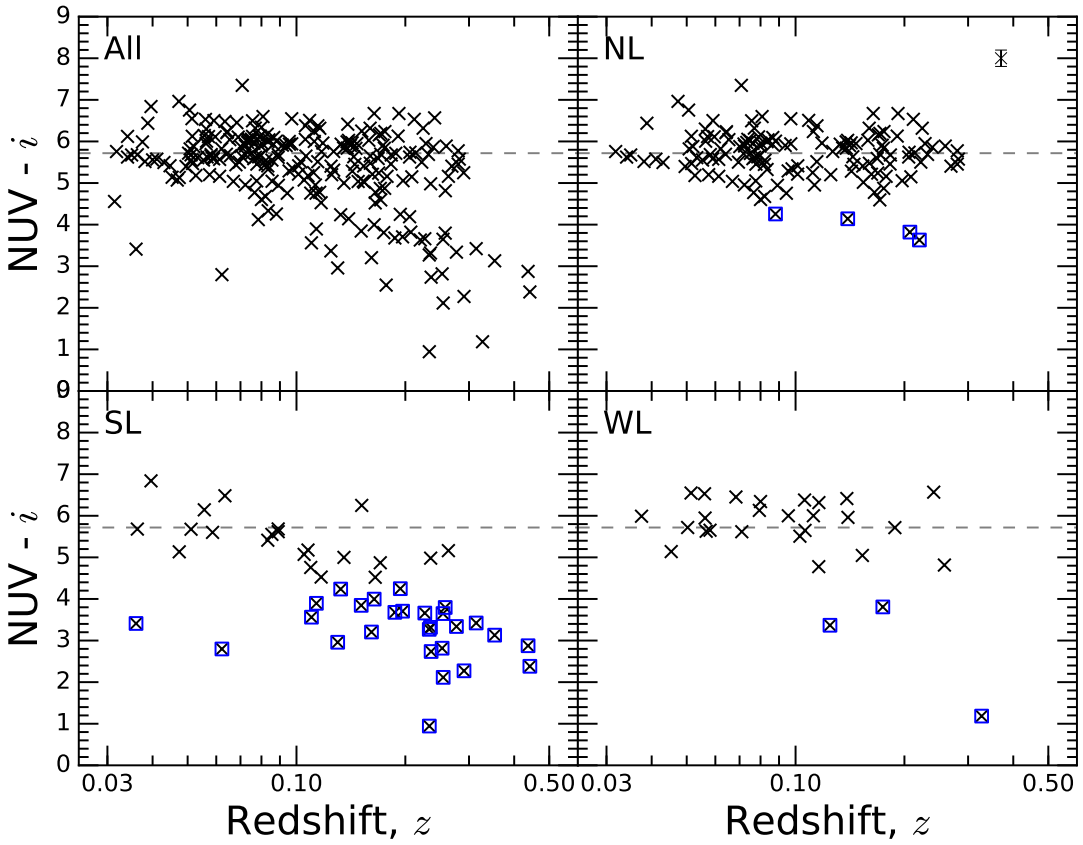

Figure 3.12: NUV–i against redshift for the 245 BCGs detected in the NUV with S/N¿3. The dashed line indicates the median colour of the passive, non-line emitting, BCGs at 5.80 mag. We define subsequent NUV–i colour offsets relative to this line. The panel is split into: full sample (top left), non line emitters (top right), strong line emitters (bottom left) and weak line emitters (bottom right.) The (blue) squares indicate those BCGs with colour offsets in excess of $> 2.5\sigma_p$ from zero, where σ_p is the scatter of the non-line emitters. The 1σ representative error on the colour is given in the top right of the figure.

for the quiescent BCGs and so we define a UV offset as the difference between the measured NUV–i and the median NUV–i value of 5.80. The non-line emitting BCGs form a relatively tight cloud around this median, with a standard deviation of $\sigma_p = 0.57$ mag, consistent with passivity.

As a fraction of the 245 BCGs with robust NUV detections, we find 16%, 32% and 4% show a significant offset, (defined as an NUV–i offset $> 2.5\sigma_p$), in the full, strong line and weak line emitting samples respectively. However we stress that the UV detections are not complete in sky coverage, or of uniform depth for those observed. Because of this we preferentially select galaxies with a UV excess. Hence we are only able to determine lower limits, as a fraction of the total BCG sample. With this in mind, we find that at least 4 ± 1 per cent of BCGs show a UV excess. This fraction is increased to 19 ± 1 per cent of BCGs known to exhibit strong optical emission lines and is 3 ± 1 per cent for those with weak lines. (As summarised in Table 3.1).

3.7 Comparing the Optical, UV and Mid-IR Photometry.

In Fig. 3.13 we display the PS1, *WISE* and *GALEX* colour offsets against one another. We see that BCGs with a significant colour offset at one wavelength are likely to, but not necessarily, exhibit a significant offset in another. This tells us that the colours at both wavelengths are likely to be due to the same phenomena. Fig. 3.13 also illustrates the importance of using multi-wavelength photometry in such an analysis. We see that not all colour bands measure BCG activity equally, due to the complementary nature of different wavelength observations. Some bands are more sensitive to certain phenomena than others, and over different timescales and redshift. In the UV for example we are especially sensitive to ongoing, unobscured star formation, whereas in the Mid-IR we can measure obscured star formation/AGN activity, and over longer timescales.

In Fig. 3.13 we see only one non-line emitting BCG, that of A1704, which has a significant offset in more than one colour index, (with a significant offset in g–r,

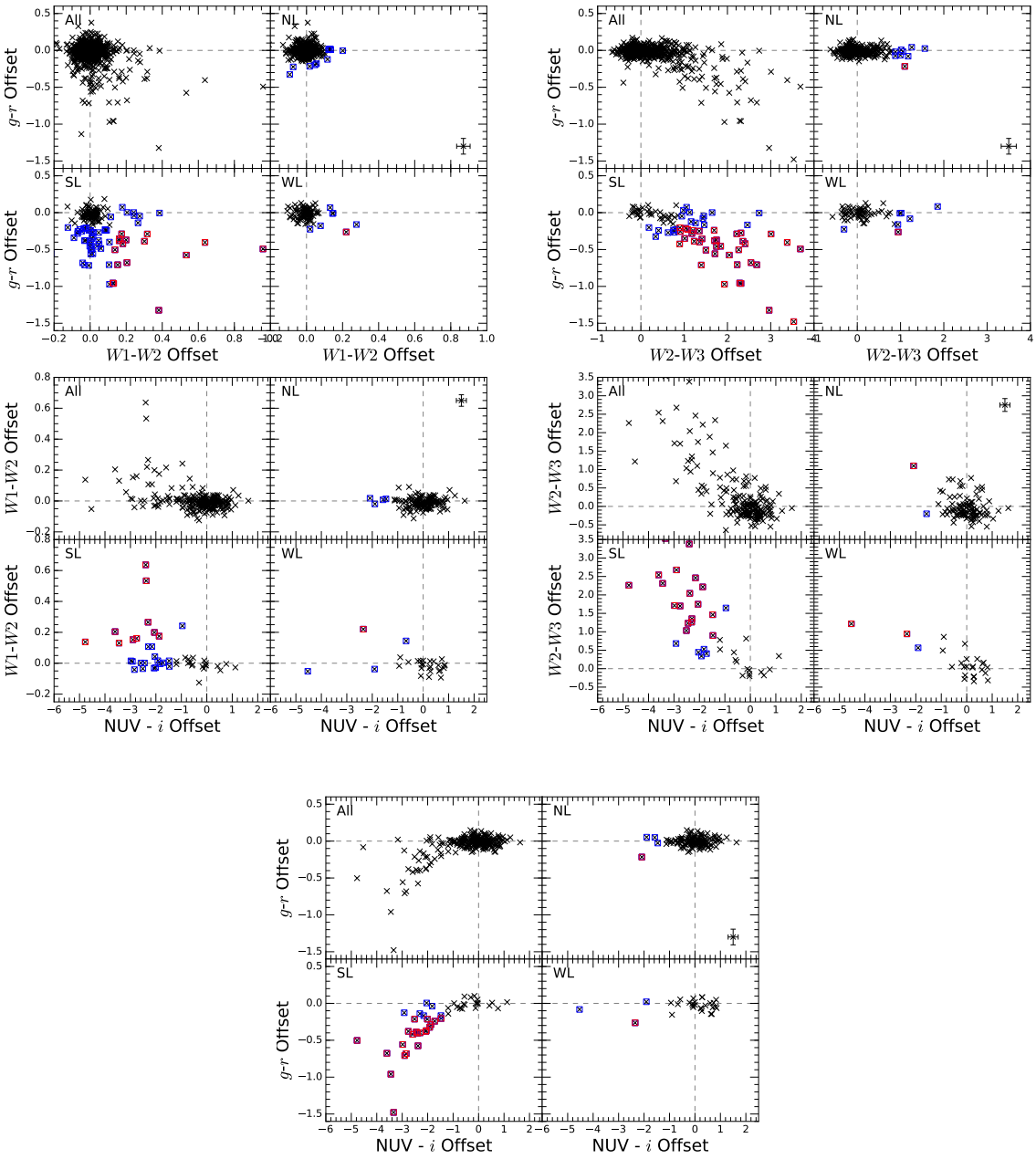

Figure 3.13: Plots of the various colour offsets against one another. The panels are split into: full sample (top left), non line emitters (top right), strong line emitters (bottom left) and weak line emitters (bottom right.) The blue squares indicate those BCGs with colour offsets in excess of $> 2.5\sigma_p$ from zero in one colour and the red squares indicate those BCGs with significant colour offsets in both colours. Note that we only display sources with a S/N >3, which limits the number of $W3$ and NUV detections. The 1σ representative errors on the colours are given in the non line emitters panel.

NUV–i and $W2$–$W3$). This particular galaxy has an SDSS spectrum of its core, which shows no emission lines. However, the imaging clearly shows an optically blue component within the BCG, but offset from the centre of the galaxy. Our prediction is that if the spectral fibre had been placed on this region then it would likely show strong emission lines, (however projection cannot be ruled out at this stage). Optical line emission offset from the BCG has been observed in a number of cluster cores (Hamer et al. 2012; Green et al., in prep) and hence is something to take into consideration when analysing activity in cluster cores.

The lack of non-line emitters, with significant offsets in multiple colours, supports our assumption that these are a fair representation of passively evolving galaxies. We believe that the few non-line emitters which are classed as active in our analysis are a result of scatter about a fixed cut-off value. The fraction of active non-line emitting BCGs can consequently provide a rough measure of the uncertainty in the active BCG fractions reported. The scatter about this colour cut-off can result from a number of sources, but photometric uncertainty and contamination should be the primary sources of this scatter. A known source of contamination, in at least two of the BCGs in this sample, is from lensed galaxies. There are clear gravitational arcs very close to the BCGs of A521 (Richard et al., 2010) and A2104 (Pierre et al., 1994). Both clusters have archival *Spitzer* observations, in which the arcs are clearly luminous in the Mid-IR. Unfortunately the lower resolution of *WISE* means the emission of the BCGs and arcs are blended, probably accounting for the significant offset seen in the $W2$–$W3$ and $W1$–$W2$ for A521 and A2104 respectively. (Note: an excess of 24μm emission was previously noted for the BCG of A521 in Hoffer et al. (2012), which is also likely a result of source blending of the arc). Given the rarity of gravitational arcs with low radius of curvature, this is unlikely to be a significant source of scatter. However, a few more may exist in such a large cluster sample that have yet to be identified as such.

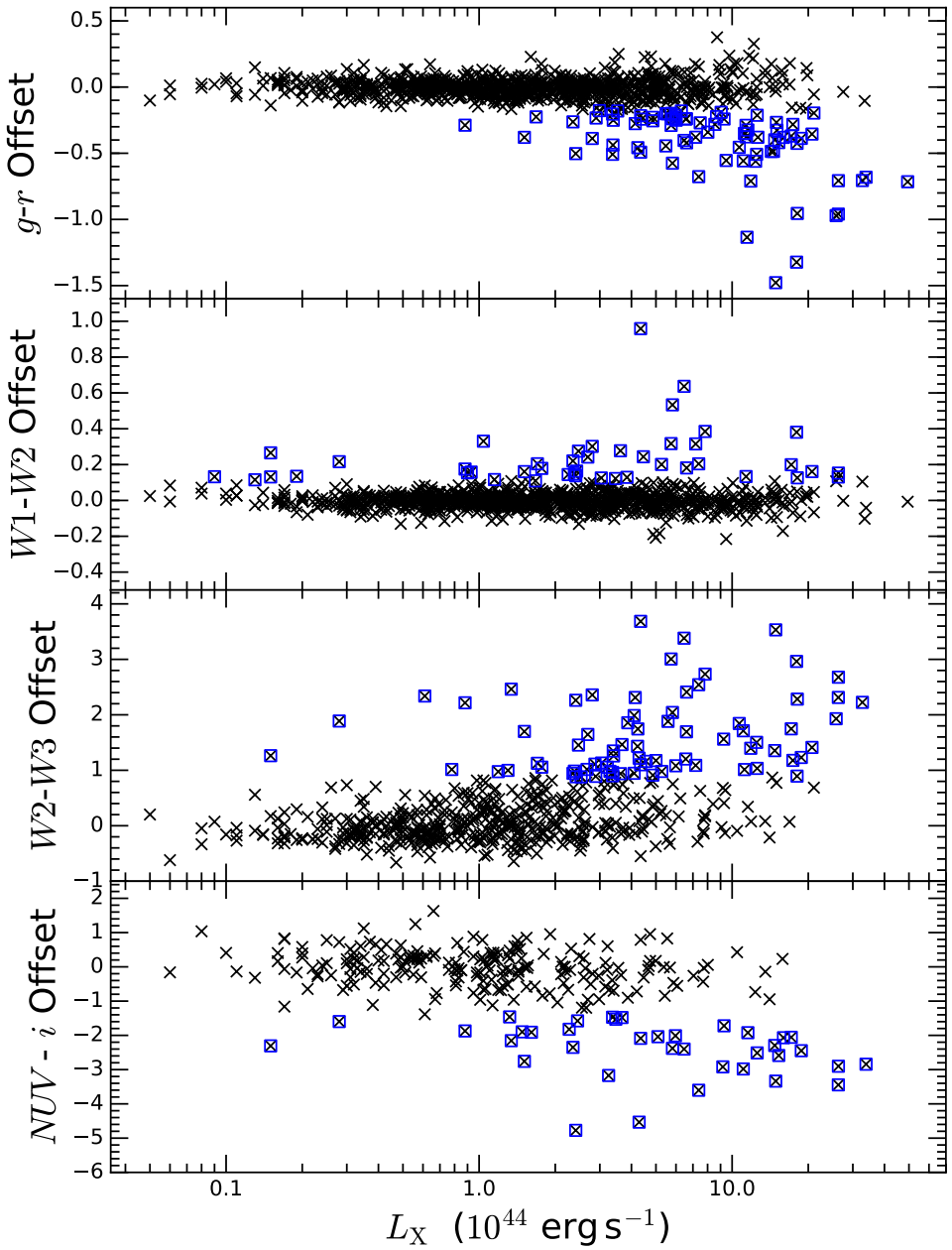

Figure 3.14: BCG colour offsets, against the X-ray luminosity of the host cluster, in the optical (top panel), Mid-IR (second and third panels) and UV (bottom panel). We see that BCGs with colours which deviate from the quiescent BCG population tend to belong to more X-ray luminous clusters, consistent with BCG activity having a strong environmental dependence. Note that the first two panels are complete, but that the $W3$ and NUV detections are limited by S/N. So, since S/N is systematically lower at high redshift, high L_X clusters are preferentially excluded by selection effects.

3.8 BCG Activity and Cluster X-ray Luminosity

The overall X-ray luminosity of a cluster is given by integrating over the more peaked emission in the core, and the more extended emission in the wings, of the cluster X-ray profile. Hence it is reasonable to assume that, given the observed strong correlation between cool core clusters and BCG activity (Chapter 1), any relationship seen between tracers of activity and L_X is indicative of this underlying link and suggestive that these clusters are also cool cores. In Fig. 3.14 we plot colour offsets against cluster L_X and find that BCGs with significant optical, Mid-IR and UV colour offsets tend to belong to more X-ray luminous clusters. However, a high X-ray luminosity does not necessarily imply BCG activity. The number and proportion of BCGs with significant colour offsets, in bins of X-ray luminosity, are presented in Table 3.2, which confirms there is an apparent association between BCG activity and host cluster gas properties. This result agrees with the observations of O'Dea et al. (2008) who found BCG IR excesses preferentially in higher X-ray luminosity clusters.

The histograms in Fig. 3.15 show the X-ray distributions for clusters with line emitting BCGs and how this compares with the overall distribution. The presence of optical emission lines is strongly associated with the X-ray properties of the host clusters, with strong line emitters preferentially located in the more X-ray luminous clusters. From Table 3.2, we see that the fraction of BCGs which show signs of activity through the presence of strong lines increases with respect to X-ray luminosity. This positive trend is in agreement with the results of Samuele et al. (2011) who found fractions of 30%, 18% and 16% for the Crawford et al. (1999) BCS sample of BCGs for the same L_X ranges respectively. Note that the apparent deficit in weak line emitting BCGs at higher X-ray luminosities is likely to be an observational effect, in which high L_X clusters are more likely to be high redshift, where the detection of weak lines is more difficult.

The presence of emission lines in BCGs can be used as tracer of cool core clusters (Heckman 1981; Hu et al. 1985; Johnstone et al. 1987; Heckman et al. 1989; Crawford et al. 1999; McDonald 2011). So given we find a link between photometric colours and emission line status, we can then deduce that peculiar photometric colours also

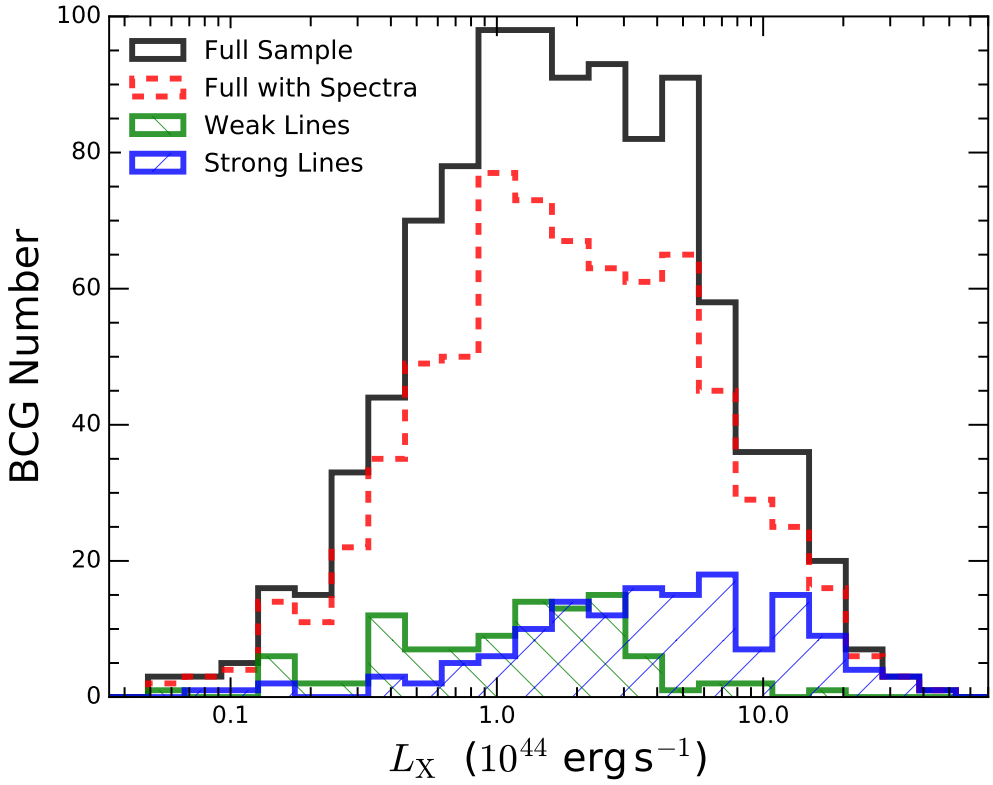

Figure 3.15: A histogram showing the host cluster X-ray luminosity distribution for the full sample of BCGs (solid black), the full sample of BCGs with spectroscopy (red dotted), as well as subsamples of BCGs with strong (blue hatch) and weak (green hatched) emission lines. We see that the presence of strong lines (hence BCG activity) is preferentially in the most X-ray luminous clusters.

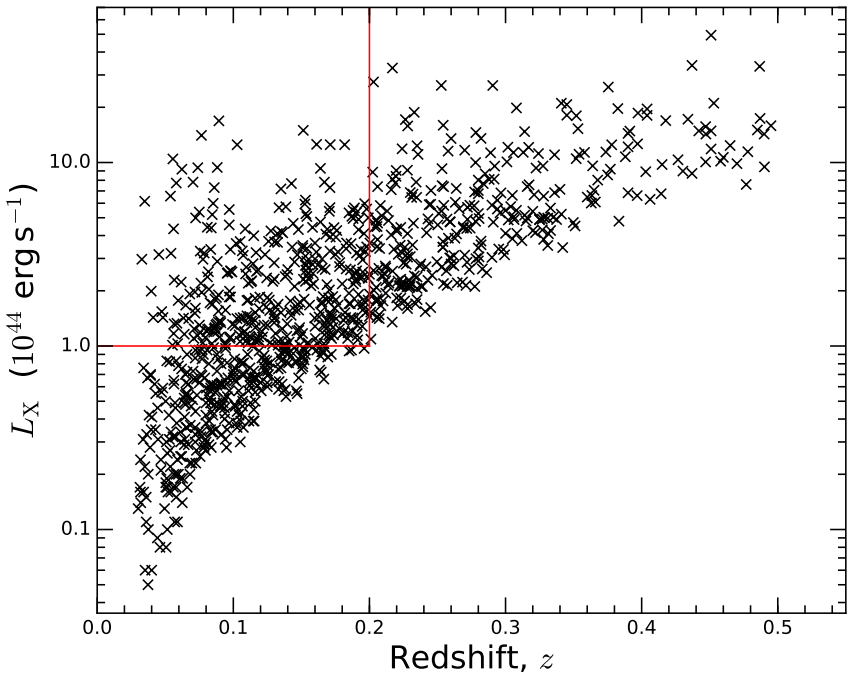

Figure 3.16: The RASS 0.1–2.4 keV X-ray luminosity and redshift for each of the 981 clusters in this sample. The solid (red) lines enclose the clusters selected in our 'X-ray luminosity complete' subsample.

acts as a tracer of cool cores. This reinforces the assumptions given above that the peculiar colour and L_X association is reflective of the likely cool core status of these particular clusters.

The strong association between BCG activity and total X-ray luminosity of the host cluster, evident through the photometric excess and optical line emission, has important implications regarding cluster selection effects. Specifically, the fraction of active BCGs one discovers in any given cluster sample is dependent on the X-ray luminosity distribution of that sample. For example, Stott et al. (2012) do not find any unusual coloured BCGs in g–r in the XCS sample, but this is not surprising given the low X-ray luminosity nature of that particular cluster sample. With this in mind we investigate the active BCG fraction for volume complete subsamples and make comparisons to the literature.

If we consider an "X-ray luminosity complete" cluster subsample defined by $L_X \geq 1 \times 10^{44}\,\mathrm{erg\,s^{-1}}$ and $z \leq 0.2$, (as indicated in Fig. 3.16), we find active BCG fractions as presented in Table 3.3, specifically that at least 14% of clusters deviate

Table 3.1: Percentage of BCGs with an optical (Opt.), Mid-IR or UV colour offset $> 2.5\sigma_p$, where σ_p is the scatter for the non-line emitting (passive) BCGs. The percentage of BCGs with a significant offset in any one of the colours is given in the "Combined" column. The "Radio" column indicates a detection only, not an excess. Percentages are presented as fractions of the full sample (All) and strong line emitting (SL), weak line emitting (WL) and non-line emitting (NL) subsamples.

	BCGs (#)	Opt. (%)	MIR (%)	UV (%)	Combined (%)	Radio (%)
All	981	8	9	4	14	52
SL	144	39	35	19	51	84
WL	100	3	8	3	11	43
NL	476	1	3	1	5	43

Table 3.2: Number of BCGs with significant colour offsets, and optical emission lines, in bins of cluster X-ray luminosity. The results suggest active BCGs are preferentially found in high $L_{\rm X}$ clusters. (Note the apparent decline in the weak line fraction in the highest $L_{\rm X}$ is likely a redshift dependence effect - specifically high $L_{\rm X}$ clusters are preferentially at high z, where the S/N in observations makes identifying weak lines difficult.)

	Total	$L_{\rm X} \geq 45$	$L_{\rm X} \geq 44$	$42 < L_{\rm X} < 44$
	981	76	671	310
g–r	79 (8%)	35 (46%)	78 (12%)	1 (1%)
$W1$–$W2$	45 (5%)	8 (11%)	36 (5%)	9 (3%)
$W2$–$W3$	75 (8%)	19 (25%)	70 (10%)	5 (2%)
NUV-i	37 (4%)	12 (16%)	34 (5%)	3 (1%)
Strong	144 (15%)	34 (45%)	127 (19%)	17 (5%)
Weak	100 (10%)	2 (3%)	61 (9%)	39 (13%)

Table 3.3: Same as Table 3.1, but for the "X-ray luminosity complete" subsample of clusters with $L_{\rm X} \geq 1 \times 10^{44}\,{\rm erg\,s^{-1}}$ and $z \leq 0.2$.

	BCGs (#)	Opt. (%)	MIR (%)	UV (%)	Combined (%)	Radio (%)
All	359	5	11	4	14	53
SL	61	23	31	16	43	90
WL	39	5	10	5	15	67
NL	177	0	5	1	6	42

Table 3.4: Same as Table 3.1, but for the subsample of clusters with $L_{\rm X} \geq 1 \times 10^{44}\,{\rm erg\,s^{-1}}$ and $z \leq 0.1$ to match the sample selection in Fraser-McKelvie et al. (2014).

	BCGs (#)	Opt. (%)	MIR (%)	UV (%)	Combined (%)	Radio (%)
All	95	3	8	2	11	61
SL	17	18	29	6	35	88
WL	14	0	7	0	7	86
NL	52	0	0	2	2	48

from passivity in at least one colour. This is comparable to our overall figure of 14% because the lower L_X and higher z sections of our full sample cancel out their relative effects.

Similarly, in Table 3.4 we summarise the BCG fractions within the subsample defined by $L_X \geq 1 \times 10^{44}\,\mathrm{erg\,s^{-1}}$ and $z \leq 0.1$. This L_X–z distribution was chosen to match that of Fraser-McKelvie et al. (2014), who find 3 ± 1 per cent of their BCGs have a W2–W3 colour in excess of 1.5, suggestive that they are likely dominated by star formation. We conversely find that $> 8\%$ of our BCGs in the same L_X–z space have a colour offset in *WISE*, increasing to at least 10% if you include the optical and UV data. This disagreement we think reflects their use of raw *WISE* colours and of a simple colour cut to select star forming galaxies. In their plot a significant number of BCGs are offset from the bulk passive cloud in colour–colour space, yet do not satisfy the colour cut used. One would expect very few BCGs in the Universe to be forming stars on the level one would expect for a classically "star forming" galaxy (like a spiral), but instead one should consider how a modest amount of star formation would make the *WISE* colours differ from the bulk passive cloud of BCGs in colour space.

An additional observational consideration for BCG activity is that the peaked X-ray emission in cool core clusters could be misinterpreted as a point source in shallow X-ray data. If the BCG of the cluster shows strong high ionisation line emission, usually, and understandably, that X-ray source is identified as an AGN. But, the cluster may still be a significant contributor. This is best illustrated by the Phoenix cluster, (McDonald et al., 2012a), where the most X-ray luminous cluster was only identified because of the SPT SZ effect detection. Therefore caution is needed when interpreting the perceived rarity of BCGs hosting strong AGN as this identification bias could be masking systems such as H1821+644 (Russell et al., 2010) and 3C186 (Siemiginowska et al., 2010) where the cluster X-ray emission is a minority contributor to the total flux, but it would still be above the X-ray flux limit of a survey once the AGN contribution is removed. We attempt to address the ambiguity between AGN and clusters in low spatial resolution X-ray data in Chapter 4.

3.9 Radio Luminosity

We find 512 BCGs (52% of total sample) have a 1.4 GHz radio detections within 45 arcsec in NVSS. In the colour offset against radio luminosity plots shown in Fig. 3.17 there appears to be a connection between the radio emission and colour offsets. The apparent trends in the top four panels are likely to be a reflection of the relation between X-ray luminosity and radio power (Hogan et al., 2015a), shown in the bottom panel, rather than suggesting that the star formation is induced or triggered by the radio activity in the BCG. This does however support the idea of a feedback cycle between radiative cooling induced star formation and AGN activity. Whereby relic radio emission still exists from previous stages of AGN activity in these galaxies.

3.10 Conclusions

We investigated the PS1 optical, *WISE* Mid-IR and *GALEX* UV photometry for Brightest Cluster Galaxies in 981 *ROSAT* All Sky Survey X-ray selected clusters. The sample consists of clusters in the redshift range, $0.03 < z < 0.5$ with an X-ray luminosity range of $5 \times 10^{43}\,\mathrm{erg\,s^{-1}} < L_X < 5 \times 10^{45}\,\mathrm{erg\,s^{-1}}$. The principal aim was to search for signs of star formation and/or AGN activity in BCGs by looking for photometric colours which deviate from that expected for a passive BCG. The main results are summarised as follows:

- At least 14 ± 3 per cent of the BCGs in our full sample show a significant colour deviation from passivity in at least one colour. In the optical we find 8 ± 1 per cent are significantly blue in $PS1$ g–r. In the Mid-IR we find at least 9 ± 3 per cent show a significant colour offset in either W1–W2 or W2–W3, with 5% showing enhanced $W2$ emission, and at least 8% showing enhanced $W3$ emission. In the NUV we find at least 4 ± 1 per cent of BCGs show an enhanced NUV emission, shown as a significant NUV-i colour offset. We stress that due to incompleteness these fractions represent lower limits for the NUV and $W3$. We interpret these colour deviations as a result of star formation

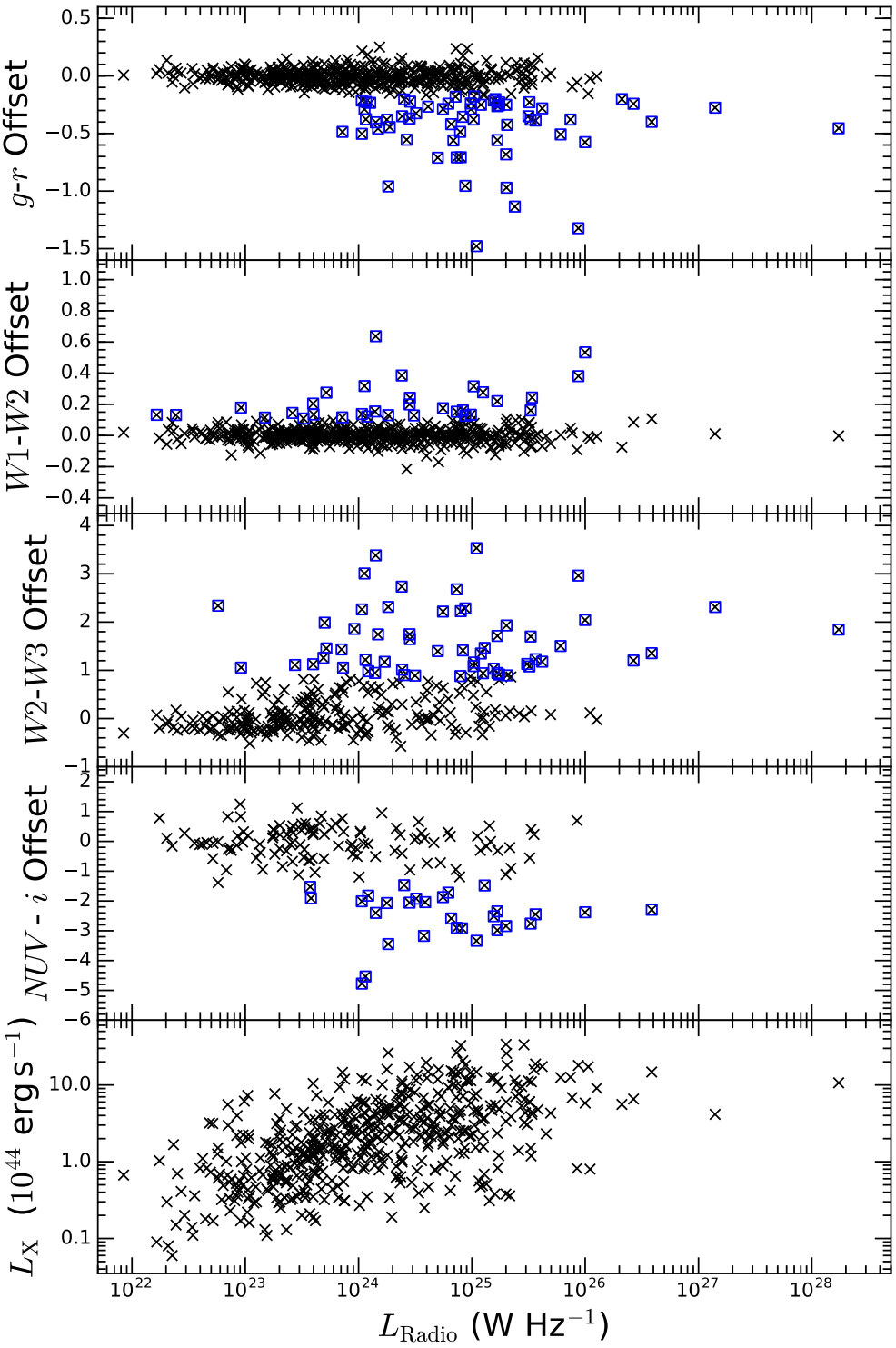

Figure 3.17: The 1.4 GHz radio luminosity of the BCGs against the optical, Mid-IR and UV colour offsets (top four panels) and host cluster X-ray luminosity (bottom panel). The (blue) squares are indicative of offsets in excess of $2.5\,\sigma_p$.

and/or AGN activity within the BCG. Details regarding each of these active BCG candidates are provided in Table 3.5.

- We find that across all wavelengths the presence of optical emission lines and atypical photometric colours are strongly associated. This reinforces our interpretation of these BCGs being "active". We find that the majority of BCGs are non-line emitting and do not exhibit signs of enhanced emission, consistent with passivity.

- We find that BCG activity has a strong association with the host cluster X-ray luminosity. Specifically, the fraction of peculiarly coloured BCGs is much higher in high $L_{\rm X}$ clusters. This has important implications for the apparent prevalence of active BCGs and the selection function of a cluster sample.

- We find that significant colour offsets in one wavelength regime is often associated with a significant offset in another, but not always. In the former case this illustrates the common origin of these colours at different wavelengths, but in the latter shows the benefit of a multi-wavelength analysis, in which we can trace activity over complimentary timescales and degrees of obscuration.

- Although this study suggests an enhanced star formation is present in a significant fraction of BCGs, it should be noted that the typical star formation rate for an active BCG is still modest. It is beyond the scope of this study, but typically BCGs only produce new stars at rates of a few tenths, to a few tens, of Solar masses per year (Hoffer et al., 2012; Fraser-McKelvie et al., 2014; Fogarty et al., 2015). Hence the overall fraction of the stellar mass of the BCG, contributed by this star formation, is typically only a few ($\sim 1-3$) per cent (Mittal et al. 2015; Loubser et al. 2016; although larger fractions are predicted for some extreme systems; Mittal et al. 2015). So, as mentioned in Chapter 1, and as will be explored in Chapter 6, the stellar mass growth of BCGs is dominated by merger events.

- We find that the BCG luminosity, in both the i and $W1$ bands, correlates with the X-ray luminosity of the host cluster. Specifically the most luminous,

and hence most massive, BCGs tend to reside in the more X-ray luminous, and hence massive, clusters.

- The optical colours of the cluster red sequence are remarkably tightly constrained given the range in $L_{\rm X}$, indicative of the homogeneity in cluster galaxies across mass and redshift. For the majority of BCGs, this is also the case. So where BCGs are passively evolving, they do so in a similar fashion to one another.

- We have shown we are able to measure photometric excesses in active BCGs up to at least $z = 0.5$, with potential to go to higher redshift. Hence, the same analysis could be applied to future, larger cluster samples. This creates opportunity with the new generation of X-ray telescopes, such as eROSITA, due to make observations in the near future, which will fill in the $L_{\rm X}$–z parameter space. Combined with large photometric surveys such as the LSST one could identify a large number of "active" BCG candidates, which would be vital in placing constraints on the prevalence of activity in BCGs and better understanding the role of feedback in these systems.

3.11 Table of "active" BCG candidates

Table 3.5: A table of those BCGs measured to be significantly offset in one colour or more (i.e. a colour offset in excess of $2.5\,\sigma_p$). The table key is as follows: (0) Cluster X-ray luminosity, in 0.1–2.4 keV band, in units of $10^{44}\mathrm{erg\,s^{-1}}$, (1) indicates whether the BCG has strong (S), weak (W) or no (N) optical emission lines or if no spectra available (-) (2) a PS1 g–r colour offset < -0.18 mag, (3) a *WISE* $W1$–$W2$ offset > 0.11 mag, (4) a *WISE* $W2$–$W3$ colour offset > 0.87 mag and (5) a *GALEX* NUV-i colour offset < -1.43 mag. (a) The symbols in these columns are as follows: If a number is present this is the colour offset value and indicates a significant deviation from passivity, '×' indicates a lack of a significant offset, '-' indicates this BCG not observed, and '..' indicates a poor S/N.

Cluster ID	BCG R.A. (J2000)	BCG DEC (J2000)	Redshift	L_{X} (0)	Lines (1)	g–r (2a)	$W1$–$W2$ (3a)	$W2$–$W3$ (4a)	NUV-i (5a)
RXJ0008.0-1151	00:07:57.0	−11:51:44	0.21	1.48	N	×	×	..	-1.90
RXJ0010.9+2909	00:10:53.4	+29:09:39	0.33	4.29	W	×	×	1.21	-4.53
A11	00:12:33.8	−16:28:07	0.15	0.88	S	-0.29	0.18	2.22	-1.87
A22	00:20:43.1	−25:42:28	0.14	3.46	N	×	0.12	..	-
MACSJ0025.4-1222	00:25:33.0	−12:23:16	0.48	11.45	-	-1.13	×	..	-
RXJ0045.9-1723	00:45:54.8	−17:23:29	0.06	0.15	W	×	0.13	×	-
S84	00:49:22.8	−29:31:12	0.11	1.77	S	×	0.18	1.06	..
Z348	01:06:49.4	+01:03:22	0.25	7.38	S	-0.68	0.20	2.54	-3.60
A145	01:06:53.3	−02:28:56	0.19	1.30	N	×	×	1.00	-
MACSJ0111.5+0855	01:11:31.5	+08:55:41	0.48	15.04	N	-0.33	×	..	-
MACSJ0150.3-1005	01:50:21.3	−10:05:30	0.36	6.61	S	-0.42	0.18	2.40	-
MACSJ0159.8-0849	01:59:49.3	−08:49:58	0.40	18.06	S	-0.43	×	0.89	-
A291	02:01:43.1	−02:11:48	0.20	5.97	S	-0.21	×	..	-2.01
A368	02:37:27.7	−26:30:28	0.22	4.23	S	×	×	1.43	-
RXJ0238.8-1258	02:38:49.3	−12:58:49	0.20	2.53	N	×	×	0.88	×
MACSJ0242.5-2132	02:42:35.9	−21:32:25	0.31	14.74	S	-0.40	×	1.35	-2.30
A383	02:48:03.3	−03:31:44	0.19	5.09	S	×	×	×	-2.04
A3088	03:07:02.2	−28:39:56	0.25	7.48	S	-0.27	×	×	-
MACSJ0326.8-0043	03:26:49.9	−00:43:51	0.45	14.29	S	-0.49	×	..	-
MACSJ0329.6-0211	03:29:41.6	−02:11:46	0.45	11.85	S	-0.71	×	1.39	-

Table 3.5: Continued

Cluster ID	BCG R.A.	BCG DEC	Redshift	L_X	Lines	g–r	$W1$–$W2$	$W2$–$W3$	NUV-i
RXJ0331.1-2100	03:31:05.9	−21:00:32	0.19	5.48	S	-0.20	×	×	-
RXJ0353.0+1941	03:52:59.0	+19:40:59	0.11	2.47	S	×	0.28	1.46	-
MACSJ0404.6+1109	04:04:33.7	+11:07:53	0.36	11.35	-	-0.29	0.14	..	-
A483	04:15:57.6	−11:32:53	0.28	5.27	-	×	×	0.97	-
MACSJ0417.5-1154	04:17:34.7	−11:54:32	0.44	33.83	S	-0.68	×	..	-2.84
MACSJ0429.6-0253	04:29:36.0	−02:53:06	0.40	12.64	S	-0.38	×	..	-
RXJ0437.1+0043	04:37:09.6	+00:43:51	0.28	8.68	N	-0.22	×	..	-
RXJ0439.0+0520	04:39:02.3	+05:20:42	0.21	5.83	S	-0.24	×	×	-
RXJ0448.2+0952	04:48:12.8	+09:53:01	0.15	2.90	-	-0.23	×	..	-
A521	04:54:06.9	−10:13:24	0.25	9.26	N	×	×	1.56	-
RXJ0505.2-0217	05:05:16.7	−02:19:24	0.23	3.05	-	×	×	1.13	-
RXJ0524.3+0329	05:24:19.1	+03:29:54	0.15	2.43	-	×	0.16	..	-
RXJ0611.0-2735	06:11:01.2	−27:35:33	0.04	0.15	S	×	0.27	1.27	-2.31
Z1121	06:31:22.7	+25:01:06	0.08	2.38	W	-	0.15	0.99	-
CIZAJ0640.1-1253	06:40:07.2	−12:53:14	0.14	7.18	-	-0.38	0.32	1.09	-
CIZAJ0710.4+2240	07:10:23.8	+22:40:02	0.29	11.30	-	-0.35	×	..	..
CIZAJ0719.5+0043	07:19:36.0	+00:42:33	0.22	9.05	-	-0.19	×	..	-
PKS745-191	07:47:31.4	−19:17:39	0.10	12.50	S	-0.51	×	1.50	-
RXJ0815.5-0308	08:15:27.8	−03:08:27	0.20	5.58	-	-0.20	×	..	-
RXJ0821.0+0751	08:21:02.3	+07:51:47	0.11	1.34	S	×	×	2.46	-2.16
RXJ0834.9+5534	08:34:55.0	+55:34:20	0.24	4.14	S	-0.28	×	2.31	×
Z1883	08:42:55.9	+29:27:26	0.19	3.37	S	-0.20	×	0.90	-1.47
Z2089	09:00:37.0	+20:53:40	0.23	6.46	S	-0.40	0.64	3.38	-2.40
MACSJ0913.7+4056	09:13:45.6	+40:56:27	0.44	14.87	S	-1.48	1.77	3.52	-3.34
Hyd-A	09:18:05.7	−12:05:43	0.05	6.56	S	-0.24	×	1.21	-
A854	09:42:01.1	+08:58:19	0.21	3.40	N	×	×	1.26	-
RBS797	09:47:12.7	+76:23:13	0.34	20.69	S	-0.36	0.16	1.41	-2.88
RXJ1000.4+4409	10:00:31.0	+44:08:43	0.15	2.25	W	×	0.14	..	×
A910	10:03:00.2	+67:07:56	0.21	3.47	-	×	×	×	-1.53
A926	10:06:40.2	+21:40:14	0.18	1.70	S	×	0.20	1.12	-

**The BCG of A1704 has an SDSS spectra on its core, which shows no emission lines. But in the imaging there is clearly an optically blue component within the BCG and just North of its core, which does not have spectroscopy. We detect this in our photometry and suspect this is associated with activity in the BCG, but projection cannot be ruled out.

Table 3.5: Continued

Cluster ID	BCG R.A.	BCG DEC	Redshift	L_X	Lines	g–r	$W1$–$W2$	$W2$–$W3$	NUV-i
MS1006.0+1202	10:08:47.7	+11:47:38	0.26	3.87	W	×	×	1.85	-
Z3146	10:23:39.6	+04:11:10	0.29	26.29	S	-0.96	0.13	2.31	-3.45
A3444	10:23:50.2	−27:15:23	0.25	15.96	S	-0.38	×	×	-2.07
A1068	10:40:44.4	+39:57:11	0.14	5.74	S	-0.29	0.32	3.01	-
A1084	10:44:32.9	−07:04:07	0.13	4.10	S	×	×	0.95	×
A1126	10:53:50.2	+16:51:02	0.09	1.19	-	×	×	0.98	×
A1211	11:14:50.3	−12:13:50	0.19	3.21	N	×	×	1.05	×
Z3959	11:15:51.8	+01:29:54	0.35	15.29	S	-0.42	×	..	-2.59
RXJ1124.5+4351	11:24:29.7	+43:51:25	0.37	8.02	S	-0.34	×	..	-
RXJ1128.1+7529	11:28:09.9	+75:29:35	0.17	0.93	-	×	0.16	..	-
MACSJ1141.6-1905	11:41:40.8	−19:05:15	0.30	3.84	-	×	0.13	..	-
A1451	12:03:16.8	−21:32:55	0.20	5.00	N	×	×	1.17	-
MACSJ1218.4+4012	12:18:28.6	+40:12:38	0.30	5.75	-	-0.20	×	..	-
RXJ1259.1+4129	12:59:08.6	+41:29:37	0.28	2.99	W	-0.18	×	..	-
RXJ1301.0-2312	13:00:58.5	−23:12:15	0.13	1.51	S	-0.38	0.16	1.70	-2.76
A1664	13:03:42.6	−24:14:42	0.13	4.24	S	-0.46	×	1.75	-3.12
A1704**	13:14:24.6	+64:34:31	0.22	4.35	N	-0.22	×	1.10	-2.09
A1750b	13:31:11.0	−01:43:38	0.08	0.61	-	×	×	2.34	×
RXJ1336.0-0331	13:35:60.0	−03:31:28	0.17	1.61	W	×	×	×	-1.91
MACSJ1347.5-1144	13:47:30.7	−11:45:09	0.45	49.41	S	-0.72	×	..	-
A1795	13:48:52.5	+26:35:34	0.06	9.19	S	×	×	×	-2.92
RBS1322	13:50:22.1	+09:40:10	0.13	3.67	S	×	×	1.46	-1.48
MACSJ1354.6+7715	13:54:43.0	+77:15:16	0.40	6.60	S	-0.24	×	1.69	-
RXJ1359.3+7447	13:59:16.9	+74:46:42	0.20	1.68	W	-0.23	×	×	-
RXJ1359.9+1414	13:59:57.3	+14:14:17	0.21	2.67	W	×	×	1.01	..
A1835	14:01:02.2	+02:52:42	0.25	26.31	S	-0.71	0.15	2.67	-2.90
RXJ1401.3+2501	14:01:17.8	+25:01:50	0.41	6.30	-	-0.18	×	..	-
MACSJ1411.3+5212	14:11:20.4	+52:12:09	0.46	10.67	S	-0.45	×	1.84	-
A1910	14:24:24.4	+25:14:28	0.23	2.41	S	-0.50	0.14	2.26	-4.77
A1918	14:25:22.5	+63:11:53	0.14	2.45	N	×	×	×	-1.58
RXJ1427.2+4407	14:27:16.1	+44:07:30	0.49	17.39	S	-0.28	×	1.17	-
RXJ1434.7+1721	14:34:42.9	+17:21:57	0.04	0.09	N	×	0.13	×	-
RXJ1447.4+0827	14:47:26.0	+08:28:25	0.38	25.77	S	-0.97	0.11	1.92	-
Z7160	14:57:15.1	+22:20:34	0.26	11.54	S	-0.32	×	×	-1.92

Table 3.5: Continued

Cluster ID	BCG R.A.	BCG DEC	Redshift	$L_{\rm X}$	Lines	g–r	$W1$–$W2$	$W2$–$W3$	NUV-i
RXJ1459.1-0842	14:59:05.2	−08:42:36	0.10	1.15	N	×	0.12	×	-
S780	14:59:28.8	−18:10:45	0.24	11.07	S	-0.56	×	1.71	-2.98
RXJ1504.1-0248	15:04:07.5	−02:48:16	0.22	32.73	S	-0.71	×	2.22	-4.72
RXJ1512.8-0127	15:12:52.6	−01:28:26	0.12	0.78	N	×	×	1.01	-
A2055	15:18:45.7	+06:13:56	0.10	3.62	W	×	0.28	0.94	-
MACSJ1532.8+3021	15:32:53.8	+30:20:59	0.34	18.10	S	-0.95	0.13	2.28	-
A2104	15:40:07.9	−03:18:15	0.15	5.26	N	×	0.20	×	-
MACSJ1551.9-0207	15:51:58.6	−02:07:50	0.30	5.47	-	-0.44	×	..	-
A2146	15:56:14.2	+66:20:52	0.23	7.82	S	×	0.38	2.73	..
PKS1555-140	15:58:21.9	−14:09:58	0.10	4.57	S	×	×	1.16	-
RXJ1600.0-0354	16:00:02.5	−03:54:35	0.27	4.39	-	-0.24	×	..	-
A2147b	16:03:38.1	+15:54:02	0.11	2.69	S	×	0.24	1.65	×
RXJ1614.3+5442	16:14:15.4	+54:43:28	0.33	3.53	N	-0.18	×	..	-
MACSJ1621.3+3810	16:21:24.7	+38:10:08	0.47	12.38	S	-0.56	×	..	-
A2204	16:32:47.0	+05:34:31	0.15	14.97	S	-0.27	×	×	-
RBS1634	17:17:07.0	+29:31:21	0.28	14.57	S	-0.49	×	..	-
Z8193	17:17:19.2	+42:26:57	0.18	3.39	S	-0.25	×	1.35	-
Z8197	17:18:11.9	+56:39:56	0.11	2.27	S	×	×	×	-1.82
RXJ1720.2+2637	17:20:10.1	+26:37:32	0.16	9.29	S	-0.24	×	×	-1.72
A2262	17:23:21.6	+23:50:39	0.23	4.10	-	×	×	1.98	-
A2270	17:27:23.5	+55:10:53	0.24	2.80	S	-0.39	0.30	2.36	-
Z8276	17:44:14.5	+32:59:29	0.08	3.29	S	×	×	0.98	-
CIZAJ1804.1+0042	18:04:08.9	+00:42:22	0.09	2.89	-	×	×	0.89	-
RXJ1817.8+6824	18:17:44.5	+68:24:25	0.29	3.38	-	-0.44	×	×	-
RGBJ1832+688	18:32:35.8	+68:48:05	0.20	4.86	S	-0.25	×	0.91	..
CIZAJ1904.2+3627	19:04:11.9	+36:26:59	0.08	0.90	-	×	0.16	×	-
CIZAJ1917.6-1315	19:17:36.2	−13:15:11	0.18	3.25	-	×	×	..	-3.17
MACSJ1931.8-2634	19:31:49.7	−26:34:32	0.35	17.98	S	-1.32	0.38	2.96	-
Cyg-A	19:59:28.3	+40:44:02	0.06	4.35	S	-0.49	0.96	3.69	-
MRC2011-246	20:14:51.8	−24:30:23	0.16	12.56	S	-0.21	×	1.03	-2.51
RXJ2020.3-2225	20:20:22.6	−22:25:32	0.29	5.58	-	×	×	1.88	-
RXJ2043.2-2144	20:43:14.6	−21:44:34	0.20	4.46	S	×	0.24	..	-
RXJ2100.0-2426	20:59:55.6	−24:25:45	0.08	0.28	-	×	0.22	1.89	-1.60
RXJ2125.4+1742	21:25:22.0	+17:43:05	0.22	3.37	-	-0.51	×	0.96	-

Table 3.5: Continued

Cluster ID	BCG R.A.	BCG DEC	Redshift	$L_{\rm X}$	Lines	g–r	$W1$–$W2$	$W2$–$W3$	NUV-i
MACSJ2134.6-2706	21:34:36.0	−27:05:55	0.36	6.01	-	-0.25	×	..	-
RGBJ2138+359	21:38:21.1	+35:58:23	0.11	1.04	-	×	0.33	×	-
MS2137.3-2353	21:40:15.2	−23:39:40	0.31	11.36	S	-0.38	×	..	-
MACSJ2149.3+0951	21:49:19.6	+09:51:37	0.38	8.55	-	-0.28	×	..	-
A2390	21:53:37.0	+17:41:42	0.23	18.77	S	-0.39	×	1.23	-2.45
RXJ2213.1-2754	22:13:05.9	−27:54:20	0.03	0.13	S	×	0.12	×	-
A2442	22:25:51.2	−06:35:34	0.09	1.32	N	×	×	..	-1.46
MACSJ2229.7-2755	22:29:45.2	−27:55:35	0.32	11.19	S	-0.35	×	1.01	-
MACSJ2243.3-0935	22:43:20.7	−09:35:18	0.45	21.05	N	-0.20	×	..	-
CIZAJ2302.6+7136	23:02:38.6	+71:36:25	0.14	2.87	-	×	×	1.11	-
RXJ2311.3-0946	23:11:18.9	−09:46:22	0.49	9.47	S	-0.55	×	..	-
RXJ2320.9-0433	23:20:54.2	−04:34:02	0.19	2.42	N	×	×	0.88	-
A2597	23:25:19.7	−12:07:26	0.09	5.99	S	-0.23	×	1.08	..
RXJ2326.3-2406	23:26:14.2	−24:06:30	0.06	0.19	N	×	0.14	..	-
A2627	23:36:42.1	+23:55:29	0.12	2.35	W	-0.26	0.22	0.94	-2.35
PKS2338+000	23:41:07.0	+00:18:33	0.28	5.81	S	-0.58	0.53	2.04	-2.38
A2667	23:51:39.4	−26:05:02	0.23	17.13	S	-0.37	0.20	1.74	-2.06
RXJ2355.4-1027	23:55:25.6	−10:27:22	0.29	3.04	N	×	0.13	..	-

Chapter 4

Recovering the Strongest AGN in Cluster Cores

The work in this chapter is adapted from the following publication:

Green et al. (2017), MNRAS, 465, 4872.

4.1 Overview

A key challenge in understanding the feedback mechanism of AGN in BCGs is the inherent rarity of catching an AGN during its strong outburst phase. This is exacerbated by the ambiguity of differentiating between AGN and clusters in X-ray observations at low spatial resolutions. If there is evidence for an AGN then the X-ray emission is commonly assumed to be dominated by the AGN emission, introducing a selection effect against the detection of AGN in BCGs. In order to recover these 'missing' clusters, we systematically investigate the colour–magnitude relation around some $\sim$ 3500 *ROSAT* All Sky Survey selected AGN, looking for signs of a cluster red sequence. Amongst our 22 candidate systems, we independently rediscover several confirmed systems, where a strong AGN resides in a central galaxy. We compare the X-ray luminosity to red sequence richness distribution of our AGN candidate systems with that of a similarly selected comparison sample of $\sim$ 1000 confirmed clusters and identify seven 'best' candidates (all of which are BL Lac objects), where the X-ray flux is likely to be a comparable mix between cluster and

AGN emission. We confirm that the colours of the red sequence are consistent with the redshift of the AGN, that the colours of the AGN host galaxy are consistent with AGN, and, by comparing their luminosities with those from our comparison clusters, confirm that the AGN hosts are consistent with BCGs.

4.2 Introduction

As discussed in Chapter 1 there is strong evidence for a cycle of gas cooling in clusters and AGN feedback in BCGs. However a key difficulty in understanding this phenomenon is the extreme rarity of catching BCGs during their active outburst stage. Due to the short duty cycle of AGN, such systems are inherently rare. But, this is further exacerbated by observational selection effects. The principal challenge is the ambiguity that exists between AGN and cluster emission in low spatial resolution X-ray observations, i.e. whether X-rays are associated with extended cluster emission or point-like emission from AGN. For example, cool core clusters, the most likely systems to host a BCG with an active nuclei, can appear as point sources in shallow X-ray data, due to their centrally peaked profile, and as a result be ignored (Pesce et al., 1990). The effect particularly applies for cool core clusters at high redshift and may have a contribution towards the apparent decrease in the cool cores fraction with redshift (Vikhlinin et al. 2007; Santos et al. 2008). This is important to bear in mind in future X-ray surveys, such as *eROSITA*, as the extent of a cool core X-ray peak profile can be as little as 10 arcsec at high redshift ($z \gtrsim 0.5$), and hence would be unresolvable with the effective PSF of 28 arcsec in *eROSITA*'s scanning mode. Additionally, moderately X-ray luminous AGN in clusters are difficult to detect above the cluster X-ray emission of the cluster core and AGN in clusters often lack optical spectral tracers of AGN activity (Martini et al., 2006). Conversely, strong AGN can have all the X-ray flux attributed to them, whilst the cluster they may reside in goes uncatalogued. The aim of this is Chapter is to address the latter issue.

When compiling an X-ray catalogue of clusters, it is common practice to classify an X-ray source as an AGN whenever evidence, such as strong high-ionisation

emission, suggests the presence of nuclear activity. This classification would remain unchanged even in the obvious presence of a galaxy overdensity in the direction of the source, since probabilistic arguments strongly favour QSO dominance of the X-ray emission in the case of a cluster / QSO chance alignment (Zenn & Ebeling, 2010). However, if the AGN host galaxy is a member of a massive galaxy cluster the X-ray emission from the AGN may be a minority contributor to the total combined AGN and cluster emission. As a result, there is an observational selection effect against detection of rich clusters with an AGN in the BCG - the very sources we need in order to better understand the feedback cycle in these systems.

A case in point is the Phoenix cluster, SPT-J2344-42 (McDonald et al., 2012a). Despite being one of the most X-ray luminous clusters known and one of the ~ 2000 brightest *ROSAT* All Sky Survey sources (RBS2043, Schwope et al. 2000), this cluster went undetected for a long time. The X-rays were attributed to AGN emission, due to the strong, broad Mg II line in the spectrum of the BCG. Only when it was later detected through the S-Z effect, via the South Pole Telescope (SPT), was it realised to be a massive cluster. A follow-up *Chandra* observation revealed the cluster emission ($6 \times 10^{45}\,\mathrm{erg\,s^{-1}}$) to be 3 times that of the AGN ($2 \times 10^{45}\,\mathrm{erg\,s^{-1}}$; McDonald et al. 2012a), and a subsequent *Hubble Space Telescope* observation revealed blue filaments in the BCG and a star formation rate of $748 M_{\odot}\,\mathrm{yr}^{-1}$ (McDonald et al., 2013).

One additional source of confusion in the literature is that some cluster-dominated X-ray sources are identified as candidate BL Lac objects. BL Lac objects (reviews: Stein et al. 1976; Falomo et al. 2014) are a class of AGN blazars, with emission over the entire electromagnetic spectra, due to non-thermal processes in a relativistic jet, orientated to be near the line of sight (Urry & Padovani 1995). They are characterised by featureless optical spectra, so detection is usually made via X-ray, radio and γ-ray detections. As a result some BCGs which exhibit a relatively bright, flat-spectrum radio source are identified as BL Lacs when the cluster is in fact the dominant source of X-rays. For example, at least 40 systems are included in the Roma BZCAT sample (the largest sample of BL Lac objects compiled to date, containing over 3500 blazar objects; Massaro et al. 2009), where the X-ray emission is

likely to be dominated by the host cluster (see Section 4.5.7 for details). Similarly, seven of the targets chosen for OVRO 40m monitoring as potential *Fermi* sources are in fact BCGs in systems where the extended X-ray emission dominates (Hogan et al. 2015b). While this has a relatively minor effect on these large samples, it is important to ensure that the correct associations are made in order to avoid the clusters with a BCG, in a rare episode of AGN activity, being lost from an X-ray flux-limited sample. We will return to this issue in the discussion.

The reverse is also possible however, in which low luminosity BL Lacs can be misidentified as clusters of galaxies (Rector et al., 1999). While relatively few clusters have been identified in subsequent X-ray pointed observations to be AGN-dominated, there are several notable cases of systems where the cluster is a minority contributor to the total X-ray emission, for example: A1366 and A2627 in Russell et al. (2013), A1774 and A2055 (Ebeling et al. 1996) and the well studied samples of 1H1821+64 and 3C186 (Hall et al. 1997; Siemiginowska et al. 2010). In these cases, it is very important to pay attention to the emission of both the cluster *and* the AGN, in order to understand the total mass of the cluster and hence the parent sample of possible clusters that could have hosted a particular AGN.

The primary goal of this chapter is to perform a systematic search for signs of a rich cluster around *ROSAT* X-ray sources identified as AGN, with the aim of recovering these 'missing' clusters with strong AGN in their cores, i.e. Phoenix cluster analogues. In order to do this we investigate the colour-magnitude relationship around the AGN and attempt to look for signs of a overdensity in red sequence galaxies. Specifically, we look for cluster red sequences with a richness comparable to those of confirmed clusters of similar X-ray luminosity to our "AGN" X-ray sources.

4.3 The Data

4.3.1 AGN Sample

Our parent AGN sample consists of all X-ray sources from the *ROSAT* All-Sky Survey (RASS) Bright Source Catalogue (Voges et al., 1999), which were attributed

to AGN emission through the combined follow-up over the past 20 years - including large spectroscopic surveys such as SDSS (Anderson et al. 2003, 2007), and 6dFGS (Mahony et al. 2010), plus targeted projects (Bauer et al. 2000; Kollatschny et al. 2008). This provides a comprehensive catalogue of AGN to a soft X-ray flux limit of 3–5$\times10^{-13}$ erg s^{-1} cm^{-2} at 0.1–2.4 keV. Within the PS1 3π footprint, and below a redshift of 0.4, this gives a sample of 3058 broad-line AGN and 412 BL Lacs. The X-ray luminosities are all drawn from the RASS, are quoted in the 0.1–2.4 keV band and corrected for Galactic absorption.

There are a further 1020 RASS BSC sources, likely to be AGN, within the PS1 3π footprint, which have not been spectroscopically confirmed. However, we restrict our analysis to spectroscopically confirmed AGN only, as without the redshift – red sequence colour relationship (see Section 4.5.1) we would not be able to verify redshift concordance between the AGN and any apparent over-density. As our working AGN sample consists of a total of 3470 spectroscopically confirmed BL Lac and broad-line AGN, our spectroscopic completeness is at least 77%. In all likelihood however the completeness is higher than this for the brighter optical counterparts, as the fainter AGN without spectroscopy are more likely to be at a redshift above our $z = 0.4$ cut-off.

4.3.2 Comparison Cluster Sample

In order to check for consistency between candidate systems and confirmed clusters we compare our observations with the cluster sample of 981 X-ray selected clusters, described in Chapter 2.

4.4 Methods

4.4.1 Optical Photometry

The PS1 3π survey (Tonry et al., 2012), introduced in Chapter 2, was used for the optical analysis; following the same procedure as for the cluster sample in Chapter 2 we extracted PS1 3π PV3 postage stamps and performed aperture photometry for

each *ROSAT* AGN. The same SExtractor settings were used, for photometry of the AGN sample, as for the cluster comparison sample. K-corrections and Galactic reddening corrections were performed in the same way also.

4.4.2 Mid-IR Photometry

The *Wide-field Infrared Survey Explorer* (*WISE*) (Wright et al., 2010) was utilised for the Mid-IR analysis - which is a survey covering the whole sky at 3.4–22 μm. From the AllWISE Source Catalogue we extract photometry for our AGN/BCG sample in the $W1$, $W2$ and $W3$ bands at 3.4, 4.6 and 12 μm respectively. We do not perform any Galactic extinction corrections as this is negligible for Mid-IR observations (Cardelli et al., 1989).

4.4.3 Red Sequence Selection

We extracted the photometry of sources within a 0.5 Mpc radius about the X-ray position, and created g–r, r–i and i–z colour-magnitude diagrams for each AGN position. The colour-magnitude diagrams were then visually inspected for signs of the linear colour–magnitude relation, i.e. the red sequence, seen in all rich clusters of galaxies. The red sequence selection algorithm (described in Chapter 2) was applied to any X-ray sources with a visually apparent red sequence, that is, a linear feature, containing at least ten sources. Figure 4.1 shows an illustrative example of the typical colour–magnitude diagrams seen around the AGN, the majority of which show no evidence for a red sequence. Figure 4.2 conversely shows the colour–magnitude diagrams around an AGN where the host galaxy is likely to be a cluster member. A prominent red sequence is evident here.

For X-ray sources where an apparent red sequence exists, the PS1 imaging were then visually inspected in order to (a) check for a galactic over-density that is visually consistent with that of a cluster, and (b) check if the AGN host was visually consistent with being a BCG – that is, at the centre of the galactic distribution of the cluster and preferably with an extended cD-like envelope. Any sources satisfying these criteria have been identified as candidate systems in the subsequent analysis.

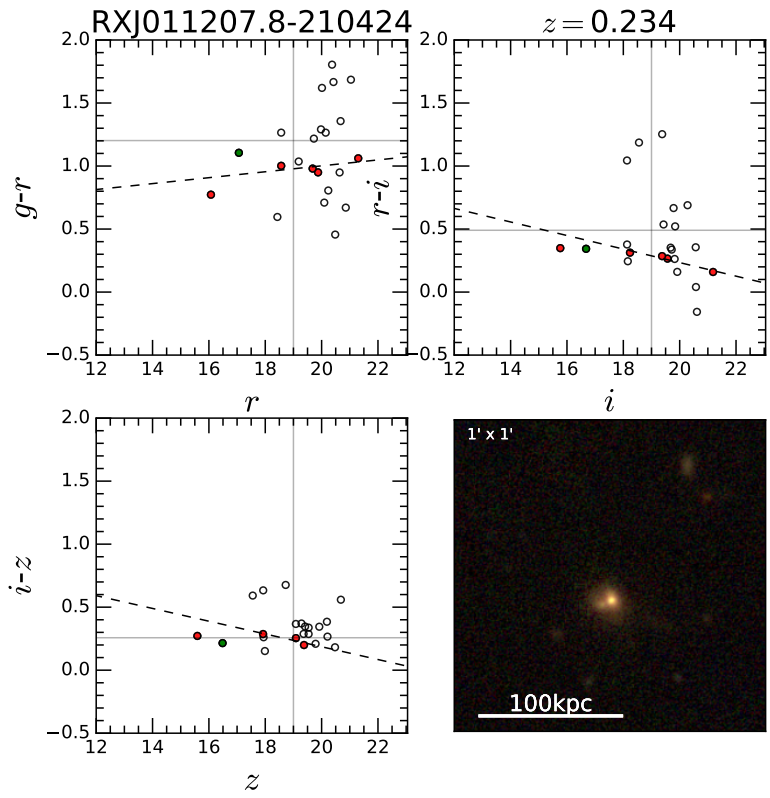

Figure 4.1: Colour–magnitude diagrams and colour composite image for AGN RXJ011207.8-210424. This illustrates the lack of a red sequence seen in the majority of the AGN.

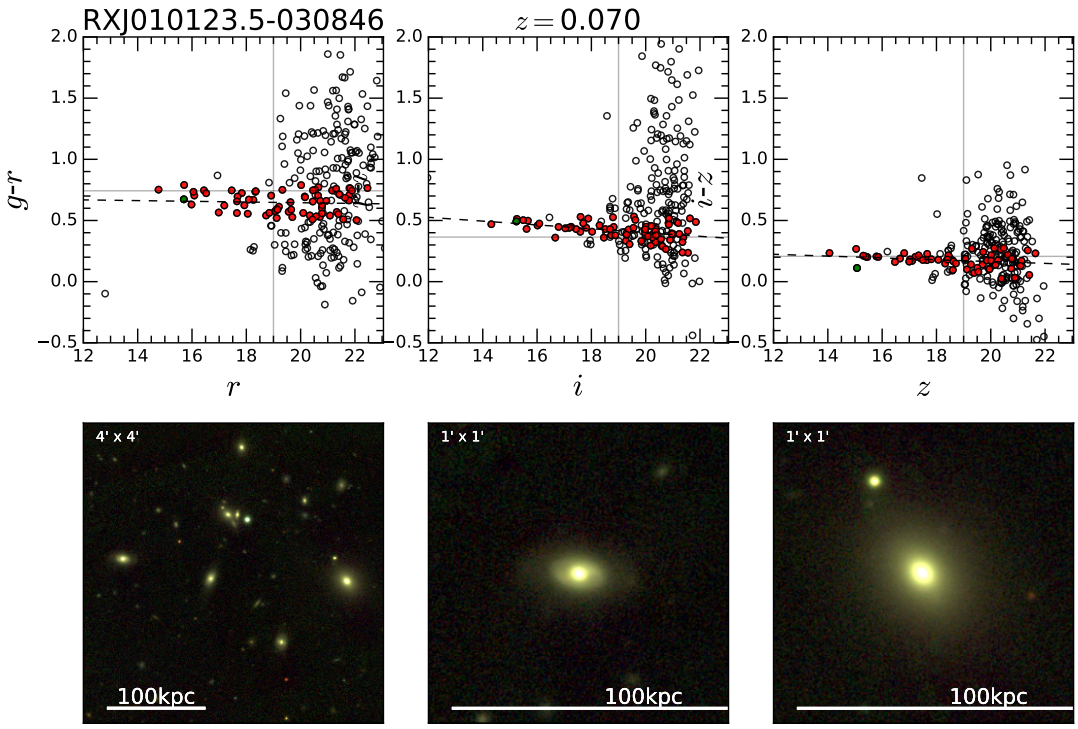

Figure 4.2: Colour–magnitude diagrams and colour composite images for RASS source RXJ010123.5-030846. This is an example of an AGN cluster candidate system, where the AGN host galaxy is likely to be a cluster member, as indicated by the apparent red sequence, but clearly not the BCG. *Bottom row*: Colour composite PS1 images, from left to right: (1) four square arcmin view of the cluster core, (2) zoomed view of the AGN host galaxy and (3) zoomed view of the BCG.

Note that in addition to these there were a number of the AGN which showed a red sequence in their colour-magnitude diagram, and hence are likely to be hosted by a cluster member, but were clearly not the central galaxy, and hence not the focus of this analysis. Figure 4.2 illustrates one such example; the colour–magnitude diagrams show a red sequence, but the AGN host galaxy is not the galaxy one would identify as the BCG. This example illustrates one of the challenges faced by the investigators, where often a better BCG candidate is only identified when viewing the wider imaging, as the AGN host and true BCG may be separated by tens of arcseconds.

4.5 Results

Of the 3058 broad-line AGN and 412 BL Lac the selection was narrowed down to 22 candidates. These are AGN which satisfy the conditions of (a) exhibiting a colour–magnitude diagram consistent with a cluster red sequence and (b) are hosted by a galaxy visually identifiable as a BCG. Interestingly we find these are almost exclusively BL Lac objects (20/22), with only two of the broad-line AGN satisfying our selection criteria. This suggests broad-line AGN are a very rare episode in the lifetime of any given system.

Our confidence in the technique used is strongly supported by the independent rediscovery of several previously identified systems where a BCG hosts a strong AGN. Some of which are well known; 1H0414+00, 1H1821+644, A2055, RXJ0909.9+3106, RXJ1745.6+3951. These five systems have had subsequent pointed X-ray observations confirming the presence of extended cluster emission in addition to the AGN. These observations allow the relative X-ray contributions to be estimated, providing context for our new discoveries - details of which are given in Section 4.5.5. The independent rediscovery of these clusters, which represent the very systems we are aiming to uncover, strongly supports the validity of our approach.

4.5.1 Cluster Membership

In order to reduce chance projection effects along the line of sight, between a cluster and an unassociated AGN, we investigate whether the AGN is consistent with cluster membership. In lieu of having the required spectroscopy to spectroscopically confirm cluster members, we utilise the relationship between observed red sequence colour and redshift for clusters (Andreon 2003; Rykoff et al. 2014; Green et al. 2016). In Chapter 2 we demonstrated that the cluster redshift of our comparison cluster sample can be photometrically estimated, using the g–r red sequence colour, to within $\Delta_z = 0.025$, at 1σ.

In Fig. 4.3 we overlay the colour of the apparent red sequences, selected around our AGN, on top of that from our cluster comparison sample. Red sequence colour is defined as the colour, given by the best fitting line of the red sequence, at a flux of 19th magnitude. We find in all of our candidate systems that the red sequence colour is consistent with the colour predicted by the confirmed redshift of the AGN. This suggests that the galactic overdensity we detect is likely at the same redshift of the AGN and hence that the host galaxy is likely a cluster member.

4.5.2 Red Sequence Richness

The optical richness of a galaxy cluster, i.e. the number of galaxies in it, scales weakly with the cluster mass (Hall et al. 1997; Johnston et al. 2007; Andreon & Hurn 2010). Hence we expect that the richness of the cluster red sequence – that is, the number of galaxies selected on the cluster red sequence – should scale with the X-ray luminosity of the cluster, (since $L_{\rm X}$ traces cluster mass). In Figure 4.4 we plot the X-ray luminosity against the red sequence richness of our cluster comparison cluster sample, where richness is defined as the number of red sequence galaxies brighter than an i-band luminosity of -19 magnitudes, (corresponding to a flux of 16.5 mag at $z = 0.03$ and 22.6 mag at $z = 0.4$). We find a weak correlation between $L_{\rm X}$ and red sequence richness for the cluster sample, but with considerable scatter. A source of scatter in the richness is that we perform our optical photometry within a fixed 0.5 Mpc aperture around the central galaxy. Hence, richness is actually a

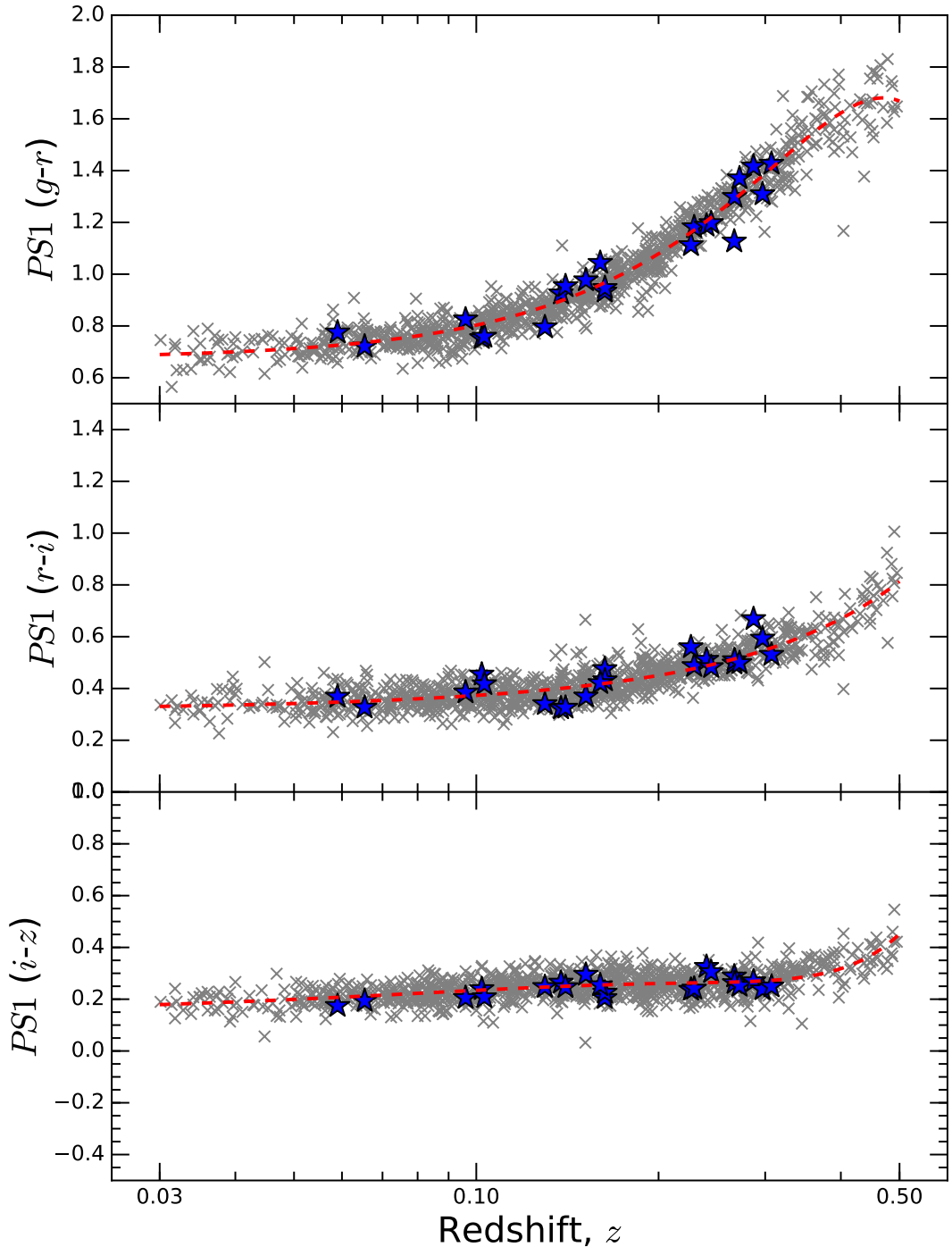

Figure 4.3: The PS1 g–r, r–i and i–z colour of the red sequence, measured at 19th magnitude, against redshift. The (grey) crosses represent the red sequence of each of the confirmed clusters from our cluster comparison sample. The (blue) stars represent the red sequence around the AGN from this work. The (red) dashed line is a best fitting line to the comparison cluster data. All of our candidate systems have a red sequence colour consistent with the given redshift of the AGN.

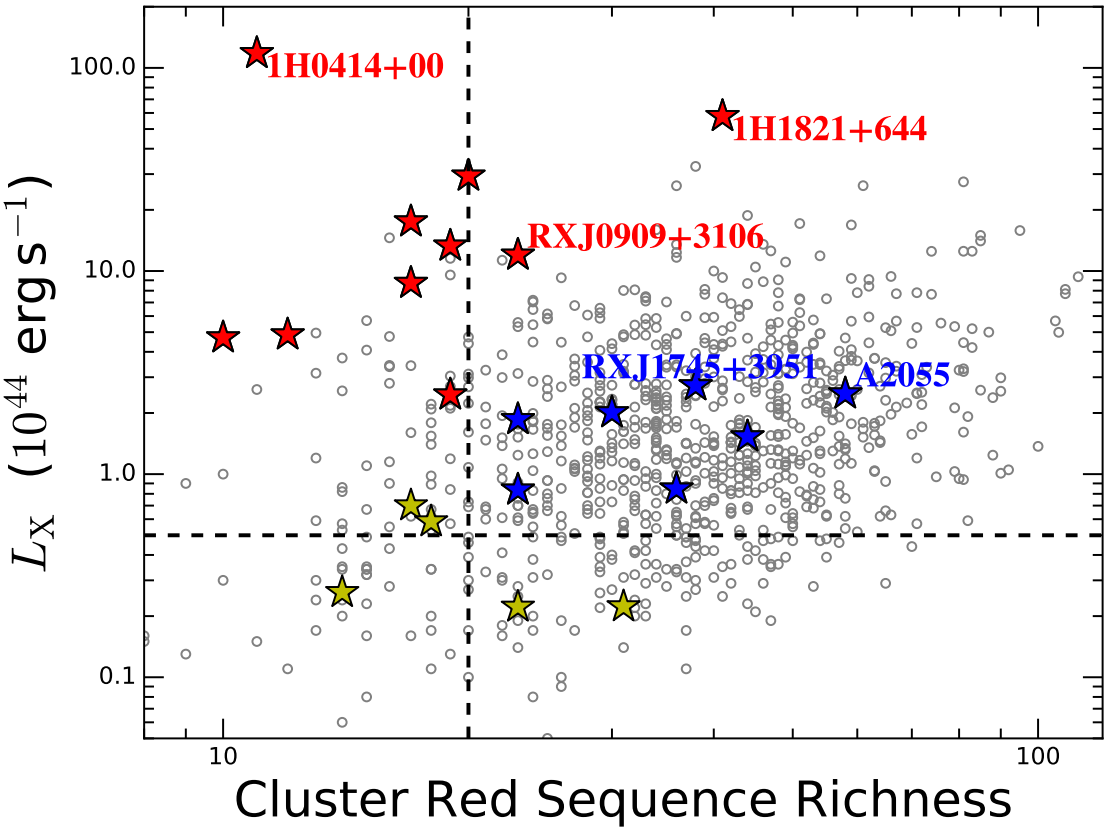

Figure 4.4: *ROSAT* All Sky-Survey X-ray luminosity against red sequence richness (number of red sequence galaxies above i-band luminosity of -19 mag). The (grey) empty circles represent the comparison cluster sample. The coloured stars represent the 22 candidate systems where we suspect the presence of a cluster around the AGN. The stars with IDs represent the previously confirmed systems which we have independently rediscovered. The different coloured stars represent distinct groupings on the plot, which are used as reference in the text, (i.e. red = high L_X for relative richness, suggesting probable X-ray point source dominance, yellow = relatively low L_X and richness, suggesting AGN in group scale environments). The blue stars represent our 'best' candidates as they best match the L_X–richness distribution of our confirmed comparison sample of clusters. The 'best' systems are those most likely to constitute a strong AGN in the BCG of a rich cluster, where the X-rays are a comparable mix of cluster and AGN emission. The dashed lines indicate the selection criteria for these 'best' candidates.

measure of galaxy density, so diffuse clusters, which tend to be unrelaxed systems that are currently undergoing, or have recently undergone, mergers will be measured with lower richness. So while for any given system one can not assume that because a cluster has a high X-ray luminosity then it will be have a substantially rich red sequence, the overall distribution does provide valuable context for our candidate AGN in cluster cores.

Applying the same procedure of measuring the richness to the 22 AGN candidate systems, we can investigate how the richness of our AGN colour–magnitude relations compare to those of confirmed clusters of similar X-ray luminosity (Fig. 4.4). By selection, we find all the candidate AGN lie within the scatter of the confirmed cluster sample in terms of richness. So, we can be reasonably confident that all these candidates represent a system where an AGN resides in the central galaxy of at least a group scale structure.

The candidate systems can roughly be divided into three distinct regions, which we colour code for clarity. The systems in the top left (red stars in Fig. 4.4), which have high X-ray luminosities relative to their richness, are most likely systems where the AGN dominates the X-ray emission. We identify two well known sources within this selection, 1H0414+00 and 1H1821+644, where the AGN is known to dominate (McHardy et al. 1992; Russell et al. 2010). With the exception of 1H1821+644, these tend to have a low richness, suggesting they are likely low mass cluster/group scale overdensities. However it is possible that some are analogues to A689, a system in which a BL Lac is known to reside in a cluster core (although not in the BCG itself) and significantly contaminates the X-ray emission. A *Chandra* observation revealed an X-ray luminosity for the cluster as $2.8 \times 10^{44}\,\mathrm{erg\,s^{-1}}$ when the BL Lac is masked (Giles et al., 2012), an order of magnitude less than the original BCS value of $3.0 \times 10^{45}\,\mathrm{erg\,s^{-1}}$. However this still represents a substantial X-ray luminosity, with a sufficient flux to be detectable as an X-ray cluster in the RASS data. Applying our red sequence selection algorithm yields a richness of 25 for this cluster, making its position in richness–L_{X} comparable to RXJ0909.9+3106, i.e. over luminous for its given richness. This supports the interpretation that these represent systems where the AGN contribution dominates by as much as an order of magnitude over that of

the cluster. Details on these systems are given in Table 4.1. The candidate systems in the lower left (yellow stars), with a low L_X and/or richness, are likely systems with a moderate AGN in a low mass cluster/group scale system. Details on these systems are given in Table 4.2.

It is the candidates in the centre however, (blue stars), which best match the richness–L_X distribution of our confirmed clusters. As such, they are the systems most likely to exhibit a comparable mix of X-ray emission from the AGN and a rich cluster component, analogous to the Phoenix cluster. We designate these systems, with a richness in excess of 22 red sequence galaxies and $L_X > 0.5 \times 10^{44}\,\mathrm{erg\,s^{-1}}$, (the dashed lines in Fig. 4.4), as our 'best' candidates. This consists of seven systems, two of which are previously identified systems (A2055 and RXJ1745.6+3951; see section 4.5.5). Details on these systems are given in Table 4.3.

We note there is a more ambiguous source, RXJ0828.2+4154, with a richness narrowly below our best candidate selection criteria, but with a comparable L_X to confirmed clusters (richness= 19 and $L_X = 2.46 \times 10^{44}\,\mathrm{erg\,s^{-1}}$). However, from a *Chandra* observation, this source appears to be point source dominated (Donahue private communication).

In Fig.4.9 we present the colour–magnitude diagrams and *gri* colour composite images of the cluster and of the BCG, for our 'best' candidates and previously confirmed systems.

4.5.3 BCG/AGN Luminosity

The luminosity of BCGs has been shown to correlate with the X-ray luminosity of their host cluster (e.g. Edge 1991; Stott et al. 2012; Green et al. 2016; Chapter 3). Hence in order to check whether our AGN host galaxies are consistent with being BCGs we check the luminosity of the AGN host galaxies in both the optical and Mid-IR. In the PS1 i-band we find the AGN host galaxies have luminosities generally consistent with those of BCGs of similar X-ray luminosity clusters (Fig. 4.5) - indicating these host galaxies have stellar masses consistent with those of BCGs. Similarly in the $W1$-band, at 3.6μm, the luminosities of the AGN hosts are generally consistent with BCGs of similar L_X (Fig. 4.6).

A challenge in the interpretation of these plots is that the AGN itself can contribute to the luminosity of the host BCG, as well as to the X-rays. Hence we maintain the colour coding utilised in Fig. 4.4 as their relative positions in richness–$L_{\rm X}$ space provide context in addressing this degeneracy. For example, we notice the majority of the red starred candidate systems appear under-luminous in i, with respect to $L_{\rm X}$, suggesting either they are dimmer in i than most BCGs or they have a higher $L_{\rm X}$ than similar clusters. But, given these sources have a low richness for their given $L_{\rm X}$, it is likely the enhancement of the X-rays, due to the dominant nature of the AGN, is the most significant factor here. 1H1821+644 is over an order of magnitude brighter, in both i and $W1$, than the most luminous BCG from our comparison sample, indicating the luminous quasar dominates the optical and MIR luminosities.

Our best candidate systems are generally well centred with respect to the confirmed BCG sample. However one of our 'best' candidate systems also appears under-luminous in L_i, RXJ0056.3-0936. However, this particular system appears to be a multi-component, dumbbell BCG (Fig. 4.9). In this dumbbell system, the northern component is more consistent with being the BCG, (with $L_i = -23.3$, placing it securely within the main distribution of BCGs in Fig. 4.5), and the BL Lac object is in the southern component. While projection effects within the cluster can not be ruled out, we identify this system as a candidate because it is likely the two components are in the early stages of a merger. This assumption is based on the findings of a follow up study with MUSE IFU spectroscopy of dumbbell BCGs, from the cluster comparison sample, which reveal the majority of dumbbell systems have kinematics consistent with the two components being bound (Green et al. in prep.; see Chapter 6). Note, as the *WISE* resolution is insufficient to resolve the two separate components of this dumbbell, the L_{W1} of this galaxy is consistent with the comparison BCGs.

4.5.4 Confirmation of AGN Nature: BCG/AGN Colours

One potential concern is that some of the sources may actually just be 'ordinary' clusters – that is a cluster without an AGN in the BCG – which were simply misiden-

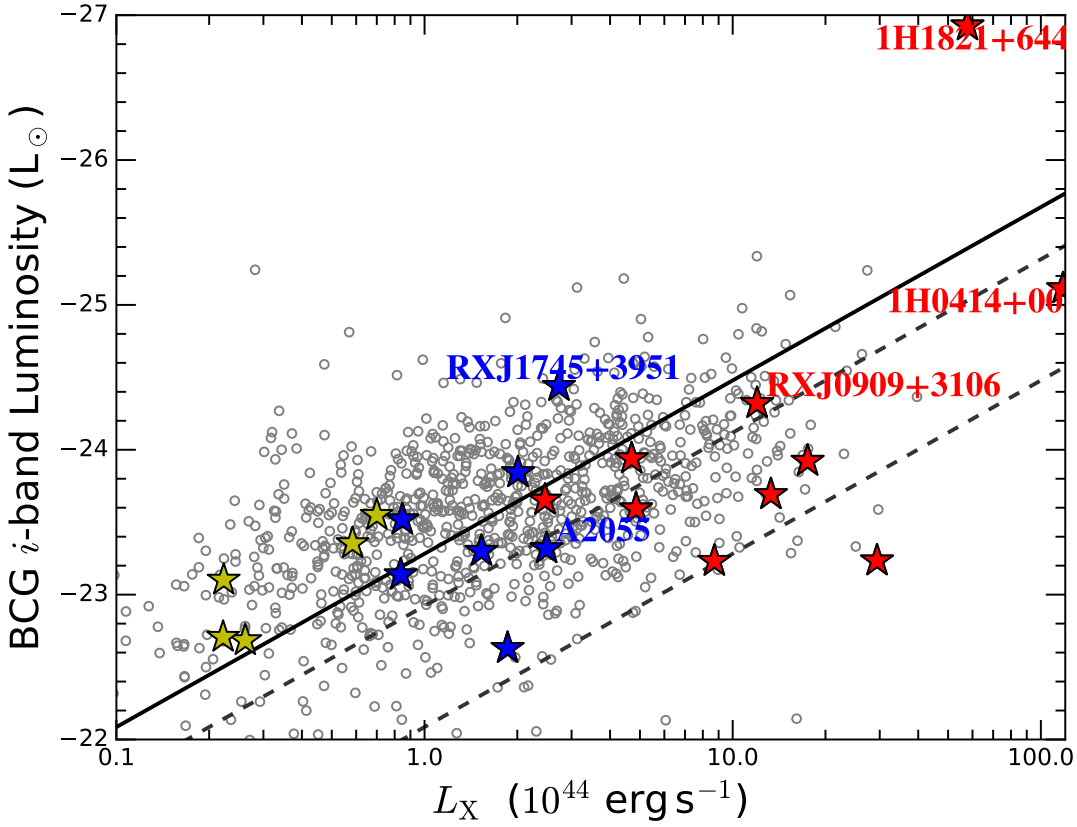

Figure 4.5: PS1 i-band luminosity against X-ray luminosity. The open (grey) circles represent the BCGs of the comparison cluster sample. The coloured stars, (where colours follow from Fig. 4.4), represent the host galaxy of the AGN. The solid line indicates the best fitting line to the cluster sample. The dashed lines show the best fitting line offset by a factor of two or ten respectively on the L_X axis. So, for example, the outer dashed line indicates the best fitting relationship of L_i–L_X for a system where L_X is increased by a factor ten, (such as if a strong AGN were contributing X-rays at a ratio of 9:1 to the X-rays from the cluster).

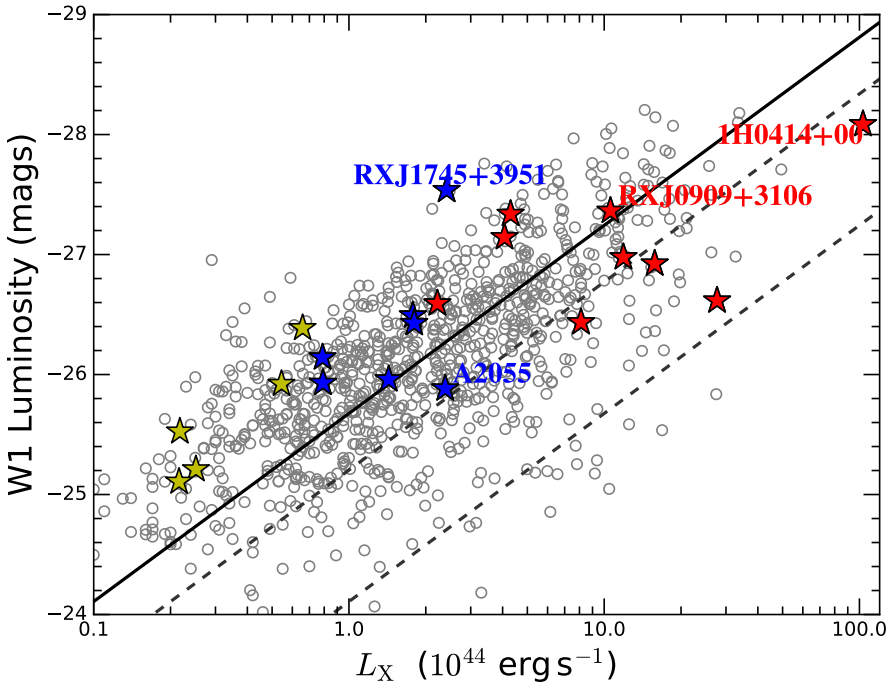

Figure 4.6: Similar to Fig. 4.5 but with *WISE* W1 (3.6μm) luminosity against X-ray luminosity. Note, there is an additional data point at $L_{W1} = 31.14$ and $L_X = 57.8$, corresponding to 1H1821+644, which is omitted to maintain visual clarity.

tified in the initial RASS X-ray analysis. With this in mind, we investigate the colours of the AGN host galaxies in order to look for properties consistent with AGN. In Green et al. (2016) (Chapter 3) we measured the colours of the BCGs of the cluster comparison sample and found the bulk population of BCGs were passively evolving. However we found that $\gtrsim 14\%$ showed significant colour offsets from passivity due to star formation and/or AGN activity in the BCG. We expect therefore that the AGN in this study should show significant offsets in colour with respect to that of a passive BCG. In addition to investigating the colours, we also check the NVSS data and find that all of our sources are detected at 1.4 GHz, another indicator of the active nature of these galaxies.

In the MIR star formation/AGN activity is characterised by enhanced emission at longer wavelengths, due to reprocessed dust emission, hence our AGN should be redder than passively evolving galaxies of similar redshift. In *WISE* observations we expect AGN to be red in both $W1{-}W2$ and $W2{-}W3$ but star forming galaxies to be red in just $W2{-}W3$. In Fig. 4.7 we overlay the *WISE* $W1{-}W2$ and $W2{-}W3$

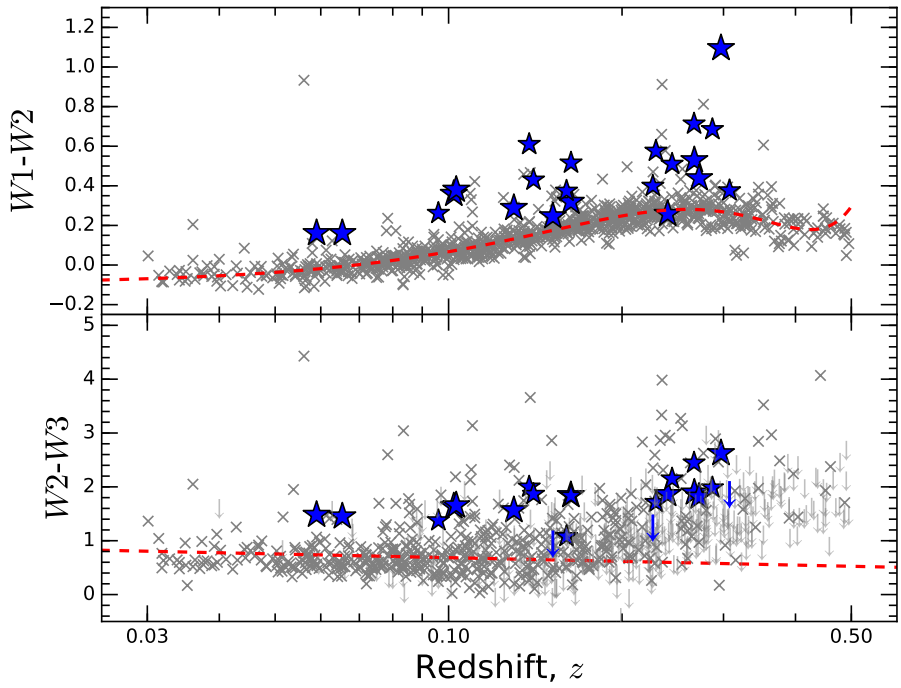

Figure 4.7: *WISE* colours against redshift. The grey crosses represent the BCGs of our cluster comparison sample. The (blue) stars represent the AGN host galaxies. Sources with a $W3$ signal to noise ratio, S/N<3, are indicated by arrows.

colours for our AGN host galaxies over those of the comparison BCG sample and find that almost all of our AGN candidates are red relative to passive BCGs in both colour indices. There is one source, RXJ2353.4-1257, which appears not to show the expected 4.5μm excess, but a archival NTT spectra is consistent with the BL Lac identification. This supports the assumption that these candidate systems are AGN, rather than a misidentified 'ordinary' clusters.

In Fig. 4.8 we overlay the PS1 3π g–r colour of our AGN host galaxies over those of the comparison BCGs. We find that the majority of our AGN hosts are significantly blue relative to the bulk population of passive BCGs at a similar redshift. Since 20/22 of these sources are identified as BL Lac objects this is as expected, given that one of the characteristics of BL Lacs is a strong blue continuum in their spectra (Massaro et al., 2012). This further supports the validity of the AGN identification.

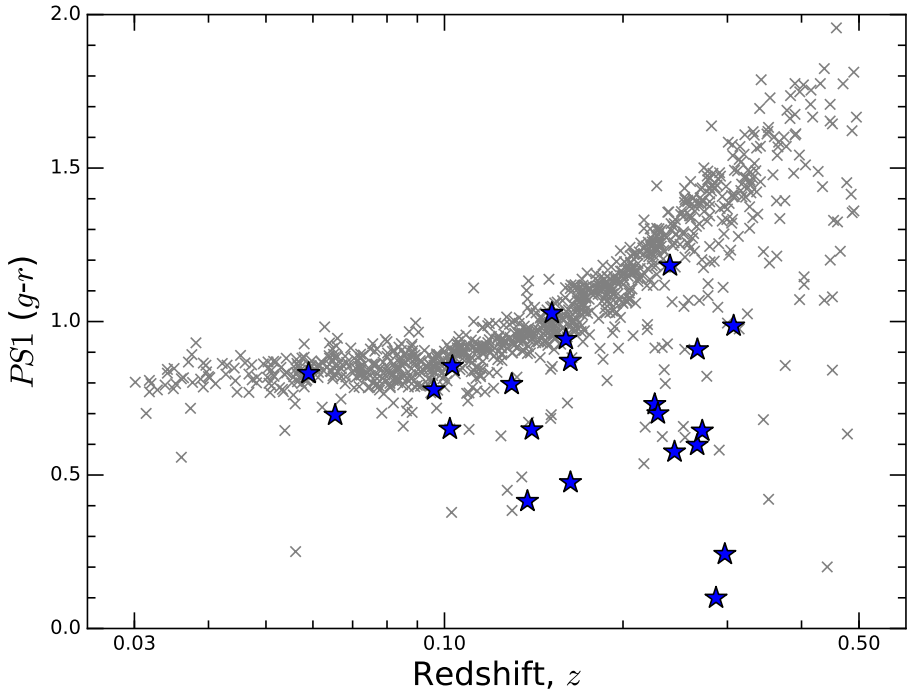

Figure 4.8: PS1 g–r colours against redshift. The grey crosses represent the BCGs of our cluster comparison sample. The (blue) stars represent the AGN host galaxies.

4.5.5 Previously Identified AGN in BCGs

In our analysis we have independently rediscovered a number of sources which have already been identified as an AGN hosted by BCG. These cover a broad range in terms of the relative AGN-to-cluster X-ray contributions, providing valuable context for the candidate systems. Where given below, the relative contribution of AGN and cluster emission are estimated from summing the relative photon counts, in *XMM-Newton* and *Chandra* imaging, which can roughly be attributed to point-source-like emission and the more extended emission (similar to the approach outlined in Russell et al. 2013). As such, they are only approximate values and do not take into consideration X-ray variability or the spectral energy distribution of the components.

1H1821+644: This highly luminous broad-line quasar resides in the BCG of a high mass, strong cool core cluster. Interestingly, the ICM around the quasar has a significantly lower entropy and temperature and steeper gradients than comparable clusters (Walker et al., 2014). Within 80 kpc the gradients and profiles are

consistent with those of cooling flows, suggesting the AGN is failing to heat ICM and offset radiative cooling as expected. From the *Chandra* analysis Russell et al. (2010), we know the quasar dominates the central region, but that the cluster is also a significant contributor of X-rays. The relative X-ray contributions are estimated as roughly one part cluster to two parts quasar. The position of this AGN in $L_{\rm X}$–Richness space (Fig. 4.4) is as expected for an X-ray source dominated by the AGN emission, characterised by a relatively low richness for a high $L_{\rm X}$. Similarly the high $L_{\rm X}$ relative to the BCG luminosity is as expected for an AGN dominated system. The extreme optical and MIR luminosity, and MIR colours, indicate the dominant nature of the quasar at these wavelengths.

H0414+009: For a long time H0414+009 has been known to be a BL Lac object hosted by a BCG (McHardy et al. 1992; Falomo et al. 1993). Archival *XMM-Newton* and *Chandra* reveal clear point source domination. This is fully consistent with the significant offset in both richness and BCG luminosity from the comparison cluster sample.

A2055: This is an example of a BL Lac object in the BCG of a known Abell cluster. From an archival *XMM-Newton* observation we estimate the relative cluster–AGN contribution as approximately 1:4. This is perhaps surprising as we expected a more comparable mix of two from its richness–$L_{\rm X}$ position. However, if we consider that the estimated cluster contribution is $\sim 0.5 \times 10^{44}\,{\rm erg\,s^{-1}}$, its position in richness–$L_{\rm X}$ space is still comfortably comparable to the cluster sample.

RXJ0909.9+3106: This appears to be a case of a BL Lac in the BCG of a group of galaxies at a redshift of 0.272. An archival *Chandra* observation shows the presence of extended cluster emission, confirming the presence of a cluster, but the X-ray emission is clearly AGN dominated (by factor of ~ 20). This is consistent with our predictions based on the richness–$L_{\rm X}$ position and the optical/MIR luminosities. Note, a drop in $L_{\rm X}$ by a factor of 20 would place it comfortably amongst the comparison cluster richness–$L_{\rm X}$ distribution.

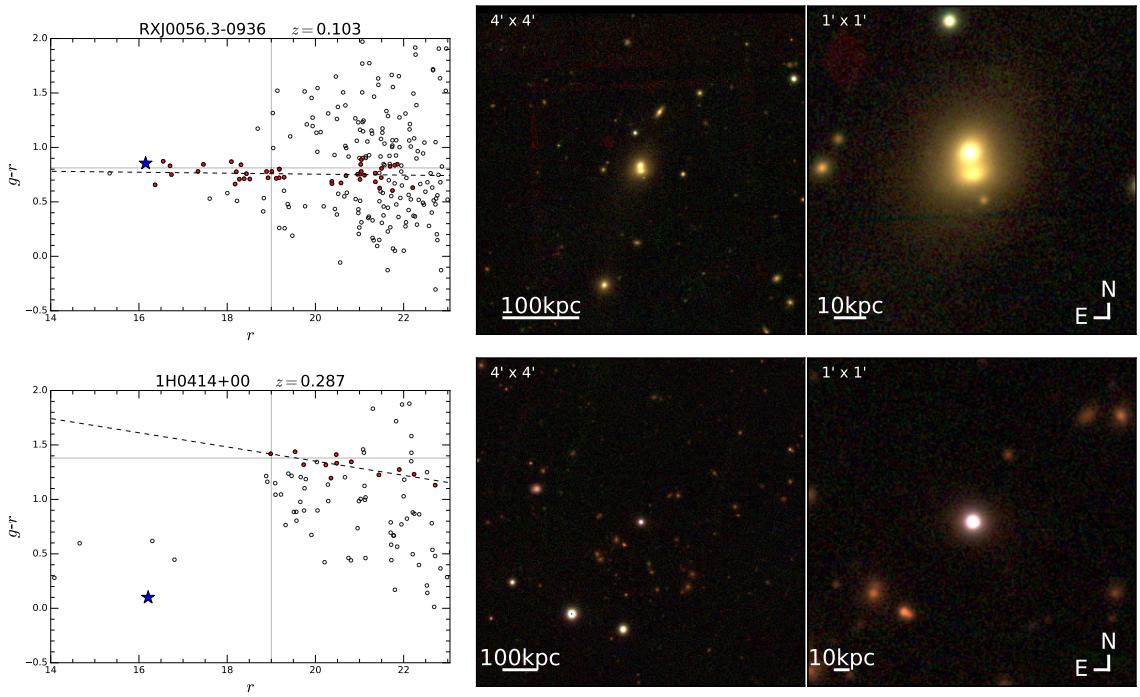

Figure 4.9: Left: The PS1 g–r colour-magnitude diagram for sources within a radius of 0.5 Mpc around the AGN position. The filled (red) circles indicate galaxies selected to be on the cluster red sequence and the dashed line shows a best fitting linear regression line to these points. The (blue) stars indicate the AGN host galaxy, believed to be the BCG. And, the intersection of the solid grey lines indicates the predicted red sequence colour, at 19th magnitude, given its redshift (as estimated from our comparison cluster sample – i.e. Fig. 4.3). Middle: *gri* colour image in a 4×4 arcmin box, centred on the BCG. Right: *gri* colour image in a 1×1 arcmin box, centred on the AGN/BCG.

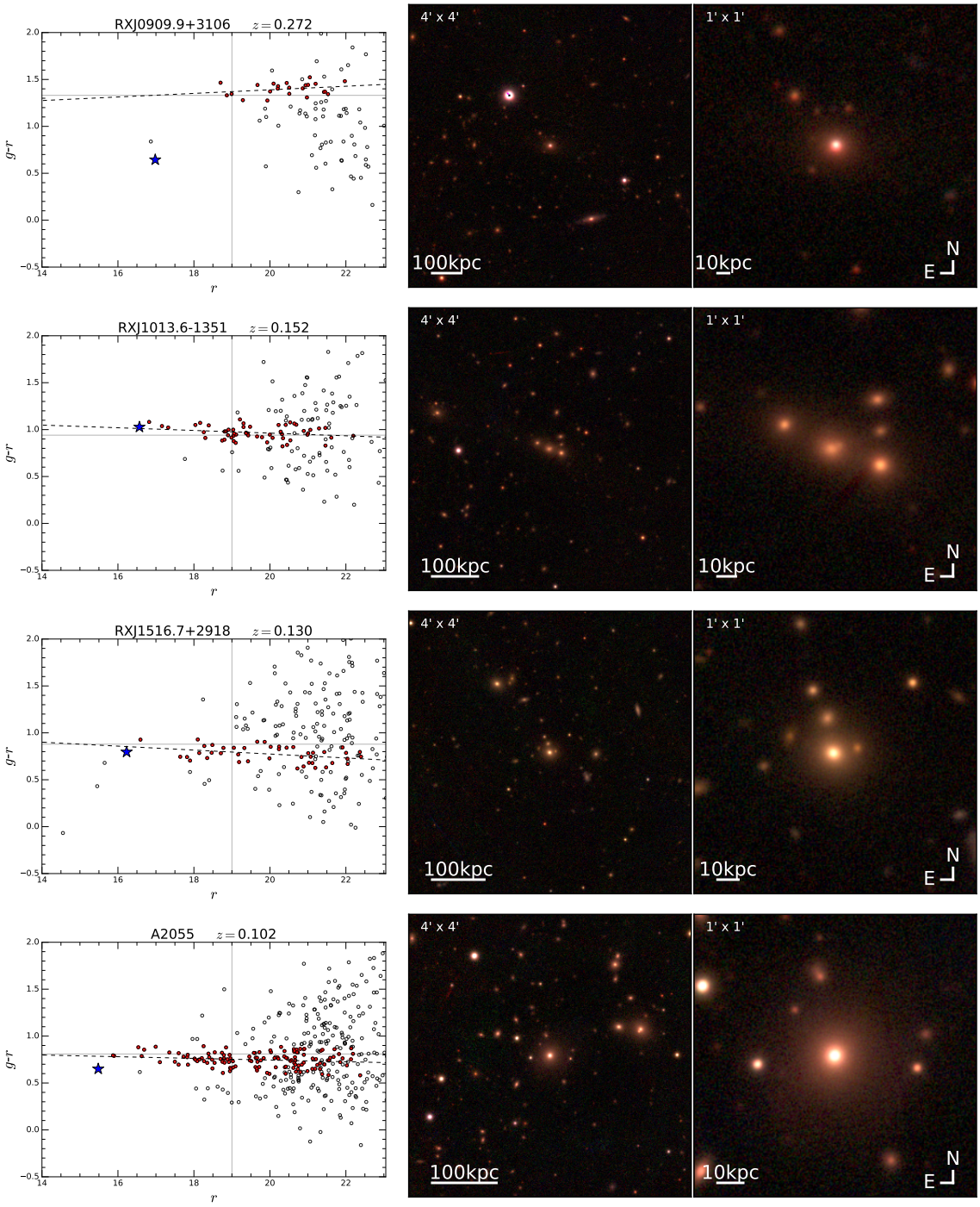

Figure 4.9: continued

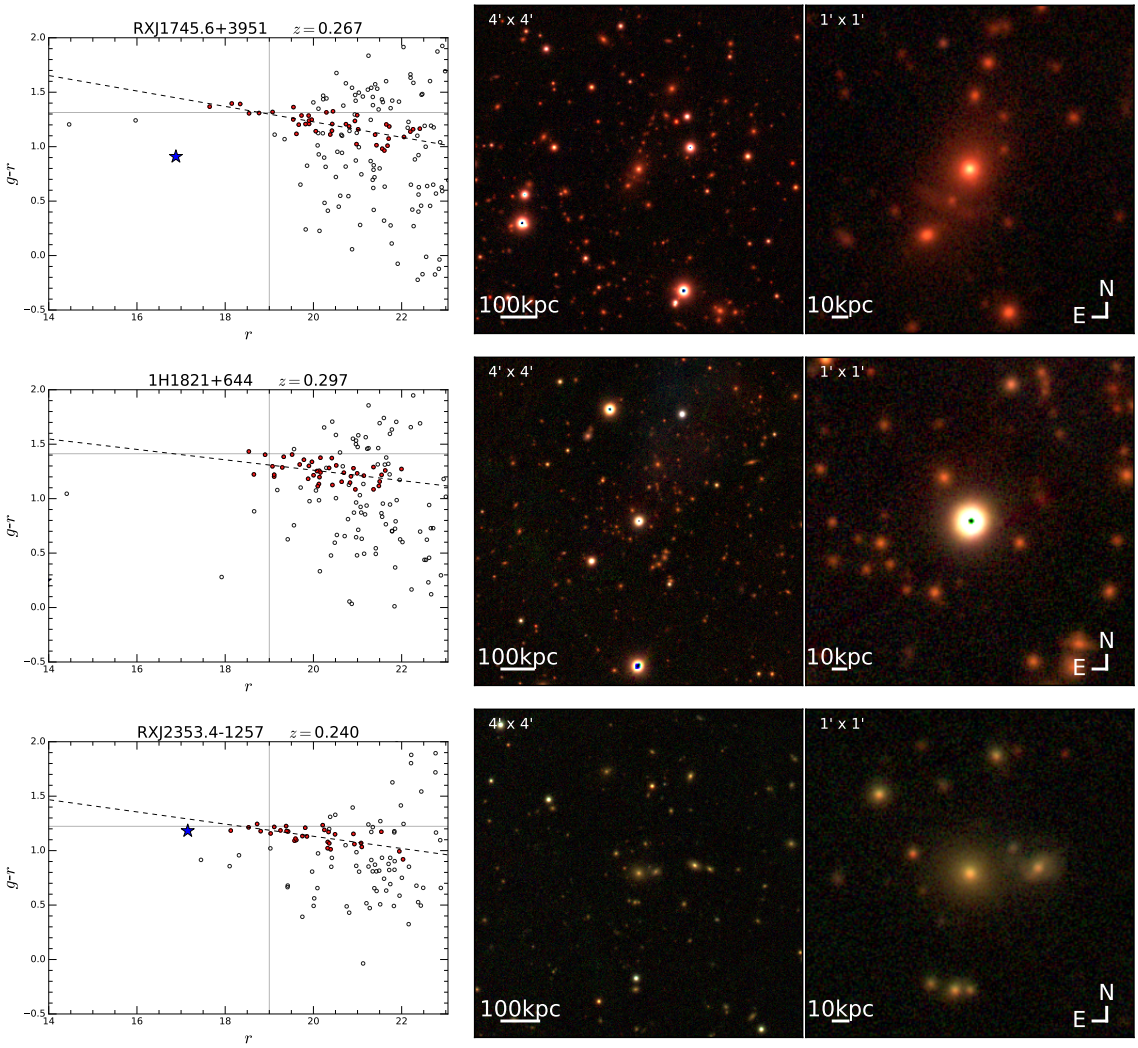

Figure 4.9: continued

RXJ1745.6+3951: This BL Lac object has a *ROSAT* HRI observation which shows extended cluster emission. Although the core could not be resolved the relative contributions of the BL Lac and the cluster were estimated by Gliozzi et al. (1999) to be roughly equal. An optical analysis revealed the presence of a gravitational arc from a strongly lensed $z = 1.06$ galaxy (Nilsson et al. 1999) confirming a high cluster mass, later estimated to be $4 \times 10^{14} M_{\odot}$ (Lietzen et al., 2008). The richness and BCG luminosities are fully consistent with other clusters at similar L_X, as expected if this roughly equal mix is genuine.

4.5.6 Clusters Previously Incorrectly Identified as AGN

There are a number of systems in which the identification of the majority of the X-ray emission has alternated between cluster and AGN. We give two illustrative examples.

Zw2089: This is a LoCuSS cluster that shows relatively broad lines in its optical spectrum, but the point source does not contribute more than 5% to the total cluster flux (Russell et al., 2013).

RXCJ0132.6-0804: Dutson et al. (2013) find that this cluster may contain a *Fermi* source in its BCG, however an archival *Chandra* observation finds the majority of the emission is from the extended emission.

Therefore, it is important to be aware that many systems are a combination of both cluster and AGN emission in X-ray data. This is illustrated in the compilation of BL Lac samples, such as the Roma BZCAT sample, where the radio and X-ray properties of clusters can be misinterpreted as being from a BL Lac.

Table 4.1: Systems which are likely AGN dominated (red stars in figures). (a) X-ray luminosity in units of 10^{44} erg s^{-1}, (b) red sequence richness.

Cluster/AGN ID	BCG R.A. (J2000)	BCG DEC (J2000)	Redshift	L_X (a)	Rich. (b)	AGN Class	Comments
1H0414+00	04:16:54.5	+01:04:56	0.287	118.00	11	BL Lac	*Chandra*/*XMM*: point source dominated
RXJ0828.2+4154	08:28:14.2	+41:53:52	0.226	2.46	19	BL Lac	*Chandra*: point source dom. (Donahue priv. comm.)
RXJ0909.9+3106	09:09:53.3	+31:06:03	0.272	12.00	23	BL Lac	*Chandra*: extended, but AGN dominated
RXJ1117.1+2014	11:17:06.3	+20:14:07	0.138	29.40	20	BL Lac	NORAS "AGN-Cluster" ID (Böhringer et al., 2000)
RXJ1140.4+1528	11:40:23.5	+15:28:09	0.244	13.30	19	BL Lac	
RXJ1442.8+1200	14:42:48.1	+12:00:40	0.163	8.72	17	BL Lac	Dumbbell; *Chandra*: point source dominated
RXJ1617.1+4106	16:17:06.3	+41:06:47	0.267	4.86	12	BL Lac	
1H1821+644	18:21:54.4	+64:20:09	0.297	57.80	41	Broad-line	*Chandra*: extended emission, but quasar dominates
RXJ2113.9+1330	21:13:53.7	+13:30:17	0.307	4.70	10	BL Lac	
RXJ2150.2-1410	21:50:15.5	−14:10:49	0.229	17.50	17	BL Lac	

Table 4.2: Systems which are likely group or poor cluster scales (yellow stars in figures). (a) X-ray luminosity in units of 10^{44} erg s^{-1}, (b) red sequence richness.

Cluster/AGN ID	BCG R.A. (J2000)	BCG DEC (J2000)	Redshift	$L_{\rm X}$ (a)	Rich. (b)	AGN Class	Comments
RXJ0039.1-2220	00:39:08.2	−22:20:01	0.065	0.22	23	Broad-line	
RXJ0110.1+4150	01:10:04.8	+41:49:50	0.096	0.26	14	BL Lac	
RXJ0656.2+4237	06:56:10.7	+42:37:03	0.059	0.22	31	BL Lac	
RXJ1053.7+4930	10:53:44.1	+49:29:56	0.140	0.70	17	BL Lac	
RXJ2336.9-2326	23:36:53.8	−23:26:26	0.160	0.31	18	BL Lac	

Table 4.3: Best candidate systems of AGN in BCG (blue stars in figures). (a) X-ray luminosity in units of 10^{44} erg s^{-1}, (b) red sequence richness.

Cluster/AGN ID	BCG R.A. (J2000)	BCG DEC (J2000)	Redshift	L_X (a)	Rich. (b)	AGN Class	Comments/X-rays Obs.
RXJ0014.3+0854	00:14:19.7	+08:54:02	0.163	0.85	36	BL Lac	
RXJ0056.3-0936	00:56:20.1	−09:36:32	0.103	1.86	23	BL Lac	BCG is a dumbbell galaxy
RXJ1013.6-1351	10:13:35.2	−13:51:29	0.152	1.53	44	BL Lac	
RXJ1516.7+2918	15:16:41.6	+29:18:09	0.130	0.84	23	BL Lac	
A2055	15:18:45.7	+06:13:56	0.102	2.49	58	BL Lac	Cluster confirmed: *XMM-Newton*
RXJ1745.6+3951	17:45:37.7	+39:51:31	0.267	2.73	38	BL Lac	Cluster confirmed: *ROSAT* HRI
RXJ2353.4-1257	23:53:25.1	−12:57:01	0.240	2.01	30	BL Lac	

4.5.7 The Roma BZCAT catalogue

Declaration: The majority of analysis for this section (§4.5.7) was carried out by Alastair Edge.

Table 4.4 lists the 41 ROSAT BSC sources which are listed in Massaro et al. (2015) as being BL Lac objects, but in which we are confident the cluster emission dominates. These results are based on a combination of this analysis, archival X-ray data, and the literature. The large majority are listed in Massaro et al. (2015) as "BL Lac-galaxy dominated", meaning their SEDs suggest dominance of the host galaxy over the nuclear emission. We note their optical spectra show strong emission lines in almost all cases (e.g. 4C+55.16/5BZGJ0834+5534, Iwasawa et al. 1999. Clusters with pointed X-ray observations are noted in the table and in all cases the extended emission dominates. While the selection method used to create the BZCAT sample is efficient in selecting BL Lacs, there is a significant number of sources that need to be filtered out to avoid contamination. Using the fraction of polarisation in the radio, as used by Edge et al. (2003), or the detection of significant extent in the RASS emission (Voges et al., 1999), would have excluded the majority of the sources listed in Table 4.4, without significantly affecting the selection of BL Lacs.

4.6 Discussion

4.6.1 Lessons for the Future

The pending launch of *eROSITA* and subsequent X-ray survey will dramatically increase the number of clusters and AGN detected in hard X-rays. The importance of having a clear context in which to place the more ambiguous sources, where there is evidence of both a rich cluster *and* an AGN, means that we should consider what this study tells us.

Firstly, the number of X-ray selected AGN that reside at the cores of rich clusters is relatively low. There are not many BCGs that are accreting close to their Eddington rate and lost to our X-ray selection. This is to be expected from the likely duty cycle of AGN and we can set a more stringent upper limit to this by

Table 4.4: BZCAT BL Lac candidates that are likely to be clusters. The Cluster IDs marked with an asterisk have archival X-ray pointed data that in all cases shows the emission to be dominated by extended emission.

BZCAT ID	Cluster ID	Redshift	Reference
5BZGJ0006+1051	Z15	0.1676	eBCS Ebeling et al. (2000)
5BZGJ0012-1628	A11	0.1510	RBSC Bauer et al. (2000)
5BZGJ0014+0854	MS0011.7+0837	0.1633	EMSS Stocke et al. (1991)
5BZGJ0027+2607	MACSJ0027.4+2607*	0.3645	MACS Ebeling et al. (2010)
5BZGJ0056-0936	RXJ0056.3-0936	0.1031	This paper
5BZGJ0123+4216	NVSS cluster	0.1856	NVSS Bauer et al. (2000)
5BZGJ0153-0118	NVSS cluster	0.2458	NVSS Bauer et al. (2000)
5BZGJ0425-0833	EXO0422-086	0.0390	REFLEX Böhringer et al. (2004)
5BZGJ0439+0520	RXCJ0439.0+0520*	0.2080	BCS Ebeling et al. (1998)
5BZGJ0656+4237	RXJ0656.1+4237	0.0590	This paper
5BZGJ0737+5941	UGC3927	0.0410	
5BZGJ0737+3517	A590	0.2104	
5BZGJ0751+1730	Z1432	0.1866	eBCS Ebeling et al. (2000)
5BZGJ0753+2921	A602	0.0621	BCS Ebeling et al. (1998)
5BZGJ0834+5534	4C+55.16*	0.2412	Iwasawa et al. (1999)
5BZGJ0856+5418		0.2594	RBSC Bauer et al. (2000)
5BZGJ0927+5327	Z2379*	0.2011	eBCS Ebeling et al. (2000)
5BZGJ0944-1347	NVSS cluster	0.1782	RBSC Bauer et al. (2000)
5BZGJ1108-0149	NVSS cluster	0.1056	RBSC Bauer et al. (2000)
5BZGJ1119+0900	RedMAPPER	0.3315	Chandra obs
5BZGJ1350+0940	RXCJ1350.3+0940*	0.1325	RBSC Hogan et al. (2015b)
5BZGJ1356-3421	PKS1353-341*	0.2227	Véron-Cetty et al. (2000)
5BZGJ1407-2701	A3581*	0.0218	REFLEX Böhringer et al. (2004)
5BZGJ1413+4339	A1885*	0.0893	BCS Ebeling et al. (1998)
5BZGJ1445+0039		0.3062	

Table 4.4: Table continued..

BZCAT ID	Cluster ID	Redshift	Reference
5BZGJ1459-1810	S780*	0.2360	REFLEX Böhringer et al. (2004)
5BZGJ1504-0248	RXCJ1504.1-0248*	0.2169	REFLEX Böhringer et al. (2004)
5BZGJ1516+2918	RXJ1516.7+2918	0.1298	This paper
5BZGJ1532+3020	MACSJ1532.8+3021*	0.3621	BCS Ebeling et al. (1998)
5BZGJ1603+1554	RXCJ1603.6+1553*	0.1097	RBSC Hogan et al. (2015a)
5BZGJ1715+5724	NGC6338*	0.0281	BCS Ebeling et al. (1998)
5BZGJ1717+2931	RBS1634	0.2782	RBSC Bauer et al. (2000)
5BZGJ1717+4227	Zw8193*	0.1829	eBCS Ebeling et al. (2000)
5BZGJ1727+5510	A2270*	0.2473	RBSC Hogan et al. (2015a)
5BZGJ1745+3951	RGB 1745+398*	0.2670	Gliozzi et al. (1999)
5BZGJ1804+0042	CIZA1804.1+0042	0.0700	CIZA Ebeling et al. (2000)
5BZGJ2003-0856	NVSS cluster	0.0572	RBSC Bauer et al. (2000)
5BZGJ2140-2339	MS2137.3-2353*	0.3130	EMSS Stocke et al. (1991)
5BZGJ2147-1019	REFLEX cluster	0.0797	REFLEX Böhringer et al. (2004)
5BZGJ2320+4146	CIZA2320.2+4146	0.1520	CIZA Ebeling et al. (2000)
5BZGJ2341+0018	NORAS cluster	0.2767	NORAS Böhringer et al. (2004)

noting that very few of the systems identified here are broad-lined AGN. Instead the large majority are BL Lacs, where orientation effects dominate. Therefore, given our parent sample of X-ray clusters is nearly 1000 in total (Green et al. 2016), the duty cycle for high accretion rate events is well below 1%, with just two clearly identifiable broad-line AGN in our sample.

The apparent high fraction of these candidate clusters which host a BL Lac may seem surprising, particularly as BL Lacs are beamed sources which would suggest a much higher number of AGN which are not aligned with our line-of-sight. However, when put in the context of the comparison cluster sample such systems are still rare. We find only 21 BL Lacs likely to be hosted by a BCG, only seven of which are in cluster candidates directly comparable to the comparison cluster sample. There are 949 such clusters, hence, the BL Lac fraction is < 1 per cent. Unification models also suggest that misaligned BL Lacs are most likely to manifest as radio galaxies (Urry & Padovani, 1995). Radio emission is common in BCGs; indeed, the majority of cool core clusters have a central radio galaxy (Burns 1990; Hogan et al. 2015a) and cool core clusters are common in X-ray selected cluster samples (e.g. 44 per cent, Hudson et al. 2010; $44 - 60$ per cent, Andrade-Santos et al. 2017). Hence, we expect a non–zero BL Lac fraction. Furthermore, as BL Lacs are usually hosted by massive elliptical galaxies then you would expect to find a non-negligible number of BL Lacs within a sufficiently large sample of such elliptical galaxies, BCGs included.

We can also place a crude limit on the angular size of the relativistic beaming cone for jets in BCGs. By assuming we are observing a completely uniform sample and that all BCGs host a low power jet, the minimum opening angle can be estimated from the fraction that happen to be beamed along our line of sight. So assuming the $\sim$7 BL Lacs, which reside in clusters comparable to our cluster comparison sample, are drawn randomly in orientation from all 949 BCGs in the $z < 0.4$ RASS clusters covered by the PS1 footprint, then only 0.74% of BCGs are beamed towards us. So the opening angle is 7.0°. If we exclude BCGs with low radio power, (approximately two thirds of the sample) using the radio luminosity function of BCGs in Hogan et al. (2015a), then the fraction of beamed objects increases to approximately 2.2% and hence the implied opening angle is 12.1°. This crude limit

is in broad agreement with limits estimated from more direct studies of superluminal motion in BL Lacs and beamed flat-spectrum radio galaxies (Jorstad et al., 2005), which suggest angles of 2–5° for Lorentz factors less than 10, as should be the case in these sources (Jorstad et al. 2005). As we do not know the full parent sample for most BL Lac parent populations this analysis can rarely be utilised. However, as BCGs represent a comprehensive parent sample then BCGs, although only providing a crude estimation, are a useful test for such an analysis. In reality of course only some fraction of the BCGs will be AGN, hence the true opening angle is likely to be broader. Clearly a significantly better constraint can be derived in the near future with the combination of *eROSITA* and new radio surveys such as VLASS, EMU and WODAN.

Although outside of the immediate scope of this work, a further subtlety to consider, in identifying ambiguous sources and understanding the feedback of AGN in cluster cores, is AGN variability. Variability has the potential to tip the balance of emission between cluster and AGN contributions at the time of some given observation. An illustrative example is NGC1275 in the Perseus cluster (O'Dea et al. 1984; Dutson et al. 2014; Fabian et al. 2015), which has exhibited a variation of at least one order of magnitude on a timescale of a few decades.

4.7 Summary and Conclusions

We use the PS1 3π survey to look for signs of a rich cluster around the full *ROSAT* All Sky Survey AGN population in the PS1 3π footprint, constituting some 3058 broad-line AGN and 412 BL Lac objects. Of these, we find 22 AGN with signs of a significant overdensity in red galaxies, suggestive of a possible cluster red sequence, and which are hosted by a galaxy visually consistent with being a BCG. We compare the properties of these candidate systems with those of a comparison sample of the $\sim$ 1000 confirmed clusters also drawn from the *ROSAT* All Sky Survey.

We identify seven best candidates, contingent on having a red sequence richness that is most comparable to the confirmed massive clusters at similar X-ray luminosities. Amongst our 22 candidate systems, five have been previously confirmed

to be a cluster with a BCG in its central galaxy, with pointed X-ray observations available, strongly validating our technique, and providing valuable context for our candidate systems.

We use the colour of the red sequence as a tracer of redshift to investigate cluster membership of the AGN. We find all our candidate systems have a red sequence colour which is similar to that of the confirmed clusters at similar redshift, indicative that the AGN and red sequence galaxies share a common redshift.

The optical and MIR luminosities of the AGN host galaxies are found to be generally consistent with those of the BCGs of the comparison clusters, at similar X-ray luminosities. This supports our visual identification of the AGN host galaxies as BCGs.

We also check the validity of the initial AGN identification by looking at the MIR and optical colours of our AGN. In the MIR we find all candidate systems show an excess MIR emission with respect to the bulk passively evolving population of comparison BCGs, suggestive of activity. In the optical we find the majority of sources are significantly blue in g–r, with respect to the passively evolving BCGs, consistent with their identification as BL Lacs.

We emphasise the need to consider the ambiguity that exists in the identification of clusters and AGN in X-ray data, and stress it is not necessarily a case of one of the other. This very simple approach of checking for optical overdensities, around X-ray selected AGN, can be utilised to correct for selection effects against the detection of strong AGN in the cores of clusters. This ultimately will provide better statistics relating to both the prevalence of, and energetics involved with, AGN in BCGs - increasing our understanding of the role of AGN feedback in this unique environment. This consideration will be particularly important in the future with the next generation of X-rays survey telescopes, such as *eROSITA*, set to uncover vast numbers of new X-ray sources; including clusters, AGN *and* the two combined.

Chapter 5

The MUSE Instrument, Target Selection, Data Reduction and Methodology

5.1 Overview

The following chapters draw on spectroscopic analysis of BCGs from the Multi Unit Spectroscopic Explorer IFU instrument. In this Chapter I will describe the principle of integral field spectroscopy, the MUSE instrument, the target selection, and outline the MUSE data reduction and techniques applied to these data in order to extract stellar and gaseous kinematics for the analysis presented in Chapters 6 & 7.

5.2 Integral Field Spectroscopy

Integral field spectroscopy (IFS) is a technique which has made great advances in our understanding of astronomical phenomena over the last decade or so. IFS observations provide spatially resolved spectra, in what are essentially three dimensional observations. The sky is imaged in two spatial dimensions, but crucially, the signal from each spatial pixel (called a spaxel) is also fed into a spectrograph, leading to a spectrum being produced for each spaxel. An integral field spectrograph is composed of two components, the spectrograph(s) and the integral field unit (IFU). The

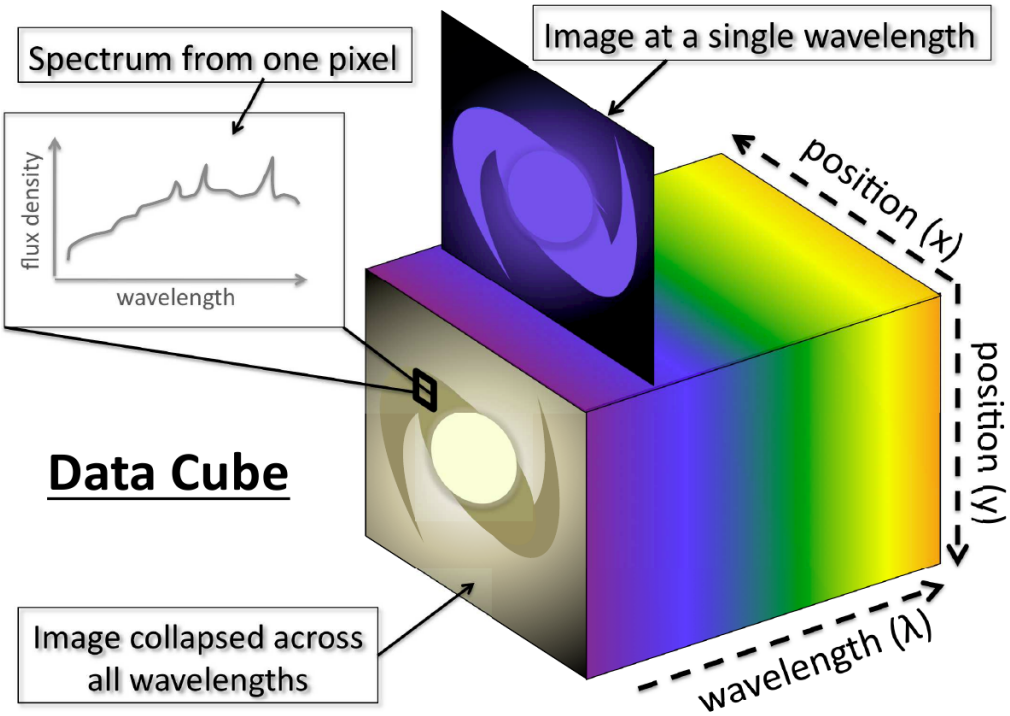

Figure 5.1: Schematic of an IFS data cube, which consists of three dimensions; two spatial dimensions and one wavelength dimension. Image credit to Harrison (2014).

role of the IFU itself is to divide up the 2D spatial plane, which can be done in a number of ways. The final product of an IFS observation is a data cube, containing the x,y spatial plane and the wavelength, λ, dimension – a schematic diagram of which is provided in Figure 5.1.

The two great advantages offered by integral field spectroscopy are the ability to observe multiple objects simultaneously, making observations of dense regions such as clusters particularly efficient, and the ability to investigate the dynamics of stars and line emitting nebulae over the spatial extent of the instrument field-of-view. Both of which will be utilised over the following chapters.

5.3 The MUSE Instrument

The Multi Unit Spectroscopic Explorer (MUSE; Bacon et al. 2010) is a second generation wide–field IFU instrument. It is located on the 8.2 m diameter UT4 of the Very Large Telescope (VLT), at the European Southern Observatory (ESO)

at Paranal, Chile. In Wide Field Mode MUSE provides a square arcmin field-of-view, with a spatial sampling of 0.2 arcsec per pixel. The wavelength coverage runs from 4750Å to 9350Å (equivalent to optical *VRI* bands), with a spectral sampling of 0.125 Å and a spectral resolution ranging from $\sim$ 3.0Å at 4800Å to $\sim$ 2.6Å at 9300Å. It produces a datacube of dimensions 300 $\times$ 300 $\times$ 3681. At the time of the observations of these data, MUSE was only available in Wide Field Mode, with natural seeing, but in the future MUSE will be available in a Narrow Field Mode – providing a 7.5 square arcsec field-of-view – and will be combined with adaptive optics.

MUSE utilises an image slicer based IFU. First the field-of-view is split into twenty-four 2.5 arcsec thick slices, or "channels", which are then fed into separate IFUs. Each of these is then split again into a further 48 slices, providing a total of 1152 'mini slits'. Each block of 48 mini-slits are in turn fed into one of the 24 spectrographs.

5.4 Target Selection

The BCGs in these Chapters are primarily drawn from the parent sample of 981 X-ray selected clusters described in Chapter 2. In order to identify the BCG for each cluster in our sample, a visual inspection of the Pan-STARRS 3π (Tonry et al., 2012) optical imaging was conducted. It was noticed that a few tens of these BCGs appear to exhibit indicators consistent with a recent/ongoing galaxy–galaxy merger, such as asymmetric envelopes, or are likely to merge in the future given the presence of a (some) substantially massive companion galaxy (galaxies). These are BCG systems with complex morphologies; primarily galaxies with multiple nuclei or very nearby companion galaxies, as well as some with plume-like asymmetric envelopes or shells.

As discussed in Chapter 1 the issue of the stellar mass growth of BCGs is a debated field of study, and BCGs in the process of ongoing mergers are rare. As such we were awarded time with MUSE to observe a subset of 32 of these complex BCGs (PI Green; programme ID 095.A-0159(A)) and investigate kinematic information for these systems (see Chapter 6). Unfortunately, only 25 of these observations were

completed within the observational period and two were taken in low grade weather conditions – leaving a total of 23 observations of sufficient quality for the analysis. Examples of the MUSE targets are presented in Figure 5.2, showing the PS1 3π i-band imaging, which shows the unusual nature of these galaxies. Details of the individual targets are given in Table 5.1.

The redshift–X-ray luminosity distribution of the MUSE targets are overlaid onto that of the parent cluster sample in Figure 5.3, from which it is clear that the MUSE targets are a fairly representative subsample of the parent clusters, in terms of their $L_{\rm X}$–z distribution, with no clear preference toward high or low X-ray luminosity clusters. Note we restricted our MUSE target list to clusters at $z < 0.25$ so that a high signal-to-noise could be achieved in relatively short exposures and the kinematics could be spatially resolved. It appears that there is a potential deficit of MUSE–selected targets in high X-ray luminosity clusters. It is possible that this could be related to the fact you may expect the more massive clusters to be the most mature and well established systems, having already undergone the majority of their growth, which may similarly be the case for their central galaxies. However, it is more likely to be due to the low number of targets. There are 784 clusters within $z < 0.25$, 65 of which are above an X-ray luminosity of $5 \times 10^{44}\,{\rm erg\,s^{-1}}$ (the $L_{\rm X}$ of the most X-ray luminous of the MUSE targets) and 23 targets are observed with MUSE. So we would expect that, if the MUSE targets are randomly drawn from the parent cluster sample, then on average only $65/(784/23) = 1.9$ MUSE targets should reside within that $L_{\rm X} > 5 \times 10^{44}\,{\rm erg\,s^{-1}}$ range. So the statistical likelihood of a BCG not residing here, due to random sampling, is quite high and hence the result is unsurprising. A similar argument explains the lack of MUSE–selected targets at the low $L_{\rm X}$ range of our cluster sample. There are only 39 clusters at $L_{\rm X}$ $< 0.23 \times 10^{44}\,{\rm erg\,s^{-1}}$ (the $L_{\rm X}$ of our least X-ray luminous MUSE–selected cluster), so you would expect only 1.1 MUSE targets to be in this $L_{\rm X}$ interval.

Due to the extended nature of BCGs and the relatively low redshift of our cluster distribution the best seeing was not a requirement for these observations. This, combined with the relatively short necessary exposure times, meant these targets were ideally suited for filling gaps in observation queue for MUSE. When experi-

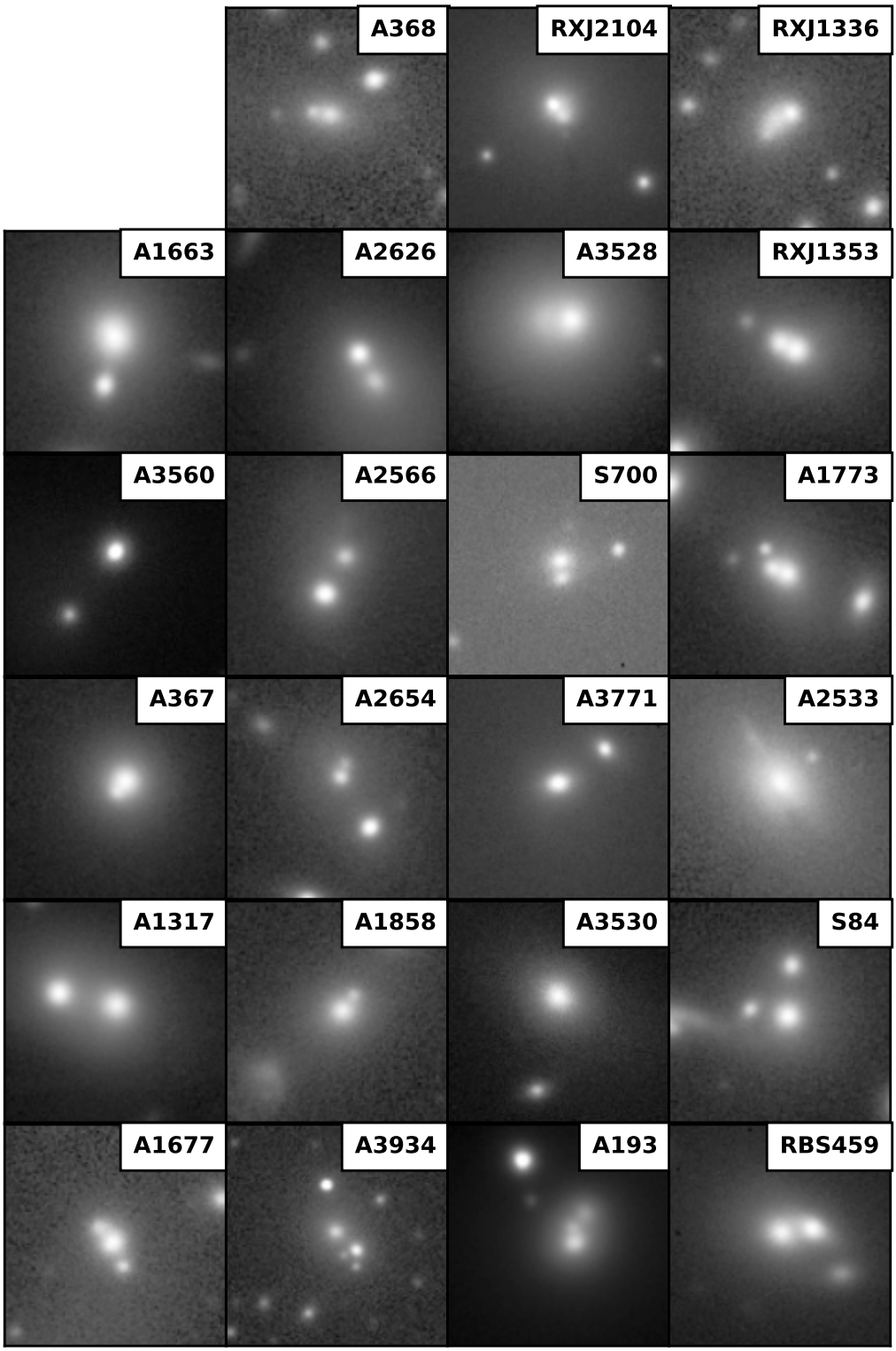

Figure 5.2: The full sample of 23 complex BCGs targeted by our MUSE programme. Tiles are PS1 3π/VST ATLAS/KiDS i-band/FORS acquisition R-band imaging, corresponding to 25 arcsec squared.

encing winds from the North, pointing limitations apply at the VLT, so in order to maximise our observational efficiency – by having targets distributed uniformly across the sky – the PS1 selected BCGs were also supplemented with Southern targets (DEC< 30 degs). These Southern sources were selected as exhibiting similar properties to our primary sample selection, but in the acquisition images of the FORS1/FORS2 spectroscopic follow-up, on the VLT, of X-ray selected REFLEX (Böhringer et al., 2004) survey clusters (Edge et al. in prep). Due to the nature of these images, this supplementary sample does not represent a comprehensive sample of the Southern sky, but can be co-added in the statistical interpretation of our primary PS1 based targets.

The selection criteria for these BCGs generally required the presence of at least one companion galaxy in close proximity to the BCG, which has a comparable luminosity to the BCG. As such, BCGs with only small satellite galaxies close to the BCG were not selected. The majority (21/23) of these observations were selected on exhibiting multiple components/nearby companions. Of these, 11 systems exhibit two, or more, substantially massive close companions. The other 10 systems exhibit a single substantial companion, often in what appear to be dumbbell-like systems. Two of these systems exhibit asymmetric envelopes (plumes), in addition to the multiple components; A2626 and A2566, and one system, RXJ1353, appears to show a shell in the outer envelope. The exceptions to this selection criteria are A2533, which was selected on exhibiting unusual star forming/dusty features, and A3560 which was selected on the appearance of a sharp shell–like substructure within its extended envelope, which is thought to represent a late stage in the merger process. Asymmetric envelopes, or plumes, seen in A2626 and A2566 and A3560, likely indicate that some interaction has already happened between the two components. This is visually similar to that of the BCG major merger of CL0958+4702 in Rines et al. (2007).

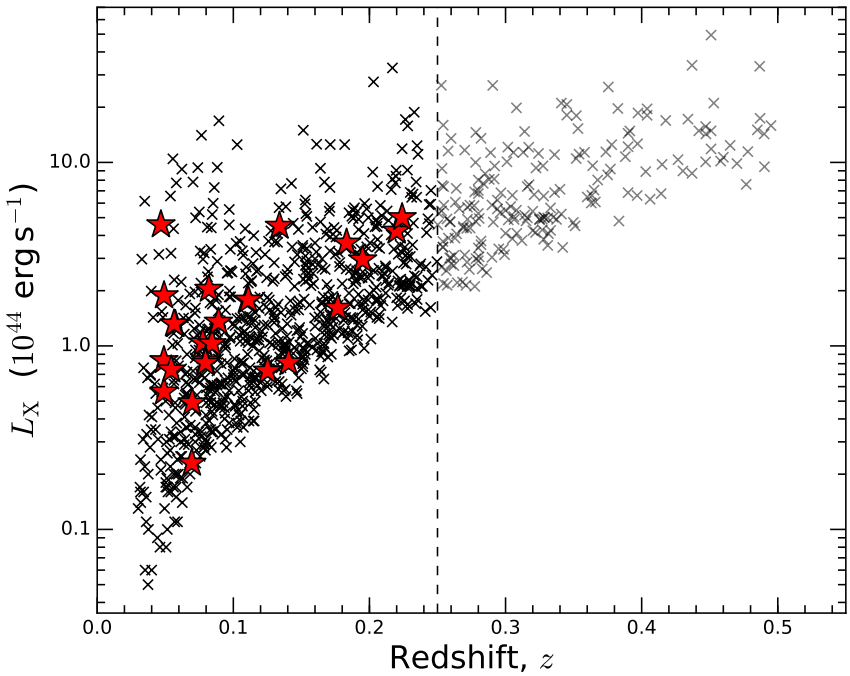

Figure 5.3: The cluster X-ray luminosity against redshift distribution. The crosses show the full parent cluster sample, with the darker crosses, left of the dashed line, showing the subset of 784 clusters below our selection threshold for MUSE follow-up of $z < 0.25$. Overlaid, as the filled (red) stars, are the position of the 23 MUSE targets. This demonstrates our MUSE targets have a broad distribution across L_X–z parameter space.

Cluster ID	Redshift	L_X (10^{44} erg s^{-1})	BCG RA (J2000)	BCG DEC (J2000)	MUSE FOV (kpc^2)	Selection
S84	0.1100	1.77	00:49:22.8	−29:31:13	117	> 3 Components
A193	0.0491	1.88	01:25:07.6	+08:41:56	56	3 Components
A367	0.0891	1.35	02:36:37.1	−19:22:17	97	2 Components
A368	0.2200	4.23	02:37:27.7	−26:30:29	208	2 Components
A1317	0.0695	0.23	11:35:12.9	−13:33:07	78	2 Components
A3528	0.0574	1.31	12:54:41.2	−29:13:40	65	2 Components
A1663	0.0843	1.03	13:02:52.6	−02:30:59	93	2 Components
A1677	0.1832	3.64	13:05:50.8	+30:54:17	180	3 Components
RXJ1336	0.1768	1.61	13:36:00.0	−03:31:29	175	3 Components
A1773	0.0776	1.04	13:42:09.6	+02:13:38	86	3 Components
RXJ1353	0.0468	4.58	13:53:26.5	−27:54:08	54	3 Components
A1858	0.1406	0.81	14:07:56.7	−04:19:26	145	2 Components
A2533	0.1110	1.78	23:07:13.9	−15:13:27	118	Dust and SF
A2566	0.0821	2.04	23:16:05.0	−20:27:48	90	2 Components
A2626	0.0565	1.32	23:36:30.5	+21:08:48	64	2 Components
A2654	0.1252	0.73	23:44:22.8	−07:25:27	131	3 Components
RBS459	0.0698	0.50	03:40:41.2	−45:41:20	78	3 Components
S700	0.0796	0.83	12:36:41.3	−33:55:33	88	2 Components
A3530	0.0544	0.74	12:54:36.1	−30:20:52	62	Shells
A3560	0.0489	0.83	13:22:22.6	−33:08:22	56	2 Components
A3771	0.0796	0.81	21:29:42.6	−50:49:27	88	2 Components
RXJ2104	0.0491	0.56	21:04:51.5	−51:49:25	56	2 Components
A3934	0.2240	5.01	22:53:32.6	−33:43:05	211	> 3 Components

Table 5.1: Cluster ID, redshift and X-ray luminosity, BCG RA and DEC, physical size of one arcmin (i.e. the dimensions of a MUSE cube) in kpc and primary reason for target selection. *Top*: clusters drawn from the parent sample defined by the PS1 footprint (Chapter 2), *bottom*: supplementary Southern targets from FORS acquisition imaging.

5.5 MUSE Observational Details and Data Reduction

Each observation of the 23 complex BCGs consisted of three exposures of 600 s each, with dithering and rotations between exposures of two arcsec and 90° respectively. Due to the extended nature of BCGs the best weather conditions were not necessary, giving a median seeing of 0.9 arcsec. As MUSE has a large field of view, which is greater than the angular spatial extent of any our target galaxies, and good flat field stability, the sky can be measured from the science exposures and no additional sky exposures were necessary.

For the data reduction the ESO supplied EsoRex reduction pipeline was used. In each case, the nearest calibration files in time to the observation were used. These calibration files include bias, wavelength calibrations, lamp and sky flat field observations, a standard star, and astrometry. Illumination lamp flat fields are taken with every observation also. The pipeline extracts the spectra, performs wavelength calibration and flat fields and then forms the data cubes. The separate cubes were then co-added, taking the median value for each spaxel.

Despite the sky subtraction in the reduction pipeline, significant sky residuals were present in the data. So the sky subtraction tool ZAP (Zurich Atmosphere Purge; Soto et al. 2016) was applied to the reduced MUSE cubes, which very effectively removed the residuals.

In order to illustrate the data quality, an example spectrum for the BCG for each of our MUSE targets are presented in Figure 5.4.

5.6 Stellar Kinematics

The signal to noise (S/N) for each pixel was estimated over a 110Å range of line-free continuum, between rest-frame wavelengths of 5220Å and 5330Å. The signal was defined as the mean flux value, and the noise as the residual between a best fitting polynomial and the data.

For the central BCG and nearby companions these S/N values were fed into

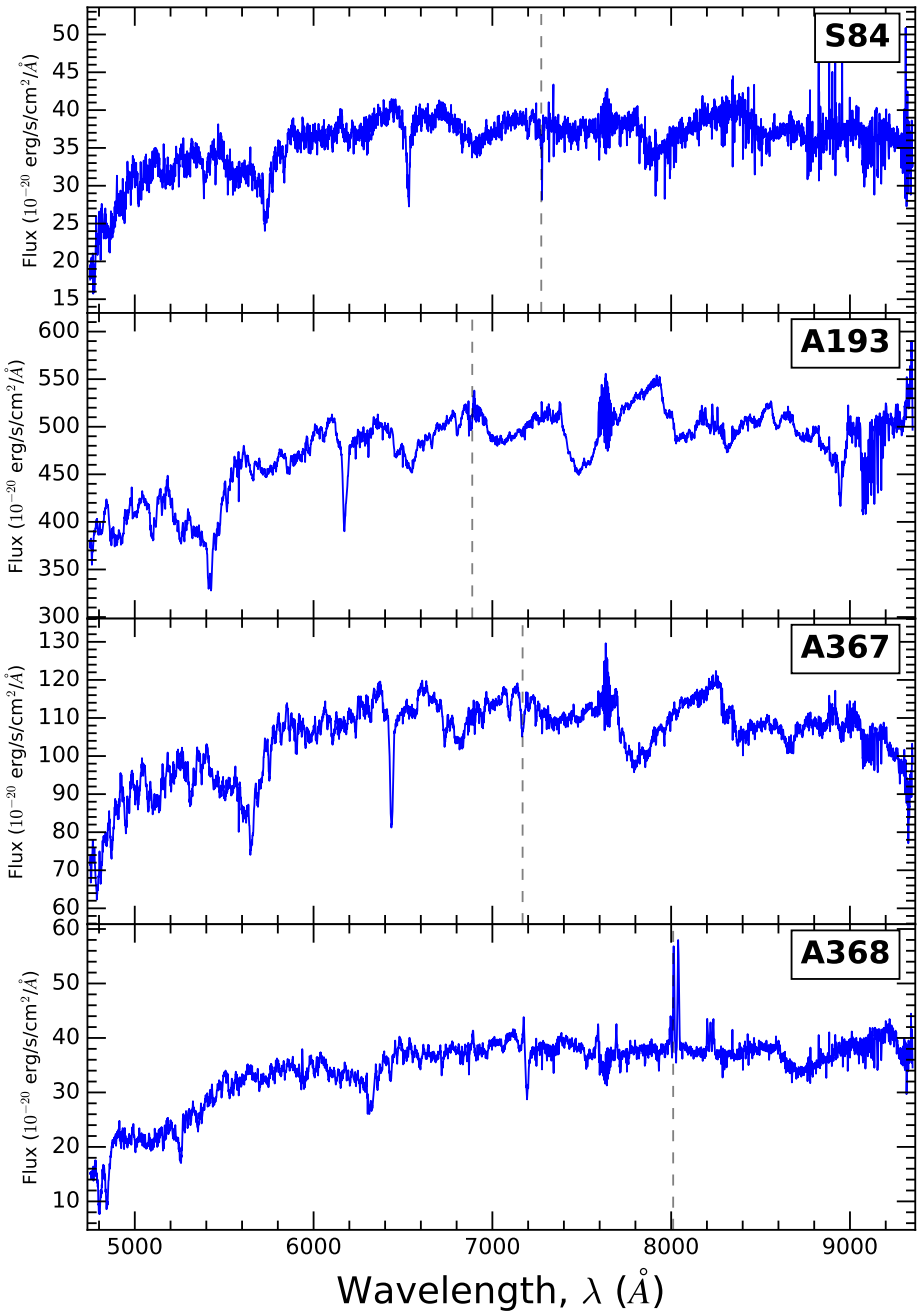

Figure 5.4: Spectrum of the BCG for each of the MUSE targets. The grey dashed line shows the position of Hα, at rest frame wavelength, $\lambda_{\rm rest} = 6563\,\mathring{A}$.

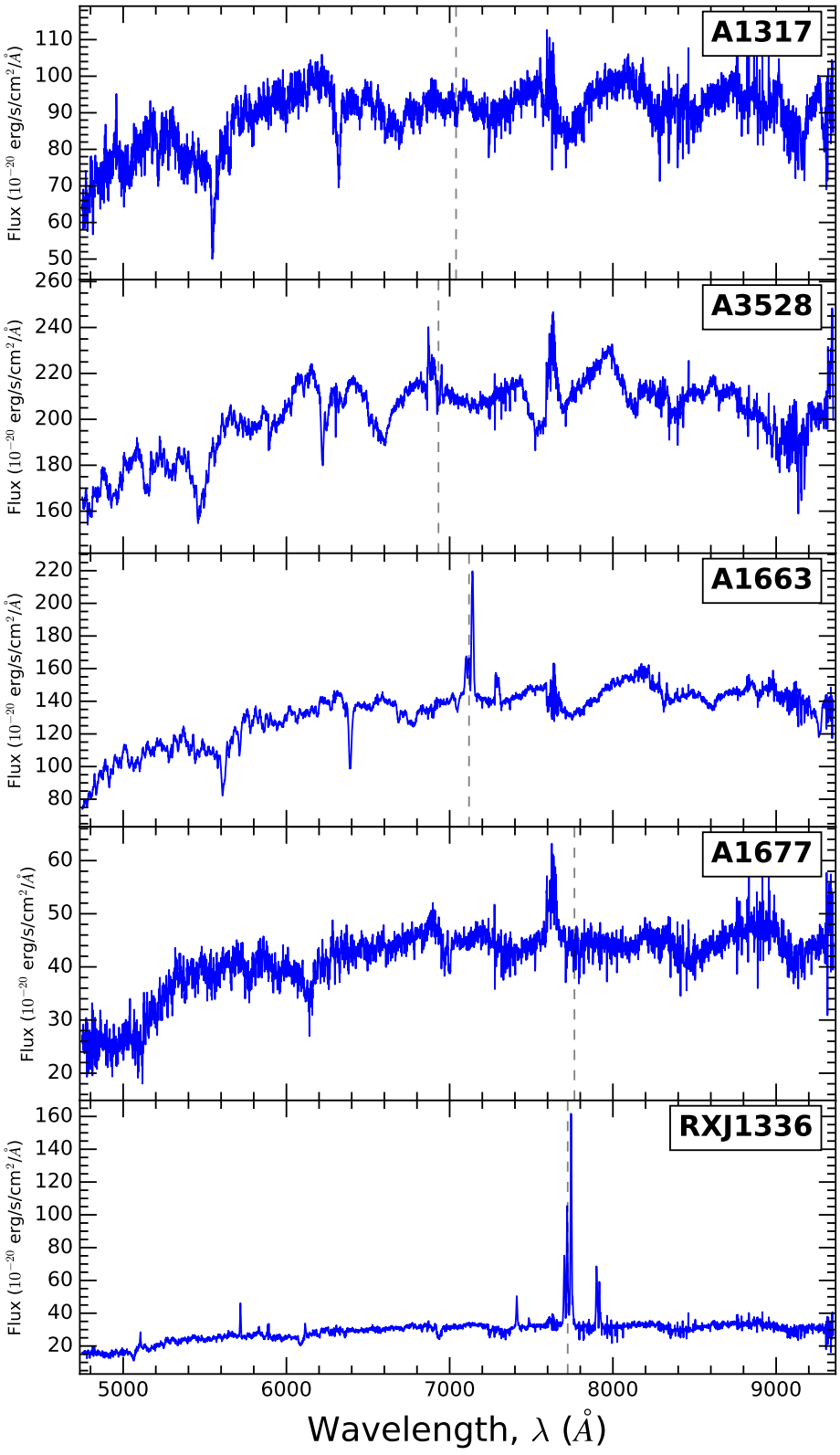

Figure 5.4: Figure continued..

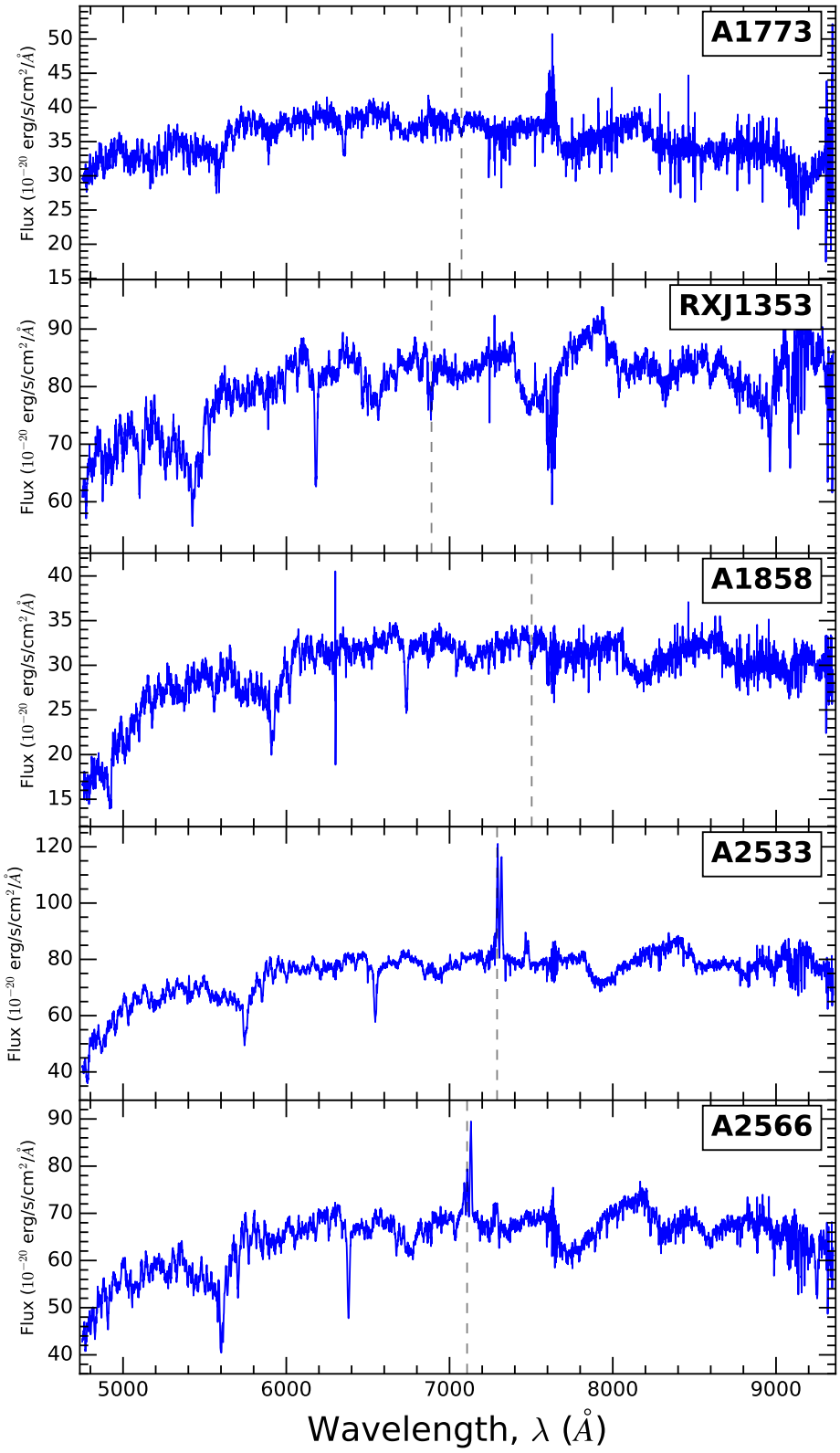

Figure 5.4: Figure continued..

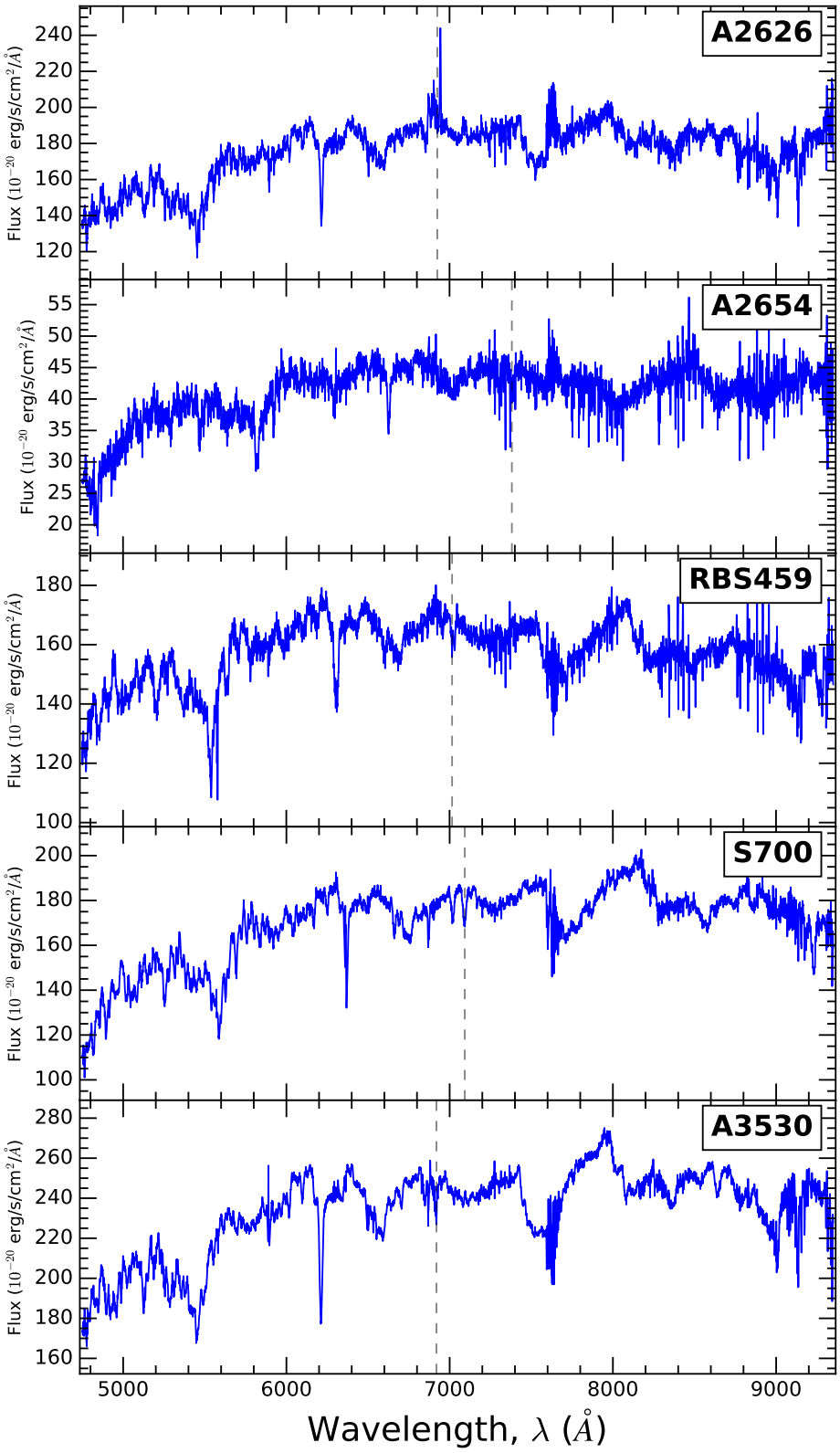

Figure 5.4: Figure continued..

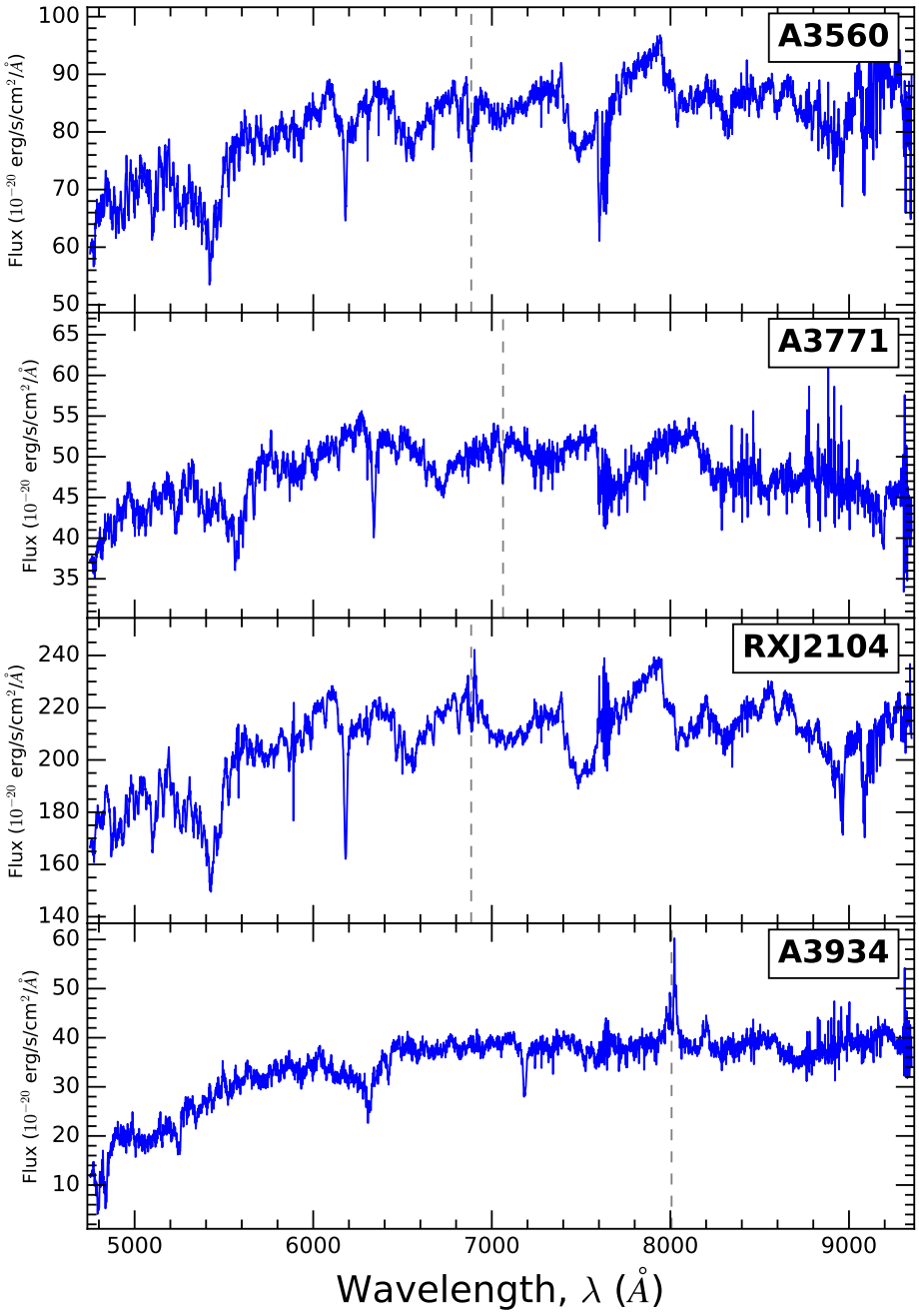

Figure 5.4: Figure continued..

the Voronoi tessellation algorithm of Cappellari & Copin (2003). The algorithm is designed to bin adjacent pixels such that each bin achieves a minimum target S/N. For measuring the stellar kinematics accurately a sufficiently high S/N is necessary, so a target S/N of 30–50 was applied to the binning, depending on the redshift of the target system. The spectrum of each bin was then given by co-adding the spectra from its constituent pixels.

The Voronoi tessellation method was found to be effective in the cluster core, where there is a roughly continuous source of signal (from the extended envelope of the BCG and very close companions), however it did not effectively bin pixels belonging to independent cluster members further from the BCG. Instead, these individual sources were selected through SExtractor (Bertin & Arnouts, 1996). The pixels belonging to each source were identified via the SExtractor segmentation setting, binned accordingly and their spectra co-added. The SExtractor detection was done with a fixed threshold across all systems, such that a sufficiently high S/N is achieved for the stellar kinematic fitting of each galaxy. Hence we were able to sample comparatively dimmer companion galaxies at lower redshift than at higher.

Stellar absorption line fitting was conducted using a Penalized Pixel-Fitting (pPXF) routine (Cappellari & Emsellem, 2004), between 4750Å and 7000Å, to the co-added spectrum of each bin (Voronoi bins and individual sources). In pPXF the line-of-sight kinematics are derived from fitting a linear combination of spectra from a template stellar library, to best match the observed spectrum. An example of a pPXF fit is given in Figure 5.5, demonstrating the effectiveness to which it can replicate a spectrum. We used the full MILES (Medium-resolution Isaac Newton Telescope Library of Empirical Spectra) library of stellar spectra (Sánchez-Blázquez et al., 2006), of resolution 2.5Å. Our MUSE observations at this wavelength have a resolution of approximately 2.7Å, so before the fitting the templates are convolved with the instrumental resolution. We followed the standard pPXF procedure of logarithmically re-binning the data and the MILES spectra and allow pPXF to fit four velocity moments (V, σ and the Gauss hermite moments of h_3 and h_4) and a fourth order polynomial, which corrects for continuum mismatch. pPXF fits the stellar library templates to the absorption lines of our MUSE spectra and determines an

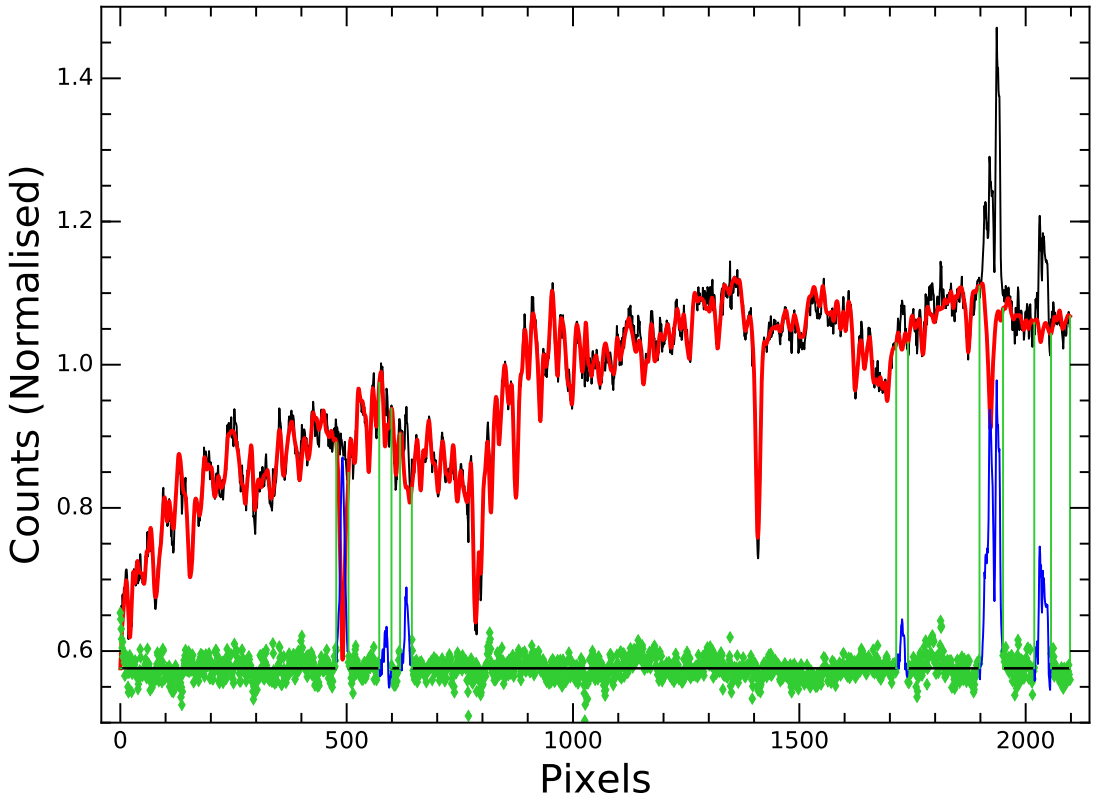

Figure 5.5: An example of the pPXF fitting to the BCG of A2566. The normalised data are given by the black line, the resulting best fitting model is given by the red line and the residuals between the data and model are given by the lime green points. Note that pPXF skips wavelength intervals around common gaseous emission lines, shown via the blue lines in the residual scatter, but still returns an estimate for the stellar absorption here.

estimate for the line-of-sight velocity, relative to the initial input redshift, and the velocity dispersion via the line width.

pPXF fitting was iteratively performed on the integrated spectrum of the BCG core, using an initial input estimate of the redshift from that of the cluster, until the true best-fitting redshift of the BCG was found. All subsequent pPXF fitting used this redshift value and hence all derived velocities are defined relative to the rest frame of the BCG. As we were investigating nearby cluster members, which may have a significant velocity offset relative to the BCG, of the order of a few thousand $\mathrm{km\,s^{-1}}$, a strong dependence on the initial guess for the velocity was identified as

important in achieving an appropriate fit. Hence we iteratively assumed an initial velocity from $-2000\,\mathrm{km\,s^{-1}}$ to $+2000\,\mathrm{km\,s^{-1}}$, in intervals of $1000\,\mathrm{km\,s^{-1}}$, with the initial estimate which achieved the minimal chi square value to the fit ultimately utilised.

The BIAS keyword in the pPXF fitting, which controls the level of bias toward gaussianity was found to have a negligible effect on the kinematics of the BCG and close companions. This effect only really contributes in low velocity dispersion galaxies ($< 150\,\mathrm{km\,s^{-1}}$). Whereas the typical velocity dispersion of a BCG is $300\,\mathrm{km\,s^{-1}}$.

As pPXF is designed to be robust and uses the user input redshift value to convert the observed wavelengths to rest frame, it is not suited for picking out sources which are background/foreground to the cluster. The code will still fit templates and return a velocity value for a source, even if it is a Milky Way star, but the fit will of course be bad. Hence it was necessary to first inspect the spectrum for each source, within the MUSE field-of-view, and determine which sources are not cluster members. Such galaxies were identified and removed from subsequent analysis, so that only cluster members had kinematics measured. Note however that these do still appear in imaging presented in Chapter 6, but are masked out in the kinematic maps. Note that the term 'cluster member' is used to denote any galaxy at approximately the same redshift as the BCG, such that pPXF will determine an accurate velocity. As inclusion of galaxies with velocities in excess of the cluster velocity dispersion has no bearing on the later analysis (as they have a probability of being bound to the BCG of zero; see Chapter 6), we do not apply a more formal velocity cut to define what is a cluster member.

5.6.1 Optical Photometry

For the most part, the photometric properties of the galaxies in our MUSE fields were measured using the optical imaging from the Pan-STARRS PS1 3π survey (Tonry et al., 2012). The i-band imaging was used due to the red sensitive nature of the PS1 telescope. The photometry was initially performed using SExtractor (Bertin & Arnouts, 1996), in which fluxes were measured using the MAG_AUTO parameter,

which measures the flux within a flexible elliptical aperture with a Kron–like radius (Kron, 1980). However, for a number of the BCGs their multiple components were blended in the SExtractor photometry and so instead GALFIT (Peng et al., 2002, 2010) was used. GALFIT takes a series of user input initial photometric estimates and fits 2D analytic functions to the light profile of each galaxy simultaneously, converging on the best–fitting parameters. When GALFIT was necessary for fitting the BCG, the photometry of all the galaxies in the field were measured in GALFIT. This was done to avoid systematic differences in the photometric results, resulting from the use of two separate photometric tools, across the same field.

On the first instance a single component Sérsic index was fit to each galaxy. Sérsic profiles are generally good approximations for elliptical galaxies, which BCGs tend to be. However Seigar et al. (2007) found that often a double component fit is necessary for BCGs, usually a Sérsic fit to the core and an exponential fit to the envelope. So a double component fit was applied when the single component fit was found to be unsuitable. The size of the postage stamp over which GALFIT operates was chosen for each field in turn, attempting to include the full extent of the BCG, whilst not including too much sky, which affects the convergence of the fit. The PSF files available from the PS1 postage stamp servers were fed into GALFIT. The initial parameters; positions, fluxes and radius, were approximated from the results of the SExtractor photometric run, with manual adjustment for blended SExtractor sources. The GALFIT fitting procedure was applied in an iterative process for each field until a suitable fit was found.

The GALFIT photometry has a reasonably high level of uncertainty in the fluxes, due to dependencies in the resulting effective radius on the Sérsic index and sky values during the fitting process. This is most difficult to do accurately for the BCGs as these are the most extended sources and ambiguity between stars belonging to the BCG and the ICL make determining the effective radius and fluxes uncertain. The GALFIT procedure was applied many times, until the level of residual between the data and model were suitably low (i.e. where the residual flux is a few per cent of that of the data). Then, in order to further sanity-check our photometric results we compare the GALFIT photometry with that of the blended SExtractor

results, to check the overall fluxes are roughly consistent. The uncertainty of the GALFIT photometry is typically at a few tenths of magnitude. In Chapter 6 these uncertainties later feed into the dynamical mass of the BCG (through the effective radius), which affects the bound probabilities and merger timescales, and the BCG–companion galaxy luminosity ratio, which adds uncertainty to the fractional stellar mass growth rate of the BCG.

Eight of the MUSE targets fall outside of the Pan-STARRS footprint (i.e. DEC$<-30\,\mathrm{deg}$) so alternative imaging data was necessary. Some of the Southern sources had been covered by surveys carried out on the the VLT Survey Telescope (VST). This 2.61 m telescope uses the OmegaCAM instrument and is on the ESO Paranal site in Chile. For A3530 and A3560, imaging from VST ATLAS (Shanks et al., 2015), in the i–band, was used. This imaging is similar to that of PS1 3π in terms of pixel scale and flux depth with a scale of 0.2 arcsec per pixel and i–band flux depth of ~ 22. For A3934 deeper VST imaging from the Kilo–Degree Survey (KiDS; de Jong et al. 2013), which has an i–band flux depth of ~ 24, was used. For RBS459, RXJ2104, A3771 and S700 however no imaging survey data could be found. So the photometry for these systems was conducted on the Focal Reducer and low dispersion Spectrograph (FORS) acquisition images. By the nature of these observations the exposures are short ($\sim 10s$), so have limited flux depth, but on the 8m VLT this is still sufficient to perform meaningful photometry. These images and the resulting photometric values are in the R–band.

The photometry carried out on these Southern systems followed the procedure described for the PS1 images. These southern systems were flux calibrated by cross matching the fluxes of stars with the United States Naval Observatory (USNO) catalogue fluxes. No corrections are made between the differing properties of the FORS acquisition R–band and that of the USNO, and the VST i–band with the USNO I–band, so the reported fluxes for these Southern targets carry a level of uncertainty of several tenths of a magnitude.

As will be explored in subsequent chapters, the photometric fluxes of the galaxies will be used primarily in the form of flux ratios between cluster galaxies and the BCGs. Hence the uncertainty that exists due the approximate flux calibrations, and

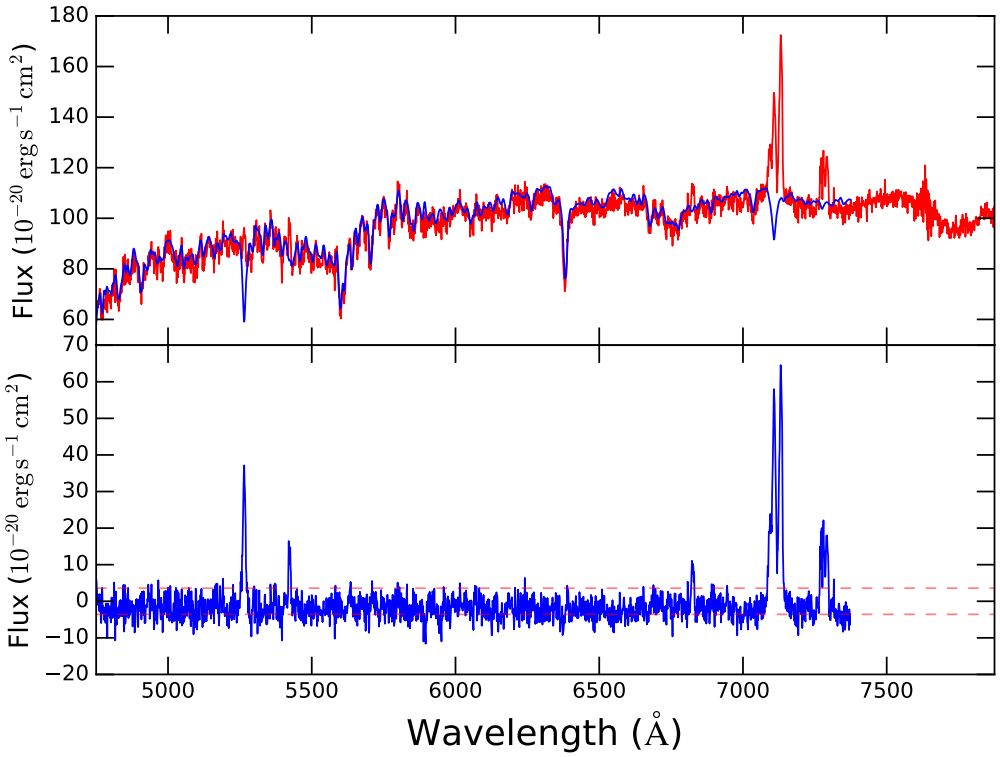

Figure 5.6: *Top:* The observed spectrum of an individual spaxel is given by the red line and the best fitting spectrum of the BCG from pPXF, scaled by the median of the data, is given by the blue line. *Bottom:* The continuum subtracted spectrum of this spaxel is given by the solid blue line and the evaluated ± value of the noise is indicated by the red dashed lines. This particular example is a spaxel near the BCG of A2566 ($z = 0.083$).

the use of short single exposure acquisition images for the southern targets, mostly cancel out. The use of flux ratios also cancels out the uncertainty associated with the adopted sky value, for both the SExtractor and GALFIT photometry, which is often difficult to accurately determine in a cluster core, with the presence of diffuse light.

5.7 Optical Emission Lines

5.7.1 Emission Line Fitting

In order to investigate the kinematics of any line emission nebulae and investigate traditional line flux ratios, a line fitting routine was applied to a whole suite of optical emission lines. However, in order to account for emission which would be otherwise be lost to stellar absorption features, the continuum was subtracted first. The continuum was determined by application of pPXF to the integrated spectra, over a broad section (2.2×2.2 arcsec), of the galaxy over which the emission line is observed (usually the BCG). As discussed above, pPXF applies a linear combination of template stellar spectra, with some velocity and dispersion, in order to replicate the observed spectra. Whilst doing so, it skips wavelength intervals immediately around common gaseous emission lines (such as Hα, Hβ [S II]) but fits common stellar absorption features (such as Na D λ5890/5896Å and Mg I λ5178Å). The resulting combination of stellar spectra, which replicate the observed spectrum, provides an estimate for the stellar absorption at the wavelengths of the common gaseous emission lines. An example of the results produced by pPXF are provided in Figure 5.5, illustrating the way it handles emission lines.

The data for each spaxel in the datacube was spatially smoothed, such that the spectra for each spaxel was the mean of the 3×3 grid of spaxels (0.6×0.6 arcsec) centred on it. This was done as a compromise between achieving a higher S/N, but at the expense of some spatial resolution. For each individual averaged spaxel, the median of its spectral continuum was then determined and the normalised best fitting template spectrum scaled by it. Then this was subtracted from the observed spectrum, giving a continuum subtracted spectrum – ready for emission line fitting – for each spaxel. An illustrative example of the spectrum for an individual spaxel, with the scaled best fitting model spectrum, is provided in the top panel of Figure 5.6, with the resulting continuum subtracted spectrum given in the bottom panel. The noise of the observed spectrum was iteratively determined by determining the standard deviation of the continuum subtracted spectrum, whilst clipping any points in excess of 3σ from the mean (which excluded emission lines from the noise

calculation).

First the Hα and [N II] triplet at $\lambda_{\rm rest}$ = 6562.8 Å and 6548.1/6583.5 Å were simultaneously fitted using a linear combination of three Gaussians. Initial estimates for the amplitude and mean of the Gaussians were determined by looking for local maxima in a wavelength interval about the expected wavelength value for Hα, given the redshift of the BCG. Then an iterative Gaussian fit was made constraining the line width and velocity of each line to be similar, such that the free parameters are the individual amplitudes and a velocity and velocity dispersion. It should be noted that the line ratio of the [N II] lines are fixed by atomic physics to be ratio of [N II] λ6548/[N II] λ6584 of 1/3. This is not fixed in the line fitting procedure, but instead used as a verification check for the accuracy of the results. A typical ratio value of 0.3 ± 0.1 is found, in fairly good agreement with the expected result. This suggests the typical uncertainty on the line intensity ratios is approximately 10 per cent. It should also be noted as Hα is a permitted line and [N II] is a forbidden line then they may not necessarily have the same velocity dispersion, as is the case for broad-line AGN. However, broad-line AGN are rare in BCGs (see Chapters 3 and 4) so the line widths are likely to be dominated by the properties of the gas. In order to verify this the spectrum for each BCG was checked for signs of of some lines being broader. In all cases the line widths were found to be roughly equivalent (e.g. Figure 6.9), justifying the similar width constraints on the permitted and forbidden lines.

The single emission line features of Hβ, [O III] and [O I] at $\lambda_{\rm rest}$ = 4861 Å, 5007 Å and 6300 Å were then fitted using a single Gaussian fit, with the velocity and velocity dispersion constrained by the Hα/[N II] values. The [S II] doublet at $\lambda_{\rm rest}$ = 6716/6731 Å was fit using a linear combination of two Gaussians, with velocities and dispersion similarly constrained. Despite the continuum subtraction a local continuum was still defined around these lines when performing the line fitting in order to account for any shift in the continuum shape due to differing levels of reddening over the spatial extent of the BCG (note some subtle reddening is demonstrated in Figure 5.6).

No prior assumption was made about the presence of optical emission lines. The

fitting routine was developed to be robust enough that it effectively picks up emission lines when present, and returns nonsensical values when not. Regions of emission line were isolated by application of a cut in the difference between χ^2 values returned by the Gaussian fit, and a linear fit, to the data.

5.7.2 Emission Line Kinematics

The line-of-sight velocity of the emission line nebulae is given by the Doppler shift of the lines away from the expected observed wavelength given by the redshift of the BCG. Hence all velocities are defined relative to the rest frame stellar velocity of the BCG. The velocity dispersion (or Full Width Half Max; FWHM) of the lines are estimated via the standard deviation, σ_g, of the Gaussian fit, following the relation $\sigma_g = \mathrm{FWHM}/2\sqrt{2\ln 2}$.

Chapter 6

Witnessing the Assembly of Brightest Cluster Galaxies with MUSE - An Investigation into the Kinematics of Merging BCGs

The work in this Chapter is in preparation for publication.

6.1 Overview

In this chapter we explore the stellar mass growth of BCGs. We use wide-field IFU observations, from the Multi Unit Spectroscopic Explorer (MUSE), of 23 cluster cores, selected on exhibiting multiple component BCGs and/or nearby massive companion galaxies in optical imaging of 784 X-ray selected clusters at $z < 0.25$. The line-of-sight stellar kinematics of all cluster galaxies within the MUSE field-of-view are measured and the likelihood of each companion galaxy being dynamically bound to the BCG is determined, with 30 per cent of total cluster galaxies having a high bound probability, $p_{bound} > 0.7$. Estimates are made for the merger timescales and subsequent average merger rates are statistically evaluated. By assuming our MUSE targets are representative of the subsample of 144 clusters from the parent cluster sample, which have massive companions within a projected separation of 20

kpc, we constrain the average stellar mass growth of BCGs since $z = 0.25$ to be between 10 ± 2 and 64 ± 15 per cent, consistent with the typical estimates of 10–20 per cent in the literature. We find that 60 per cent of projected mergers are minor mergers (luminosity ratios greater than 1:4) but that major mergers account for 65 per cent of the BCG stellar mass growth.

6.2 Introduction

The stellar assembly of BCGs due to mergers is a debated topic in cluster galaxy evolution, with a number of conflicting results. Models by De Lucia & Blaizot (2007) found that only 20–30% of the stellar mass of the BCGs have assembled by $z \sim 1$, suggesting significant growth by a factor of ~ 4 via mergers between $z = 1$ and $z = 0$. However, a number of observations suggest more modest mass growth factors of ~ 2 over the same redshift interval (e.g. Lidman et al. 2012, 2013; Burke & Collins 2013), which are more consistent with later models (e.g. Tonini et al. 2012; Laporte et al. 2013; Shankar et al. 2015). However, there are also a number of observational studies which find no evidence for significant mass growth over this time (e.g. Whiley et al. 2008; Collins et al. 2009; Stott et al. 2008, 2010).

Nevertheless, the emerging consensus is that BCGs grow in stellar mass by a factor of ~ 2 since $z < 1$, with observational results (Lidman et al., 2012, 2013; Lin et al., 2013; Burke & Collins, 2013) consistent with model predictions (Tonini et al., 2012; Laporte et al., 2013; Shankar et al., 2015). However, there is some disagreement between the models and observations at low redshift with observational evidence suggesting that the majority of this growth occurs at $z > 0.5$, followed by a decline in the growth rate at lower redshift (Liu et al., 2009, 2015; Lin et al., 2013; Oliva-Altamirano et al., 2014; Inagaki et al., 2015).

As discussed in Chapter 1 the estimation of BCG stellar mass growth can be broadly categorised into: (1) studies statistically comparing BCGs at high and low redshift (e.g. Aragon-Salamanca et al. 1998; Stott et al. 2008, 2010; Lidman et al. 2012), (2) statistical studies using the fraction of BCGs with close companions as a merger proxy (e.g. Edwards & Patton 2012; Burke & Collins 2013; Liu et al. 2009,

2015) and (3) studies using spectroscopy of individual systems to confirm whether companions are dynamically bound and likely to merger (e.g. Jimmy et al. 2013; Edwards et al. 2016). In this Chapter we attempt, for the first time, to combine the second and third of these techniques.

The objective of this Chapter is to study the sample of BCGs, with morphologies consistent with ongoing/future mergers, introduced in Chapter 5. Using wide-field IFU observations we aim to determine the relative stellar velocities of BCGs and nearby companion galaxies and determine the likelihood of the companions being bound to the BCG. By estimating the merger timescales for each galaxy we aim to use a statistical approach to estimate the average merger rate, and the corresponding rate of stellar mass growth, for the BCGs within the wider representative parent cluster sample.

Integral spectroscopy, and specifically the MUSE instrument, provides a powerful tool to study galaxy mergers. In order to understand the dynamics of close companion galaxies, and then compare that with the kinematics of cluster members further from the cluster core, we need spectroscopy of lots of cluster members – which MUSE, with its wide field-of-view, efficiently provides. Further to this, by selection, a number of the BCGs have very close companion galaxies (within a few arcsecs) and therefore a reasonably high spatial resolution is needed to spatially resolve the stellar kinematics of the core where multiple components exist. The 0.2 arsec pixel scale of MUSE makes this possible. Additionally, as MUSE uses an image slicer, it avoids the issue of proximity constraints between the positioning of arms in IFUs which rely on fibres. Long–slit observations on the other hand would be an inefficient way of observing multiple galaxies in the wider field and careful considerations regarding their orientations would be necessary to capture the very nearby multiple components.

It should be stressed that the cores of galaxy clusters are a very dense environment and hence the likelihood of chance alignment of cluster members is quite high. These projection effects mean that the true dynamics between any individual system of galaxies may never be fully determinable through line-of-sight kinematic measurements. However, with a sufficiently large sample of merger–like BCGs a

statistical approach can be adopted in order to minimise said projection effects.

6.3 Results

6.3.1 Stellar Kinematic Maps

The line-of-sight stellar velocities and velocity dispersions are determined as described in Chapter 5 and presented in Figures 6.1–6.23. The figures also include an i-band survey image (from Pan-STARRS 3π in most incidences) showing the full MUSE field-of-view and, where applicable, the GALFIT model and residuals. Each figure also contains a table showing the derived properties of the galaxies (the calculation of which is discussed in subsequent sections). Note that the displayed stellar velocity of companion galaxies in the kinematic maps are often truncated as they exceed the limits on the velocity colourbar. These limits are chosen to emphasise the velocity structure of the BCGs and their closest companions.

In Figures 6.1–6.23 it appears that in some of the stellar velocity dispersion maps that the dispersion is at a minimum towards to the BCG core and increases at larger radii. An increasing velocity dispersion with respect to radius is expected and observed in elliptical galaxies (Cappellari et al., 2006), in agreement with these data. Although it should be stressed that the selection criteria means the broadening of lines due to the supposition of separate galaxies is common, making a quantitative analysis of this observation impractical. The velocity dispersion of most of the BCGs, whilst showing an increase at larger radii, tend to only increase to $\sim 400 - 500$ $\mathrm{km\,s^{-1}}$ (compared to typical values of $\sim 300 - 400$ $\mathrm{km\,s^{-1}}$ in the core). As the median (mean) velocity dispersions for the clusters are 635 $\mathrm{km\,s^{-1}}$ (647 $\mathrm{km\,s^{-1}}$), it is likely that these stars are still bound to the BCGs, as opposed to being stars of the ICL. It should also be noted however that whilst the Voronoi binning provides bins of approximately equal minimum S/N in the overall spectra, the absorption features at higher radii are much weaker and so the line fitting is more uncertain.

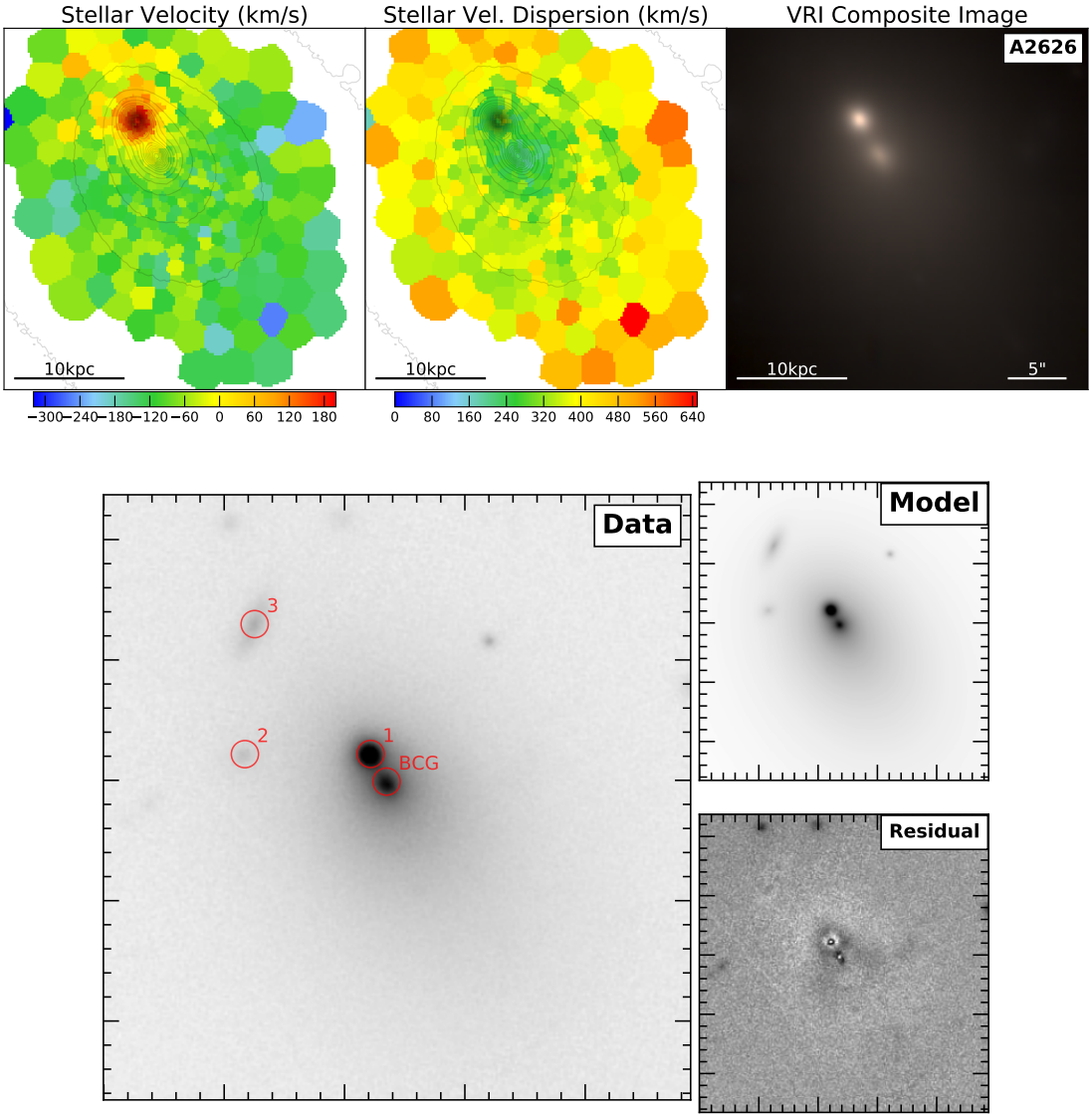

ID	Separation (kpc)	Velocity ($\mathrm{km\,s^{-1}}$)	Vel. Disp ($\mathrm{km\,s^{-1}}$)	Flux (±0.1 mag)	L_{BCG}/L_{comp}	R_e (kpc)	M_{dyn} $\log_{10}(M_\odot)$	P_{bound} (%)	t_{merge} $\log_{10}$(yr)
A2626 BCG	0.0	0 ± 18	273 ± 23	13.3	1.0	15.3	12.13		
A2626 comp 1	3.5	191 ± 11	282 ± 13	16.4	17.2	1.1	11.01	92	8.10
A2626 comp 2	15.6	-831 ± 177	175 ± 246	19.5	295.3	1.4	10.71	0	9.01
A2626 comp 3	22.3	677 ± 143	66 ± 290	18.0	73.1	3.0	10.19	0	9.32

Figure 6.1: A2626: *Top:* MUSE stellar kinematic maps zoomed on the BCG (from left to right: velocity, velocity dispersion and *VRI* composite image of collapsed MUSE cube). *Middle:* PS1/VST/(FORS) *i*-band (*R*–band) image covering full MUSE FOV, on which photometry is performed, with galaxy ID numbers. If used, GALFIT best-fitting model and residuals are given. *Bottom:* Properties of BCG and cluster galaxies (with ID numbers matching those of above figure).

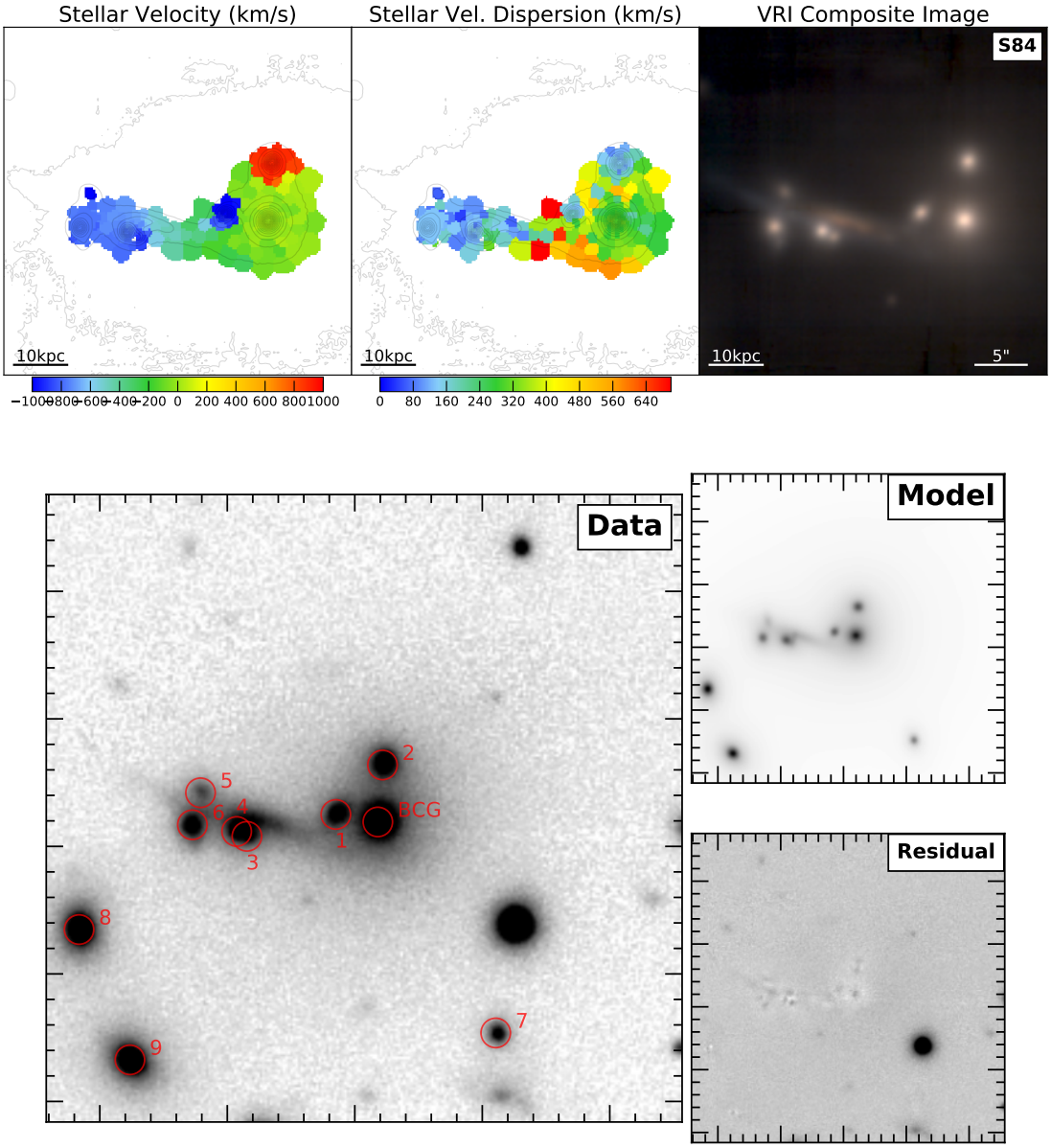

ID	Separation (kpc)	Velocity ($\mathrm{km\,s^{-1}}$)	Vel. Disp ($\mathrm{km\,s^{-1}}$)	Flux (mag)	L_{BCG}/L_{comp}	R_e (kpc)	M_{dyn} $\log_{10}(M_\odot)$	P_{bound} (%)	t_{merge} $\log_{10}$(yr)
S84 BCG	0.0	0 ± 8	352 ± 9	15.0	1.0	11.6	12.22		
S84 comp 1	8.1	-1013 ± 9	183 ± 11	17.3	8.0	4.4	11.24	0	8.57
S84 comp 2	10.8	901 ± 6	166 ± 10	16.3	3.2	8.6	11.44	0	8.63
S84 comp 3	24.9	-886 ± 14	237 ± 19	19.4	57.3	2.6	11.22	0	9.06
S84 comp 4	26.7	-772 ± 7	157 ± 11	16.5	3.8	7.1	11.31	0	9.06
S84 comp 5	34.0	-1663 ± 55	71 ± 65	19.1	43.3	2.2	10.12	0	9.53
S84 comp 6	35.0	-779 ± 70	145 ± 97	17.2	7.5	3.1	10.88	0	9.31
S84 comp 7	45.7	956 ± 76	206 ± 100	18.1	16.6	1.1	10.72	0	9.48
S84 comp 8	60.0	213 ± 100	262 ± 118	16.2	3.0	3.0	11.39	56	9.23
S84 comp 9	64.9	1255 ± 120	290 ± 122	16.1	2.8	3.8	11.57	0	9.37

Figure 6.2: S84: Similar to Fig. 6.1.

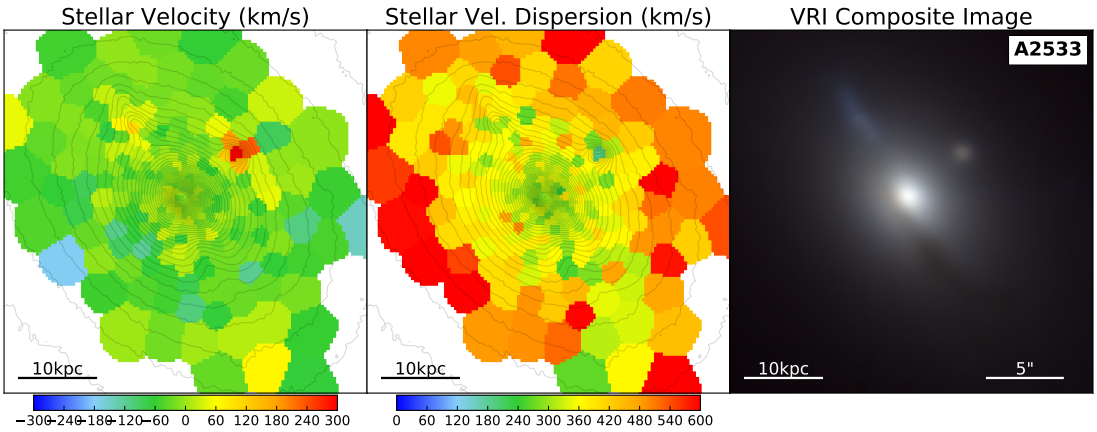

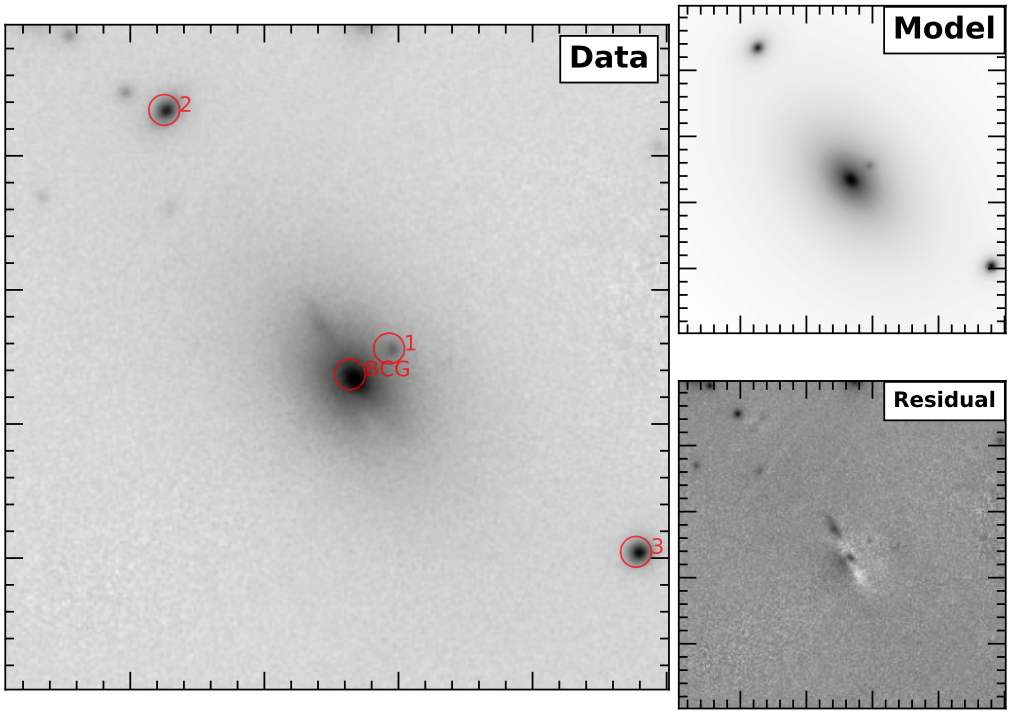

ID	Separation (kpc)	Velocity ($\mathrm{km\,s^{-1}}$)	Vel. Disp ($\mathrm{km\,s^{-1}}$)	Flux (mag)	L_{BCG}/L_{comp}	R_e (kpc)	M_{dyn} $\log_{10}(M_\odot)$	P_{bound} (%)	t_{merge} $\log_{10}$(yr)
A2533 BCG	0.0	0 ± 11	363 ± 15	14.3	1.0	20.8	12.50		
A2533 comp 1	8.6	355 ± 8	207 ± 7	19.1	90.9	2.8	11.14	84	8.62
A2533 comp 2	59.3	1115 ± 32	119 ± 48	17.5	19.8	2.9	10.68	0	9.60
A2533 comp 3	61.8	-532 ± 40	197 ± 59	17.9	27.9	1.2	10.72	0	9.60

Figure 6.3: A2533: Similar to Fig. 6.1.

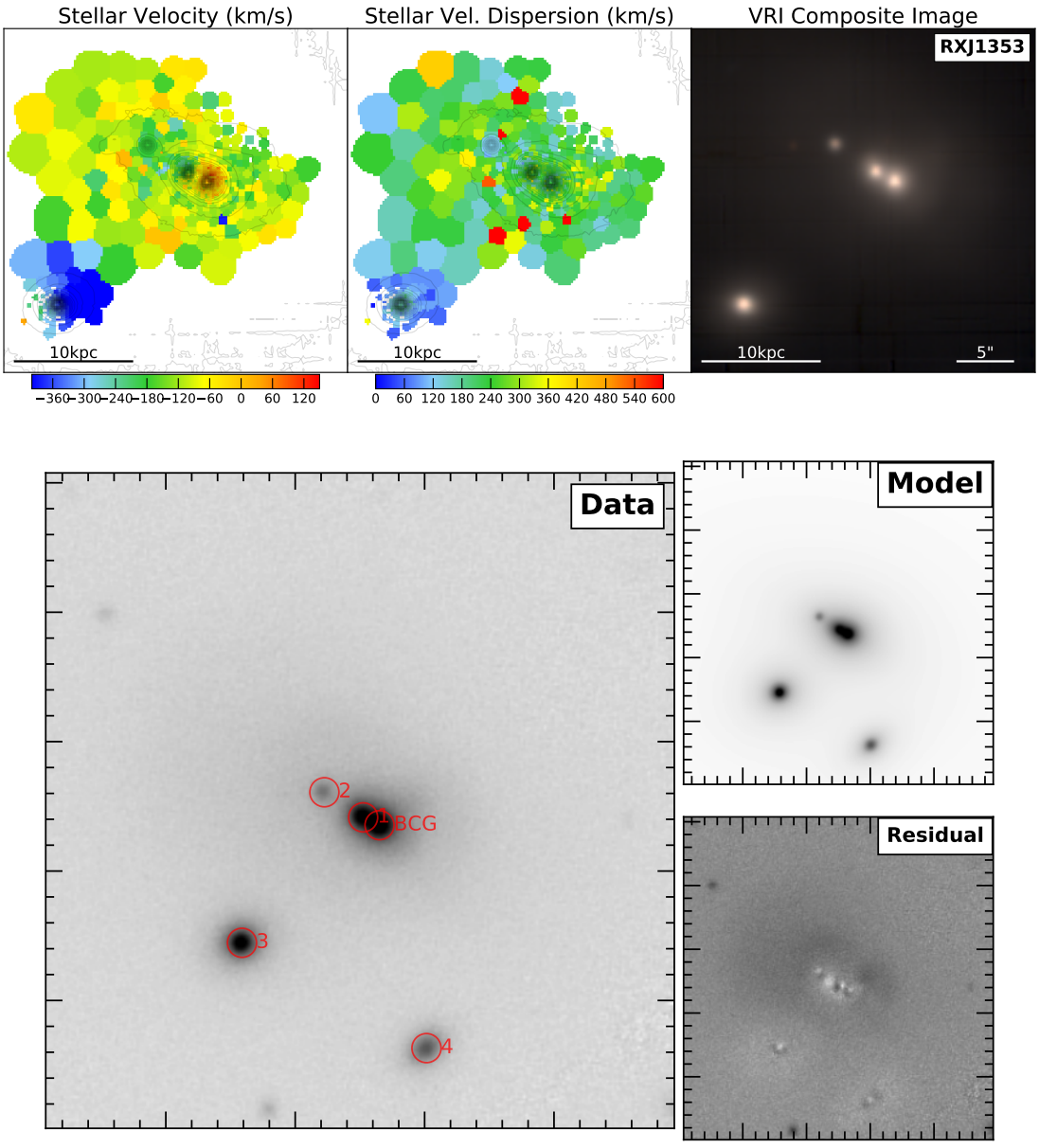

ID	Separation (kpc)	Velocity ($\mathrm{km\,s^{-1}}$)	Vel. Disp ($\mathrm{km\,s^{-1}}$)	Flux (mag)	L_{BCG}/L_{comp}	R_e (kpc)	$\log_{10}(M_{dyn})$ $\log_{10}(M_\odot)$	P_{bound} (%)	t_{merge} $\log_{10}$(yr)
RXJ1353 BCG	0.0	0 ± 16	272 ± 19	14.8	1.0	18.1	12.19		
RXJ1353 comp 1	1.7	-129 ± 17	266 ± 20	15.0	1.1	7.3	11.78	96	7.55
RXJ1353 comp 2	5.9	-181 ± 90	100 ± 123	18.3	25.6	0.0	8.22	91	9.17
RXJ1353 comp 3	16.5	-342 ± 10	150 ± 13	15.7	2.2	2.5	10.83	64	9.00
RXJ1353 comp 4	20.8	-148 ± 74	111 ± 92	17.2	8.7	1.5	10.33	85	9.09

Figure 6.4: RXJ1353: Similar to Fig. 6.1.

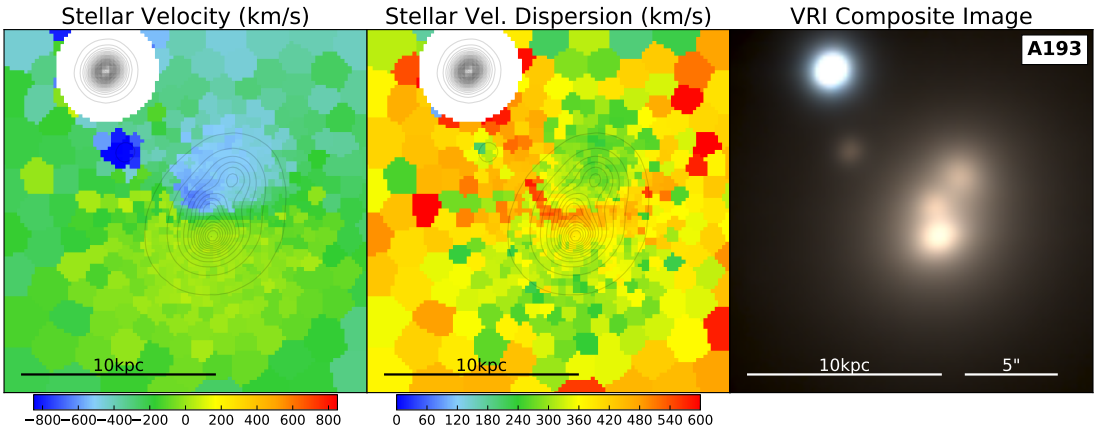

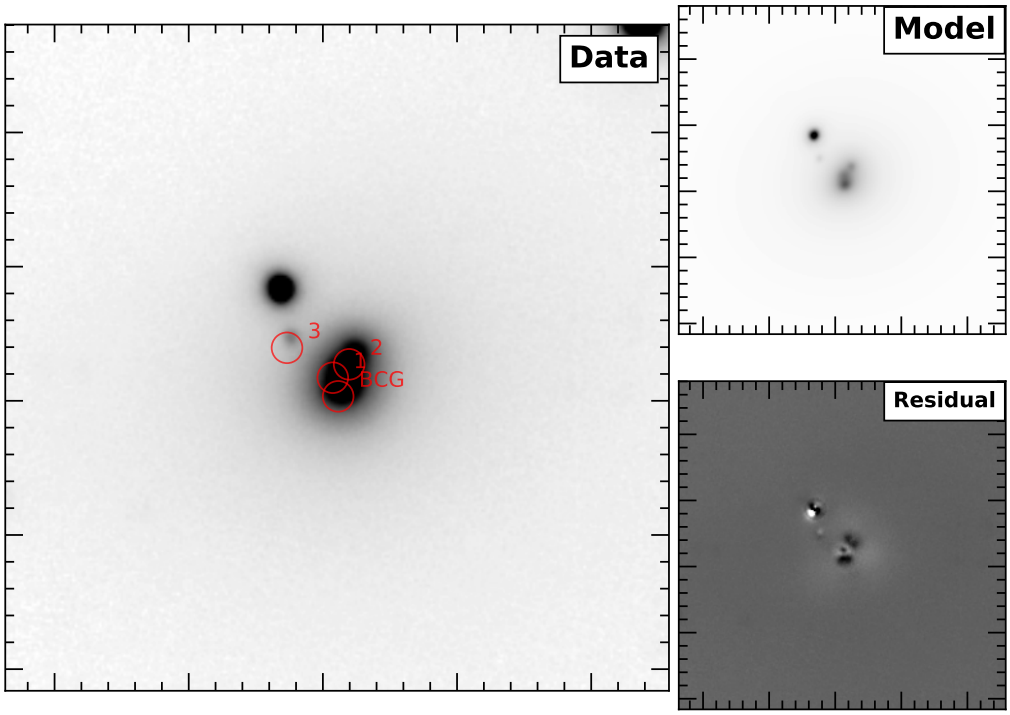

ID	Separation (kpc)	Velocity ($\mathrm{km\,s^{-1}}$)	Vel. Disp ($\mathrm{km\,s^{-1}}$)	Flux (mag)	L_{BCG}/L_{comp}	R_e (kpc)	M_{dyn} $\log_{10}(M_\odot)$	P_{bound} (%)	t_{merge} $\log_{10}$(yr)
A193 BCG	0.0	0 ± 11	345 ± 13	13.5	1.0	8.5	12.07		
A193 comp 1	1.7	-551 ± 12	358 ± 11	15.8	8.4	1.0	11.19	81	7.91
A193 comp 2	3.0	-502 ± 9	330 ± 12	14.3	2.1	9.1	12.07	77	7.88
A193 comp 3	6.2	-803 ± 20	245 ± 18	18.4	90.2	0.0	8.42	0	9.29

Figure 6.5: A193: Similar to Fig. 6.1.

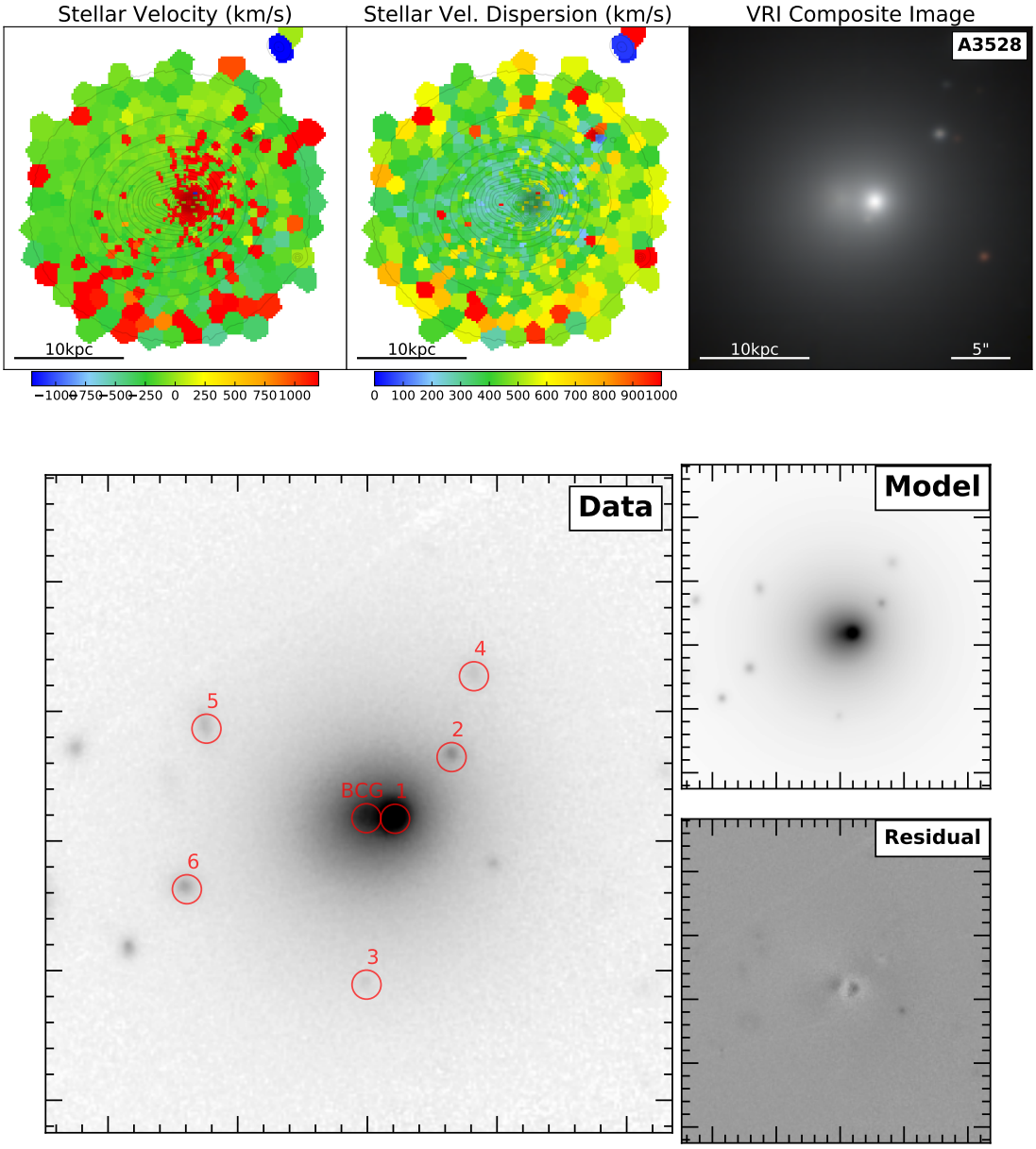

ID	Separation (kpc)	Velocity ($\mathrm{km\,s^{-1}}$)	Vel. Disp ($\mathrm{km\,s^{-1}}$)	Flux (mag)	L_{BCG}/L_{comp}	R_e (kpc)	M_{dyn} $\log_{10}(M_\odot)$	P_{bound} (%)	t_{merge} $\log_{10}$(yr)
A3528 BCG	0.0	0 ± 24	329 ± 25	12.9	1.0	11.6	12.17		
A3528 comp 1	2.9	1310 ± 16	359 ± 15	14.4	4.2	3.1	11.67	0	8.00
A3528 comp 2	10.7	328 ± 44	396 ± 34	18.2	137.8	0.8	11.17	73	8.71
A3528 comp 3	17.0	-1213 ± 73	74 ± 96	19.5	457.9	1.1	9.87	0	9.30
A3528 comp 4	18.2	-1242 ± 92	53 ± 204	19.0	291.2	0.8	9.43	0	9.46
A3528 comp 5	18.7	1999 ± 95	59 ± 105	19.0	293.5	0.6	9.42	0	9.48
A3528 comp 6	19.7	-982 ± 69	70 ± 101	18.7	216.0	0.5	9.47	0	9.48

Figure 6.6: A3528: Similar to Fig. 6.1.

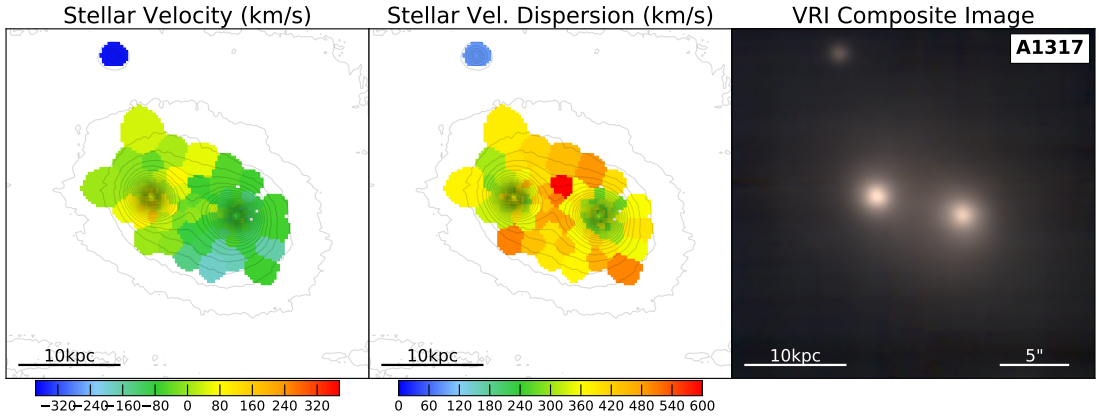

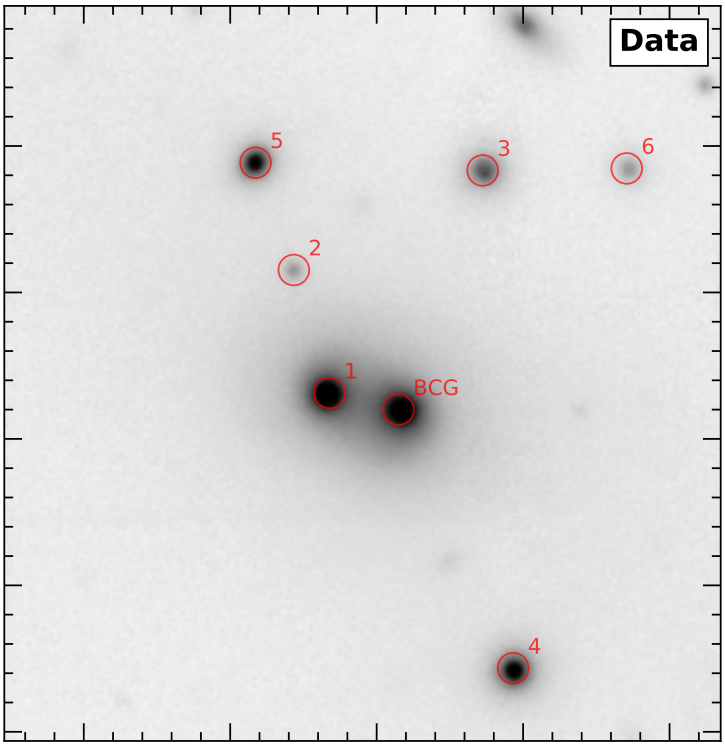

ID	Separation (kpc)	Velocity ($\mathrm{km\,s^{-1}}$)	Vel. Disp ($\mathrm{km\,s^{-1}}$)	Flux (mag)	L_{BCG}/L_{comp}	R_e (kpc)	M_{dyn} $\log_{10}(M_\odot)$	P_{bound} (%)	t_{merge} $\log_{10}$(yr)
A1317 BCG	0.0	0 ± 15	338 ± 17	14.3	1.0	6.8	11.95		
A1317 comp 1	8.1	121 ± 16	370 ± 18	14.8	1.6	4.3	11.84	91	8.23
A1317 comp 2	20.0	-291 ± 203	97 ± 266	17.9	27.5	2.8	10.49	51	9.02
A1317 comp 3	29.1	101 ± 296	143 ± 413	17.0	12.6	2.0	10.68	84	9.13
A1317 comp 4	32.5	-816 ± 472	251 ± 622	16.2	6.1	2.0	11.17	0	9.19
A1317 comp 5	32.7	190 ± 587	327 ± 707	16.4	7.3	2.2	11.43	63	8.96
A1317 comp 6	38.1	524 ± 212	97 ± 250	18.5	47.3	1.5	10.22	0	9.55

Figure 6.7: A1317: Similar to Fig. 6.1.

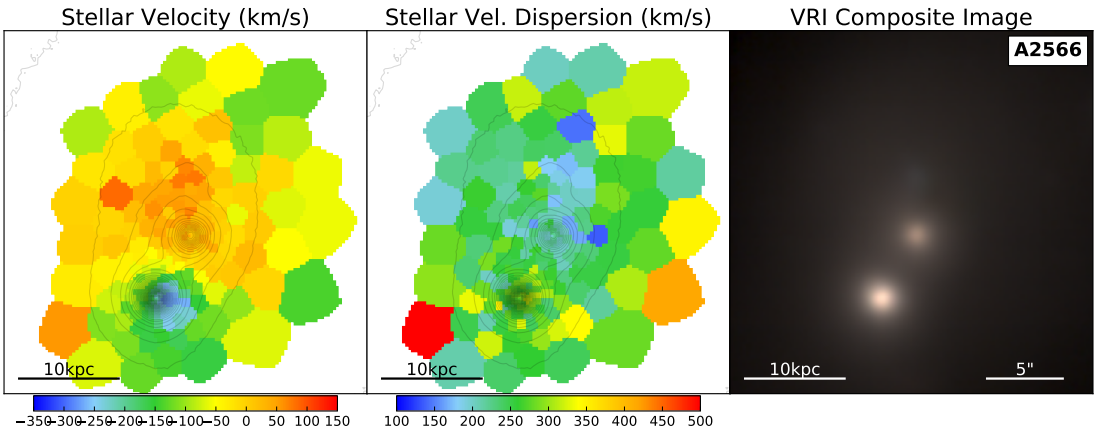

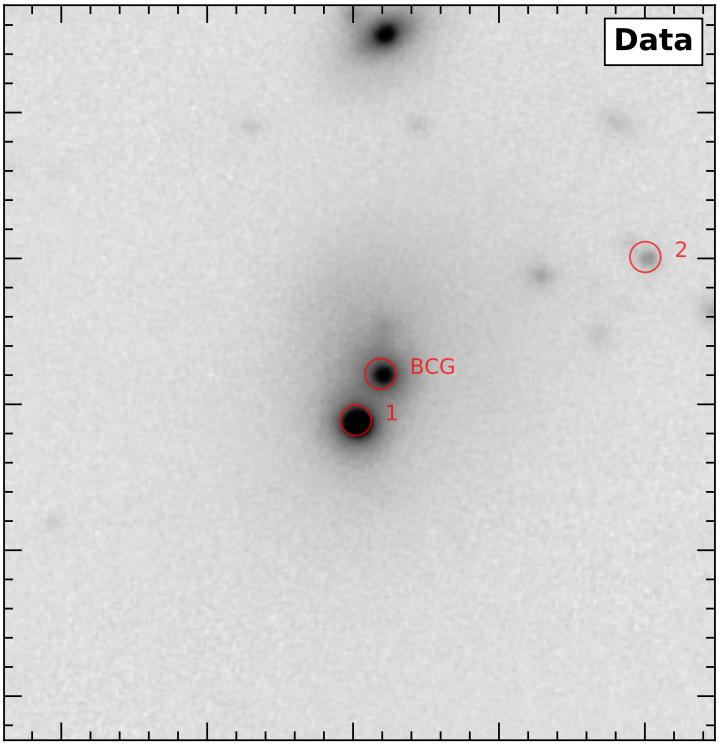

ID	Separation (kpc)	Velocity ($\mathrm{km\,s^{-1}}$)	Vel. Disp ($\mathrm{km\,s^{-1}}$)	Flux (mag)	L_{BCG}/L_{comp}	R_e (kpc)	M_{dyn} $\log_{10}(M_\odot)$	P_{bound} (%)	t_{merge} $\log_{10}$(yr)
A2566 BCG	0.0	0 ± 8	245 ± 11	15.5	1.0	7.0	11.69		
A2566 comp 1	6.8	-217 ± 9	308 ± 10	15.4	0.9	5.4	11.78	76	8.17
A2566 comp 2	37.7	-910 ± 29	74 ± 38	19.7	45.7	1.4	9.96	0	9.62

Figure 6.8: A2566: Similar to Fig. 6.1.

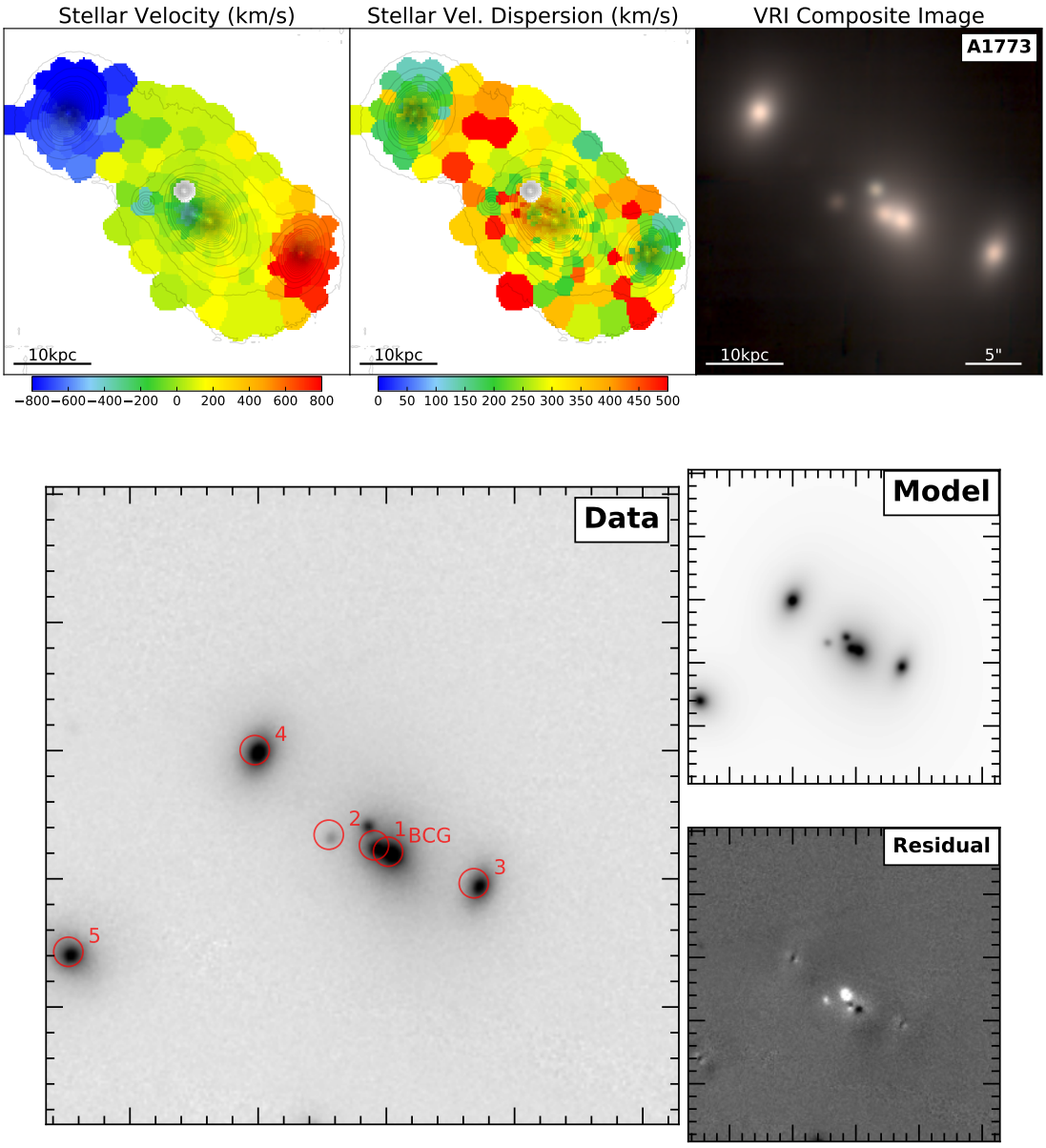

ID	Separation (kpc)	Velocity ($\mathrm{km\,s^{-1}}$)	Vel. Disp ($\mathrm{km\,s^{-1}}$)	Flux (mag)	L_{BCG}/L_{comp}	R_e (kpc)	M_{dyn} $\log_{10}(M_\odot)$	P_{bound} (%)	t_{merge} $\log_{10}$(yr)
A1773 BCG	0.0	0 ± 13	368 ± 14	14.4	1.0	14.1	12.35		
A1773 comp 1	2.1	-337 ± 16	372 ± 17	16.1	4.5	4.4	11.86	91	7.80
A1773 comp 2	8.6	-418 ± 10	227 ± 9	18.4	36.9	0.8	10.71	76	8.75
A1773 comp 3	12.8	659 ± 10	258 ± 13	16.1	4.7	2.8	11.34	38	8.73
A1773 comp 4	23.4	-815 ± 9	263 ± 11	15.5	2.6	3.8	11.49	0	8.95
A1773 comp 5	46.8	-553 ± 46	186 ± 54	15.6	2.9	4.0	11.21	0	9.34

Figure 6.9: A1773: Similar to Fig. 6.1.

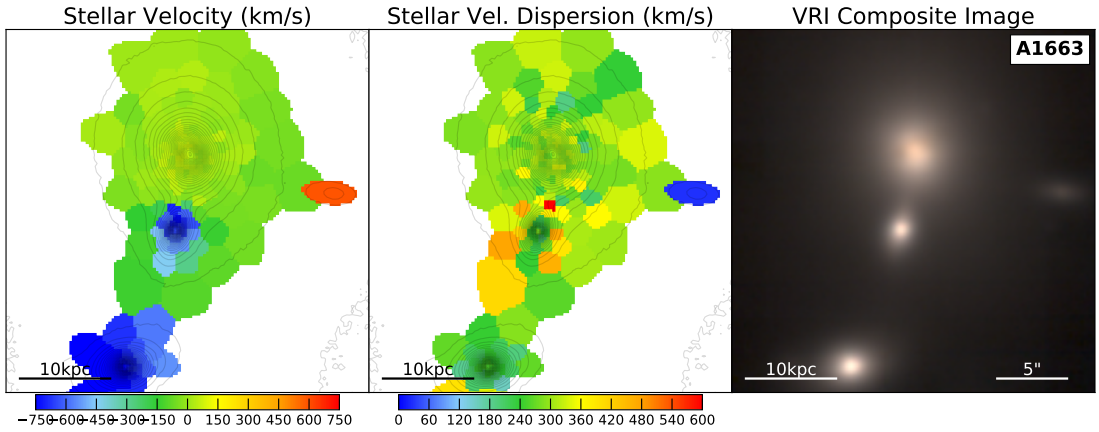

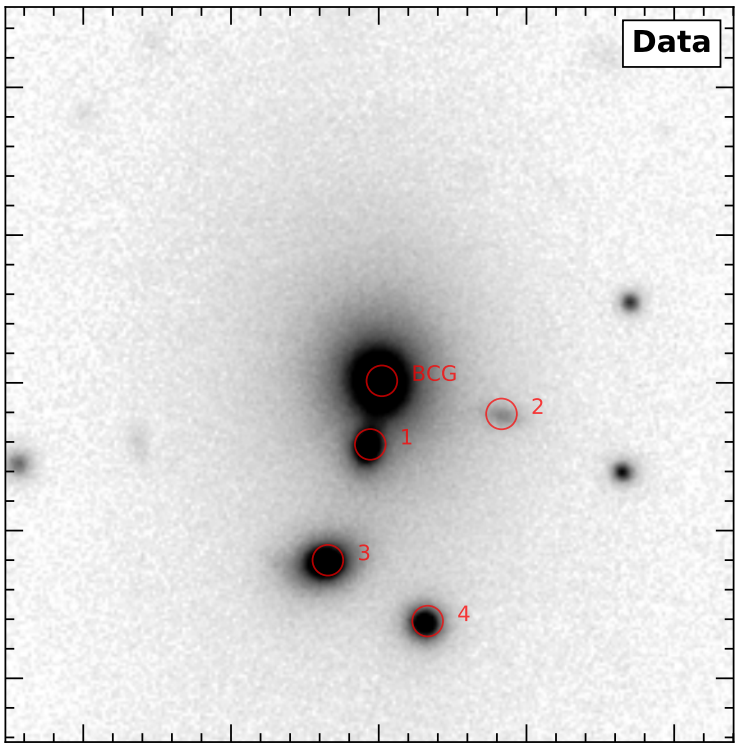

ID	Separation (kpc)	Velocity ($\mathrm{km\,s^{-1}}$)	Vel. Disp ($\mathrm{km\,s^{-1}}$)	Flux (mag)	L_{BCG}/L_{comp}	R_e (kpc)	M_{dyn} $\log_{10}(M_\odot)$	P_{bound} (%)	t_{merge} $\log_{10}$(yr)
A1663 BCG	0.0	0 ± 11	339 ± 12	14.4	1.0	7.6	12.01		
A1663 comp 1	8.5	-691 ± 10	253 ± 13	16.6	7.8	2.1	11.19	0	8.60
A1663 comp 2	16.3	565 ± 388	32 ± 151	17.7	22.0	4.5	9.74	0	9.32
A1663 comp 3	24.5	-753 ± 8	268 ± 10	15.7	3.5	4.0	11.52	0	8.96
A1663 comp 4	32.0	-401 ± 71	192 ± 91	17.0	11.3	2.1	10.95	0	9.25

Figure 6.10: A1663: Similar to Fig. 6.1.

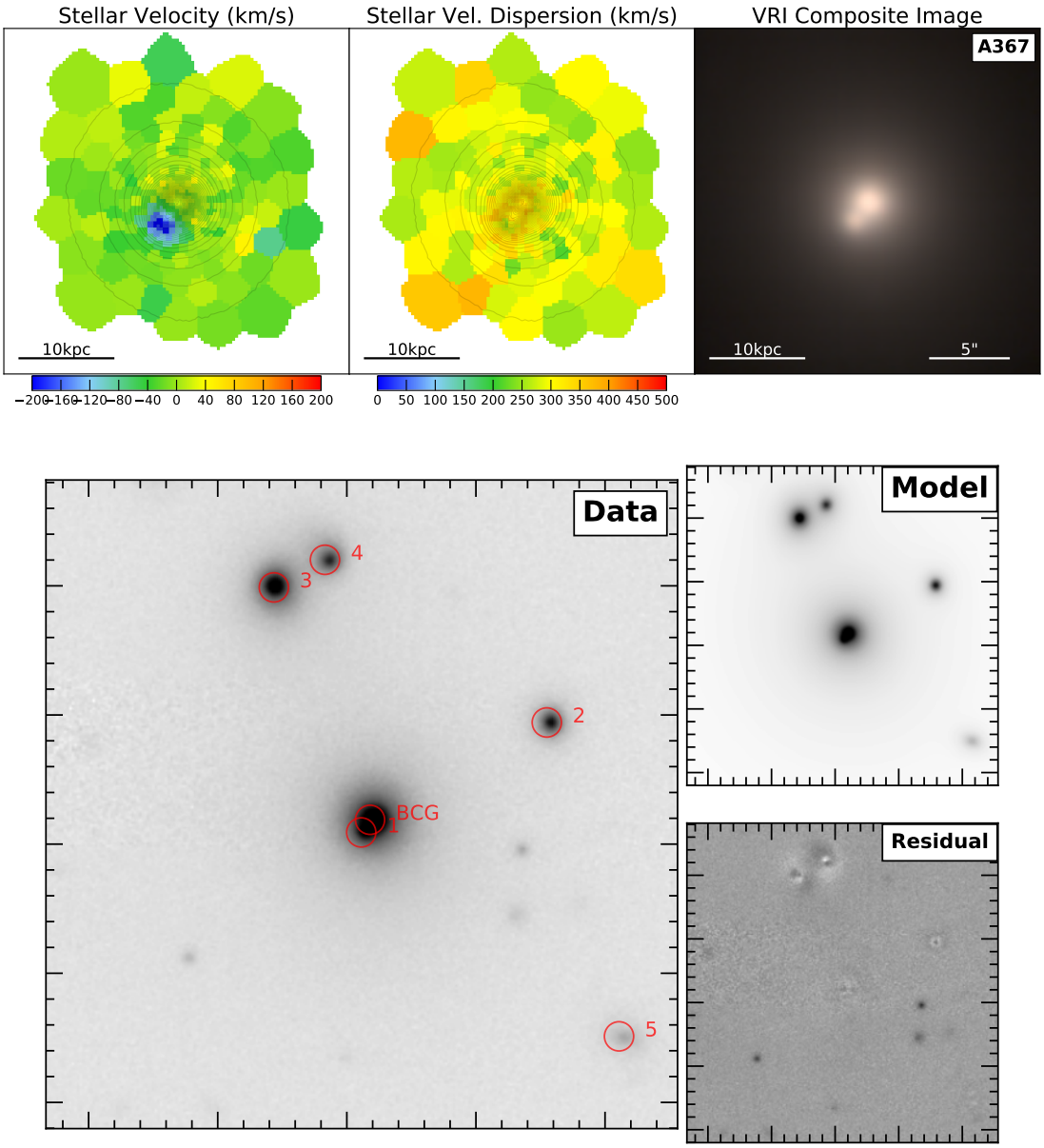

ID	Separation (kpc)	Velocity ($\mathrm{km\,s^{-1}}$)	Vel. Disp ($\mathrm{km\,s^{-1}}$)	Flux (mag)	L_{BCG}/L_{comp}	R_e (kpc)	M_{dyn} $\log_{10}(M_\odot)$	P_{bound} (%)	t_{merge} $\log_{10}$(yr)
A367 BCG	0.0	0 ± 9	406 ± 10	14.2	1.0	18.8	12.56		
A367 comp 1	2.5	-167 ± 12	281 ± 13	18.1	34.2	0.3	10.45	96	8.13
A367 comp 2	32.7	-753 ± 33	174 ± 56	17.4	17.9	0.8	10.46	0	9.41
A367 comp 3	40.7	-1665 ± 48	262 ± 60	15.8	4.2	4.5	11.55	0	9.17
A367 comp 4	42.7	-1867 ± 42	197 ± 51	16.5	8.2	7.1	11.51	0	9.21
A367 comp 5	53.5	197 ± 66	38 ± 34	18.6	54.1	2.4	9.60	78	9.72

Figure 6.11: A367: Similar to Fig. 6.1.

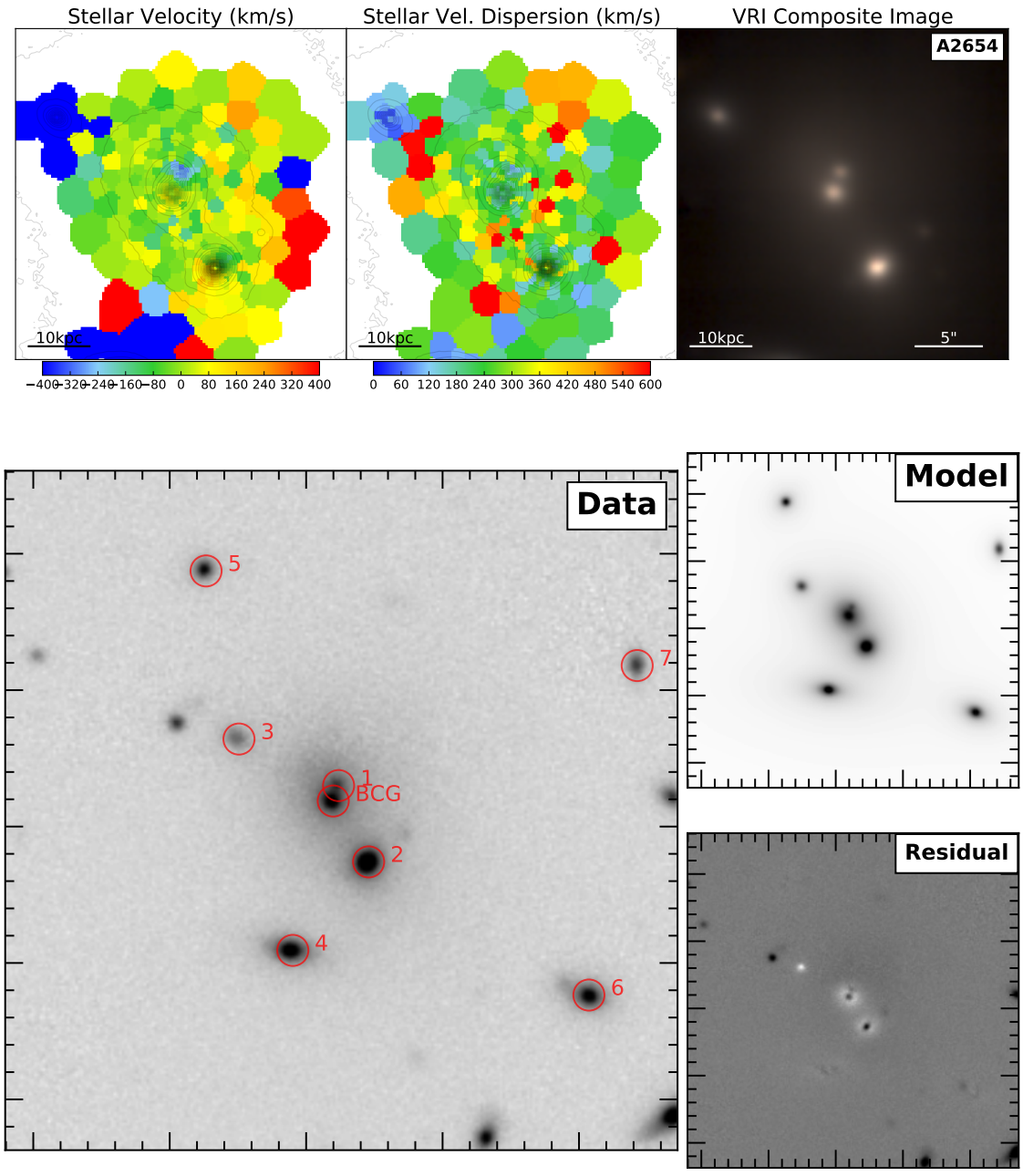

ID	Separation (kpc)	Velocity ($\mathrm{km\,s^{-1}}$)	Vel. Disp ($\mathrm{km\,s^{-1}}$)	Flux (mag)	L_{BCG}/L_{comp}	R_e (kpc)	M_{dyn} $\log_{10}(M_\odot)$	P_{bound} (%)	t_{merge} $\log_{10}$(yr)
A2654 BCG	0.0	0 ± 12	224 ± 16	15.9	1.0	9.1	11.73		
A2654 comp 1	3.3	-263 ± 15	195 ± 17	19.3	22.9	2.2	11.00	82	8.09
A2654 comp 2	14.1	29 ± 17	298 ± 16	16.5	1.8	3.7	11.58	96	8.55
A2654 comp 3	22.5	-1060 ± 17	59 ± 45	18.2	8.3	2.2	9.95	0	9.40
A2654 comp 4	30.9	-1396 ± 10	121 ± 12	17.1	2.9	4.3	10.87	0	9.26
A2654 comp 5	52.5	4 ± 12	169 ± 18	18.6	12.0	1.8	10.78	99	9.36
A2654 comp 6	64.1	-357 ± 11	174 ± 15	17.7	5.3	2.7	10.99	0	9.54
A2654 comp 7	66.5	-1188 ± 11	86 ± 26	18.9	15.8	1.8	10.21	0	9.79

Figure 6.12: A2654: Similar to Fig. 6.1.

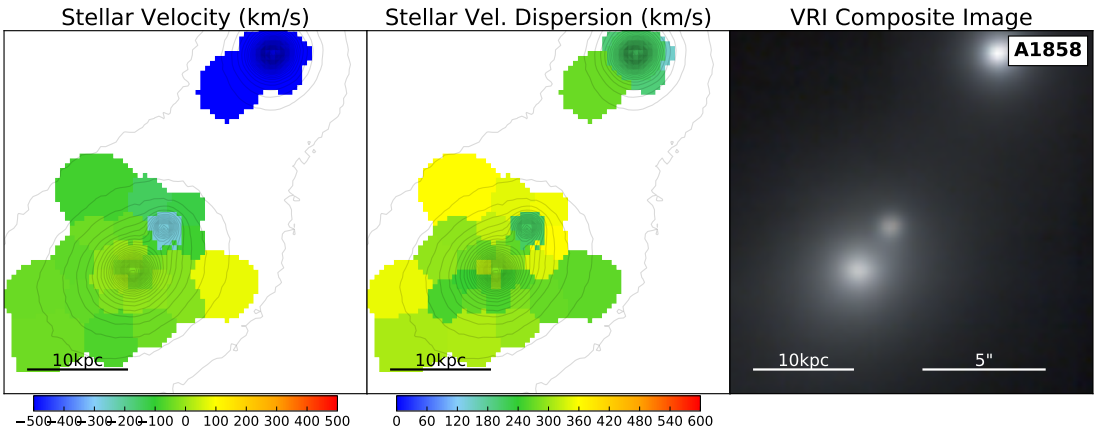

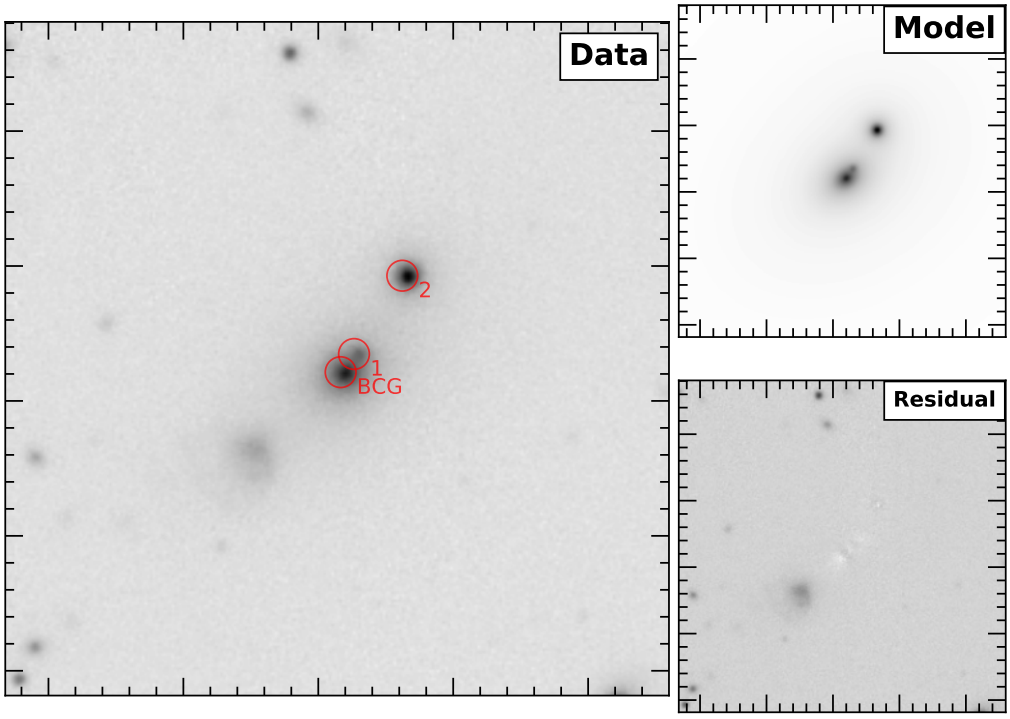

ID	Separation (kpc)	Velocity ($\mathrm{km\,s^{-1}}$)	Vel. Disp ($\mathrm{km\,s^{-1}}$)	Flux (mag)	L_{BCG}/L_{comp}	R_e (kpc)	M_{dyn} $\log_{10}(M_\odot)$	P_{bound} (%)	t_{merge} $\log_{10}$(yr)
A1858 BCG	0.0	0 ± 10	340 ± 11	15.7	1.0	13.0	12.24		
A1858 comp 1	5.1	-242 ± 39	243 ± 32	18.4	12.3	8.4	11.77	89	8.05
A1858 comp 2	26.0	-958 ± 50	236 ± 61	16.7	2.5	6.0	11.59	0	8.97

Figure 6.13: A1858: Similar to Fig. 6.1.

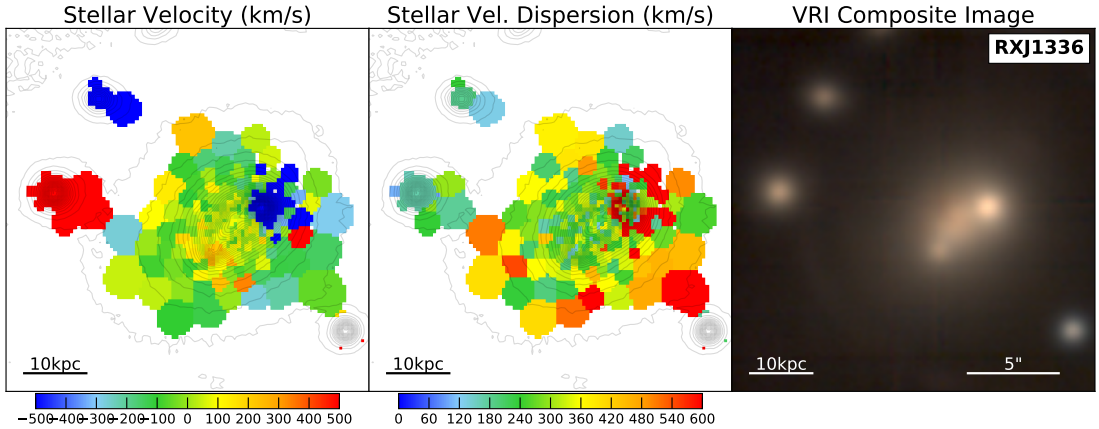

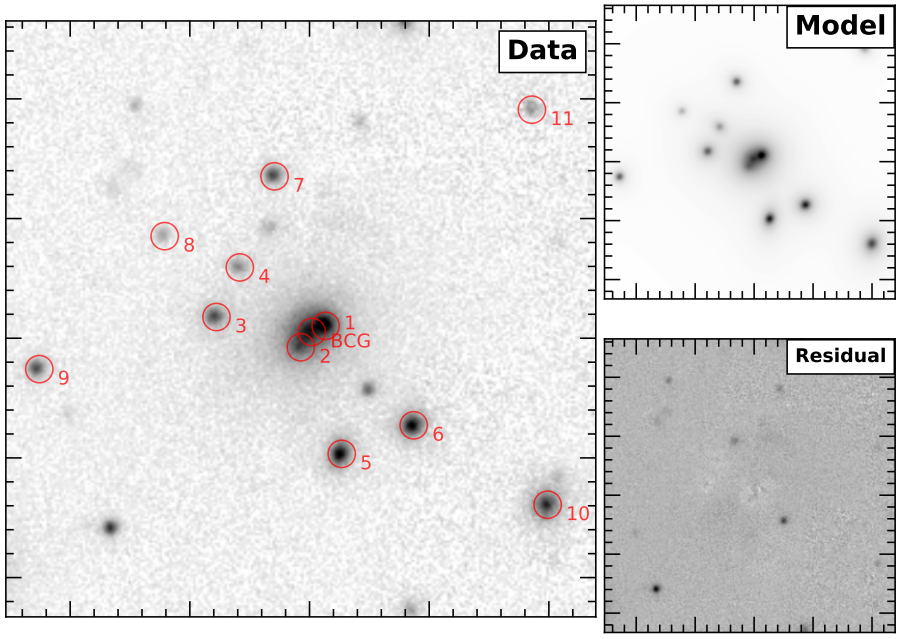

ID	Separation (kpc)	Velocity ($\mathrm{km\,s^{-1}}$)	Vel. Disp ($\mathrm{km\,s^{-1}}$)	Flux (mag)	L_{BCG}/L_{comp}	R_e (kpc)	M_{dyn} $\log_{10}(M_\odot)$	P_{bound} (%)	t_{merge} $\log_{10}$(yr)
RXJ1336 BCG	0.0	0 ± 30	262 ± 29	16.6	1.0	8.0	11.80		
RXJ1336 comp 1	4.6	-1720 ± 36	348 ± 35	17.1	1.5	4.1	11.76	0	8.17
RXJ1336 comp 2	5.7	179 ± 22	252 ± 21	17.8	2.9	6.6	11.69	85	8.13
RXJ1336 comp 3	29.4	573 ± 59	186 ± 76	17.8	2.9	5.6	11.36	0	9.09
RXJ1336 comp 4	29.5	-2569 ± 63	208 ± 56	18.5	5.6	6.9	11.55	0	9.04
RXJ1336 comp 5	38.3	1043 ± 97	358 ± 99	17.4	2.0	5.1	11.88	0	9.05
RXJ1336 comp 6	42.1	1974 ± 84	270 ± 98	17.5	2.3	2.9	11.40	0	9.24
RXJ1336 comp 7	48.8	-64 ± 78	231 ± 94	18.6	6.1	1.3	10.89	85	9.29
RXJ1336 comp 8	53.5	-343 ± 90	14 ± 85	19.5	13.7	1.9	8.69	0	10.15
RXJ1336 comp 9	83.9	158 ± 65	186 ± 84	18.8	7.1	0.8	10.53	6	9.64
RXJ1336 comp 10	89.1	-2243 ± 87	214 ± 113	17.4	2.0	5.2	11.44	0	9.93
RXJ1336 comp 11	95.4	1249 ± 46	161 ± 34	19.6	15.1	1.6	10.69	0	10.49

Figure 6.14: RXJ1336: Similar to Fig. 6.1.

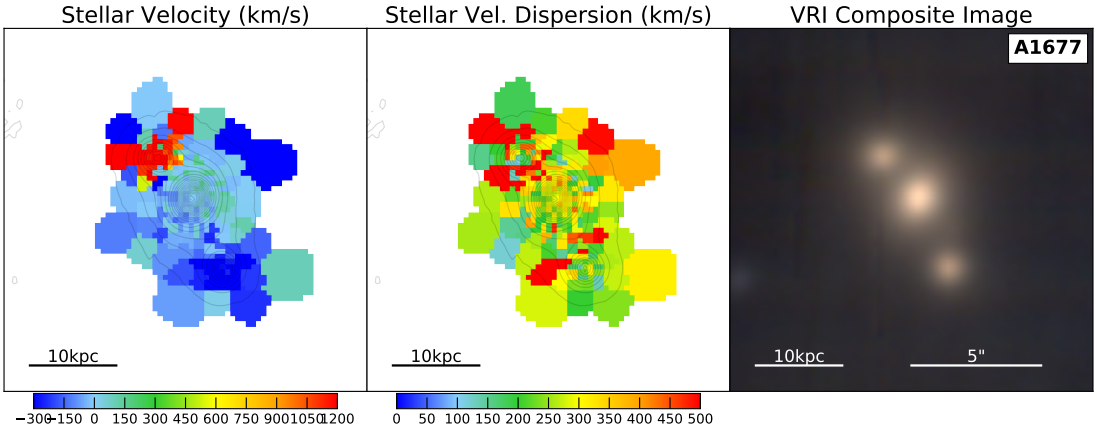

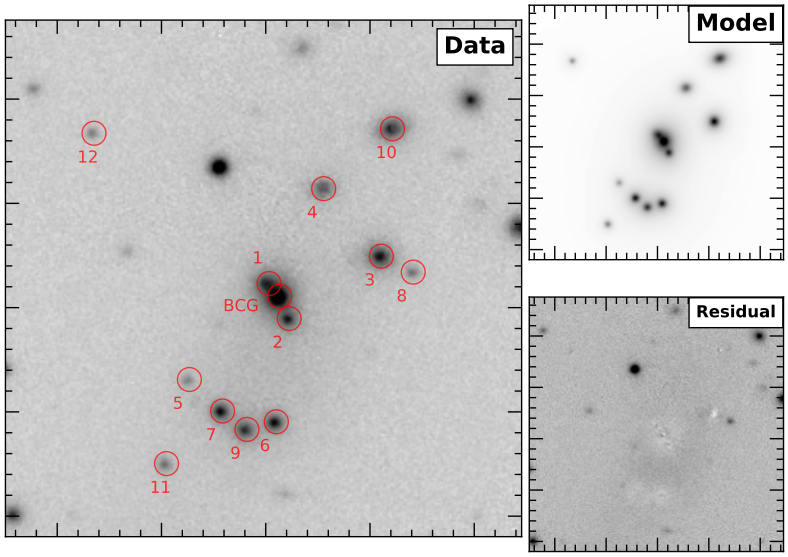

ID	Separation (kpc)	Velocity ($\mathrm{km\,s^{-1}}$)	Vel. Disp ($\mathrm{km\,s^{-1}}$)	Flux (mag)	L_{BCG}/L_{comp}	R_e (kpc)	M_{dyn} $\log_{10}(M_\odot)$	P_{bound} (%)	t_{merge} $\log_{10}$(yr)
A1677 BCG	0.0	0 ± 20	330 ± 22	16.4	1.0	10.0	12.11		
A1677 comp 1	6.0	1219 ± 27	203 ± 28	18.4	6.0	2.5	11.08	0	8.48
A1677 comp 2	8.7	-313 ± 31	251 ± 26	18.2	5.1	2.6	11.28	76	8.59
A1677 comp 3	39.3	0 ± 201	199 ± 272	17.9	3.8	2.1	10.99	99	9.17
A1677 comp 4	41.8	984 ± 237	211 ± 318	18.0	4.3	3.2	11.23	0	9.29
A1677 comp 5	44.3	267 ± 118	174 ± 147	19.8	23.2	0.6	10.30	38	9.43
A1677 comp 6	45.2	44 ± 196	225 ± 240	17.8	3.5	3.3	11.29	93	9.14
A1677 comp 7	46.2	-51 ± 266	285 ± 340	18.0	4.4	1.9	11.27	92	9.16
A1677 comp 8	48.8	-57 ± 187	165 ± 198	20.4	37.9	0.0	8.51	91	10.01
A1677 comp 9	49.4	24 ± 175	214 ± 234	18.2	5.2	2.5	11.13	96	9.23
A1677 comp 10	72.7	278 ± 189	213 ± 234	18.7	8.3	2.3	11.09	0	9.20
A1677 comp 11	72.8	384 ± 152	154 ± 155	19.9	24.2	0.4	10.05	0	10.38
A1677 comp 12	88.9	966 ± 93	75 ± 109	20.0	26.7	0.0	7.72	0	13.28

Figure 6.15: A1677: Similar to Fig. 6.1.

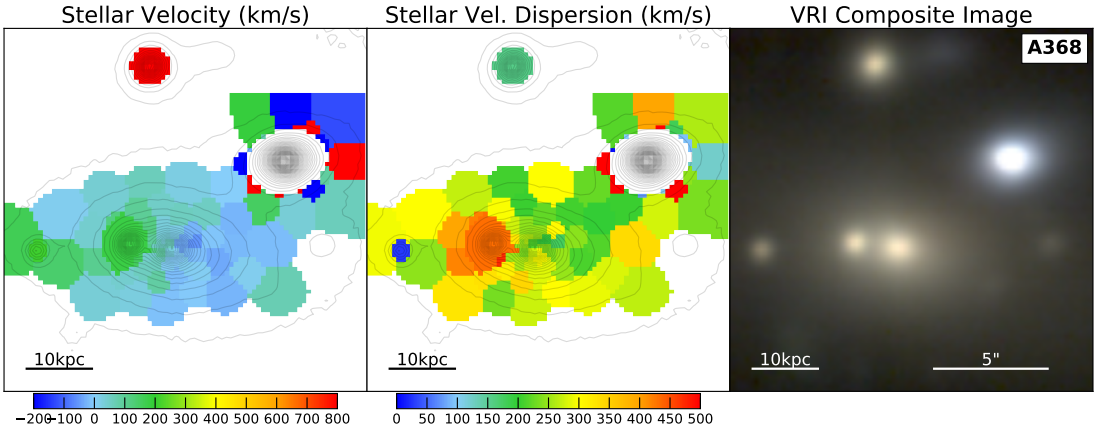

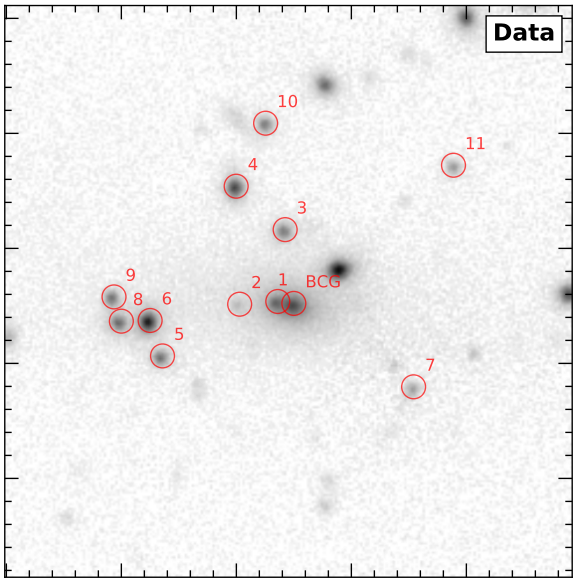

ID	Separation (kpc)	Velocity ($\mathrm{km\,s^{-1}}$)	Vel. Disp ($\mathrm{km\,s^{-1}}$)	Flux (mag)	L_{BCG}/L_{comp}	R_e (kpc)	M_{dyn} $\log_{10}(M_\odot)$	P_{bound} (%)	t_{merge} $\log_{10}$(yr)
A368 BCG	0.0	0 ± 14	307 ± 15	16.5	1.0	18.1	12.30		
A368 comp 1	6.1	149 ± 64	455 ± 58	20.5	39.5	2.2	11.72	93	8.15
A368 comp 2	20.5	182 ± 609	31 ± 437	19.7	19.1	4.7	9.74	84	9.27
A368 comp 3	28.1	891 ± 20	173 ± 27	19.2	11.7	3.9	11.13	0	9.14
A368 comp 4	49.4	1555 ± 23	220 ± 24	18.8	8.4	3.2	11.26	0	9.35
A368 comp 5	53.5	-1891 ± 15	101 ± 15	19.5	15.3	2.9	10.55	0	9.60
A368 comp 6	54.7	2095 ± 31	301 ± 32	18.2	4.5	4.2	11.65	0	9.28
A368 comp 7	55.2	150 ± 10	100 ± 13	20.2	29.0	2.8	10.51	77	9.47
A368 comp 8	65.6	946 ± 20	156 ± 28	19.0	10.0	3.8	11.03	0	9.54
A368 comp 9	68.0	-638 ± 18	145 ± 23	19.5	16.2	2.8	10.84	0	9.61
A368 comp 10	69.0	-494 ± 17	102 ± 25	19.5	16.2	3.1	10.58	0	9.70
A368 comp 11	79.8	-326 ± 15	109 ± 21	20.1	27.9	2.7	10.58	0	9.86

Figure 6.16: A368: Similar to Fig. 6.1.

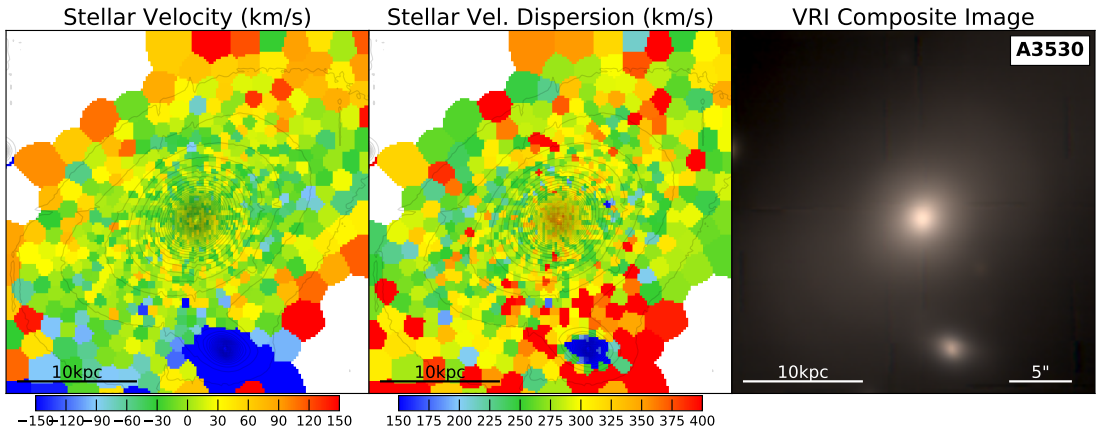

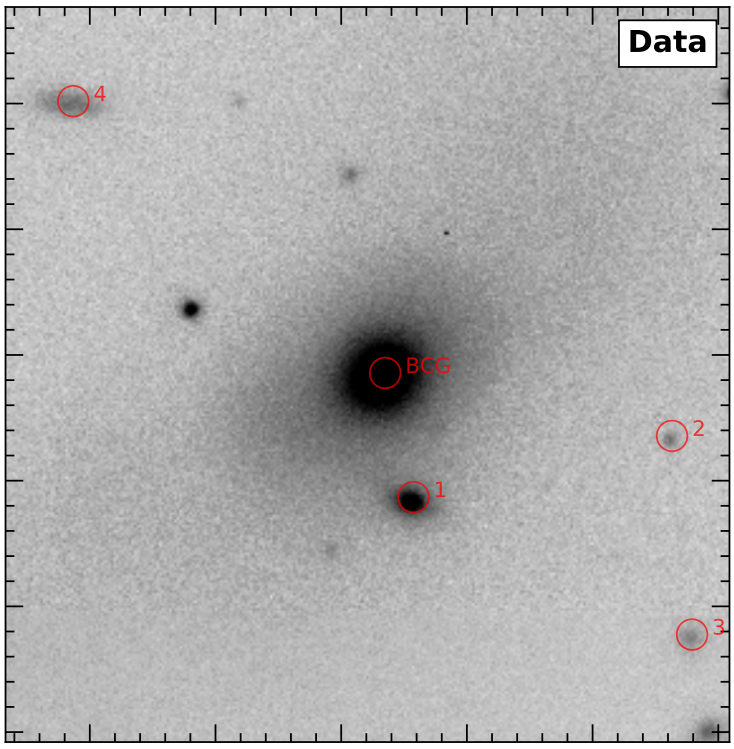

ID	Separation (kpc)	Velocity ($\mathrm{km\,s^{-1}}$)	Vel. Disp ($\mathrm{km\,s^{-1}}$)	Flux (mag)	L_{BCG}/L_{comp}	R_e (kpc)	M_{dyn} $\log_{10}(M_\odot)$	P_{bound} (%)	t_{merge} $\log_{10}$(yr)
A3530 BCG	0.0	0 ± 10	365 ± 11	9.3	1.0	6.2	11.98		
A3530 comp 1	11.1	-647 ± 7	131 ± 11	12.2	14.9	1.6	10.51	0	8.92
A3530 comp 2	25.6	-369 ± 28	62 ± 52	15.6	341.9	0.6	9.47	0	9.60
A3530 comp 3	35.2	798 ± 146	34 ± 409	14.7	151.2	1.1	9.19	0	9.82
A3530 comp 4	36.1	-448 ± 43	76 ± 78	13.5	49.2	1.8	10.07	0	9.56

Figure 6.17: A3530: Similar to Fig. 6.1.

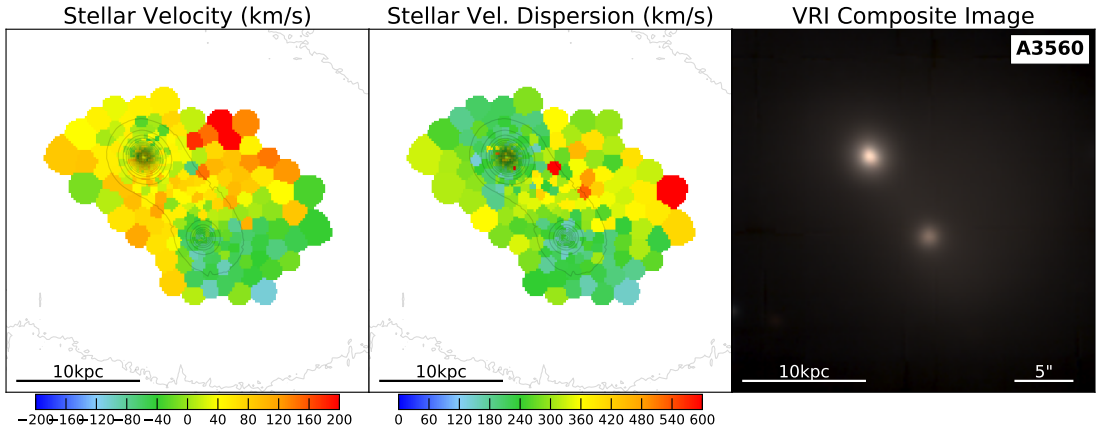

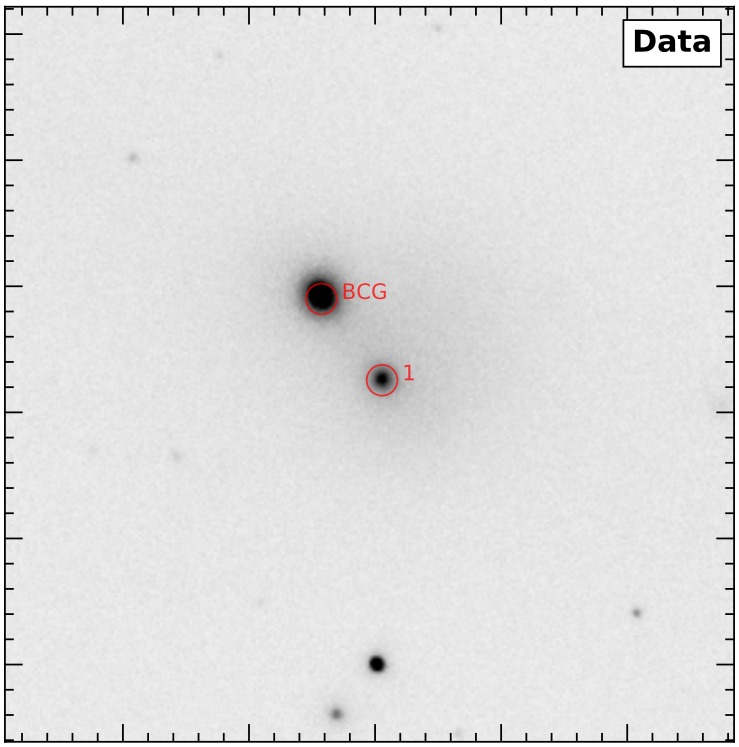

ID	Separation (kpc)	Velocity ($\mathrm{km\,s^{-1}}$)	Vel. Disp ($\mathrm{km\,s^{-1}}$)	Flux (mag)	L_{BCG}/L_{comp}	R_e (kpc)	M_{dyn} $\log_{10}(M_\odot)$	P_{bound} (%)	t_{merge} $\log_{10}$(yr)
A3560 BCG	0.0	0 ± 16	293 ± 20	14.6	1.0	2.9	11.46		
A3560 comp 1	8.0	-66 ± 14	213 ± 17	14.8	1.1	5.1	11.43	91	8.34

Figure 6.18: A3560: Similar to Fig. 6.1.

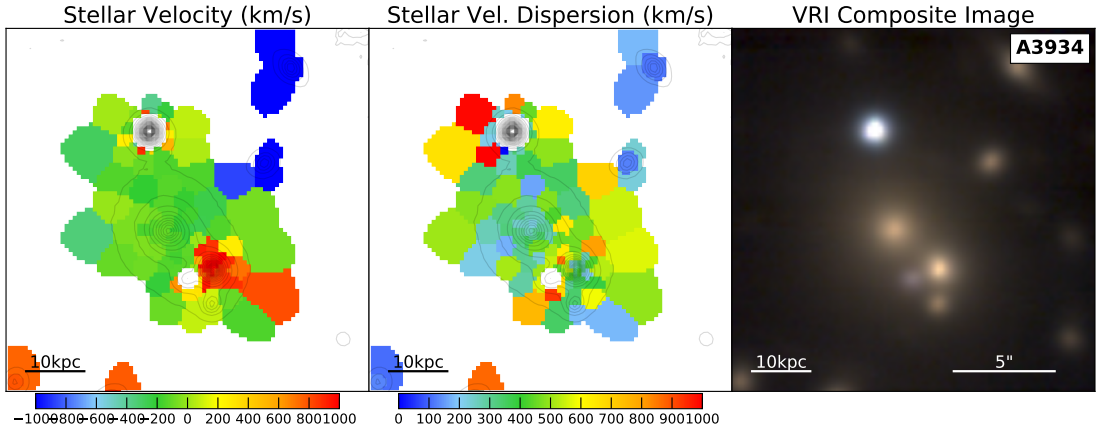

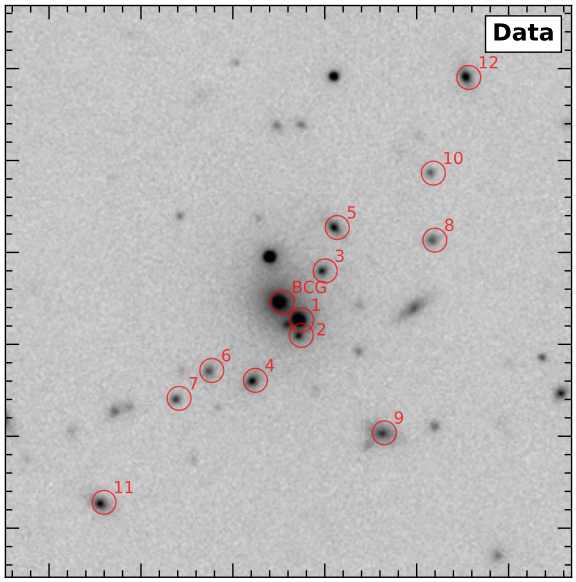

ID	Separation (kpc)	Velocity ($\mathrm{km\,s^{-1}}$)	Vel. Disp ($\mathrm{km\,s^{-1}}$)	Flux (mag)	L_{BCG}/L_{comp}	R_e (kpc)	M_{dyn} $\log_{10}(M_\odot)$	P_{bound} (%)	t_{merge} $\log_{10}$(yr)
A3934 BCG	0.0	0 ± 17	321 ± 18	17.1	1.0	6.3	11.88		
A3934 comp 1	9.9	1083 ± 23	380 ± 27	17.2	1.1	6.1	12.01	0	8.43
A3934 comp 2	14.5	237 ± 21	348 ± 24	20.2	16.7	1.4	11.30	68	8.65
A3934 comp 3	20.0	-1178 ± 50	133 ± 71	19.9	13.7	1.8	10.57	0	9.16
A3934 comp 4	31.2	2839 ± 82	254 ± 130	19.2	6.9	2.8	11.33	0	9.13
A3934 comp 5	35.0	-1041 ± 54	119 ± 70	19.4	8.5	2.3	10.59	0	9.40
A3934 comp 6	37.1	927 ± 44	136 ± 50	20.2	17.4	2.1	10.65	0	9.41
A3934 comp 7	53.3	-242 ± 56	159 ± 63	20.5	23.6	1.5	10.65	0	9.41
A3934 comp 8	62.2	582 ± 271	1046 ± 0	20.3	19.4	2.0	12.40	0	9.11
A3934 comp 9	62.6	1117 ± 53	154 ± 47	18.9	5.3	3.9	11.04	0	9.52
A3934 comp 10	75.0	3509 ± 41	78 ± 59	20.8	31.5	1.6	10.07	0	11.35
A3934 comp 11	101.3	-131 ± 44	163 ± 48	19.3	7.7	2.5	10.90	42	9.35
A3934 comp 12	110.2	-1848 ± 55	174 ± 77	19.3	7.5	2.2	10.89	0	10.59

Figure 6.19: A3934: Similar to Fig. 6.1.

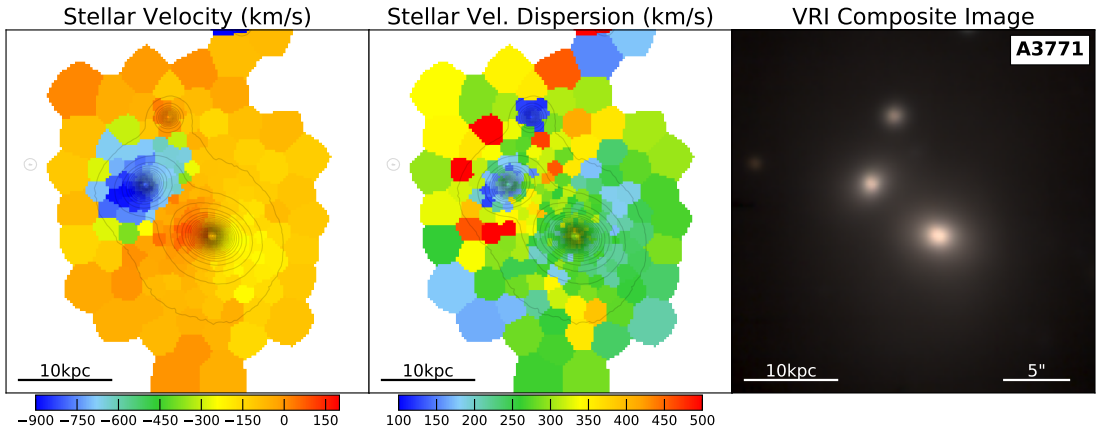

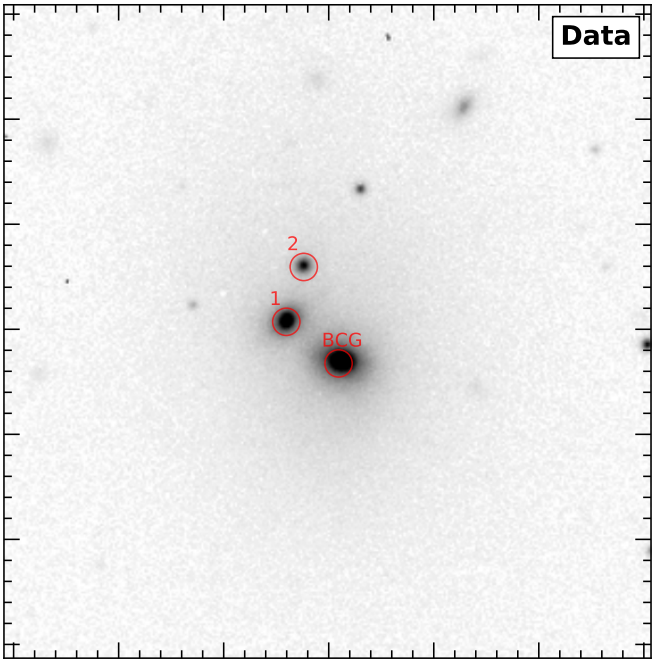

ID	Separation (kpc)	Velocity ($\mathrm{km\,s^{-1}}$)	Vel. Disp ($\mathrm{km\,s^{-1}}$)	Flux (mag)	L_{BCG}/L_{comp}	R_e (kpc)	M_{dyn} $\log_{10}(M_\odot)$	P_{bound} (%)	t_{merge} $\log_{10}$(yr)
A3771 BCG	0.0	0 ± 9	331 ± 10	14.6	1.0	5.7	11.87		
A3771 comp 1	8.9	-699 ± 8	209 ± 11	16.0	3.6	2.3	11.07	0	8.66
A3771 comp 2	13.7	91 ± 6	138 ± 10	16.8	7.7	3.5	10.89	90	8.74

Figure 6.20: A3771: Similar to Fig. 6.1.

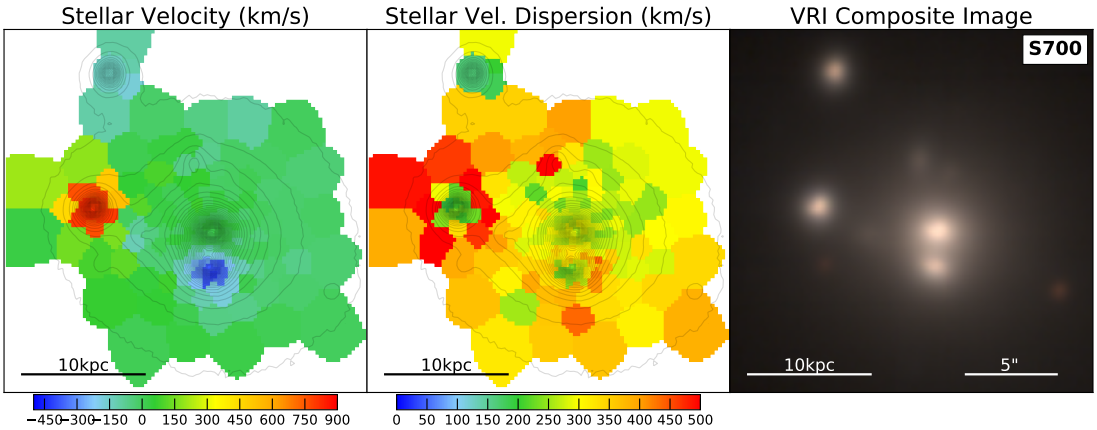

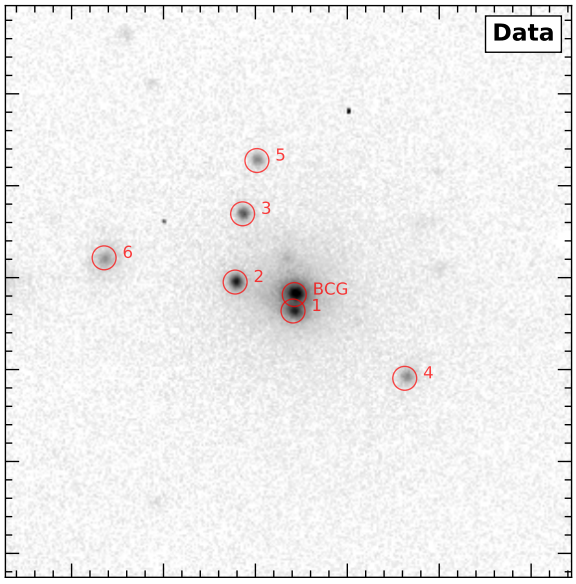

ID	Separation (kpc)	Velocity ($\mathrm{km\,s^{-1}}$)	Vel. Disp ($\mathrm{km\,s^{-1}}$)	Flux (mag)	L_{BCG}/L_{comp}	R_e (kpc)	M_{dyn} $\log_{10}(M_\odot)$	P_{bound} (%)	t_{merge} $\log_{10}$(yr)
S700 BCG	0.0	0 ± 10	304 ± 11	16.0	1.0	3.0	11.51		
S700 comp 1	2.7	-370 ± 13	281 ± 14	17.4	3.4	1.5	11.13	66	8.12
S700 comp 2	9.7	791 ± 9	228 ± 14	17.1	2.5	3.2	11.29	0	8.63
S700 comp 3	15.5	-151 ± 49	165 ± 67	18.7	11.6	1.0	10.49	67	8.91
S700 comp 4	22.4	528 ± 36	95 ± 60	18.9	14.4	1.2	10.11	0	9.35
S700 comp 5	22.4	-632 ± 39	96 ± 46	19.4	21.1	0.9	9.98	0	9.39
S700 comp 6	31.2	-734 ± 39	86 ± 56	18.3	8.0	2.0	10.23	0	9.46

Figure 6.21: S700: Similar to Fig. 6.1.

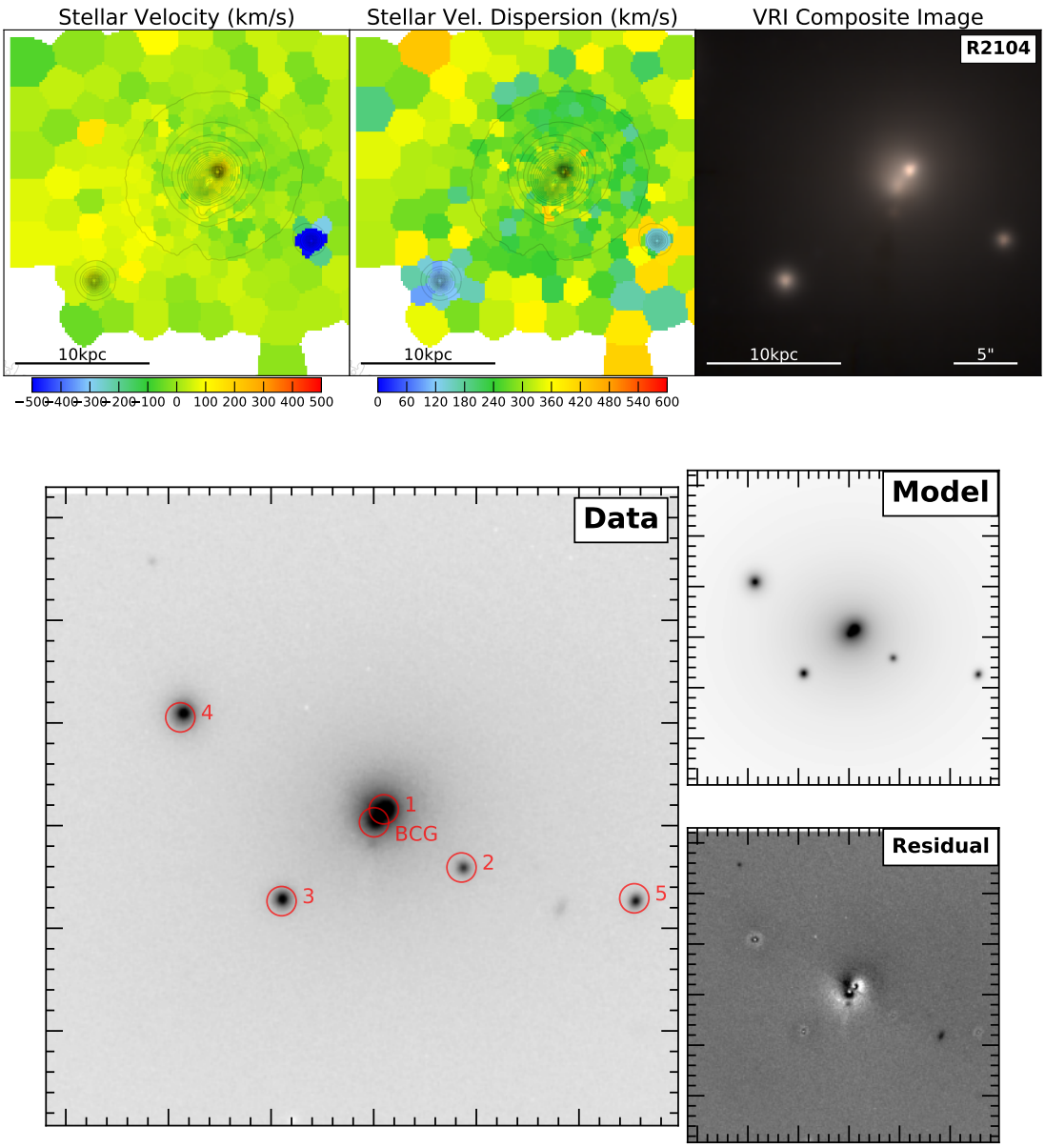

ID	Separation (kpc)	Velocity ($\mathrm{km\,s^{-1}}$)	Vel. Disp ($\mathrm{km\,s^{-1}}$)	Flux (mag)	L_{BCG}/L_{comp}	R_e (kpc)	M_{dyn} $\log_{10}(M_\odot)$	P_{bound} (%)	t_{merge} $\log_{10}$(yr)
R2104 BCG	0.0	0 ± 11	325 ± 13	14.2	1.0	6.3	11.89		
R2104 comp 1	1.5	35 ± 11	290 ± 12	18.7	60.3	1.4	11.13	98	7.70
R2104 comp 2	9.0	-549 ± 100	138 ± 146	18.2	38.9	0.5	10.09	0	8.96
R2104 comp 3	11.0	7 ± 6	118 ± 11	17.6	22.4	0.9	10.15	99	8.87
R2104 comp 4	20.0	-96 ± 103	139 ± 135	16.4	7.3	1.6	10.56	87	9.00
R2104 comp 5	24.7	-115 ± 98	124 ± 123	18.2	38.9	0.6	10.00	82	9.26

Figure 6.22: RXJ2104: Similar to Fig. 6.1. Note the GALFIT convergence is poor here, likely due to the shallow FORS acquisition image.

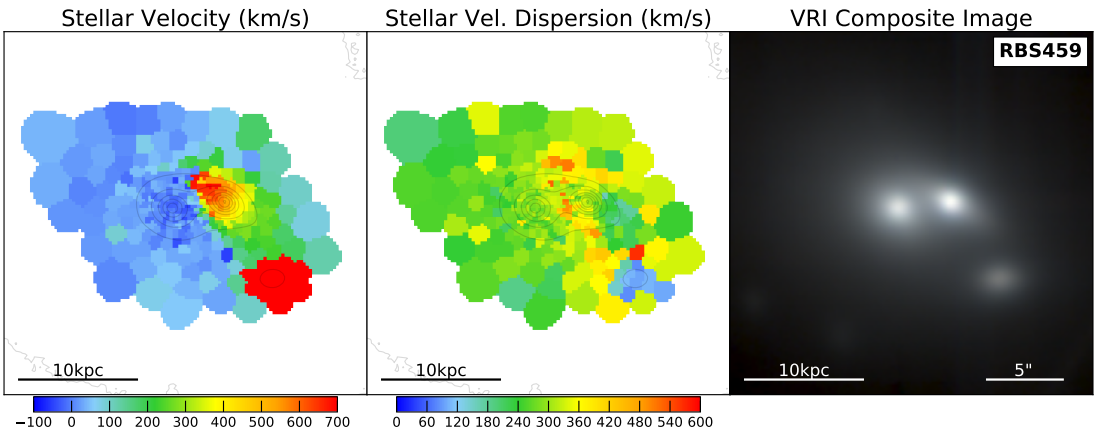

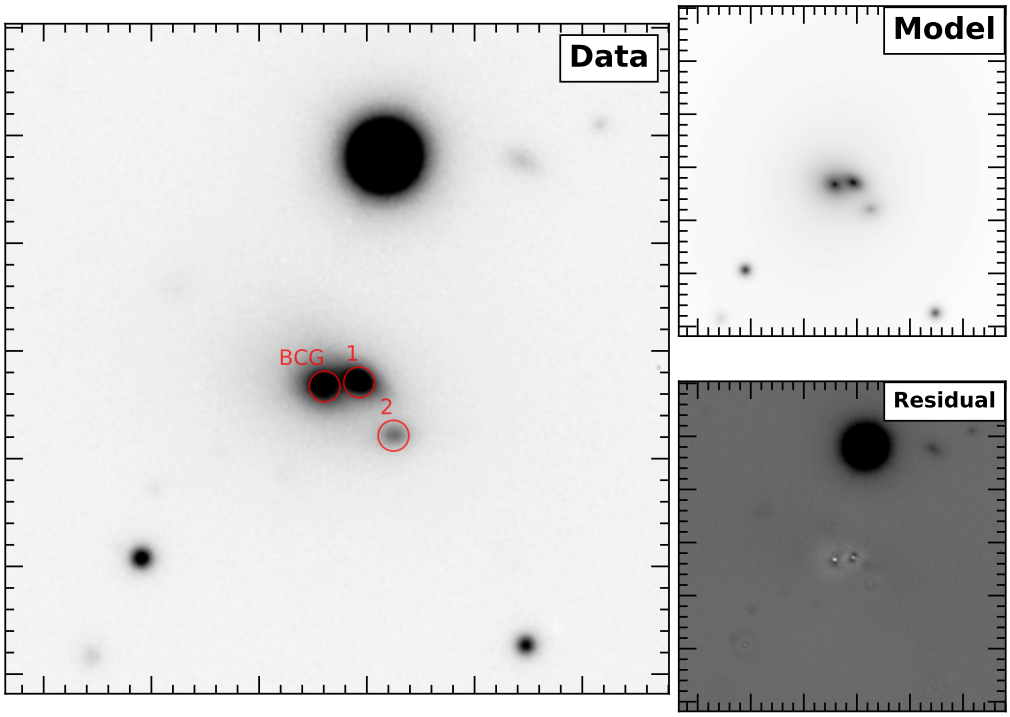

ID	Separation (kpc)	Velocity ($\mathrm{km\,s^{-1}}$)	Vel. Disp ($\mathrm{km\,s^{-1}}$)	Flux (mag)	L_{BCG}/L_{comp}	R_e (kpc)	M_{dyn} $\log_{10}(M_\odot)$	P_{bound} (%)	t_{merge} $\log_{10}$(yr)
RBS459 BCG	0.0	0 ± 12	352 ± 14	16.5	1.0	20.2	12.46		
RBS459 comp 1	4.2	554 ± 11	330 ± 14	18.7	7.3	2.2	11.45	82	8.21
RBS459 comp 2	10.1	996 ± 8	102 ± 12	20.0	24.0	2.4	10.47	0	8.89

Figure 6.23: RBS459: Similar to Fig. 6.1.

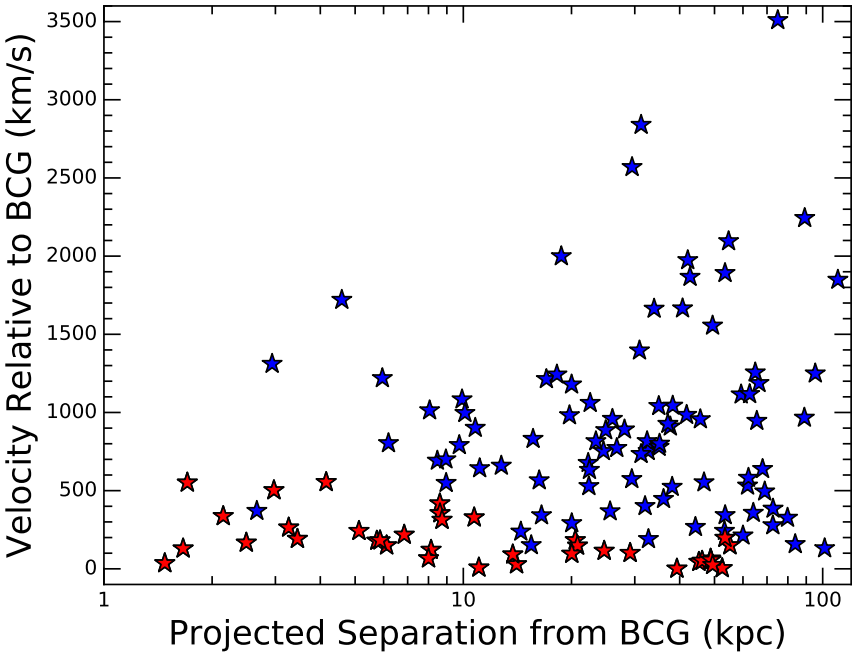

Figure 6.24: Line of sight velocity, with respect to the rest-frame of the BCG, against the projected distance from the BCG. The red stars indicate the subset of galaxies with $P_{bound} > 0.7$ (see §6.3.4)

6.3.2 Velocity vs Separation

The line-of-sight velocity for all cluster members within the MUSE field-of-view are presented against their projected spatial separation from the BCG in Figure 6.24. This plot contains 125 galaxies confirmed to be cluster members across our 23 clusters. It appears from the figure that there is a higher proportion of companion galaxies with small velocity offsets from their BCG ($v \leq 500$ km s^{-1}) at small projected separations ($r_{sep} < 20$ kpc) than at greater separations. We would expect that if our target selection has been effective and we have selected merging BCGs then we would find a high proportion of companion galaxies with small spatial and velocity offsets (indicating they are likely to be dynamically bound).

The companion galaxies are split into two samples – those within a projected radius of 20 kpc from the BCG, and those further away – and their relative distributions are presented in the histograms in Figure 6.25. The figure confirms an enhanced fraction of galaxies with small velocity offsets in the $r < 20$ kpc sample

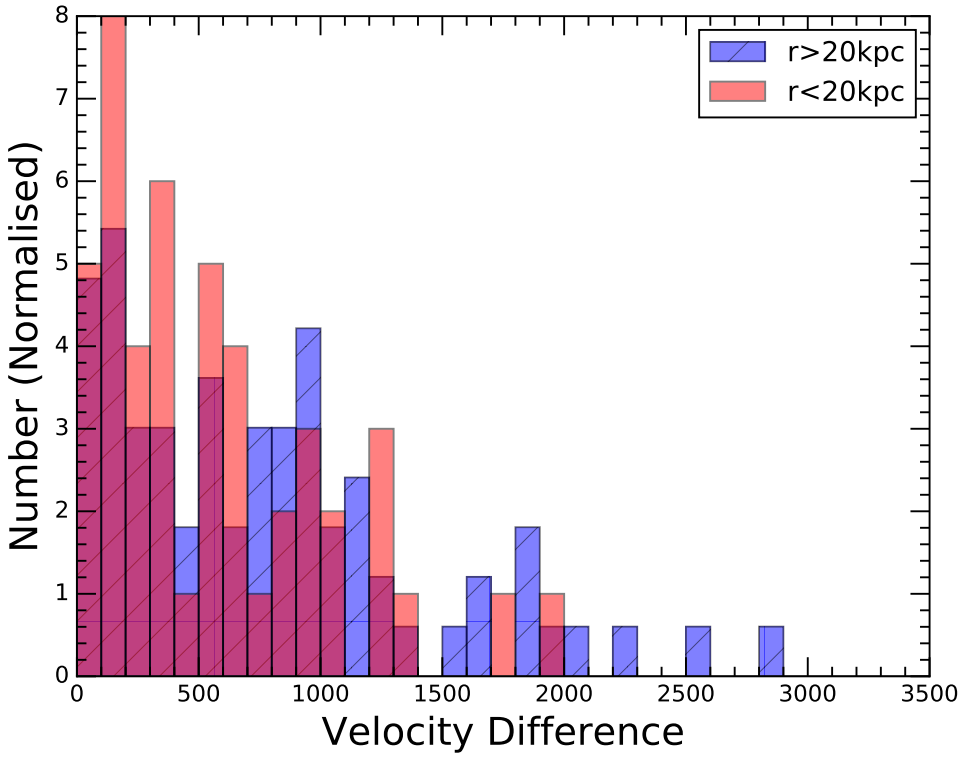

Figure 6.25: Histograms of the line-of-sight velocity, with respect to the rest-frame of the BCG, of galaxies within a projected radius of 20 kpc from the BCG (red) and of galaxies outside of 20 kpc (blue). The total numbers are normalised to be equal across the two subsamples.

than the $r > 20$ kpc sample. The set of $r > 20$ kpc galaxies appear to exhibit a broader distribution of velocities than the close companion galaxies, with a mean velocity of 560 $\mathrm{km\,s^{-1}}$, and a standard deviation in their distribution of 460 $\mathrm{km\,s^{-1}}$, for the $r < 20$ kpc galaxies, compared to a mean and standard deviation of 810 $\mathrm{km\,s^{-1}}$ and 700 $\mathrm{km\,s^{-1}}$ respectively for the $r > 20$ kpc galaxies. The cumulative fraction distribution in Figure 6.26 shows that for the $r < 20$ kpc sample, ~ 50 per cent have $v < 300$ $\mathrm{km\,s^{-1}}$, whereas for the $r > 20$ kpc sample, the 50 per cent mark occurs at $v \sim 700$ $\mathrm{km\,s^{-1}}$.

6.3.3 Bound Fraction: A Simple Statistical Approach

In this section we utilise a simple statistical approach to determine the effectiveness of our target selection in identifying BCG mergers, that is BCGs which have a likely bound companion. In order to do this we must define some conditions for boundedness. The stars within a BCG are, by definition, bound to it and experience the same potential as any external galaxy. So the velocity and radial distance of the stars in a BCG places constraints on the likely values of the critical velocity and separation radius, v_{crit} and R_{crit}, for a bound companion galaxy. We therefore use the typical velocity dispersion of the stars in the BCG of $\sim 300\,\mathrm{km\,s^{-1}}$ as our value for v_{crit} and the typical effective radius of BCGs of 20 kpc for R_{crit}. These match the values utilised in Merrifield & Kent (1991) (hereafter MK91) in their analysis of bound satellites to BCGs (as derived from Cowie & Hu 1986). We verify the validity of $v_{crit} = 300\,\mathrm{km\,s^{-1}}$ by investigating the velocity dispersion of the 12 single cored BCGs in our MUSE observations, (ignoring the multicomponent sources where the superposition of two separate stellar populations inflates the observed dispersion), and find a fully consistent median stellar velocity dispersion of $305\,\mathrm{km\,s^{-1}}$. This is slightly higher than the median value of $274\,\mathrm{km\,s^{-1}}$ for 375 BCGs from Lauer et al. (2014), but this likely reflects the different selection between their optically selected clusters and our X-ray selected systems (which are generally higher mass). We also verify the value of $R_{crit} = 20$ kpc by comparing with the effective radius of 120 BCGs in Graham et al. (1996), which have a mean of 25 kpc and median of 16 kpc.

We follow the procedure outlined in MK91 in order to determine the bound fraction, and define boundedness as a galaxy within v_{crit} *and* R_{crit}. We find that the fraction of galaxies within a projected radius of $r \leq 20$ kpc, which satisfy our bound condition of $v \leq 300\,\mathrm{km\,s^{-1}}$, is $p_1 = 17/47 = 0.36$. We assume a standard error in p_1 of $[p_1(1-p_1)/n_1]^{1/2}$, and find $p_1 = 0.36 \pm 0.11$ at 90% confidence interval. This fraction is consistent with the value of $p_1 = 0.32 \pm 0.11$ from MK91. For comparison we need to determine the fraction of cluster galaxies which lie at distances greater than 20 kpc from the BCG, but which also have velocities $v < 300\ \mathrm{km\,s^{-1}}$. We find this fraction, $p_2 = 22/78 = 0.28 \pm 0.08$. This is fully consistent with the value of $p_2 = 0.28 \pm 0.07$ in MK91, suggesting the wider cluster environments to our multiple

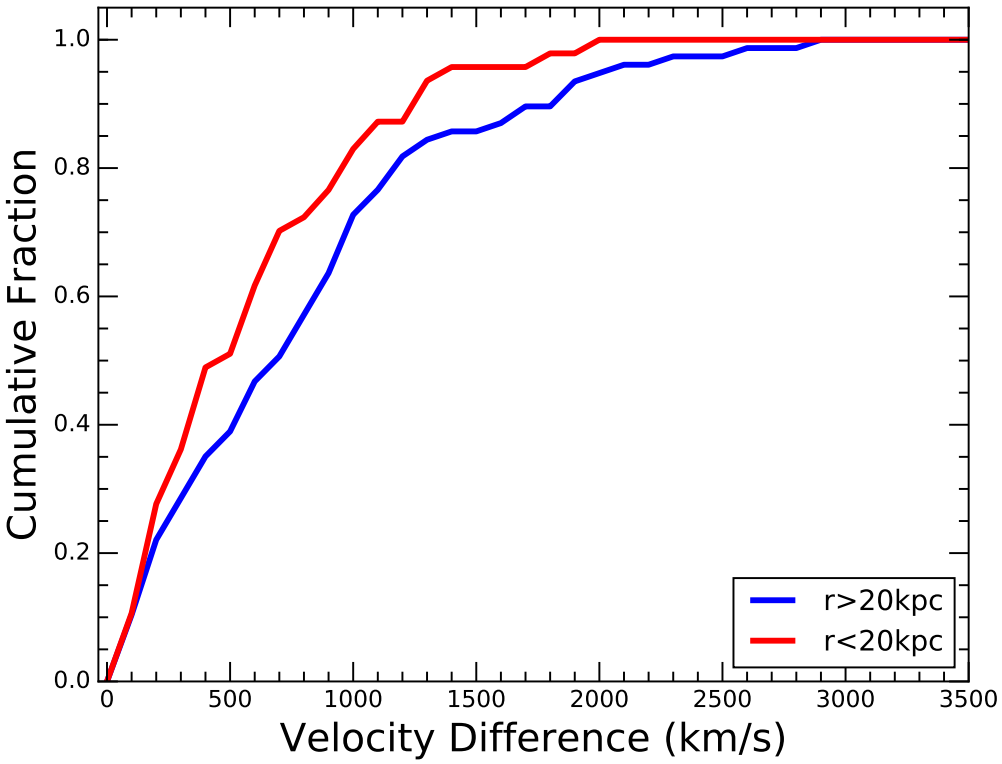

Figure 6.26: Cumulative fraction of the line of sight velocity, with respect to the rest-frame of the BCG, of galaxies within a projected radius of 20 kpc from the BCG (red) and of galaxies outside of 20 kpc (blue).

component BCGs have a similar distribution of galaxy velocities as those in MK91. The relative excess of bound galaxies within 20 kpc is then given by comparing our values of p_1 and p_2 using the following equation,

$$p_b = (p_1 - p_2)/(1 - p_2). \tag{6.3.1}$$

By propagating errors through a Monte Carlo simulation, we find a bound fraction of $0.11^{+0.14}_{-0.11}$ at 90% confidence intervals. This is consistent, within the errors, of the bound fraction of 0.06 ± 0.15 found in MK91. This is surprising given our selection criteria of morphologically selected merger candidates, whereas the selection of the 60 clusters in MK91 were based on X-ray flux alone. However, this analysis is very simplistic and provides large errors. A more sophisticated analysis is therefore needed. The simple approach assumes that boundedness is satisfied only when $v < 300$ km s^{-1} and separation, $r < 20$ kpc. However, in reality the likelihood of a companion galaxy being bound is dependent on the separation and velocity combined in a non-linear way, as well as the mass of the BCG. With full spectroscopic information we can go further and determine the bound probability for each individual galaxy.

6.3.4 Bound Probability

A galaxy is regarded as bound to the BCG if the potential energy it feels from the BCG is equal to, or exceeds, its own kinetic energy; i.e. if the following is satisfied:

$$v^2 R_p \leq 2GM_{dyn} sin^2\alpha \, cos\alpha, \tag{6.3.2}$$

(Beers et al., 1982), where v and R_p are the velocity offset and projected radial separation with respect to the BCG, G is the gravitational constant, M_{dyn} is the dynamical mass of the BCG and α is the angular separation between the galaxy and BCG. As the separation is only measured in projection and the velocity is only measured in the line-of-sight we must investigate whether the above inequality is satisfied across all angular separations. The bound probability is thus given by the fraction of angles for which equation 6.3.2 holds.

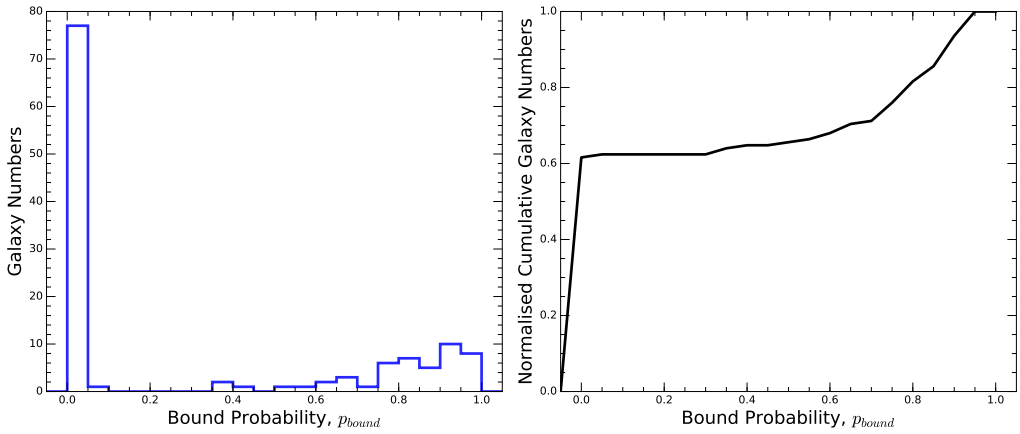

Figure 6.27: *Left:* Histogram showing the distribution of the bound probability values for the cluster galaxies. *Right:* Cumulative distribution of bound probabilities, normalised to unity.

Dynamical masses are estimated using the following equation (Cappellari et al., 2006):

$$M_{dyn} = \frac{5R_e\sigma^2}{G} \tag{6.3.3}$$

where R_e is the effective radius (half-light radius). R_e assumes spherical symmetry, so for galaxies which have a high ellipticity by nature, this is a very rough estimate. The velocity and velocity dispersion for each galaxy is measured as the median value of all the spaxels within an aperture of radius, $R_{ap} = 1$ kpc, positioned on the galaxy core. Small apertures are used in an effort to avoid contamination of the measured velocity and velocity dispersion by very close companions, which may be offset in velocity. Where there is a superposition of separate stellar systems at different velocities this manifests as an artificially enhanced apparent velocity dispersion, which would contaminate the dynamical mass measurements. Since $R_{ap} < R_e$ an aperture correction is made to the velocity dispersion to scale it to R_e using $\sigma_{cor} = \sigma(R_{ap}/R_e)^{-0.066}$ (Cappellari et al., 2006).

The bound probability is determined for each cluster member, within each MUSE observation, and given in the Tables in Figs. 6.1 to 6.23. A histogram showing the bound probability distribution is presented in Figure 6.27. The figure shows there is a bimodal distribution in which the majority of the galaxies have a bound probability of zero and hence are not dynamically bound to the BCG, or are likely to be bound,

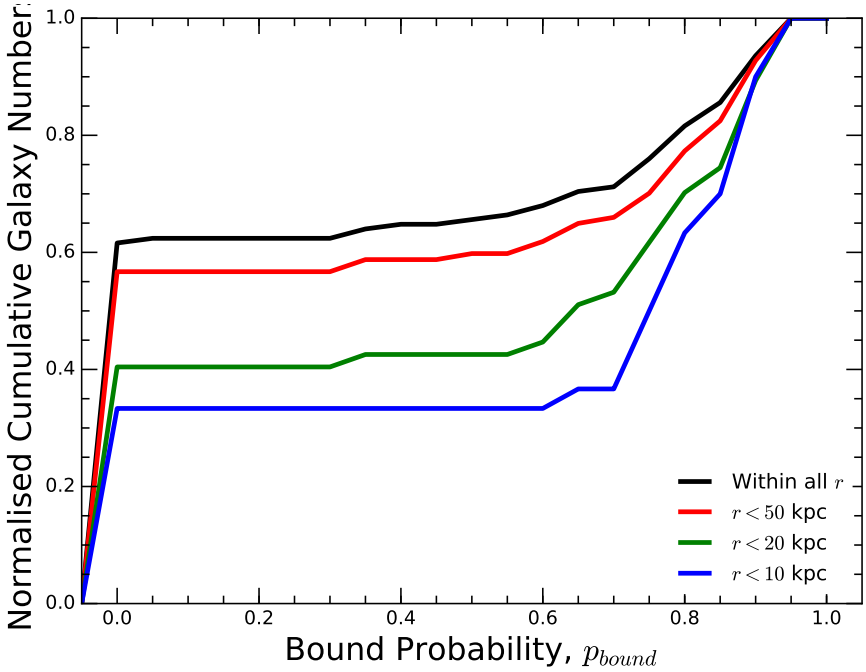

Figure 6.28: Cumulative distribution of bound probabilities, normalised to unity. The data presented shows all cluster members in black, all cluster members within 50 kpc of the BCG in red, 20 kpc in green and 10kpc in blue.

with probabilities approaching one. The fraction of companion galaxies with a finite bound probability, or non-zero bound probability (i.e $p_{bound} > 0$) therefore places an upper limit on the overall bound fraction. We find that 38 ± 5 per cent (assuming Poisson errors; 47/125) have a non-zero bound probability, $p_b > 0$. The right panel of Figure 6.27 shows the same distribution of bound probabilities but as a cumulative fraction of the cluster members. In Figure 6.28 the cumulative fraction of cluster members is given as a function of bound probability, but split into samples of those galaxies within 50, 20 and 10 kpc of the BCG.

In the subsequent two paragraphs we will discuss the quantitative results for systems with a bound probability higher than 70 per cent, i.e. where $p_b > 0.7$. Whilst the authors acknowledge that this value is rather arbitrary, we believe it presents a reasonable value at which the probability of the galaxy being bound to the BCG can be said to be sufficiently 'high'. Besides, this is intended as an illustrative example only and the subsequent analysis estimating merger rates and stellar mass growth utilises the individual bound probabilities as a factor in the calculations, so

is unaffected by this definition. The resulting values for an alternative definition of high bound probabilities can be retrieved from Figure 6.28.

Considering bound probabilities in excess of 70 per cent as high bound probabilities we find that 30±5 per cent (assuming Poisson errors; 37/125) have a high bound probability, $p_b > 0.7$. (These are indicated by the red filled stars in Figure 6.24). With the exception of three systems, A1663, A3530 and S84, all the clusters in the main sample have at least one companion which has a high probability ($p_b > 70\%$) of being bound to the BCG. This highlights the effective nature of our target selection. However, a significant number of these bound galaxies are not the very nearby companions, on which the target selection was made, but are cluster members further away from the BCG. We find that of the clusters selected with multiple component BCGs/nearby companions, only 16/21 (76 per cent) have a companion, on which the selection was made, which is likely to be bound.

Of the 30 cluster galaxies projected within 10 kpc of a BCG, we find 63 ± 15 per cent (where errors are assumed Poisson; i.e. 19/30) have bound probabilities, $p_b > 70\%$, (for comparison, the fraction outside of 10 kpc is 18/95, corresponding to 19 ± 4 per cent). Similarly, within a projected radius of 20 kpc we find 49 ± 10 per cent (23/47) of the galaxies have $p_b > 70\%$ (c.f. the fraction outside of 20 kpc is 14/78, corresponding to 18 ± 5 per cent). And within a projected radius of 50 kpc, which is the aperture often used to define close pairs in the literature when using pair fractions as a proxy for mergers (e.g. Edwards & Patton 2012; Burke & Collins 2013), we find 35 ± 6 per cent (23/47) of the galaxies have $p_b > 70\%$ (c.f. the fraction outside of 20 kpc is 3/28, corresponding to 10 ± 6 per cent). This suggests a possible contamination level due to projection, within the population of galaxies confirmed as cluster members, as high as $\sim 37\%$, $\sim 51\%$ and $\sim 65\%$ within a projected radius of 10, 20 and 50 kpc respectively. Although of course these are upper limits since galaxies may be within a true physical separation of 20 kpc say, but have a sufficiently high velocity that it is does not satisfy the bound criteria. Edwards & Patton (2012) use the Millennium Simulation to estimate contamination due to projection of unrelated cluster members and find a contamination level of 50 per cent within 50 kpc apertures and 40 per cent within 30 kpc. Our results

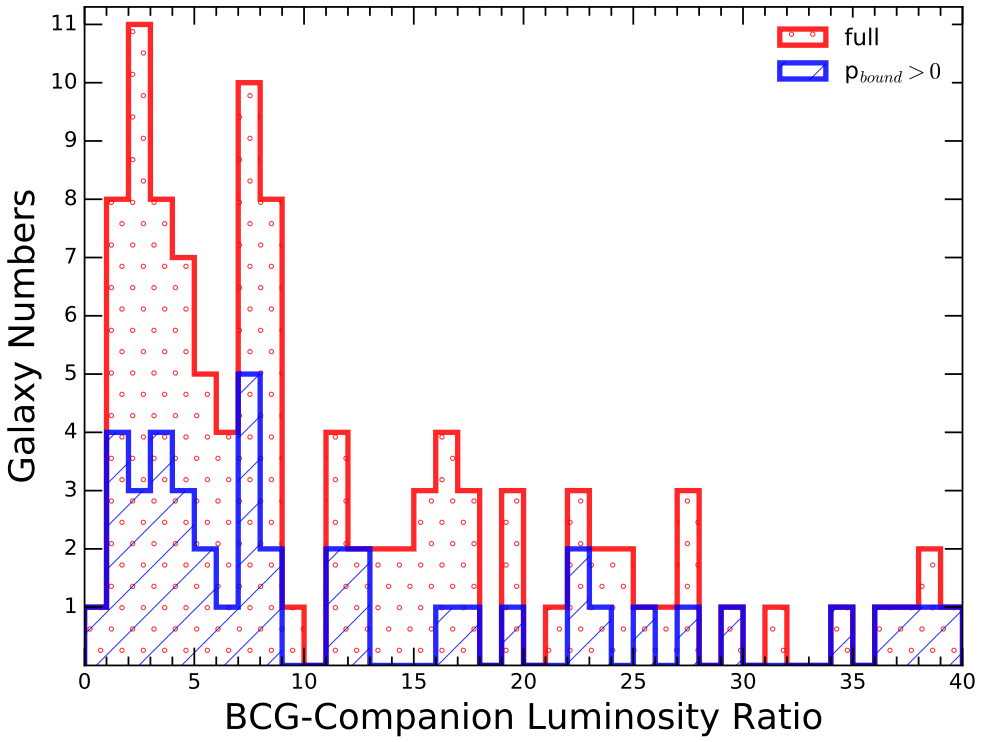

Figure 6.29: Histograms showing the distribution of the luminosity ratios between each cluster galaxy and the BCG of that host cluster. The red distribution shows the luminosity ratios for all of the 125 cluster galaxies, whereas the blue distribution shows the subset of cluster galaxies with a non-zero bound probability.

are broadly similar to these values. The absolute contamination level, when sources foreground and background to the cluster are included, would of course be higher.

In Figure 6.29 we present the distribution of the luminosity ratio between each cluster galaxy and the BCG of its host cluster, showing the full sample and the subset with a non-zero bound probability. We find the luminosity (mass) ratio distribution of (possible) bound galaxies are representative of the distribution of the full sample. So our subset of bound galaxies do not appear to favour low luminosity ratio companions over high ones, and vice-versa.

6.3.5 Merger Timescales

In order to estimate the average merger rates and stellar mass growth rates we need to constrain the merger timescales for the bound galaxies.

Dynamical Friction Timescale

We can estimate the timescale over which dynamical friction would cause a cluster galaxy to spiral toward the cluster centre by assuming their motion along a circular orbit around the BCG in an isothermal density distribution. The dynamical friction timescale, t_{fric}, is given by the expression (Eq. 7-26 in Binney & Tremaine 1987),

$$t_{fric} = \frac{2.64}{\ln(\Lambda)} \left(\frac{r_i}{2\,\mathrm{kpc}}\right)^2 \left(\frac{v_c}{250\,\mathrm{km\,s^{-1}}}\right) \left(\frac{1\times10^8}{M_{sat}}\right) \mathrm{Gyr}, \tag{6.3.4}$$

where $\ln(\Lambda)$ is the Coulomb logarithm, r_i is the radius of the orbit, v_c is the circular velocity of the satellite and M_{sat} is the mass of the orbiting satellite. From our data we assume M_{sat} to be the dynamical mass of the companion galaxy, v_c to be the line of sight velocity and r_i to be the projected separation between the companion and the BCG. As the assumed value for v_c is the minimum possible velocity, and r_i is the minimum possible separation, under the generally invalid assumption that the line of sight is tangential to the orbit of the companion, the calculated dynamical friction timescale is a lower limit. It is useful to note however that the assumption of circular orbits may not in itself be valid and N-body simulations which allow eccentric orbits (e.g. van den Bosch et al. 1999) have shown shorter dynamical timescales. We assume $\ln(\Lambda)$=2, consistent with Dubinski et al. 1999; Edwards & Patton 2012; Burke & Collins 2013; Bellstedt et al. 2016 and the justification of the appendix of Milosavljević & Merritt (2001). However, we note that the choice of $\ln(\Lambda)$ is often rather arbitrary, with a number of definitions used (Boylan-Kolchin et al. 2008; and references there-in).

Dynamical friction timescales are approximate, but it is instructive to evaluate the order of magnitude none the less. The timescales we derive vary from the order of a fraction of a Myr to tens of Gyrs depending on their velocity, separation and mass. The dynamical friction timescale is strongly dependent on the mass of the companion galaxy, as well as its velocity and separation. As such, massive companion galaxies, with small spatial and velocity offsets relative to the BCG were found to have very short dynamical friction timescales ($\lesssim$Myr), in some cases shorter than the crossing time required to reach the BCG. These short timescales resulted in high average merger rates and stellar mass growths by factors of tens, driven by

a few exceptional systems. We conclude that dynamical friction is therefore not the best measure for merger timescale, reflecting the fact that the process of dynamical friction is dominant over the larger scale cluster environment, but by the time the galaxy has reached the cluster core and is bound to the BCG, then localised orbiting around a common centre of mass dominates.

Close pair merger timescales

At large radial separation from the BCG, dynamical friction is the dominant process drawing in cluster members towards the cluster centre. However, at distances less than a few tens of kpc from the BCG the cluster environment becomes less important and galaxies merge over timescales consistent with that of the field. Hence we use the equation for merger timescales estimated in Kitzbichler & White (2008) (hereafter KW08), calibrated from merger timescales in the Millennium Simulation (Springel et al., 2005). That is, for sources within $50h^{-1}$ kpc (equivalent to ~ 70 kpc in our assumed cosmology) of the BCGs and with velocity differences < 300 km/s,

$$t_{merge} = 2.2\,\mathrm{Gyr}\,\frac{r_{sep}}{50\,\mathrm{kpc}}\left(\frac{M_{comp}}{5.5\times10^{10}M_{\odot}}\right)^{-0.3}(1+z/8)\,, \tag{6.3.5}$$

where r_{sep} and M_{comp} are the separation and mass of the companion galaxy. We use the dynamical mass measurements for M_{comp}. For sources with $300 < \Delta v < 3000$ $\mathrm{km\,s^{-1}}$ conversely the estimated merger timescale is given by

$$t_{merge} = 3.2\,\mathrm{Gyr}\,\frac{r_{sep}}{50\,\mathrm{kpc}}\left(\frac{M_{comp}}{5.5\times10^{10}M_{\odot}}\right)^{-0.3}(1+z/20)\,. \tag{6.3.6}$$

In Fig. 6.30 the KW08 merger timescales are compared with the dynamical friction timescale. The dynamical friction timescales have been clipped to have a lower limit of the crossing time. We find that the KW08 estimates are significantly longer for most of the companion galaxies, as has been discussed in the literature (Kitzbichler & White, 2008; Conselice, 2009; Williams et al., 2011). The very different set of estimates illustrates the level of uncertainty associated with the assumed merger timescales when investigating galaxy mergers. In order to remain consistent with most of the literature on BCG growth, we adopt the merger timescale estimates from KW08 for sources within a projected separation of 70 kpc of the BCG, but adopt

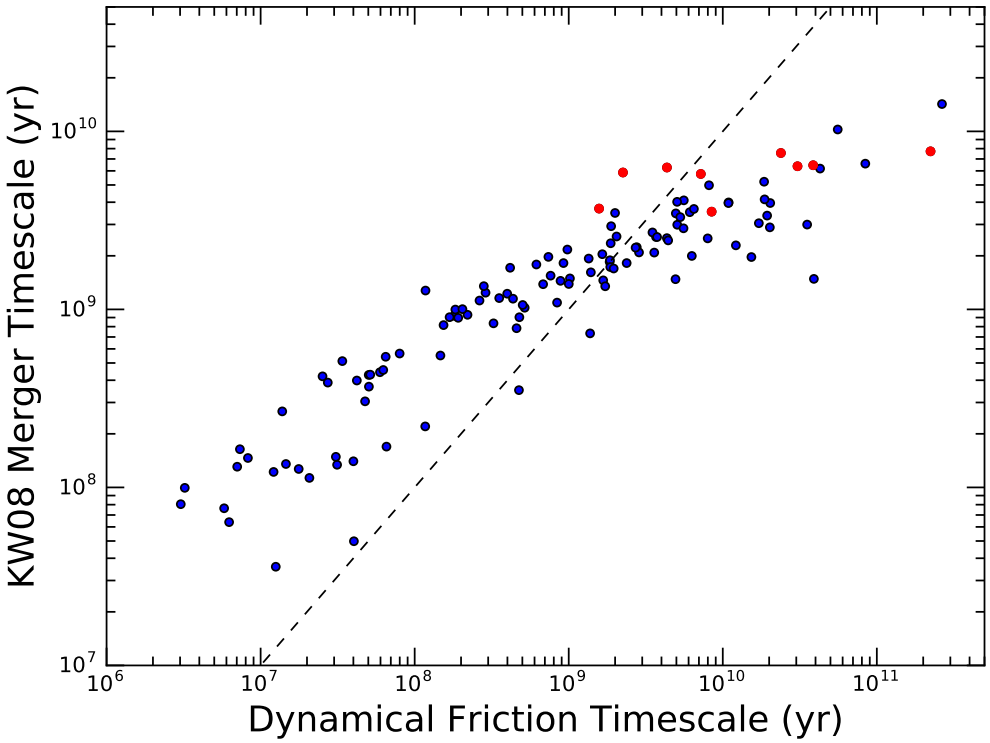

Figure 6.30: The estimated dynamical friction timescale against the merger timescale estimated by the formula of Kitzbichler & White (2008). The dashed line is a line of equality and the points coloured in red are those outside of the 70 kpc scale where the KW08 predictions apply.

the dynamical friction timescale value for the few galaxies at $r_{sep} > 70$ kpc. The estimated merger timescale for each galaxy is given in the tables in Figs 6.1–6.23. The distribution of merger timescales are presented in Figure 6.31 and the median merger timescale is 1.5 Gyr and 0.6 Gyr for the full sample of cluster galaxies and the subset of cluster galaxies with a non-zero bound probability respectively. Clearly the galaxies which are bound to the BCG generally have shorter estimated merger timescales, as we would expect.

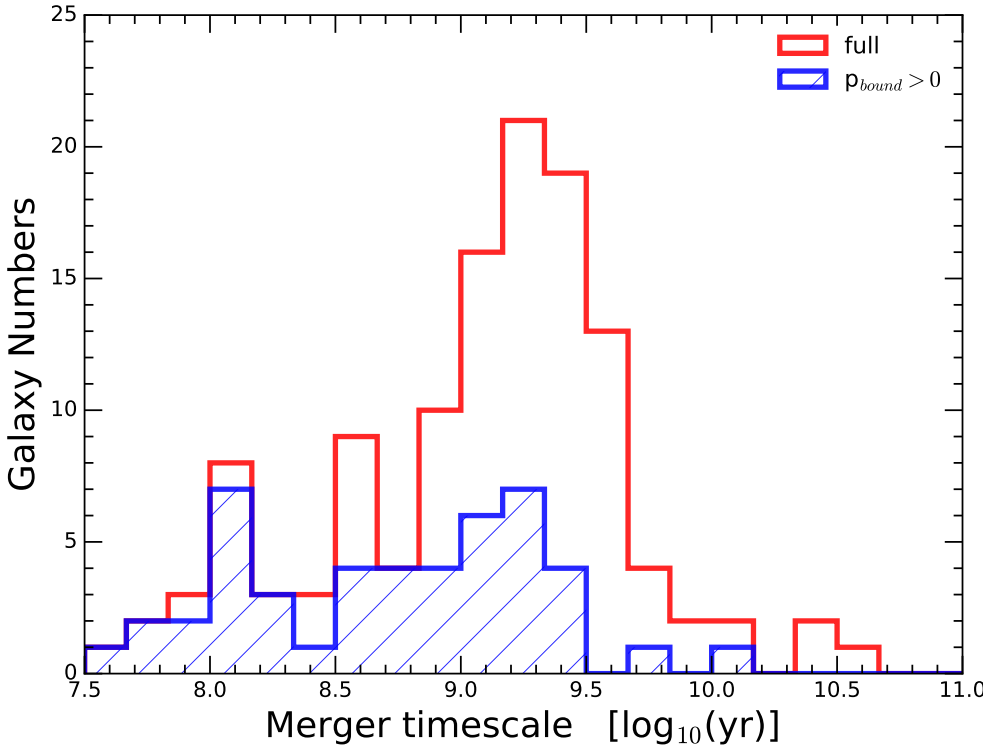

Figure 6.31: Histograms showing the distribution of merger timescales. The red distribution shows the merger times for all of the 125 cluster galaxies, whereas the blue distribution shows the subset of cluster galaxies with a non-zero bound probability.

6.3.6 Merger Rates and the Stellar Mass Growth Rate of BCGs

When a companion galaxy merges with the BCG we can estimate the fractional mass growth of the BCG in that merger as,

$$\Delta M_{BCG} = \left(\frac{M_{comp}}{M_{BCG}}\right) f_{mass}, \tag{6.3.7}$$

where M_{comp} and M_{BCG} are the mass of the companion galaxy and BCG respectively and f_{mass} is the fraction of mass from the companion transferred to the BCG during the merger. As luminosity is more directly observable, than say dynamical masses, which is derived from several observables, we determine the mass ratio from their luminosity ratios. That is, we assume the companion galaxy and the BCG have the same mass to light ratio, such that we can substitute $M_{comp}/M_{BCG} = L_{comp}/L_{BCG}$ into equation 6.3.7. A number of semi-analytic models indicate that a significant fraction of the stellar mass of a merging companion galaxy ends up in the diffuse ICL (e.g. 80% in Conroy et al. 2007; 45% in Puchwein et al. 2010), and so we chose a value of $f_{mass} = 0.5$, consistent with the literature (e.g. Liu et al. 2009, 2015; Burke & Collins 2013; Lidman et al. 2013; Groenewald et al. 2017). Since the selection of a value of f_{mass} is rather arbitrary we propagate an error of $f_{mass} = 0.5 \pm 0.2$ throughout our analysis.

We can estimate the mass growth per year for an individual merger by dividing the mass growth of that merger by the merging timescale (i.e. $\Delta M_{BCG}/t_{merge}$). So then the average mass growth, per year, of the 23 BCGs observed by MUSE, is given by,

$$\langle \Delta M_{MUSE} \rangle = \frac{1}{N_{obs}} \sum^{N_{comp}} p_b \left(\frac{\Delta M_{BCG}}{t_{merge}}\right), \tag{6.3.8}$$

where N_{obs} is the number of MUSE observations (i.e. 23), N_{comp} is the number of cluster members within the MUSE field-of-view and p_b is the bound probability for each cluster member. Errors are propagated through a Monte Carlo simulation. Since there is a typical uncertainty in the merger timescale of a factor of a few, we assume an error in the merger timescale such that it can vary by a factor of two, and with a typical conservative uncertainty in the photometry of a few tenths of a

magnitude, we assume an error of ± 0.2 mag on the flux measurements, in addition to the assumed error of ± 0.2 on the value of f_{mass}. So across our 23 systems we find an average fractional BCG mass growth per Gyr of 110^{+40}_{-30} per cent. The average merger rate, (given by equation 6.3.8 but whilst excluding the M_{BCG} term), is $7.0^{+1.3}_{-1.1}$ mergers per Gyr. However, these systems are of course the exceptional cases, selected on a strong likelihood of merging.

In order to determine a meaningful average growth rate across the wider cluster population we need to constrain how common comparable systems to these 23 MUSE targets are. As these MUSE targets are drawn representatively from a statistically significant parent cluster sample we can estimate the fraction of comparable systems within the parent sample. Within the selection redshift of $z < 0.25$ there are 784 clusters, of which 16 of the 23 MUSE targets are drawn. If we assume that these 23 systems are representative of all systems likely to merge at any one time then the average fractional mass growth, since $z \sim 0.25$, is given by,

$$\langle \Delta M_{BCG} \rangle = f_{pair} \, \langle \Delta M_{MUSE} \rangle \, t_{z=0.25}, \tag{6.3.9}$$

where $t_{z=0.25}$ is the lookback time since $z = 0.25$ (i.e. 2.88 Gyr) and f_{pair} is the fraction of total systems in a likely state of merging.

We can determine lower limits for the average BCG merger rates and mass growth in our full cluster sample by incorrectly assuming that the 23 systems in this study are the only merger–like BCGs in the full cluster sample of 784. Under this assumption $f_{pair} = (23/784)$ and the average fractional BCG growth across our parent cluster sample is, $\langle \Delta M_{BCG} \rangle = 0.9^{+0.03}_{-0.03}$, where the errors are propagated through a Monte Carlo simulation as above but with an additional Poisson error on f_{pair}. So the lower limit for mass growth from $z = 0.25$ to the present is a 9 ± 3 per cent increase in BCG stellar mass. The limiting average merger rate is $f_{pair}/t_{merge} = 0.20^{+0.02}_{-0.02}$ mergers per Gyr. And if we restrict the analysis to only major mergers, defined as companions within a luminosity ratio of 1:4, then the average stellar mass growth due to major mergers is $7.6^{+0.3}_{-0.2}$ per cent and the average major merger rate is $0.08^{+0.02}_{-0.01}$ per Gyr.

In reality the MUSE targets only represent a subset of comparable systems within the parent cluster sample. The PS1 3π imaging was revisited looking for BCGs with

significantly luminous companions, within projected separations of 20 kpc, and selected as red sequence galaxies (Chapter 2). A total of 144 comparable systems were found, corresponding to 18 ± 2 per cent (144/784) of the clusters. If we assume that the average merger rate and growth rate across the 23 MUSE targets is representative of all such systems then $f_{pair} = (144/784)$ and $\langle \Delta M_{BCG} \rangle = 0.57^{+0.20}_{-0.17}$. Hence we find an average stellar mass growth of 57^{+20}_{-17} per cent since $z = 0.25$ and a merger rate of $1.3^{+0.02}_{-0.1}$ mergers per Gyr. Considering only major mergers, the merger rate is $0.49^{+0.12}_{-0.08}$ major mergers per Gyr corresponding to an average stellar mass growth from major mergers of 47^{+18}_{-14} per cent.

6.4 Discussion

6.4.1 BCG Mass Growth

In estimating the average stellar mass growth and merger rates across the full parent cluster sample above, we have assumed the MUSE targets are representative of all these 144 systems. However, in reality they are a more extreme subsample than most in terms of projected proximities of companion galaxies, as we requested observations for the most 'interesting' systems when making our MUSE target selection. Hence the values evaluated under this assumption are likely representative of upper limits, as opposed to reasonable average values. A greater number of MUSE observations will be required to sample a more representative set of BCGs in order to estimate the average mass growth, free from selection effects. So from our analysis we can only say with a reasonable level of certainty that the average stellar mass growth of the BCGs in our 784 clusters, from $z = 0.25$ to the present, is likely somewhere between our lower limit value of 9 ± 3 per cent and our upper limit value of 57^{+20}_{-17} per cent.

The redshift range covered by our targets lies within the period where observations suggest a decline in the stellar mass growth rate of BCGs, relative to that at higher redshift. Indeed, a number of observational studies suggest very little growth below $z \sim 0.4$, with growth rates toward the lower limit values we estimate. Oliva-Altamirano et al. (2014), for example, find no significant mass growth between

$z = 0.27$ and $z = 0.09$ and Lin et al. (2013) find mass growth < 10 per cent since $z = 0.5$. Liu et al. (2009) estimate a BCG mass growth rate of 2.5 ± 1.7 per cent per Gyr, corresponding to 7 ± 5 per cent since $z = 0.25$. However it should be noted Liu et al. (2009) restrict their analysis to ongoing mergers of BCGs which show morphological distortions, so do not account for interactions yet to begin and so this is likely a lower limit. Other studies suggest a more significant, but still modest mass growth. For example, Inagaki et al. (2015) estimate a mass growth of 2–14 per cent growth between $z = 0.2$ and $z = 0.4$ (similarly Shankar et al. (2015) estimate 10 per cent over the same period), which by assuming a constant growth rate is equivalent to growth between 6 and 22 per cent since $z = 0.25$. Similarly Liu et al. (2015) estimate a growth of 35 ± 15 per cent since $z = 0.6$, which is equivalent to growth since $z = 0.25$ of 17 ± 7 per cent, assuming a constant growth rate, and Groenewald et al. (2017) find a mass growth of 24 ± 14 per cent since $z = 0.32$.

The observational literature therefore appears to suggest a much more modest mass growth than our upper limit value, with typical values of 10–20 per cent. This is more consistent with our lower limit value. Although it should be noted that the semi-analytic models do generally predict more significant mass growth, for example Laporte et al. (2013) predicts a mass growth of 40 per cent since $z = 0.3$. Although the BCG mass growth does appear to flatten out at $z < 0.4$ in the Tonini et al. (2012) model. Interestingly, whereas most observational estimates are derived from studies of major mergers, Edwards & Patton (2012) find mass growth by as much as 10 per cent over 0.5 Gyr at $z \sim 0.3$ when incorporating minor mergers also. Assuming a constant growth rate, this corresponds to a 58 per cent over the 2.875 Gyr since $z = 0.25$.

It should of course be stressed that our analysis is predicated on a number of assumptions. The principal assumption is that the observations in our PS1 imaging are a representative snapshot of BCGs at any given time. Which leads to the assumption that, as such, the estimated merger timescales for the MUSE targets can be inverted to derive average merger rates and that these merger rates can be extrapolated over the lookback time of 2.875 Gyr since $z = 0.25$. However, this is complicated by selection effects in which the merger rate, and subsequent mass

growth rate, values are dominated by the few very nearby bound companions, of comparable luminosity to the BCG. In fact, 65 per cent of the average mass growth rate comes from a companion galaxy, within a luminosity ratio of 1:2 with the BCG, in just six of the systems: RXJ1353, A2566, A2654, A1317, A3560 and A3934. Excluding these six clusters from our analysis entirely gives $N_{obs} = 17$, so with $f_{pair} = 144/784$, we find an average merger rate of $1.3^{+0.2}_{-0.2}$ mergers per Gyr and an average mass growth of 26^{+8}_{-7} per cent since $z = 0.25$, which is much more consistent with the literature.

Whilst we have selected the targets preferentially on exhibiting potential major mergers, a significant number of potential minor mergers were serendipitously identified by virtue of the wide field-of-view of MUSE. Minor mergers, i.e. mergers between galaxies with flux ratios higher than 1:4, account for 62 per cent of the mergers in our MUSE targets. Yet, despite this, the stellar mass growth is clearly dominated by the less frequent major mergers, which account for 82 per cent of the estimated mass growth. The dominance of major mergers in driving BCG growth mass growth is consistent with the results of the literature (Lidman et al., 2012; Liu et al., 2009, 2015). However, we stress that selection effects almost ensure this dominance. It is likely that a much higher fraction of the BCGs will undergo minor mergers than the 144 (of 784) clusters which satisfy our MUSE target selection. So in reality the relative weighting between major and minor mergers in BCG mass growth is likely more equal than our results suggest. It should also be noted that the different treatment between studies, some of which include minor and major mergers, whereas others include just major mergers, and the inconsistent definition of a major merger, accounts for some of the broad distribution of literature values for BCG mass growth.

The overall fraction of BCGs in our parent cluster sample which satisfy our target selection, i.e. contain a substantially massive companion galaxy projected within a radius 20 kpc of the BCG is 144/784 (18 ± 2 per cent assuming Poisson errors). We compare this value to pair fractions reported in the literature. Liu et al. (2009) for example find that 8 ± 1 per cent of BCGs (40/515) have a companion within a projected separation of 30 kpc and luminosity ratio 1:4 and Edwards & Patton

(2012) find a higher fraction of 15 ± 3 per cent satisfying the same criteria, consistent with Liu et al. (2015) which find 14 ± 7 of BCGs in a state of major merging (although small number statistics apply with only 4/29 total clusters). Hence our value is generally higher than the literature values, especially considering our more conservative aperture of 20 kpc as opposed to 30 kpc. One possible explanation is that this reflects different cluster selection, where the Liu et al. (2009) and Edwards & Patton (2012) clusters are optically selected, whereas our clusters are X-ray selected.

6.4.2 Notes on Individual Clusters

A193: The triple nucleus of the BCG of Abell 193 was the subject of Seigar et al. (2003), who conclude the galaxies are likely part of a common system. From the MUSE kinematics (Fig. 6.5) we can confirm that this is indeed, in all likelihood, a three-way bound system. The two most northern components are separated from one another by a velocity of only 45 $\mathrm{km\,s^{-1}}$ and a projected distance of 2 kpc, so are almost certainly bound. The southern most nuclei is separated by ~ 548 $\mathrm{km\,s^{-1}}$, but is sufficiently close that the probabilities of the two northern components being bound to the southern component are 79 and 74 per cent.

A3530, a BCG with shells: The BCG of Abell 3530 was selected on the appearance of shells in the optical imaging (Fig. 6.32). Shells are thought to represent a late stage of the merger process (Quinn, 1984; Hernquist & Spergel, 1992; Cooper et al., 2011) where the discontinuities in surface brightness are believed to be due to separate stellar populations as a companion galaxy is accreted into the main one. It is thought that stars of the companion galaxy are stripped by the interaction and oscillate in the potential of the main galaxy. The velocity of the stars is at its lowest at the turning points of the oscillation, leading to a pile up of stars at these points, producing a series of arc-like discontinuities in the luminosity profile. The different motion of these stars should therefore, in principle, be observable in the stellar kinematics of the host galaxy.

In order to test this we measure the median line-of-sight velocity and velocity

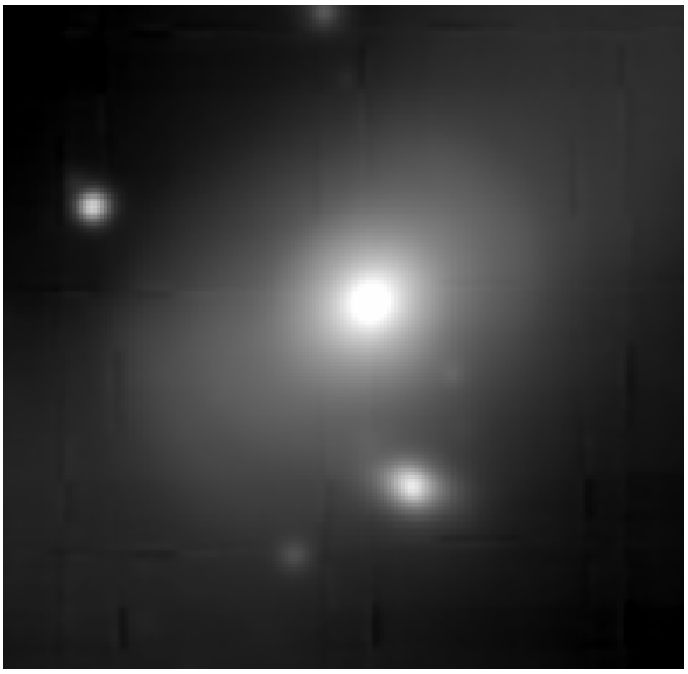

Figure 6.32: Broadband image of A3530, made from the collapsed MUSE cube, showing the shells in this particular galaxy. Note that this is best viewed in the electronic version. North is up and East is right.

dispersion of the BCG of A3530 in overlapping concentric elliptical wedges (i.e. quarter of an elliptical annulus), of thickness 0.6 arcsec (equivalent to $\sim$ 0.6 kpc), centred on semi-major axis radius, R. In Figure 6.33 we plot the surface brightness, velocity and velocity dispersion of the BCG as a function of radius. The semi-major axis is defined 45 degrees clockwise from north and R is defined with positive values toward the north-west from the BCG centre and negatively to the south-east. The kinks in the surface brightness profile demonstrate the discontinuities where the arcs are located, however, no clear trend is visible in the structure of the velocity and dispersion profiles at these radii. Perhaps a higher spatial resolution in the binning of the data may be necessary to constrain this further. However, it should be noted that this may represent an orientation effect, in which in order to observe the shell structure then a significant quantity of the oscillating motion of the stars must occur in plane of the sky, which is orthogonal to the line-of-sight velocity measurements we can make.

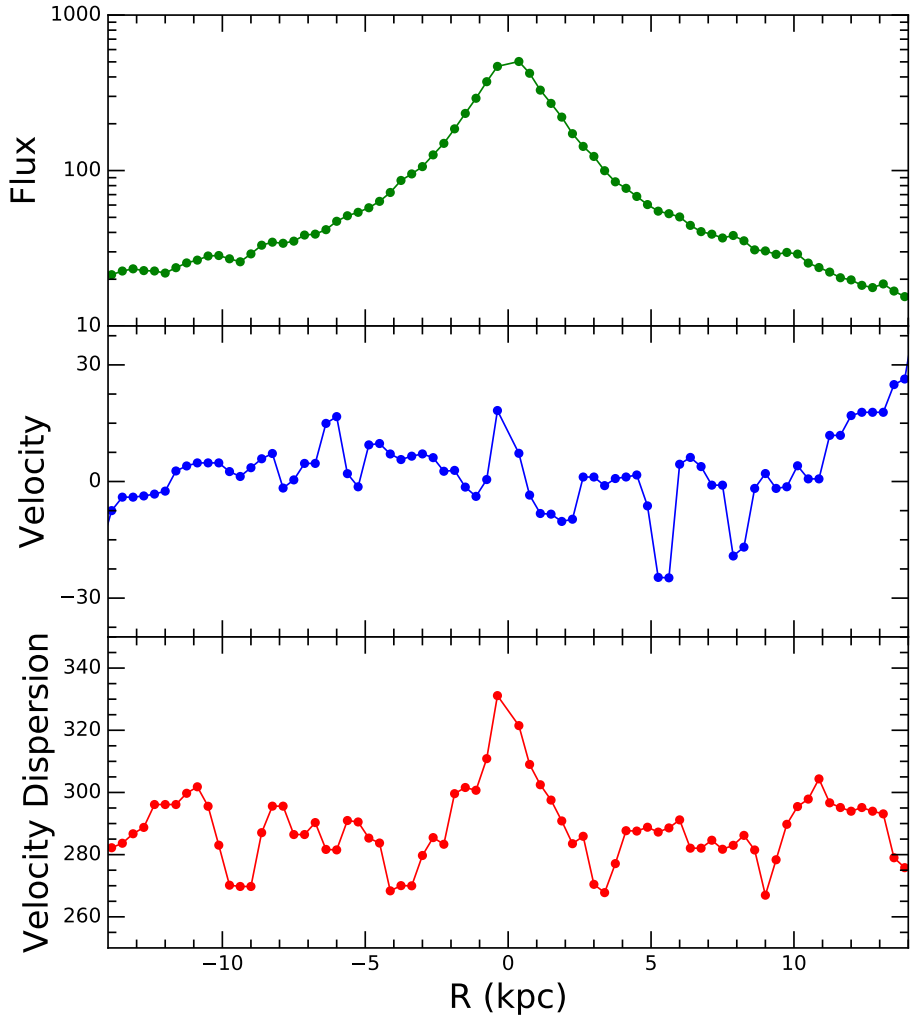

Figure 6.33: The mean flux, median velocity and median velocity dispersions within a series of of concentric overlapping elliptical wedges centred on the semi-major axis radius, R, for the BCG of A3530. The velocity and velocity dispersion are in units of $\mathrm{km\,s^{-1}}$ and the flux is arbitrary. The kinks in the surface brightness profile represent the discontinuities where shells appear in the broadband imaging.

6.4.3 Rotation of BCGs

The rotational properties of massive early-type galaxies scales with their stellar mass, such that the typical angular momentum parameter (Emsellem et al., 2007) decreases with increasing stellar masses (Brough et al., 2017; Veale et al., 2017). At the most massive end of the galaxy mass function, BCGs therefore tend to be what are called slow rotators with low angular momentum, although fast rotating BCGs do exist (e.g. Jimmy et al. 2013; Oliva-Altamirano et al. 2017). From visual inspection of the BCGs targeted with MUSE we find no evidence for significant rotation in their stellar kinematics, with the exception of Abell 3771 (Fig. 6.20). The BCG of A3771 has a clear rotational structure and a rotational velocity of some ~ 200 km s^{-1}. Calculation of the angular momentum parameter for all BCGs would be an interesting exercise, but, by the nature of our target selection, measuring the velocity and velocity dispersions as a function of radius, without contamination from nearby companion galaxies, would not be without challenge.

6.5 Summary and Conclusions

We observe 23 cluster cores with the wide-field Multi Unit Spectroscopic Explorer (MUSE), targeting systems with a BCG likely to undergo a merger, based on optical imaging of $\sim$ 800 X-ray selected clusters at $z < 0.25$. These are systems with a multiple component BCG or nearby massive companion galaxies. We determine the line-of-sight stellar kinematics for all cluster galaxies within the MUSE field-of-view and evaluate a likelihood for each one being bound to the BCG of that system. Of the 125 cluster galaxies with spectroscopy, 30 per cent have a high bound probability, $p_{bound} > 0.7$.

We statistically explore the projected stellar mass growth of these BCGs and place constraints on the average growth rate across the full parent cluster sample. We estimate merger timescales for each of the galaxies and estimate average merger rates and BCG stellar mass growth from these. Assuming these 23 MUSE targets are the only potential merging systems in the parent cluster sample we find a lower limit to the average stellar mass growth of BCGs since $z = 0.25$ of 9 ± 3 per cent.

However, in the optical imaging of the parent cluster sample we find 144/784 clusters have a comparably massive (i.e. luminous) companion within a projected radius of 20 kpc of the BCG, which may be expected to merge soon. So, by assuming that the average merger and mass growth rates from the MUSE targets are representative of the 144 similar systems, we find an average mass growth of 57^{+20}_{-17} per cent since $z = 0.25$. As we have selected the most extreme systems for MUSE observations this is likely an upper limit. We can conclude therefore that the average stellar mass growth of BCGs since $z = 0.25$ is between 9 ± 3 and 57^{+20}_{-17} per cent. The typical literature values of 10–20 per cent of mass growth over this period favour more modest growth than our upper limits.

Although the target section favours major mergers we serendipitously identify a significant fraction of minor mergers by virtue of the wide field-of-view afforded by MUSE. We find that 62 per cent of estimated mergers are in fact minor mergers, but that they account for only 18 per cent of the BCG mass growth. Although selection effects favour an overestimation of the major merger contribution.

In order to better constrain the average BCG stellar mass growth rate a larger and more representative sample of BCGs will need to observed with instruments like MUSE. Nevertheless, since wide spread use of integral field spectroscopy is the desirable next step in observational astrophysics, the techniques utilised in our analysis should help lay the groundwork for subsequent studies of the stellar growth rate of BCGs, using a statistically significant number of IFU observations.

Chapter 7

Optical Line Emission in the Core of Clusters of Galaxies

The work in this Chapter is in preparation for publication.

7.1 Overview

We present MUSE IFU observations of ten clusters found to exhibit optical line emission in their core. The morphologies and kinematics are reported and found to vary greatly between systems. Line intensity ratios are generally found to be similar across the systems and with a comparison sample of Hα filaments in cool cores, suggesting a more complex mix of ionisation mechanisms than either star formation or AGN. Two systems (A2533 and A2566) are discovered with the bulk of the line emission offset from the BCG. A *Chandra* observation of A2566 confirms the X-ray peak is offset from the BCG and is cospatial with the offset optical line emission, matching past observations. This is likely a result of sloshing of the ICM, due to a large scale interaction. Most striking is A2533 which has a 40 kpc long filament of gas across the BCG, spatially coincident with dust obscuration and star formation, as well as cold molecular gas revealed by an ALMA observation. A connection between the offset gas and the X-ray peak cannot be definitively established, however the data appears to favour ICM sloshing within the plane of the sky. The likelihood of the observed gas having originated from a cooling flow or a merger are discussed for

a number of systems and evidence is presented for a potential gas disk around the BCG of A2626, ionisation by an AGN in A1663, as well as a possible unravelling of a spiral galaxy in S84.

7.2 Introduction

As discussed in Chapter 1, and indicated at Chapter 3, there is a strong association between the thermodynamical state of the ICM – i.e. whether it is a cool core cluster or not – and the presence of optical line emission in the cluster core. In this Chapter we aim to explore the properties of any optical line emission in the MUSE observations of BCGs selected for the merger analysis of Chapter 6.

7.3 Data

The details regarding the target selection and reduction of the MUSE data are given in Chapter 5, as are details on the emission line fitting procedure and derivation of the emission line kinematics.

Following the striking line emission found in some of these systems (see § 7.4), follow up observations with *Chandra* for two of the cluster cores, A2533 and A2566, have been awarded, as well as an ALMA observation of A2533.

7.3.1 X-ray Observations

Observations on the *Chandra X-ray Observatory* were awarded for Abell 2566 and Abell 2533 (PI Edge; ObsID 19595). An observation of A2566 was taken on 2016–09–30 with a 20 ks exposure. A 40 ks exposure observation of A2533 with *Chandra* is scheduled for late July. These were/are to be taken on the Advanced CCD Imaging Spectrometer (ACIS) with the ACIS-S detector in VFAINT mode.

7.3.2 ALMA Observation

An observation on the Atacama Large Millimeter/submillimeter Array (ALMA) was awarded for Abell A2533 (PI Green; project ID 2016.1.01573.S). ALMA is a

radio interferometer observatory, tuned to millimetre and sub-millimetre frequencies. The observation was taken on 2016–12–01, with an 80 min exposure, with the 12m array in the C40-3 configuration on band 3. This provides an instrumental angular resolution of 0.95 arcsec. However, the data was only released by the observatory a few weeks prior to the submission of this thesis, so only a minimal analysis has been conducted so far.

Data Analysis: ALMA is designed to detect CO emission, which is emitted by cold molecular gas and is commonly used as a tracer for the more abundant molecular hydrogen, H_2. The morphology and kinematics of the molecular gas can be measured by fitting the CO emission lines. To this end we fitted the CO(1-0) line, following an almost identical procedure as outlined in Chapter 5 for the optical emission lines. First the ALMA cube was spatially binned such that each pixel was the mean value across the 6×6 grid of spaxels (1.08×1.08 arcsec) centred on it. Again, this was done as a compromise between achieving a higher S/N, but at the expense of some spatial resolution. The final continuum subtracted data, reduced by the observatory, was used, so no additional continuum subtraction was necessary. The CO(1-0) line at 115.3 GHz (i.e. $\lambda = 2.6$ mm) was then fitted using a single Gaussian fit, where the initial estimates were based on a location of the local peak in a smoothed fit to the overall spectrum. Similar to the MUSE data, no prior assumption was made about the presence of emission line. The fitting routine was developed to be robust enough that it effectively picked the line when present, and returns nonsensical values when not. A cut in the difference between χ^2 values, returned by the Gaussian fit and a linear fit to the data, was then applied to isolate the CO emission.

7.4 Results

Of the 23 primary MUSE targets, we find that ten of the cluster cores have the presence of optical line emission. Properties of these ten systems are summarised in Table 7.1. A variety of morphologies are uncovered, again revealing the complex nature of ionised gas seen in cluster cores (e.g. Wilman et al. 2006; Hatch et al.

Cluster ID	Redshift	$L_{\rm X}$ ($10^{44}\,{\rm erg\,s^{-1}}$)	$L_{\rm H\alpha}$ ($10^{40}\,{\rm erg\,s^{-1}}$)	Description of Line Emission
S84	0.1100	1.77	12.1	Linear with continuum
A368	0.2200	4.23	10.1	Asymmetric extended on BCG core
A3528	0.0574	1.31	0.4	Compact on BCG core
A1663	0.0843	1.03	2.4	Bulk on core with a filament
RXJ1336	0.1768	1.61	32.9	Extended on BCG core
A2533	0.1110	1.78	20.2	Bulk offset from BCG core
A2566	0.0821	2.04	9.0	Bulk offset from BCG core
A2626	0.0565	1.32	4.8	Bulk on BCG core, with filaments
RXJ2104	0.0491	0.56	1.5	Peak on BCG core with filament
A3934	0.2240	5.01	1.8	Compact on BCG core

Table 7.1: Cluster ID, redshift, 0.1–2.4 keV band X-ray luminosity, Hα luminosity and qualitative description of the spatially resolved line emitting gas.

2007; Hamer et al. 2012, 2016), with the spatial extent varying dramatically between systems. In the case of two of the clusters, A3528 and A3934, the only line emission presence is compact and on the core of the BCG. In the five of the clusters the bulk of the line emission is on the BCG core but also spread over a significant spatial extent: A368 and RXJ1336, for example, exhibit an extended clumpy morphology and A1663, A2626 and RXJ2104 exhibit some filamentary structure. Most strikingly however, there are three systems where the bulk of the line emission is offset from the BCG core. In S84, the line emission is cospatial with significant stellar continuum, and hence could be associated with a galaxy, but in the other two, A2533 and A2566, the offset line emission is mostly distinct from any significant stellar continuum.

7.4.1 Gaseous Kinematics

The Hα kinematic maps for each system are presented in Figures 7.1 to 7.10.

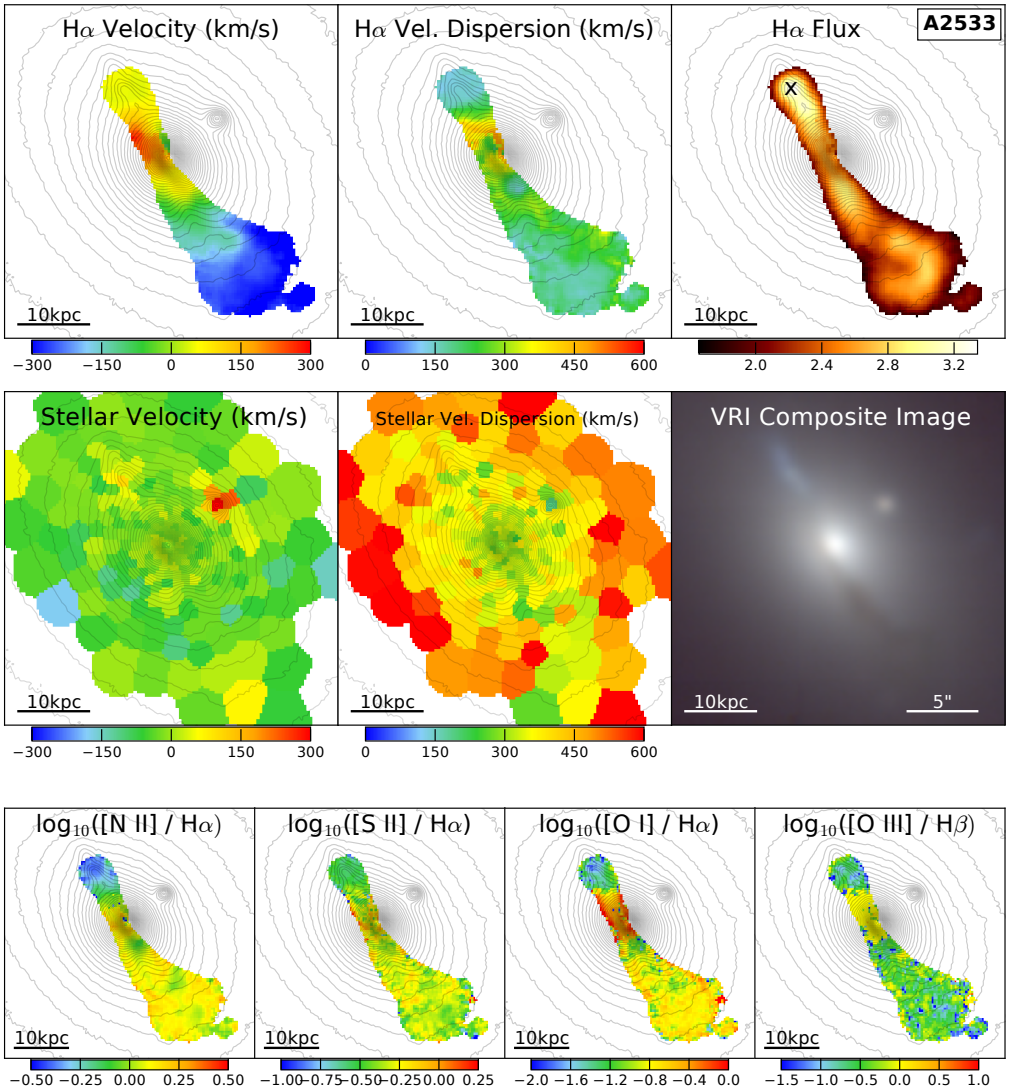

Figure 7.1: Optical line emission diagnostics of the core of A2533. The spatially resolved Hα kinematic maps are given in the top row, with the stellar kinematic maps (Chapter 6) given for reference in the middle row. The spatially resolved line intensity ratios are given in the bottom row. The grey contours in the emission line maps represent the stellar continuum, at arbitrary levelling. The Hα flux is presented in a log scale, with units $10^{-20}\,\mathrm{erg\,s^{-1}\,cm^{-2}\,\AA^{-1}}$, and the black cross represents the Hα peak. The VRI composite continuum image is presented with a square root scale. The orientation is such that north is up and west is right.

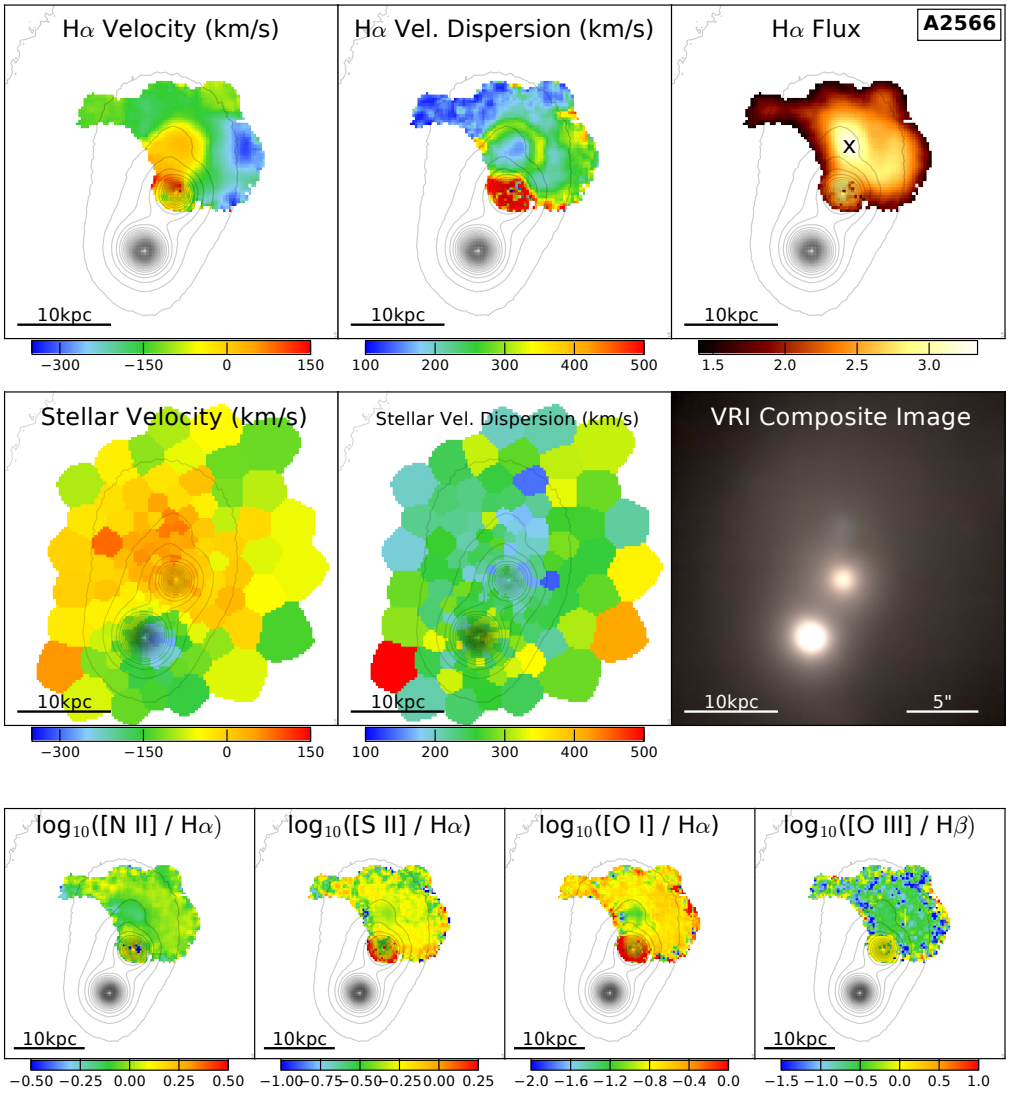

Figure 7.2: Same as Fig. 7.1, but for the core of A2566.

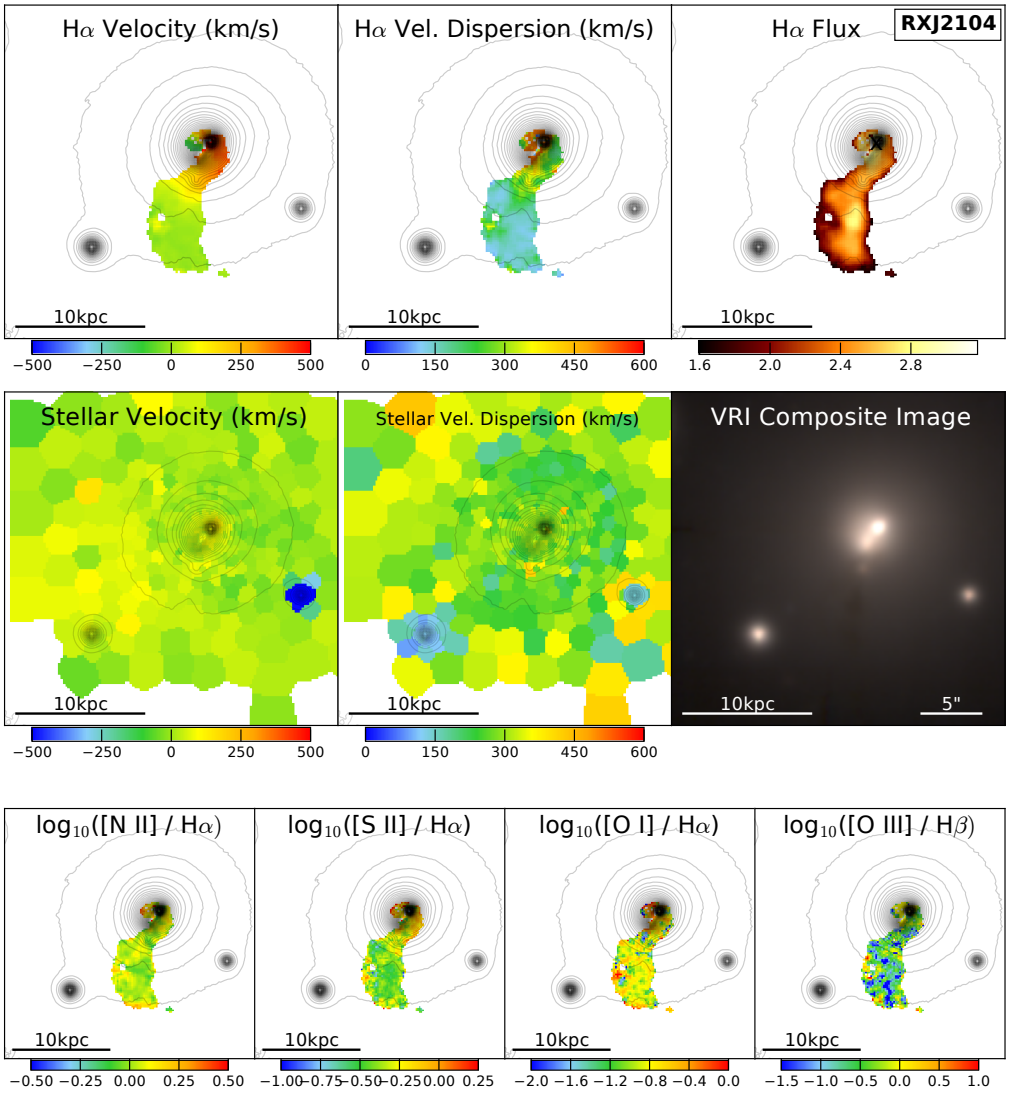

Figure 7.3: Same as Fig. 7.1, but for the core of RXJ2104.

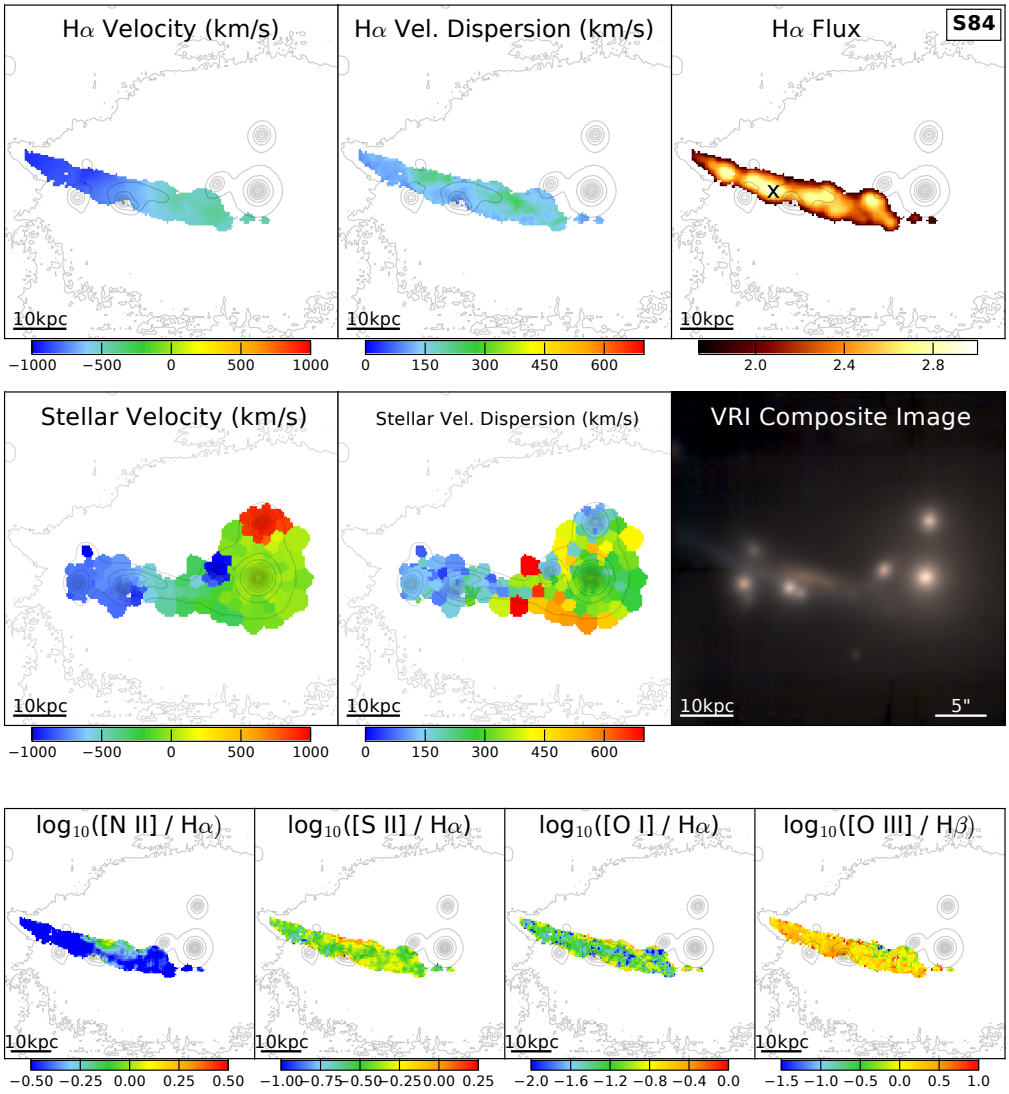

Figure 7.4: Same as Fig. 7.1, but for the core of S84.

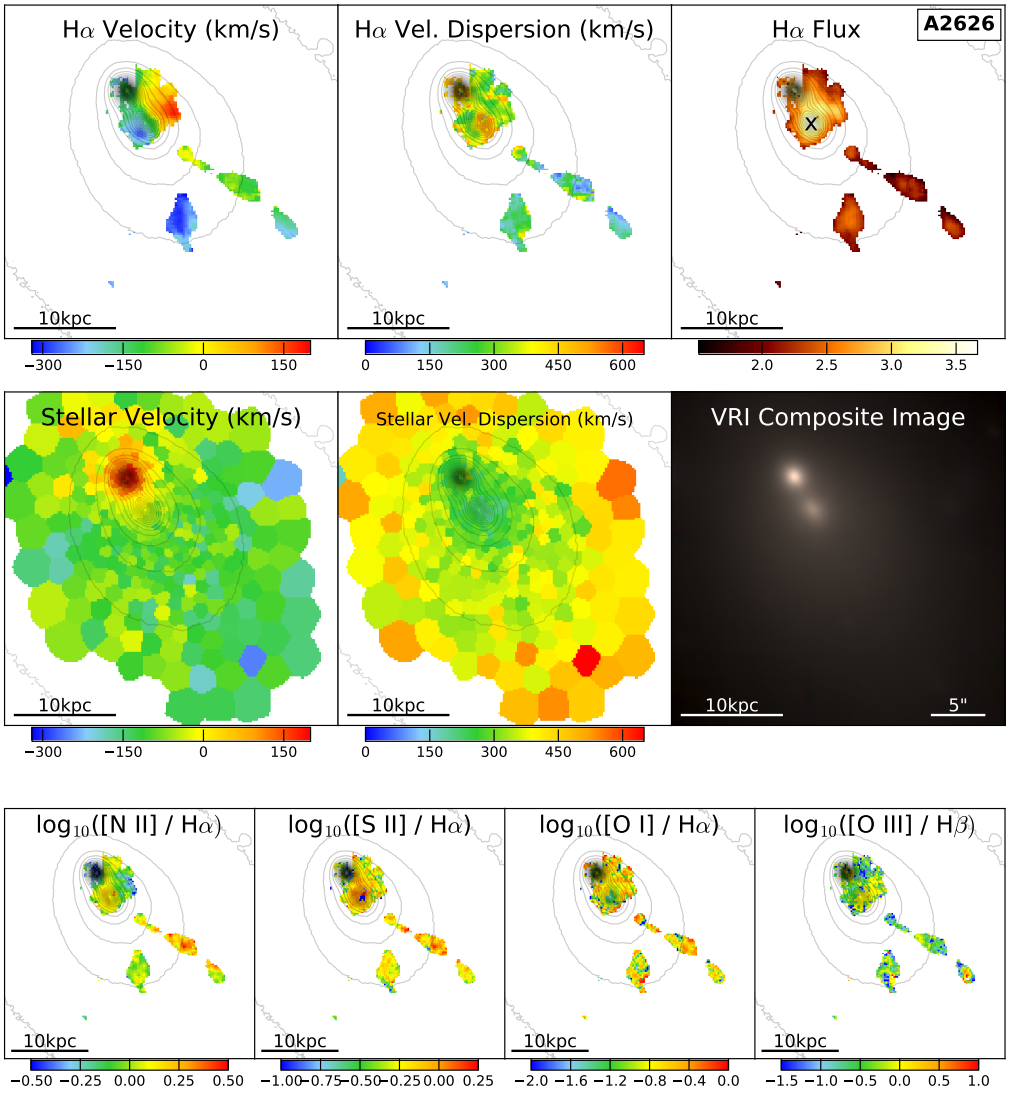

Figure 7.5: Same as Fig. 7.1, but for the core of A2626.

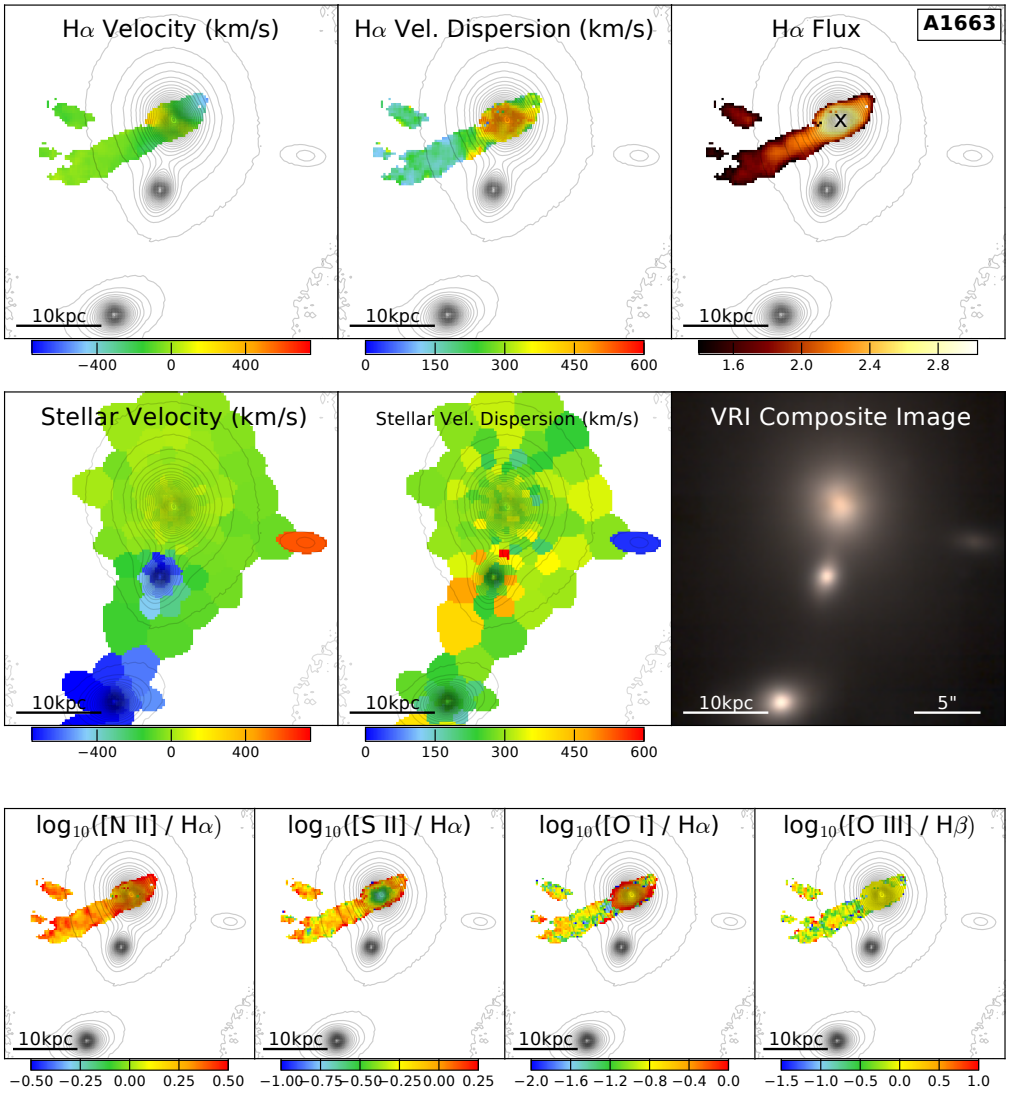

Figure 7.6: Same as Fig. 7.1, but for the core of A1663.

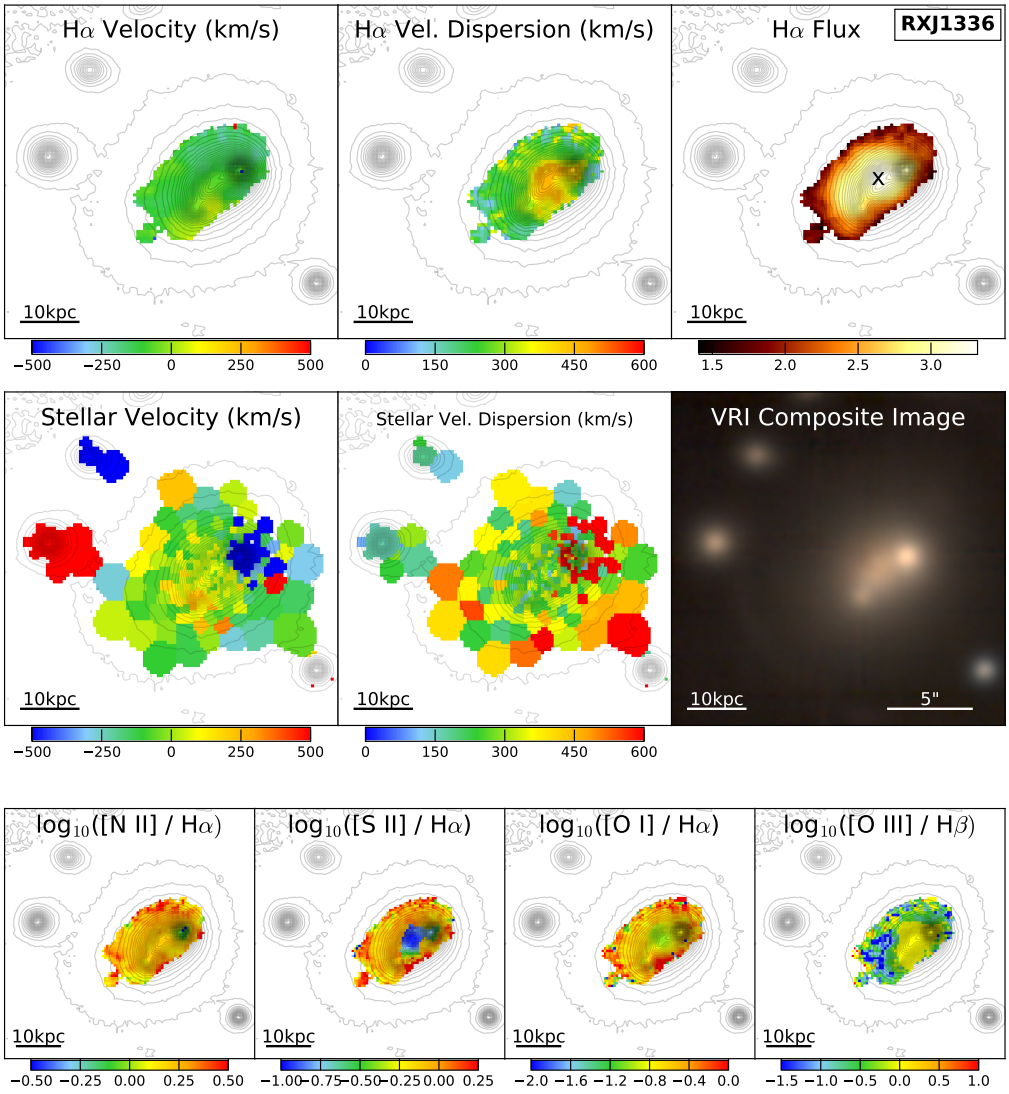

Figure 7.7: Same as Fig. 7.1, but for the core of RXJ1336.

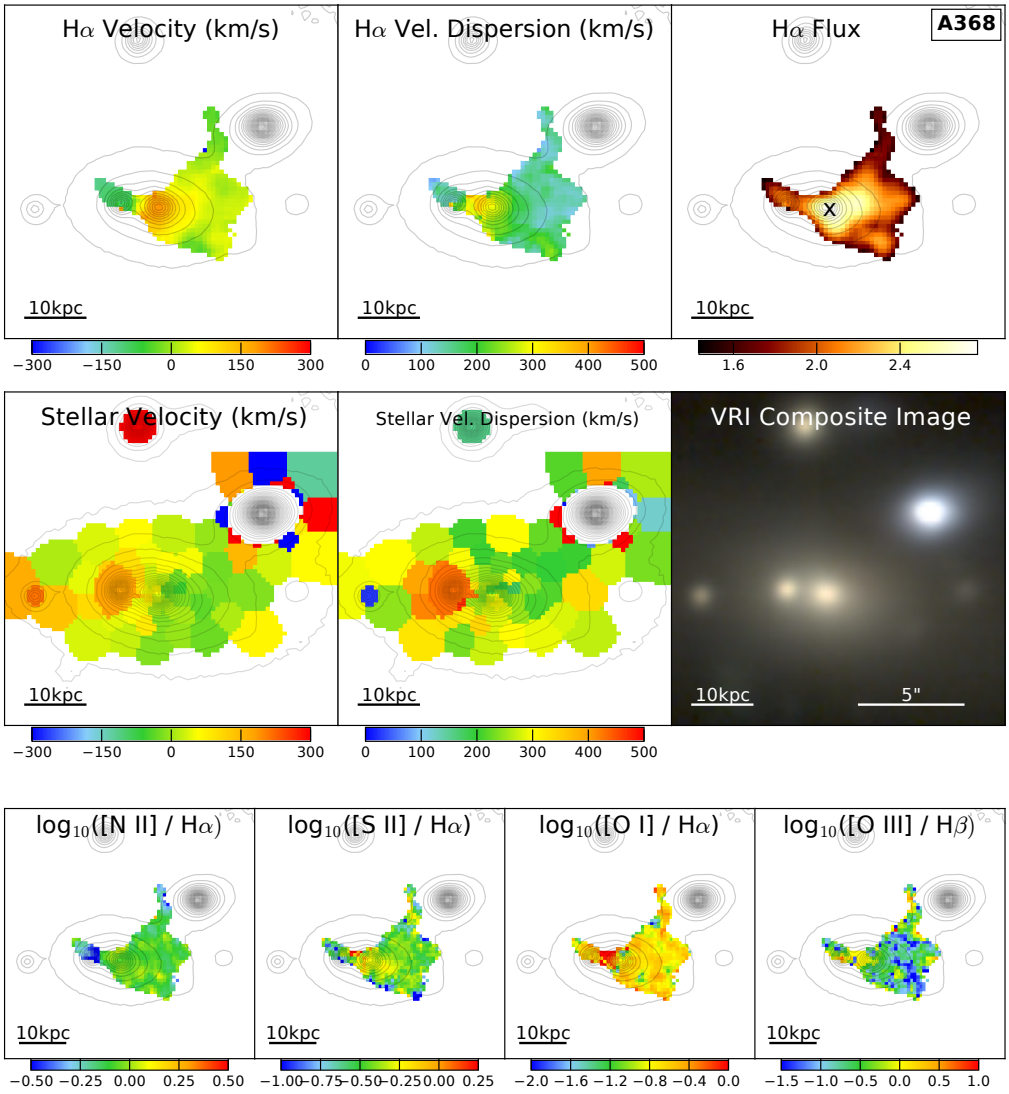

Figure 7.8: Same as Fig. 7.1, but for the core of A368.

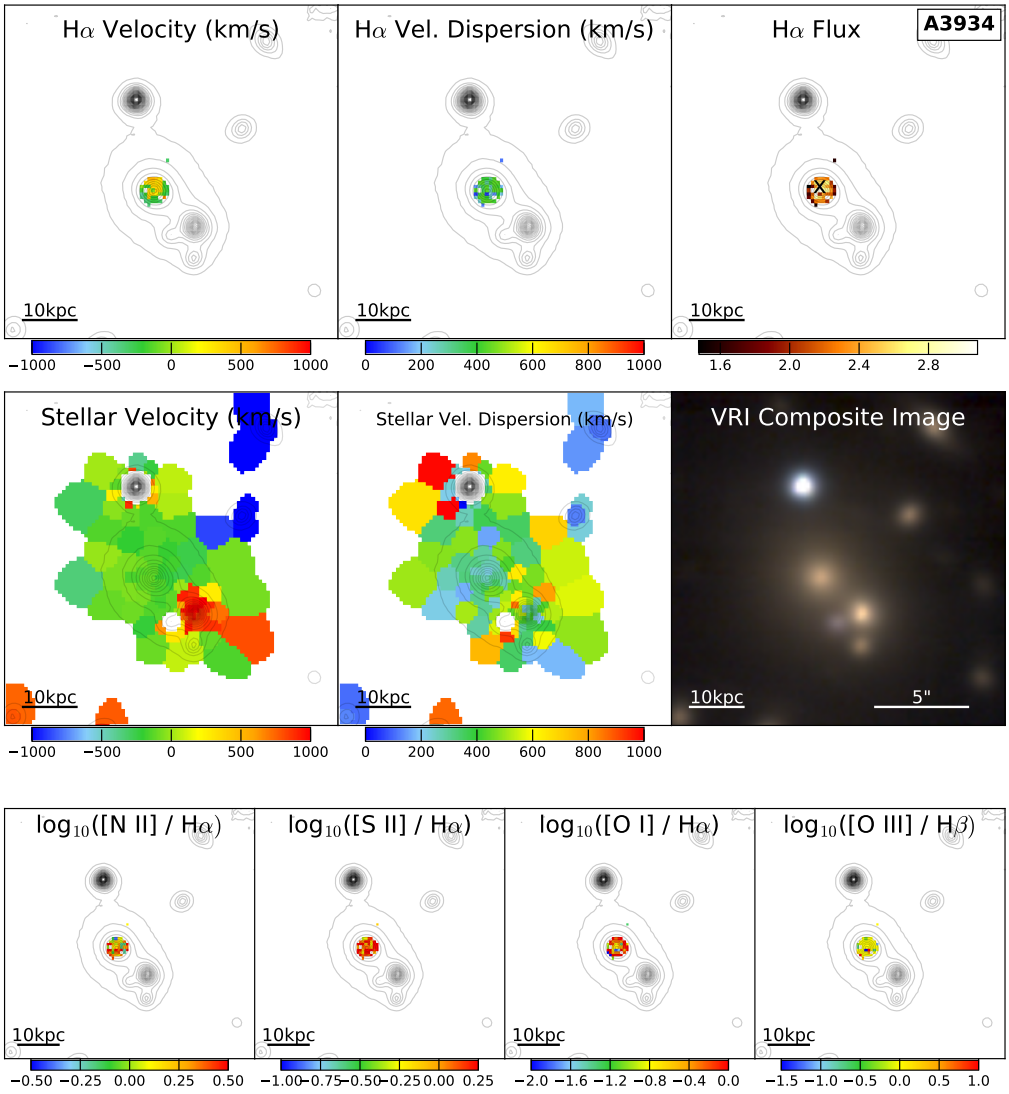

Figure 7.9: Same as Fig. 7.1, but for the core of A3934.

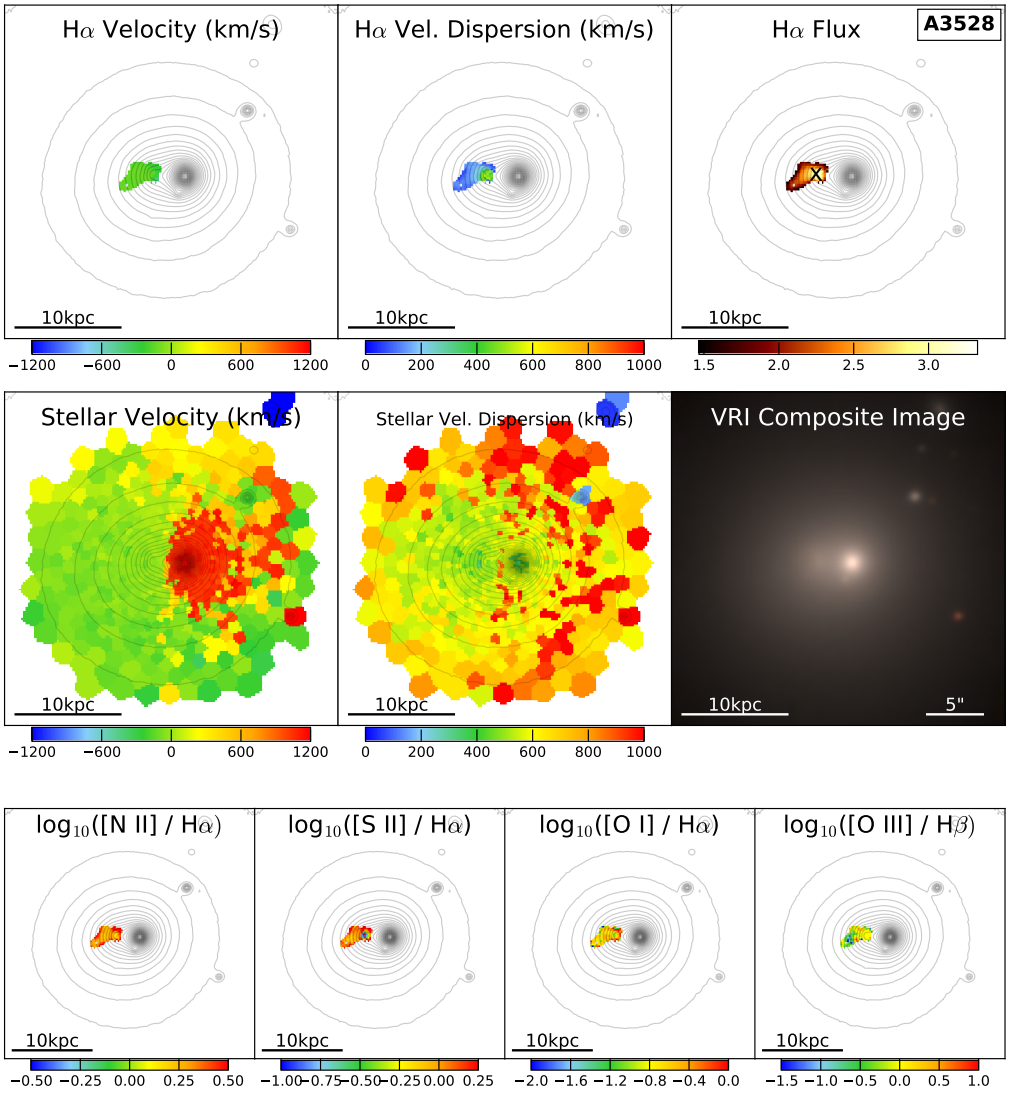

Figure 7.10: Same as Fig. 7.1, but for the core of A3528.

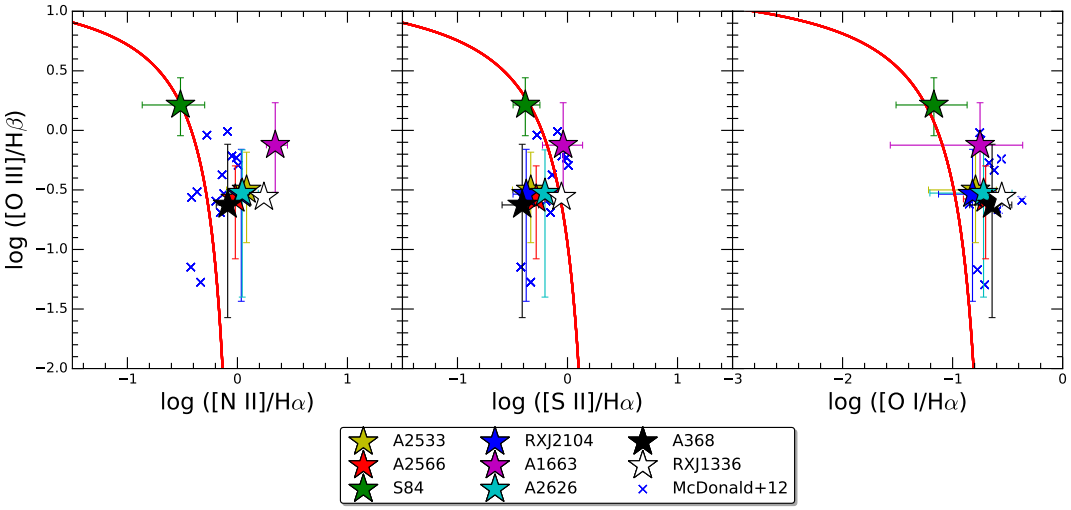

Figure 7.11: BPT diagrams showing the median line intensity ratios of each of our systems. The filled stars are the median values for each of our MUSE observations, the blue crosses are the values of the optical emission line filaments in nine cool core clusters from McDonald et al. (2012b) and the red line in each panel represents the extreme starburst limit of Kewley et al. (2006). The error bars represent the 16th and 84th percentiles in the distribution of line intensity ratios for individual spaxels (Fig. 7.13).

7.4.2 Line Intensity Ratios

The spatially resolved line intensity ratios for each system are presented alongside the kinematic maps in Figures 7.1 to 7.10, which reveal the ionisation properties of the gas. Line intensity ratios can be compared on a series of diagnostic diagrams, in what is known as a BPT analysis (Baldwin et al., 1981), which has traditionally been used to distinguish between star forming or AGN dominated systems (Kewley et al., 2006). In Figure 7.11 we present the BPT diagnostic diagrams showing the median line intensity ratio values for each system and in Figure 7.13 we present the individual spaxel–by–spaxel BPT diagrams. Note that we omit any BPT analysis of A3528 and A3934 as these are not spatially resolved, due to the limited number of spaxels containing ionised gas. Note that the intensity ratios of emission lines at similar wavelengths are used in order to reduce any impact from reddening of the spectrum.

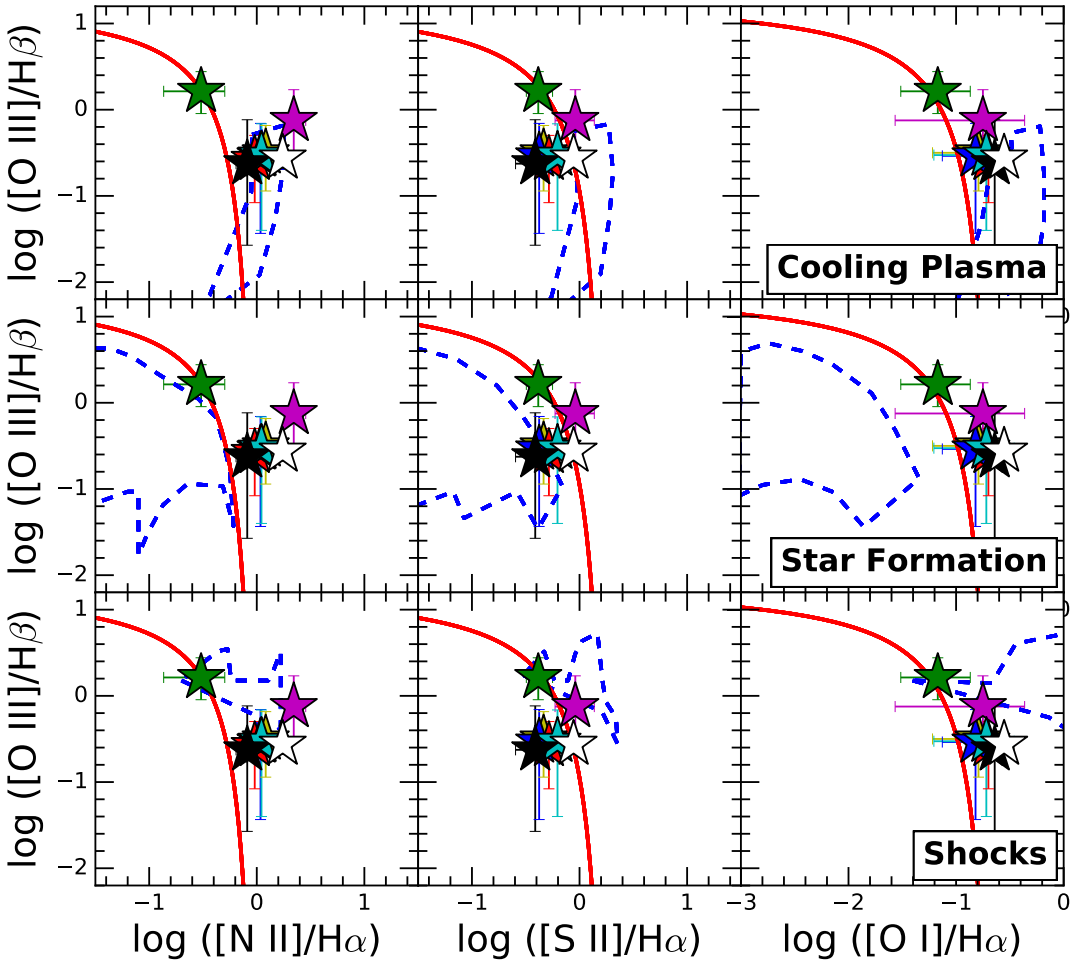

Figure 7.12: The same as Figure 7.11 but with additional model predictions overlaid, enclosed by the blue dashed lines. The parameter space of the model predictions are taken from the grids of Figure 14 in McDonald et al. (2012b). The top row shows model predictions for self-ionisation from a condensing plasma (from Voit et al. 1994), the middle row shows photoionisation from young stars (from Kewley et al. 2001) and the bottom row shows ionisation by shocks (from Allen et al. 2008).

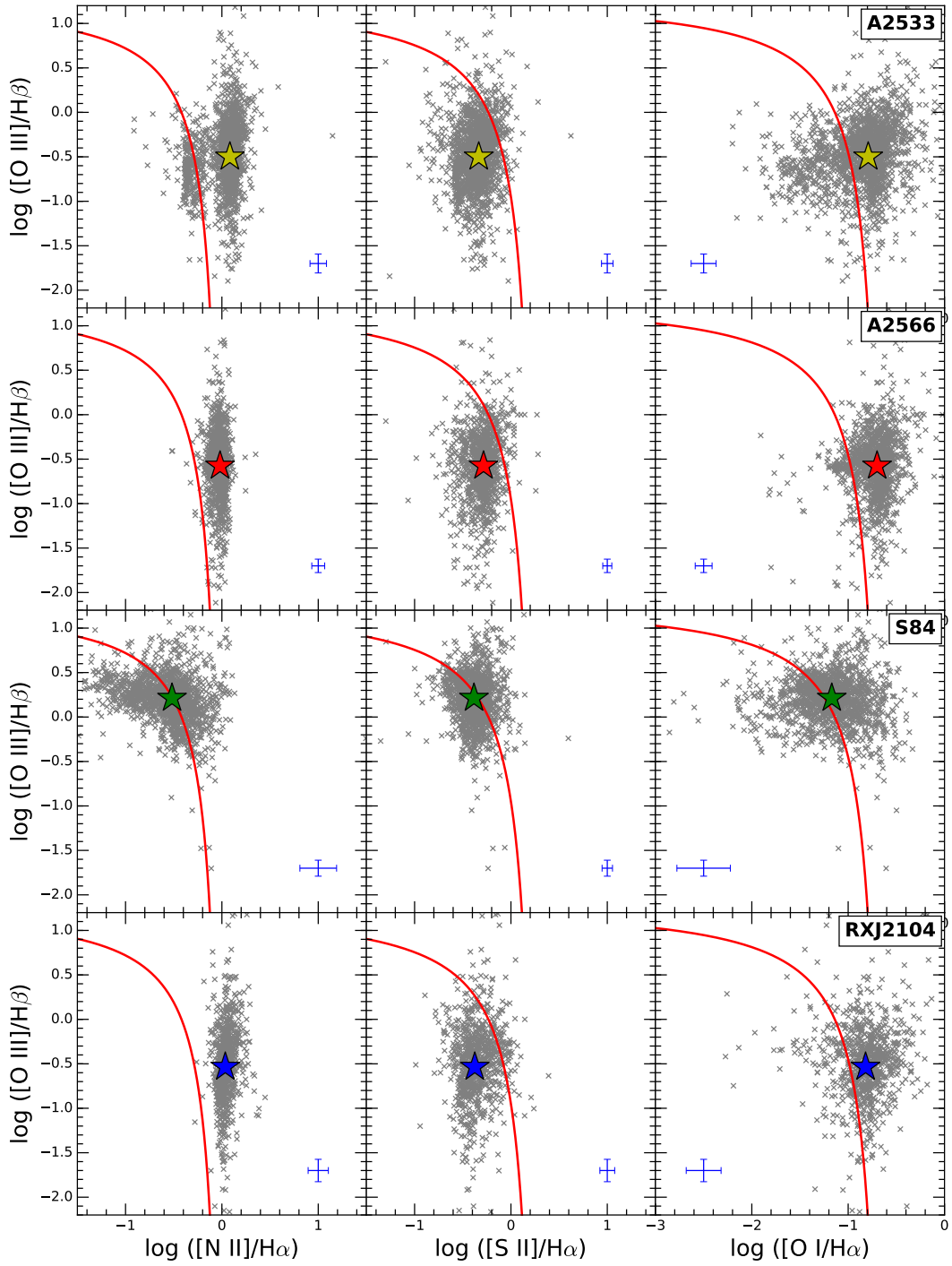

Figure 7.13: BPT diagnostic diagrams for each cluster. The grey crosses are the line intensity ratios measured in individual spaxels, the filled coloured stars represent the median ratio values and the red line in each panel represents the extreme starburst limit of Kewley et al. (2006). Representative error bars are given in each panel which show the typical 1σ error on the line intensity ratios, as propagated from the uncertainty of the Gaussian fittings to each emission line.

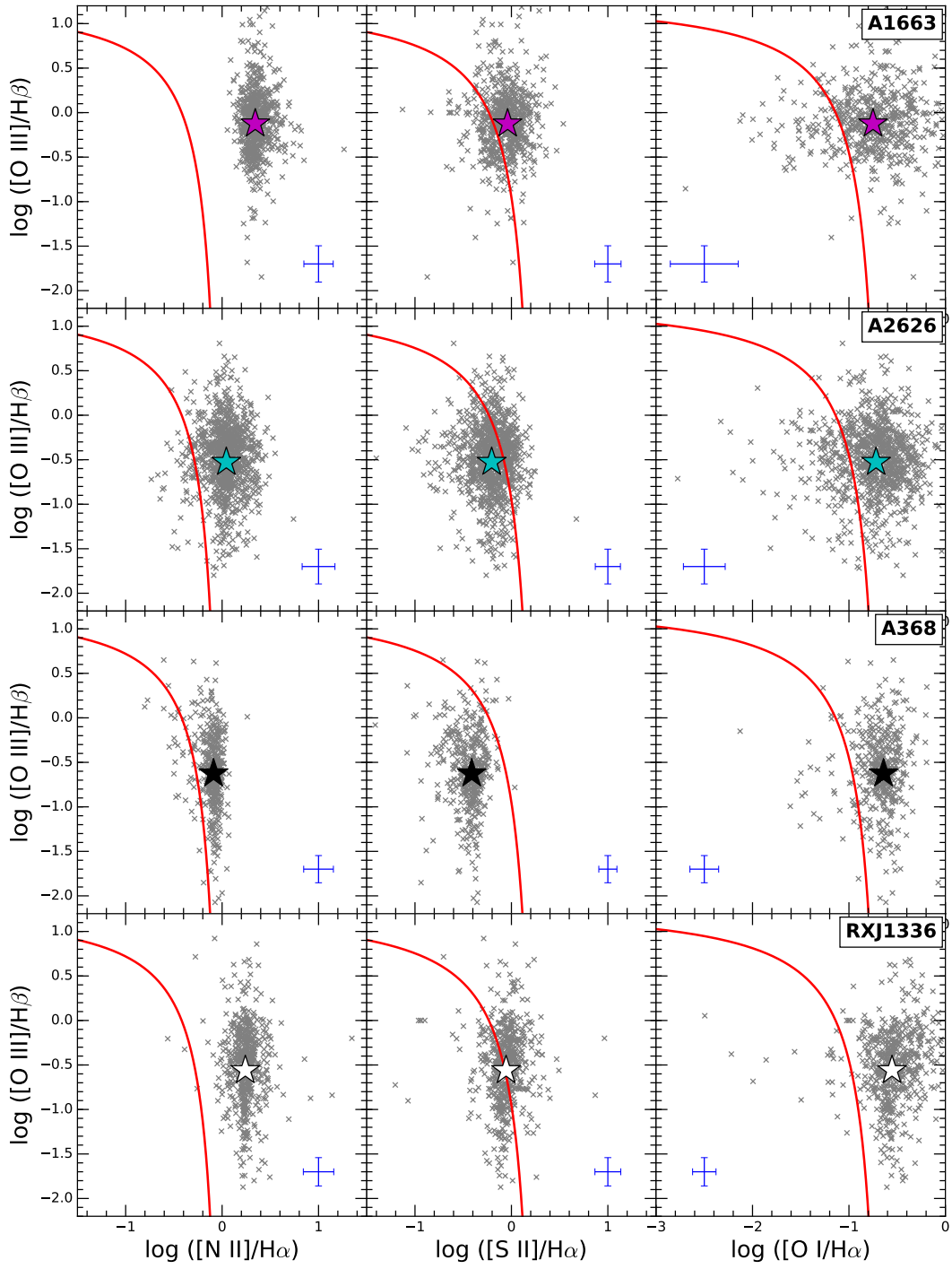

Figure 7.13 (cont.): Figure continued..

7.5 Discussion

7.5.1 Sources of ionisation

In the combined BPT diagrams of Figure 7.11 we find that the line intensity ratios for all but two of the systems (A1663 and S84) are grouped together. The majority of these systems do not consistently favour one side of the traditional division between a system dominated by either star formation or an AGN (Kewley et al., 2006). The [S II]/Hα ratio values are generally smaller than the extreme starburst limit, indicative of ionisation from star formation, but, the [N II]/Hα and [O I]/Hα values are too high to be pure star formation. This degeneracy between the ionisation properties is well established for ionised gas in cluster cores. To illustrate this we display on the figure the line intensity ratios measured by McDonald et al. (2012b) of optical line emitting filaments in nine cool core clusters. These filaments have very similar values as the majority of our line emitting nebulae. This indicates the ionisation source for gas in cluster cores is often more complex than ionisation by star formation and/or AGN alone.

In McDonald et al. (2010) the Hα filaments used above for comparison are shown to be consistent with having originated from cooling of the ICM. Later, McDonald et al. (2012b) investigated a number of possible ionisation scenarios for the filaments and, based on the line intensity ratios, conclude that the ionisation is caused by a combination of stellar and non-stellar processes. They find that ionisation by X-rays from the ICM is likely to contribute, but that ionisation by a combination of star formation and shocks best describes the line intensity ratios observed. The similar line intensity ratios measured in most of our systems would therefore be consistent with this scenario also. We test this further by overlaying the model predictions, from different ionisation sources, from McDonald et al. (2012b), to the average line intensity ratios for our MUSE targets (Figure 7.12). The figure shows that no one set of models, from self-ionisation of the ICM, star formation or shocks, accurately matches the observational data – but as McDonald et al. (2012b) quantitatively evaluate, are likely to be better described by a combination of these three sources.

There are two obvious outliers in our observations however, A1663 and S84. The

gas of A1663 has much higher line intensity ratios than the others, lying to the right of the Kewley et al. (2006) extreme starburst line. This is consistent with values expected for low-ionisation nuclear emission-line regions (LINERS; Heckman 1980), suggesting AGN emission is the primary source of ionising energy. The intensity ratios for S84 conversely are consistent with ionisation from star formation, as the median line intensity ratios lie essentially on the extreme starburst line in all diagnostic diagrams. This is consistent with the optical imaging which shows a significant blue stellar continuum cospatial with the ionised gas. The ionisation properties and the presence of the significant stellar continuum suggest that this system is distinct from the other line emitting nebulae, and likely not associated with cooling of the ICM. More discussion on this will saved for § 7.5.2 below.

7.5.2 Notes on Individual Systems

This section will explore the properties of the more remarkable line emission features present in these systems.

A2566: The majority of the optical line emission in the core of this cluster is spatially offset from the BCG, to the north-west (Fig. 7.2). The peak of the line emission is 5.2 kpc away from the core of the BCG. The offset line emission in A2566 was first reported in the VIMOS observations of Hamer et al. (2016). They discussed the similarities between the offset nature of the line emission with that observed in A1991, A3444 and Ophiuchus in Hamer et al. (2012), which were all demonstrated to be linked to an offset in the X-ray peak. However, they also note the presence of a nearby companion galaxy to the BCG (which is 6.8 kpc away and has a velocity offset of $238 \pm 10\,\mathrm{km\,s^{-1}}$ from our analysis in Chapter 6) and an asymmetric extent in the stellar envelope of the BCG, in the direction of the line emission, which indicates ongoing interaction between the two galaxies. Hence the offset emission in A2566 could be due to a gas–rich merger between these two galaxies. Whereas the offset line emission in the three cases of Hamer et al. (2012) were found to be cospatial with the X-ray peak, the lack of high resolution X-ray data for A2566 at the time meant they could not confirm a link between the offset line emission and

the dynamical state of the ICM.

Using the recent *Chandra* observation however we can now investigate the X-ray properties of this cluster. The surface brightness profile of the X-ray emission is strongly centrally peaked, suggesting this is likely a cool core cluster. This is consistent with the well established connection between cool core clusters and optical line emission (e.g. Crawford et al. 1999; Cavagnolo et al. 2008). In Figure 7.14 the *Chandra* X-ray data contours are overlaid onto the Hα kinematic map which shows the X-ray peak is clearly offset from the BCG and is spatially coincident with the optical line emission. This is similar to the observations of the three systems with offset line emission in Hamer et al. (2012) and suggests there likely exists a causal link between the dynamical state of then ICM and the offset ionised gas in A2566. The X-ray contours also show a higher concentration of isophotes toward the north and west of the X-ray peak, and elongation in the opposite directions. This morphology is consistent with an interpretation that the density peak of the ICM is in the process of sloshing (Ascasibar & Markevitch, 2006; Markevitch & Vikhlinin, 2007; ZuHone et al., 2010, 2011) and has been disturbed away from the BCG position toward the north and the west, leading to the skewed trailing contours opposite to its direction of motion. The 3D trajectory of the X-ray peak is however difficult to interpret. Therefore, in light of these X-ray data, the interpretation that the ionised gas originates from a cool core, with the offset emission due to sloshing of the ICM, is clearly favoured over the gas–rich galaxy–galaxy merger scenario, where the ICM would be less affected.

The kinematics of this nebulae are complex with some structure indicated. The velocity profile of the line emission along a radial axis is presented in Figure 7.15. The bulk of the gas is red–shifted with respect to the stellar continuum of the BCG, however there is a loop protruding from the peak position of the line emission, which is moving toward the line-of-sight (relative to the rest frame of the bulk of the projected extent of the gas). The velocity dispersion map reveals the boundary of this loop. As the peak of the optical line emission lies here, coincident with a region of blue stellar continuum, this could be interpreted as the observer viewing a line emitting filament along the line-of-sight.

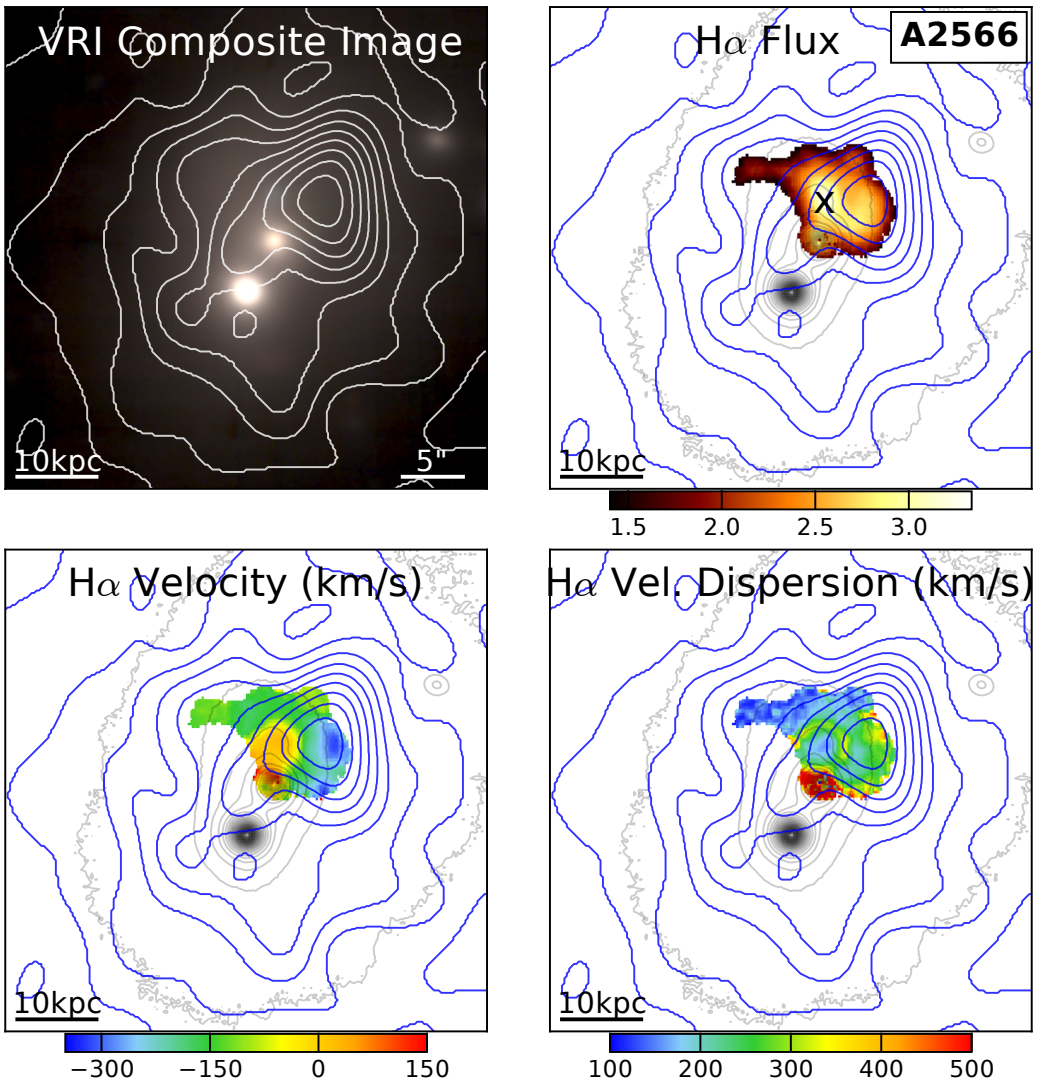

Figure 7.14: X-ray contours from *Chandra*, shown in white (*top left*) and blue, overlaid onto the stellar continuum and Hα maps for A2566. The kinematic maps are as described in Fig 7.1 and X-ray contours have arbitrary levelling. The peak of the X-ray emission is clearly offset from the BCG position and spatially coincident with the offset optical line emission.

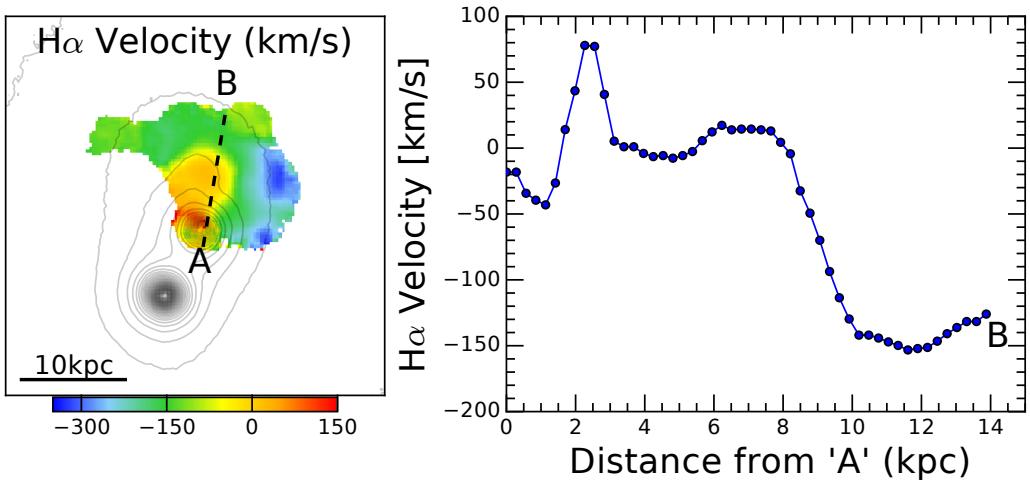

Figure 7.15: Velocity profile for A2566. *Left:* The Hα velocity map. *Right:* The Hα velocity profile along the major axis of the line emitting filament, indicated by the dashed black line in left panel.

The BPT diagnostic diagrams (Fig. 7.13) show that the majority of the ionised gas has line intensity ratios consistent with that of the Hα filaments of McDonald et al. (2012b) and most of the other systems studied here. This, combined with the peaked X-ray surface brightness profile suggests the gas is likely to have originated from cooling of the ICM and that the ionisation is likely a combination of star formation and non-stellar processes, such as X-ray photons from the surrounding ICM and shocks (McDonald et al., 2012b). There is region north of the BCG, (see Fig. 7.2), where there is a blue stellar continuum. This region shows smaller flux intensity ratios than the surrounding gas, particularly in the [O I]/Hα ratio, which is consistent with stellar photoionisation. So it is likely the young blue stars we see are a significant source of the ionisation locally. The star formation is likely to be in-situ, originating from the cooling flow. An observation in the CO, with an instrument like ALMA, would be useful to explore whether there is a significant mass of cold molecular gas here, as was observed for A1991 (Hamer et al., 2012).

The BCG of A2566 is a confirmed radio source, with a luminosity from NVSS of $L_{1.4\mathrm{GHz}} = 4.1 \times 10^{23}\,\mathrm{W\,Hz^{-1}}$. The radio emission is spatially coincident with the BCG and the line intensity ratios of the gas coincident with the BCG core show some high values, which are consistent with ionisation from an AGN. However, this

only occurs locally to the BCG with no clear ionisation radiating from the BCG core outward to the bulk of the gas. Suggesting the active nucleus is not a dominant source of the ionisation throughout most of the gas.

A2533: Probably the most striking system in our observations is Abell 2533 (see Fig. 7.1). There is a strong linear feature of optical line emission with a projected spatial extent of ~ 40 kpc and a peak-to-peak velocity gradient of ~ 500 km/s. The integrated flux of the Hα emission is $6.7 \times 10^{-15}\,\mathrm{erg\,s^{-1}\,cm^{-2}}$. The line emission is spatially coincident with clear features in the optical continuum, specifically a filament of blue star formation to the north-east of the BCG core, and a strong dust lane to the south-west. The presence of dust obscuration against the stellar component of the BCG suggests the dust and ionised gas to the south-west is foreground to the bulk of the stars in the BCG.

The kinematics of the ionised gas are complex. The velocity is blue–shifted (relative to the line-of-sight rest frame of the BCG) in the south-west (SW), but shifts to being red–shifted whilst still in the dust lane to the SW. The velocity gradient then appears to flatten out toward the north-east (NE), with a pile up of Hα flux at the NE end, before then looping back on itself toward the cluster core, giving rise to the maximum red–shifted velocity just NE of the core. The superposition of two separate velocity components in this region is revealed as an enhanced velocity dispersion here. We present the velocity profile along the filament in Fig 7.16. The 3D motion of the gas is difficult to interpret, but comparing the gaseous and stellar kinematics (Fig. 7.1) indicates the two are clearly decoupled.

On first inspection, the fact the gas SW of the BCG is blue–shifted and foreground to the main stellar component of the BCG and the gas on the opposite end of the filament is red–shifted, may suggest the gas is in outflow. However, on closer inspection the complex velocity structure suggests otherwise. If this were a nuclear outflow we would expect the switch between a positive and negative velocity to occur at the core of the BCG. However, from Fig 7.16 this happens at a galactic-centric radius of 6.5 kpc to the SW. The filament also does not go through the precise centre of the BCG, as we would expect if it were to originate from a central the supermas-

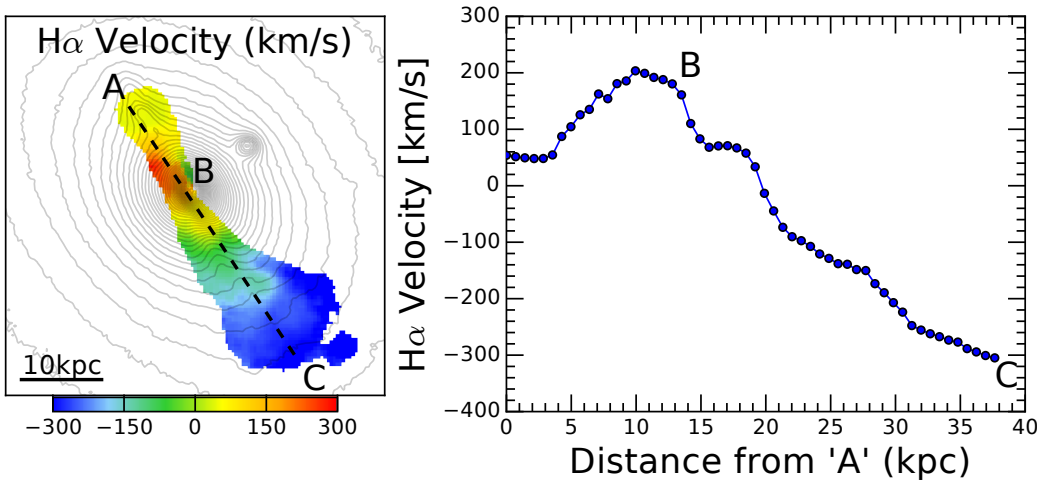

Figure 7.16: Velocity profile for A2533. *Left:* The Hα velocity map. *Right:* The Hα velocity profile along the major axis of the line emitting filament, indicated by the dashed black line in left panel.

sive black hole Further to this an NVSS observation of the BCG indicates it is also only a weak radio source ($L_{1.4\mathrm{GHz}} = 1.5 \times 10^{23}\,\mathrm{W\,Hz^{-1}}$), suggesting little significant nuclear activity. Additionally, the line intensity ratios of the gas are not consistent with the values expected for ionisation by AGN activity. These considerations all make the nuclear outflow scenario unlikely.

Instead, the line intensity ratios for most of the gas are consistent with the $H\alpha$ filaments in known cool core clusters from McDonald et al. (2012b), suggesting the ionised gas may originate from cooling of the ICM, with a similar ionisation mechanism to McDonald et al. (2012b). The exception to this is the region NE of the BCG core, where there is a clear blue continuum (see Fig. 7.2). In this region the filament shows line intensity ratios smaller than the extreme starburst limit of Kewley et al. (2006), suggesting the ionisation in this region is dominated by stellar photoionisation from the young stars which are visible in the broadband continuum. This section of differing ionisation properties is clearly distinguishable in the spaxel-by-spaxel BPT diagrams (Fig. 7.13).

The very long 40 kpc spatial extent of the optical line emission in the core of A2533 is reminiscent of that seen in some other clusters, for example the ~ 50 kpc filaments in A1795 (Cowie et al., 1983; Crawford et al., 2005). The filaments in

A1795 have a wealth of observational data which includes evidence of in-situ star formation (McDonald et al., 2014) and the presence of molecular gas (Salomé & Combes, 2004; McDonald et al., 2012c). These data suggest that the most likely scenario for A1795 is that the gas, and subsequent young stars, originate from condensation of the cooling ICM. So a line emitting filament of this extent originating from a cooling flow is not unprecedented.

The notable distinction between A2533 and A1795 however is that, while the core of A1795 has long filaments, the majority of the ionised and molecular gas is cospatial with the BCG core, whereas in A2533, the majority of the line emission is significantly offset from the BCG core. Indeed, even the gas which is closest to the BCG centre is slightly offset to it by ~ 1 kpc to the SE. The peak of the Hα flux in A2533 is at a galactic-centric radius of 11.7 kpc to the NE of the BCG core. As we have just discussed for A2566, offset line emission, in the few observations that exist, have been consistently associated with an X-ray peak offset from the BCG, likely due to ICM sloshing. The ionised gas in A2533 can consequently be interpreted in a similar way. We predict that this represents another example of ICM sloshing – this time mostly within the plane of the sky, with the sloshing along the major axis of the filament – and it is expected that the X-ray peak will be coincident with the offset line emission.

In Figure 7.17 we present the kinematic maps of the CO(1-0) line, measured by ALMA. Clearly there is a very strong association between the molecular gas and the ionised gas – the CO emission almost perfectly traces the MUSE derived Hα maps, both in terms of line intensity and kinematics. Similarities between ionised and atomic gas is well established in the literature (e.g. Edge 2001; Salomé & Combes 2004; Salomé et al. 2006). The molecular gas shows the same offset nature, with the peak CO emission matching the position of the Hα peak, offset from the BCG centre by ~ 12 kpc. The velocity profile is very similar, ranging from negative velocities in the SW to positive values in the NW, but with the complex superposition of two velocity components just NW of the BCG centre. The measured velocity dispersions in the ALMA observation are systematically smaller than the MUSE derived values, this is consistent with the ionised gas being hotter and more

turbulent than the molecular gas, but differences due to instrumental effects can not be ruled out. Hamer et al. (2012) previously demonstrated that A1991 has $1.9 \times 10^9\,M_{\odot}$ of molecular gas, coincident with the offset optical line emission and X-ray peak. This indicated that cooling flows can deposit cold molecular gas in isolation of, and away from, the BCG. If indeed the ICM of A2533 is undergoing sloshing also, then these ALMA data would confirm this suggestion.

Without high resolution X-ray data however we are unable to definitively link the offset gas with the dynamical state of the ICM at this time. A *Chandra* observation has been approved and is scheduled to be observed in July 2017 and will be included in the journal edition of this analysis (Green et al. in prep.). When the *Chandra* data become available we will be able to not only test whether the X-ray peak is offset, but also properties of any interaction and the level of sloshing, if present. Sloshing caused by a relatively minor interaction where the sloshing is induced by the gravitational pull of a passing subcluster should lead to the offset X-ray peak, but without the presence of significant shocks. Conversely however if there has been a significant interaction with an infalling group/subcluster then this should be visible with strong shocks in the ICM profile (Markevitch & Vikhlinin, 2007; ZuHone et al., 2010), particularly as it is likely we are viewing this system in the plane of the sky. The proximity of the shocks to the cluster core would also be indicative of the timescale since this interaction occurred and distinguish between a recent interaction, with close-by shocks, or a more long-lived precession of the BCG and X-ray peak, with larger scale shock features.

A further possibility for the origin of the gas is that it originated from a core penetrating merger of a gas–rich cluster member with the BCG. However, the lack of a significant nearby companion galaxy in the optical imaging may suggest this scenario is unlikely. It is possible that the excess blue continuum to the north-east is a remnant of this galaxy however. Fortunately, the ALMA data will enable us to determine the molecular gas mass of the filament and hence set a lower limit on the stellar mass of this hypothetical gas–rich galaxy. Unfortunately however, due to time constraints, this will not be possible prior to submission of this thesis. This will however be presented in the journal submission version of this analysis in the

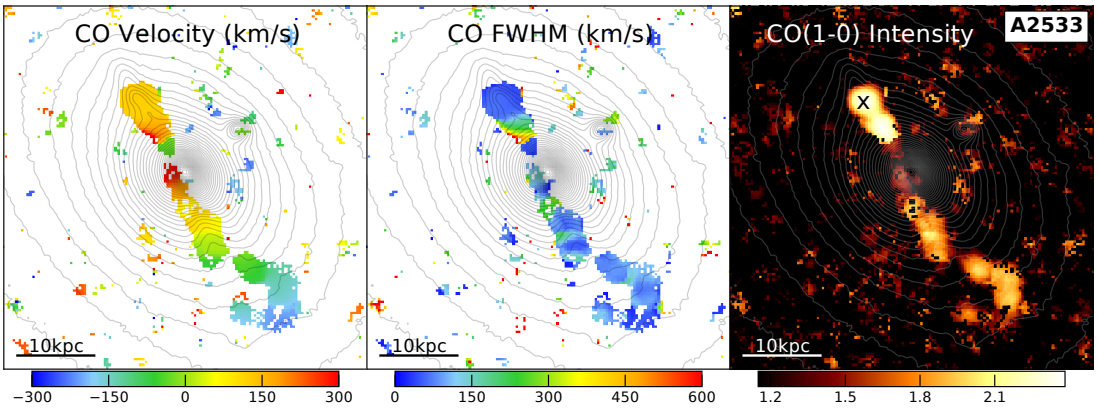

Figure 7.17: The spatially resolved CO(1-0) kinematic maps and flux for A2533, from an ALMA observation. The contours represent the stellar continuum, at arbitrary levelling. The CO line flux is presented in a log scale, with units mJy/beam, and the black cross represents the peak CO emission. The orientation is such that north is up and west is right.

near future (Green et al. in prep).

S84: The cluster core of Abell-S84 has a linear feature of optical line emission, with a spatial extent of 50 kpc (Fig. 7.4). The ionised gas does not appear to be associated with the BCG, but is instead spatially coincident with a significant quantity of stellar continuum of the same elongated morphology. From the GALFIT photometry applied in the previous chapter, we find that the linear feature has an i–band magnitude of ~ 17 mag. The velocity profile along this feature, presented in Fig. 7.18, spans from ~ -900 km s^{-1} in the NE to ~ -400 km s^{-1} in the SW.

The ionisation properties of the gas is distinct from the majority of our observations, with the line intensity ratios suggesting it is star formation dominated. This is consistent with the strong optical stellar continuum in this region, which is clearly blue along the extent of its major axis. This could perhaps result from in-situ star formation within a filament of gas, however, there is also red continuum emission toward the centre of the body, which would instead be more visually consistent with the view of an edge on spiral galaxy. This suggests this system is likely to be distinct

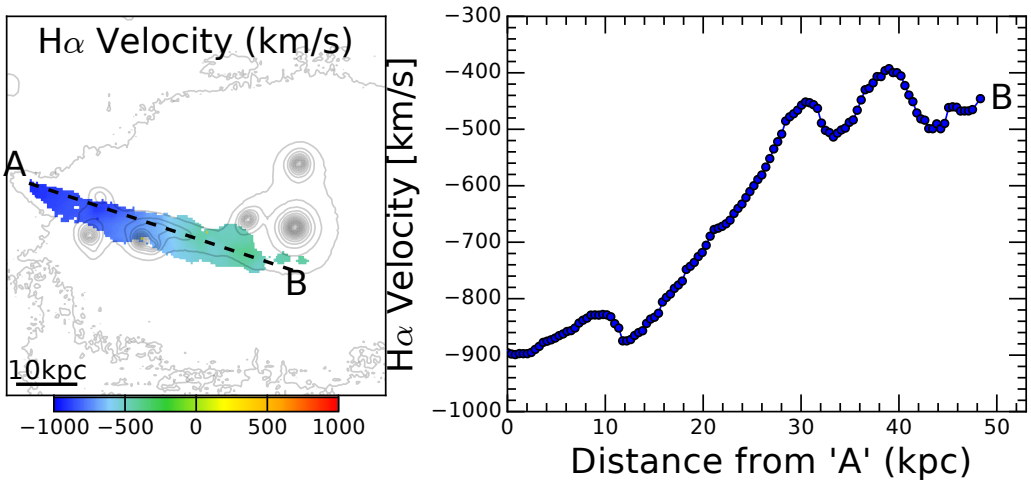

Figure 7.18: Velocity profile for S84. *Left:* The Hα velocity map. *Right:* The Hα velocity profile along the major axis of the line emitting feature, indicated by the dashed black line in left panel.

from the other clusters which exhibit optical emission lines due to the ionisation of radiatively cooled intracluster gas.

If this linear feature were indeed an edge-on spiral then the 50 kpc spatial extent of the gas/stars would suggest this is a particularly large galaxy. Whilst the velocity profile of the linear feature does show a velocity gradient we would expect a steeper turnover if this were the rotation curve of a spiral. Interestingly however, there are four galaxies toward the western end of the linear feature which have velocities all within 85 $\mathrm{km\,s^{-1}}$ of each other and, with an average velocity of -821 $\mathrm{km\,s^{-1}}$, have velocities broadly consistent with the linear feature in this region. This suggests that perhaps one, or more, of these galaxies have interacted with a spiral galaxy and the long linear feature is an edge-on-view of the unwinding of the spiral structure due to tidal forces. The morphology is consistent with perturbations spirals undergo during galaxy–galaxy interactions, as seen in many systems in the Arp-Madore *catalogue of southern peculiar galaxies and associations* (Arp & Madore, 1987), e.g. AM 1950-380, IC1908 (Arp & Madore, 1987; Rampazzo & Sulentic, 1992).

As the linear feature and aforementioned galaxies have a significant velocity offset from the BCG, of several hundred $\mathrm{km\,s^{-1}}$, then it is unlikely any of this interaction is associated with the BCG, with their apparent proximity likely to be due

to projection along the line-of-sight. Hence it is possible the potential interaction is occurring in the cluster outskirts, with the spiral galaxy having been recently accreted into the cluster environment, which would be consistent with this galaxy being gas rich.

RXJ2104-5149: The spatial distribution of the stellar continuum and the line emitting gas in this cluster core are curious (Fig. 7.3). The ionised gas is extended across an 11 kpc plume/filament to the south of the BCG core. There is a significant quantity of line emission offset from the BCG, with 47% of the flux coming from a region in excess of 4 kpc away from the BCG core and a secondary Hα peak 5.3 kpc south of the BCG. The line emission to the south is spatially coincident with an obscuring dust lane, suggesting it is foreground to the bulk of the stellar component of the BCG. The velocity profile of line emission is at rest with respect to the stars of the BCG at the furthest point from the BCG itself and then increasingly red–shifted toward the centre of the BCG. As the dust indicates the gas is in front of most of the stars then these kinematics would suggest the gas is infalling.

The optical stellar continuum shows complexity with multiple nuclei. There is a more diffuse nucleus, which we define as the BCG and then a much more compact source immediately to the NW, and there is essentially no velocity offset between these two nuclei along the line-of-sight (-35 ± 11 km/s). The primary Hα peak is coincident with the compact nucleus whereas the BCG itself shows significant Hα absorption. A small notch of excess continuum is observed to the south, coincident with the ionised gas, between the BCG nucleus and the dust lane. There is also an additional galaxy 20 kpc south-east, with an equally small velocity offset of -28 ± 6 km/s.

A potential explanation for the source of this gas is that this system represents a core penetrating gas–rich merger, where the compact stellar source to the north-west is the core remnant of the merged galaxy. The ionised gas could have been, and still be in the process of being, stripped from this galaxy during the merger. However, there is no obvious disturbance to the envelope of the BCG which would suggest an ongoing interaction.

An alternative, but unlikely scenario is that the compact source represents an offset AGN, which may have been perturbed from the centre of BCG during an interaction with the galaxy seen in the SE. The line emitting gas could then be a nuclear outflow from this AGN, with the dust having been entrained in this outflow. However, this is inconsistent with the apparent velocity profile. Also, crucially, the intensity line ratios of the gas are not consistent with AGN dominated ionisation and there is no radio detection associated with the compact source.

Alternatively, given that the line intensity ratios are similar to the ionisation properties associated with cool core filaments, this may represent just that. The substantial quantity of offset line emission may indicate some sloshing, but the apparent association between the gas and the compact source is hard to explain in this scenario.

A2626: Abell 2626 is well studied cluster at $z = 0.055$. It is a known cool core cluster (White et al., 1997; Wong et al., 2008) with a central cD elliptical galaxy (a.k.a. IC5338 and 3C464) with a clear double-nuclei (see Fig. 7.5). The south-west nuclei, which we will refer to as the BCG, is known to exhibit strong optical emission (Johnstone et al., 1987; Crawford et al., 1999). It is likely that these two nuclei are already in the process of merging, indicated by the velocity offset and spatial separation of only 191 ± 11 km s^{-1} and 3.5 kpc between the two nuclei, and the clear asymmetric extent in the cD envelope along the common axis of the nuclei, toward the SW.

The distribution of optical line emission is peaked on the core of the BCG, consistent with Crawford et al. (1999), however the MUSE observations also reveal the presence of two faint line emitting filaments toward the SW of the BCG. The core emission accounts for 85% of the Hα flux, but is not symmetric about the BCG core. There is extended emission to the N and NW, which archival *Hubble Space Telescope* (*HST*) imaging shows dust obstruction coincident with. The ionised gas shows a velocity gradient across the BCG from -260 km s^{-1} in the SE to $+150$ km s^{-1} in the NW extension. The *HST* imaging also reveals a thin dust lane across the core of the BCG in a NW–SE orientation. The velocity of the gas is consistent

with either rotation or nuclear outflow.

The filaments account for 15% of the Hα flux and the kinematics reveal some velocity gradient, with the filaments becoming increasingly blue–shifted with increasing radial distance from the BCG. However, without any noticeable dust obscuration, identifying whether the gas is foreground or background to the BCG, and therefore differentiating between outflowing or infalling gas, is not possible.

The *XMM-Newton* and *Chandra* X-ray observations of Wong et al. (2008) show that the X-ray peak is spatially coincident with the BCG and the bulk of the optical line emitting gas, as is typical for a cool core cluster with line emission. The X-rays also show an extension to the N–NW, coincident with the dust in the *HST* imaging and the line emission in our MUSE observation. Wong et al. (2008) also confirm a hard X-ray point source due an AGN associated with the BCG.

A number of radio observations at different frequencies exist for the core of A2626 (Gitti et al., 2004; Gitti, 2013; Ignesti et al., 2017; Kale & Gitti, 2017). The BCG is a strong radio jet galaxy (a.k.a 3C464), but unusually, is also surrounded by a diamond shaped set of four radio arcs (Kale & Gitti, 2017). It has been proposed that the set of radio arcs could result from precessing radio jets to the north and south, with the gravitational influence of the second nuclei to the north-east contributing to the precession (Wong et al., 2008; Gitti, 2013). A radio jet from the BCG was observed at 1.5GHz in Gitti et al. (2004), orientated toward the SW, in the same direction as the line emitting filaments, suggesting perhaps the ionised gas in these filaments has been entrained in the radio jets.

Interestingly, the velocity gradient in the ionised gas coincident with the BCG core is orientated perpendicular to the radio jet. Hence it is unlikely that the velocity structure of the gas represents a nuclear outflow. Instead, the velocity structure is better described by a rotating disk of ionised gas around the BCG, analogous to that seen in other cool core clusters, e.g. Hydra-A (Hamer et al., 2014). This gas, which is likely to have originated from cooling of the dense ICM, could be in the process of disk accretion onto the AGN within the BCG, leading to the jets perpendicular to this disk. The cospatial nature of the dust lane across of the BCG with this rotating gas supports this scenario, with the dust being part of the edge-on disk.

A1663: The spatial distribution of the ionised gas in Abell 1663 is fairly typical (Fig 7.6), with the bulk of the gas centred on the BCG and a line emitting filament to the SE. However, this system stands out from the others in this sample because of the consistently higher line intensity ratio values than expected for typical line emission regions in cool core clusters. The BPT diagnostic diagrams indicate ionisation consistent with LINERs. It should be pointed out that line ratios in the traditional LINER parameter space may also be attributable to photoionisation by hot evolved stars, particularly in extended regions of emission (e.g. Belfiore et al. 2016; and references therein), however there is evidence for an AGN in the BCG of A1663 so the LINER interpretation is still favoured. Unfortunately no high resolution X-ray observation exists to identify an AGN point source, but there are radio observations which reveal this BCG has significant radio emission, with an NVSS luminosity of $L_{1.4\,\mathrm{GHz}} = 6.24 \times 10^{23}\,\mathrm{W\,Hz^{-1}}$. GMRT observations in Giacintucci et al. (2007) show radio lobes to the north and south of the BCG, with spatial extents of tens of kpc. The optical filament itself appears to hug the outskirts of the southern radio lobe, suggesting a potential dynamical link between the ionised gas and the radio emitting plasma.

RXJ1336-0331: The BCG of RXJ1336-0331 appears to be a triple component galaxy (see Fig.7.7), however our stellar kinematic analysis suggests that, with a velocity offset of 1680 $\mathrm{km\,s^{-1}}$, the third, most northern, component is likely a projection effect. A *HST* observation, presented in Cooke et al. (2016b) shows clear dust obscuration across the BCG and Cooke et al. (2016b) determine a modest star formation rate $3.76\,M_{\odot}\,\mathrm{yr^{-1}}$ from the NUV. This is consistent with the NUV excess that we measured in the BCG in Green et al. (2016) (Chapter 3). We find strong optical line emission over a $\sim 23 \times 13$ kpc extent across the BCG (Fig. 7.7). The line intensity ratios however are not consistent with star formation being the dominant source of ionisation. Cooke et al. (2016b) tentatively attribute the star formation in RXJ1336-0331 as resulting from the assumed major merger, similar to SDSS J1531+3414 (at $z = 0.335$) in which the star formation is thought to be con-

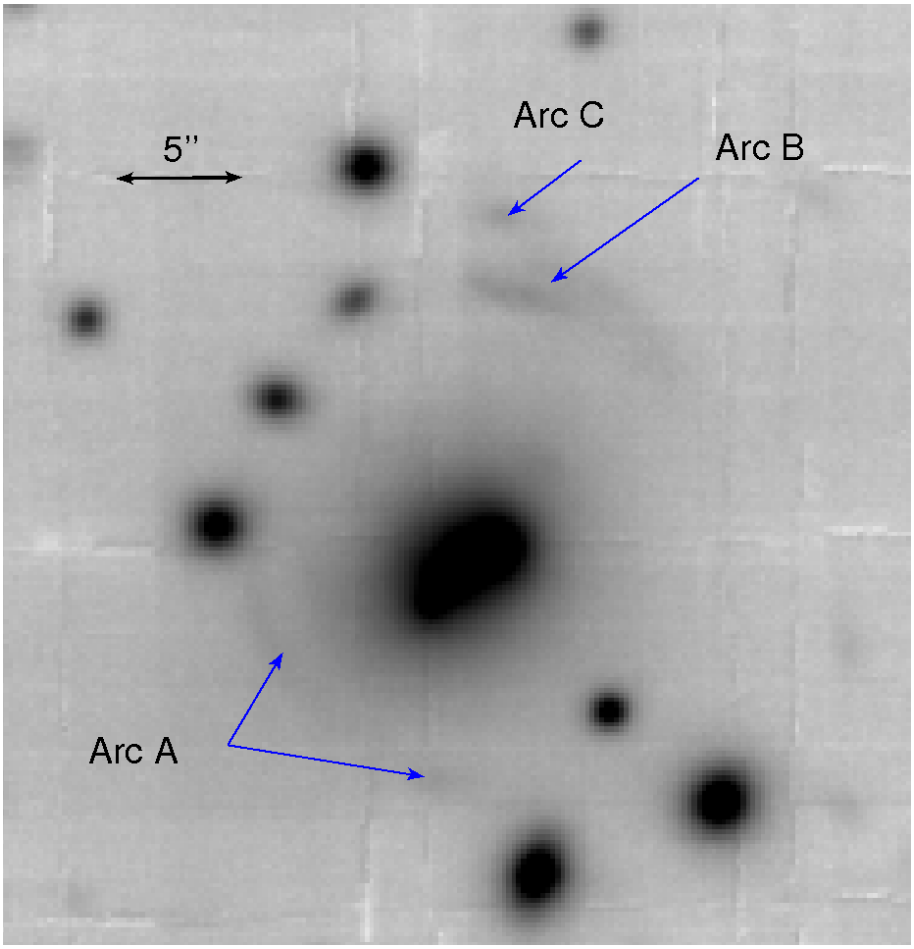

Figure 7.19: MUSE broadband continuum image for RXJ1336-0331 showing the three distinct gravitational arcs.

nected to the major merger of the BCG (Tremblay et al., 2014). From our analysis in Chapter 6 we find the central and south-eastern components have a separation of only 4.6 kpc and 180 $\mathrm{km\,s^{-1}}$ and a luminosity ratio of 2.9, confirming this likely represents a major merger. So the star formation may result from the merger, however, without high resolution X-ray data to confirm whether it is a cool core cluster not, a connection to cooling of the ICM can not be ruled out either.

RXJ1336-0331 is known to exhibit strong gravitational arcs and was included in the *HST* follow up of Sloan Giant Arcs Survey (SGAS; Bayliss et al. 2011; Gladders et al. in prep). It shows a set of three gravitational arcs, as shown in Figure 7.19, and from fitting the O II doublet we determine the following redshifts for the gravitationally lensed galaxies: $z = 0.956$ for Arc A, $z = 1.474$ for Arc B and $z = 0.963$ for Arc C.

A368: The BCG of Abell 368 has a clear double component, with separations of 6.1 kpc and 149 $\mathrm{km\,s^{-1}}$ between the galaxies, as such they are likely to be dynamically bound ($p_{bound} = 93\%$). An archival *HST* image reveals clear dust obscuration in the BCG, to which the optical line emission we observe is spatially coincident. From Chapter 3 we know the BCG shows an excess in the $W3$, indicating probable star formation. Hoffer et al. (2012) determine a central gas entropy of $50\,\mathrm{keV\,cm^2}$ for the cluster, which would classify it as a weak cool core (Hudson et al., 2010). It is however above the apparent critical threshold of $30\,\mathrm{keV\,cm^2}$ associated with cool cores and BCG activity (Cavagnolo et al., 2008), so it is reasonable to assume therefore that the star formation and ionised gas result from the merger of these two galaxies.

7.5.3 Offset Line Emission

The MUSE and *Chandra* observations of A2566 above confirm a spatial coincidence between offset line emission and an offset X-ray peak, similar to A1991, A3444 and Ophiuchus (Hamer et al., 2012). This suggests that offset line emission in cluster cores is likely to be linked to the state of the ICM, specifically, that offset line emission is indicative of sloshing of the ICM. Based on this, we predict that the offset line emission present in A2533 is of a similar nature and that the X-ray peak

has been decoupled from the BCG position.

The total number of systems confirmed to exhibit optical line emission offset from the BCG is still small, so more observations are needed to reaffirm the sloshing interpretation when offset line emission is present. However, within a sample of 73 VIMOS IFU observations, targeting cluster cores known to exhibit line emission, Hamer et al. (2016) find only four systems with offset line emission, suggesting this phenomena is rare. It is interesting to note however that all such systems with offset line emission have been discovered in integral field spectroscopy of cluster cores. Previously using long slit spectroscopy it is unlikely that slits would have been placed in such a way that the offset line emission would have been detected. Also, so far the spatial offset between the line emission and BCG have only been observed to be of the order of a few kpc. This may indicate that this phenomena only results when a minor disturbance to the ICM occurs, on a scale such that sloshing is induced, but which does not destroy the relaxed cool core nature of the ICM. However, this may also be an observational effect, where systems with more significant spatial offsets exist but have yet to be detected because of the narrow observational field historically associated with targeted spectroscopy. It is possible that MUSE, with its uniquely wide field-of-view will uncover such systems. However, with IFU observations becoming more common, with surveys such as the Sydney-Australian-Astronomical-Observatory Multi-object Integral-Field Spectrograph survey (SAMI, Croom et al. 2012), we expect more examples of offset line emission will be uncovered in the near future.

7.5.4 Galaxy Merger Driven Line Emission?

It has been proposed that optical line emission and star formation in BCG can be triggered by mergers. As our target selection was primarily based on morphologies consistent with mergers this sample can provide some useful insight into this. It should be stressed that the following is for illustrative purposes only and that the assumptions are not valid. From our parent cluster sample of 784 clusters, only 144 have cluster cores which would satisfy our target selection, i.e. contain a massive companion galaxy within a projected radius of 20 kpc – giving a generous upper limit

on the fraction of BCGs which are likely to undergo mergers of 18 per cent. Of our 23 MUSE targets only 10 have optical line emission. So assuming the MUSE targets are representative of all BCG mergers (when in actual fact selection favours the most likely mergers) and assuming that all the optical line emission in our observations result from mergers (which from the discussion above is not the case) then that would suggest 44 per cent (10/23) of mergers lead to line emission – giving an upper limit on the fraction of BCGs expected to show line emission due to mergers of 8 per cent (0.44*0.18). So the rarity of merging BCGs alone suggests that, whilst merging can cause line emission, it is not sufficient to account for the high fraction of line emitting BCGs (32%; Crawford et al. 1999) that are observed. The strong association between optical emission lines and cool core clusters (e.g. Cavagnolo et al. 2008; McDonald et al. 2010) support the idea that most ionised gas in cluster cores originates from the cooling ICM. Indeed, within our MUSE targets, all those with high resolution X-ray data have cool core like X-ray profiles. It is only in S84, RXJ1336, A368, A3934 and RXJ2104 that the cooling flow scenario (and related AGN feedback cycle) is not favoured above the possibility of merger induced line emission. Until such targets receive *Chandra* observations no more can be said to distinguish between these two scenarios.

7.6 Summary and Conclusions

We observed 23 cluster cores with the wide-field Multi Unit Spectroscopic Explorer (MUSE), targeting systems with a BCG likely to undergo a merger. Of these, ten were discovered to show optical emission lines in the cluster core. The morphology of these gaseous nebulae were found to be varied, ranging from compact sources with spatial extents of only ~ 4 kpc, centred on the BCG, to 40 kpc long filaments offset from the BCG.

We measured the line intensity ratios and, with the exception of Abell 1663 and Abell S84, found that they were similar to one another and Hα filaments in known cool core clusters. The average ionisation properties for most of the systems suggest a more complex mix of ionisation mechanisms than either star formation or AGN

alone. However, A1663 was found to be more consistent with ionisation from an AGN, whereas S84 conversely was best described by star formation. Also spatial variation was discovered for the intensity ratios for some of the systems, suggesting that localised variations in the ionisation source do occur.

Two systems were discovered in which the majority of the line emission is offset from the BCG, Abell 2533 and Abell 2566. A *Chandra* observation of A2566 confirmed the X-ray peak was offset from the BCG and was cospatial with the offset optical line emission, matching the observations of A1991, A3444 and Ophiuchus in Hamer et al. (2012). This is consistent with the scenario in which the X-ray peak has been perturbed away from the BCG by sloshing of the ICM, due to a large scale interaction. Which suggests the cooling of the ICM can occur in isolation of, and away from, the BCG.

The most striking system observed however was A2533, with evidence suggesting this is perhaps the first example of ICM sloshing viewed such that the bulk of the activity is across the plane of the sky. We discovered a 40 kpc long filament of optical line emitting gas spanning the BCG, spatially coincident with dust obscuration and star formation on opposing sides of the BCG centre, but with the peak optical line emission offset from the BCG core by $\sim$ 12 kpc. With an ALMA observation we revealed the presence of cold molecular gas, which was found to almost perfectly trace the morphology and kinematics of the ionised gas. We predict therefore that the offset gas is the result of gas sloshing and that the X-ray peak is expected to be offset from the BCG and spatially coincident with the offset gas. Along with A1991, this would be one of two cases where CO emission has been confirmed offset from the BCG in an assumed cooling flow scenario – showing that cool core clusters can continue to undergo significant cooling and deposit cold molecular gas in isolation of the central galaxy. However, until a scheduled *Chandra* observation is taken, a connection between the offset gas and an offset X-ray peak cannot be definitively established.

Additionally, we discussed the likelihood of the observed gas having originated from a cooling flow or a merger for A368, RXJ2104-5149 and RXJ1336-0331. And we presented evidence for a potential gas disk around the BCG of A2626, ionisation

by an AGN in A1663, as well as a possible unravelling of a spiral galaxy in S84.

Chapter 8

Summary and Conclusions

The location of Brightest Cluster Galaxies (BCGs), at the centre of the clusters of galaxies, suggests a strong link between the formation and evolution of the BCG and that of the host cluster; with their unique environment distinguishing the evolution of BCGs from that of other massive ellipticals. In this thesis I have explored some of the contributing factors to the unique evolution of BCGs. In particular, I have explored the interaction between BCGs and radiative cooling of the surrounding intracluster medium, which leads to the presence of multi-phase gas and fuels star formation and AGN activity in these central galaxies. I have also investigated the continued stellar mass assembly of BCGs via galaxy–galaxy mergers at low redshift.

In Chapter 3 a multi-wavelength exploration of the photometric colours of BCGs was presented. Drawn from a representative sample of 981 X-ray selected clusters, the aim was to estimate the prevalence of star formation and AGN activity in BCGs from such a sample. This was done by identifying galaxies with colours which deviate from that expected for a passively evolving BCG. It was found that, whilst the majority of BCGs are consistent with passivity, at least 14 per cent showed a significant colour offset in at least one colour regime, which would be consistent with star formation and/or AGN activity. At optical wavelengths 8 per cent were found to be blue relative to the red sequence, 9 per cent were found to have excess red emission in the mid-IR and at least 4 per cent shown to exhibit enhanced NUV emission. A strong association was discovered between significant colour offsets and optical line emission, with offset BCGs usually also exhibiting strong optical line emission –

reinforcing the interpretation of these BCGs being "active". A strong association was also discovered between BCG colour and the X-ray luminosity of the host cluster, with a higher proportion of high X-ray luminosity clusters showing significant colour offsets. This correlation therefore has implications regarding the proportion of active BCGs one would discover and the selection function of a sample of clusters. The overall conclusion of this chapter is therefore that a significant fraction of BCGs are in fact active, contrary to their "red and dead" reputation. The interpretation is that this activity is connected to radiative cooling of the ICM, as is well established in the literature (e.g. Rafferty et al. 2008; Hoffer et al. 2012; Rawle et al. 2012), which is supported by the connection between BCG colour and the presence of line emission, suggestive of multi-phase gas (e.g. Crawford et al. 1999; Cavagnolo et al. 2008; McDonald et al. 2010). As such, this simple technique of identifying active BCGs, and by extension cool core clusters, via BCG colours, could be utilised in the future with the advent of yet wider and deeper photometric surveys, such as the LSST, and combined with increasing numbers of clusters, from X-ray survey telescopes such as eROSITA, as well as the increased numbers of optically selected systems. This could act as the first round towards the identification of interesting objects for detailed follow-up. Follow-up which could include X-ray observations (e.g. with *Chandra*), optical and NIR imaging (e.g. with E-ELT, *HST* and *JWST*), integral field spectroscopy (e.g. with MUSE) and radio observations (e.g. with SKA) – all which combined are expected to greatly further our understanding of the feedback cycle between the cooling of the ICM and BCG activity.

In Chapter 4, the ambiguity between cluster emission and AGN emission in low resolution X-ray data was addressed. When analysing X-ray data, if evidence suggests a strong AGN exists, the X-rays are generally attributed to the AGN. However, when the AGN is in a rich cluster, and particularly hosted by the BCG, the cluster emission may still be a significant contributor. This leads to a selection effect against the detection of BCGs with strong ongoing AGN activity (such as occurred for the Phoenix cluster; McDonald et al. 2012a), yet, studying such systems is vital in understanding AGN feedback. To this end, a systematic investigation of the colour–magnitude relation around $\sim$ 3500 *ROSAT* selected AGN was conducted in order

to recover such 'missing' clusters. 22 systems were found in which an overdensity of red galaxies exists, consistent with the cluster red sequence, and where the AGN host galaxy is visually consistent with a BCG. Of these, six 'best' candidates were identified which have a red sequence richness similar to that of confirmed clusters of the same X-ray luminosity, suggesting their X-ray contribution is likely a comparable mix of AGN and cluster emission. The evidence suggests these are new examples of the relatively rare systems where a substantially powerful AGN, still in the outburst process (note that radio emission from AGN activity over a much longer timescale is common in BCGs), is located in the centre of a substantially massive cluster. High resolution X-ray observations of these systems have been requested in order to confirm whether this indeed the case. Identification of such systems will ultimately provide better statistics relating to both the prevalence of, and energetics involved with, AGN in BCGs – increasing our understanding of the role of AGN feedback in this unique environment. Consideration of the issues addressed in this Chapter will be particularly important in the future with the next generation of X-rays survey telescopes, such as *eROSITA*, set to uncover vast numbers of new X-ray sources; including clusters, AGN *and* the two combined.

Keeping with the theme of BCG activity, in Chapter 7 the properties of optical line emitting nebulae in ten cluster cores were explored with IFU data from MUSE. The morphologies and kinematics of these nebulae were found to be varied, as is common for ionised gas in cluster cores (e.g. Wilman et al. 2006; Hatch et al. 2007; Hamer et al. 2012, 2016). The line intensity ratios revealed most of the systems have similar average ionisation properties to one another and known Hα filaments in cool core clusters, and suggest a more complex mix of ionisation sources is necessary than either star formation and/or AGN in isolation (McDonald et al., 2012b). Some spatial variation in the intensity ratios for some of the systems was measured however, suggesting localised variation in the ionisation source. The likelihood of the observed gas having originated from a cooling flow or a merger were discussed for RXJ2104-5149 and RXJ1336-0331, with little evidence to favour one over the other. Evidence was also presented for a potential gas disk around the BCG of A2626 (which is a strong radio source), ionisation by an AGN in A1663, as well as

a possible unravelling of a spiral galaxy in S84. The main results however were related to two systems which exhibit offset line emission, in which the majority of the gas is spatially offset from the BCG. With new a *Chandra* observation of one such system, Abell 2566, a spatial coincidence between the X-ray peak and line emission was confirmed, both offset from the BCG. This matches the observations of similar systems in Hamer et al. (2012) and indicates that cooling of the ICM can occur in isolation of, and away from, the BCG. The offset X-ray peak and disturbed X-ray contours for A2566 are suggestive of possible sloshing of the ICM (Markevitch & Vikhlinin, 2007). The most striking system however is Abell 2533. It is shown to exhibit a 40 kpc long filament of offset line emission, which is spatially coincident with dust and star formation in the stellar continuum. A significant quantity of cold molecular gas, revealed by an ALMA observation of the CO(1-0) line, is also found, which almost perfectly traces the ionised gas. The cluster is currently awaiting a *Chandra* observation, however the prediction is that this represents another example of ICM sloshing – this time mostly within the plane of the sky – so it is expected that the X-ray peak will be coincident with the offset line emission. If this is indeed confirmed to be the case, the significant quantity of molecular gas and spatially coincident star formation would demonstrate that significant mass depositions of cold gas can occur in cluster cores, offset from the BCG. Such rare systems therefore present the opportunity to study the cluster cooling flow scenario in isolation from the AGN feedback which BCGs provide.

At the centre of a dense environment, BCGs are expected to grow significantly through mergers (Dubinski, 1998; De Lucia & Blaizot, 2007; Laporte et al., 2013), however there is suggestion that little growth occurs below $z \sim 0.5$ (Lin et al., 2013; Oliva-Altamirano et al., 2014). In Chapter 6, IFU observations of 23 cluster cores with MUSE – which were selected on close companions to, or multiple components within, the BCG – were presented in order to address the issue of late stellar assembly of BCGs. The stellar kinematics for each cluster galaxy within the MUSE field-of-view were evaluated and the likelihood of each galaxy being bound to their host BCG determined. Of the 125 cluster galaxies with spectroscopy, 30 per cent were found to have a high bound probability, $p_{bound} > 0.7$. The merger timescales for

each of the galaxies were estimated and the average merger rates and BCG stellar mass growth derived. Constraints on the average stellar mass growth of BCGs since $z = 0.25$ were placed at between 9 ± 3 and 57^{+20}_{-17} per cent. The typical literature values of 10–20 per cent of mass growth over this period favour more modest growth than the upper limits. Unfortunately however, selection effects do not permit tighter constraints on the mass growth rate. It was found that the estimates were dominated by extrapolation of a few very nearby, very massive companion galaxies and that when these particular systems were excluded a mass growth rate consistent with the literature values was discovered. Although the target selection favours major mergers, a significant fraction of likely minor mergers were serendipitously discovered by virtue of the wide field-of-view afforded by MUSE. It was found that 62 per cent of estimated mergers were in fact minor mergers, but that they account for only 18 per cent of the BCG mass growth – however it should be stressed that our selection favours an overestimation of the major merger contribution. Despite the evaluated constraints being broad, it has been demonstrated that a non-negligible BCG stellar mass assembly is still under way at low redshift. In order to better constrain the average BCG stellar mass growth rate however a larger and more representative sample of BCGs will need to observed, with instruments like MUSE – and indeed an extension of this project, including a further ten similar observations, has been awarded (PI Green; ESO programme ID 099.A-0862(A)). Plans also include a similar analysis of a control sample of cluster cores, which have been observed with MUSE, but selected on optical line emitting features seen in the VIMOS observations of Hamer et al. (2016). Nevertheless, since integral field spectroscopy is becoming more wide spread, with extensive IFS being the logical next step in observational astrophysics, the techniques utilised in this analysis should help lay the groundwork for subsequent studies; demonstrating the potential power of using a statistically significant number of IFU observations to study the stellar growth rate of BCGs.

It has been demonstrated throughout this thesis therefore that BCGs are not necessarily in a simple state of being. BCGs at low redshift are often assumed to be passive galaxies, with all their eventful evolutionary activity behind them; but as the findings in this thesis show, a significant proportion of BCGs within the last 5

billion years are still actively involved with the interplay between the themselves and the ICM, forming stars and fuelling AGN, and are still in the process of hierarchical growth via major and minor mergers.

8.1 Financial Acknowledgements

This thesis would not have been possible without the financial support from the Science and Technology Facilities Council (STFC) grant ST/K501979/1.

8.2 Scientific Acknowledgements

The work in this thesis has made use of the following astronomical resources:

All Chapters make use of data from the Pan-STARRS1 Surveys (PS1), which have been made possible through contributions by the Institute for Astronomy, the University of Hawaii, the Pan-STARRS Project Office, the Max-Planck Society and its participating institutes, the Max Planck Institute for Astronomy, Heidelberg and the Max Planck Institute for Extraterrestrial Physics, Garching, The Johns Hopkins University, Durham University, the University of Edinburgh, the Queen's University Belfast, the Harvard-Smithsonian Center for Astrophysics, the Las Cumbres Observatory Global Telescope Network Incorporated, the National Central University of Taiwan, the Space Telescope Science Institute, and the National Aeronautics and Space Administration under Grant No. NNX08AR22G issued through the Planetary Science Division of the NASA Science Mission Directorate, the National Science Foundation Grant No. AST-1238877, the University of Maryland, Eotvos Lorand University (ELTE), and the Los Alamos National Laboratory.

Chapters 3 & 4 use data from AllWISE, which makes use of data from WISE, which is a joint project of the University of California, Los Angeles, and the Jet Propulsion Laboratory/California Institute of Technology, and NEOWISE, which is a project of the Jet Propulsion Laboratory/California Institute of Technology. WISE and NEOWISE are funded by the National Aeronautics and Space Administration.

Chapters 5, 6 and 7 are based on observations made with ESO Telescopes at the

Paranal Observatory under programme ID 095.A-0159(A).

Chapter 7 makes use of the following ALMA data: ADS/JAO.ALMA#2016.1.01573.S. ALMA is a partnership of ESO (representing its member states), NSF (USA) and NINS (Japan), together with NRC (Canada), NSC and ASIAA (Taiwan), and KASI (Republic of Korea), in cooperation with the Republic of Chile. The Joint ALMA Observatory is operated by ESO, AUI/NRAO and NAOJ.

The scientific results reported in this Chapter 7 are based in part on observations made by the Chandra X-ray Observatory.

The research in this thesis has made use of the NASA/IPAC Extragalactic Database (NED) which is operated by the Jet Propulsion Laboratory, California Institute of Technology, under contract with the National Aeronautics and Space Administration.

Bibliography

Abell G. O., 1958, ApJS, 3, 211

Abell G. O., Corwin Jr. H. G., Olowin R. P., 1989, ApJS, 70, 1

Allen M. G., Groves B. A., Dopita M. A., Sutherland R. S., Kewley L. J., 2008, ApJS, 178, 20

Allen S. W., Evrard A. E., Mantz A. B., 2011, ARA&A, 49, 409

Anderson S. F., et al., 2003, AJ, 126, 2209

Anderson S. F., et al., 2007, AJ, 133, 313

Andrade-Santos F., et al., 2017, ApJ, 843, 76

Andreon S., 2003, A&A, 409, 37

Andreon S., Hurn M. A., 2010, MNRAS, 404, 1922

Aragon-Salamanca A., Ellis R. S., Couch W. J., Carter D., 1993, MNRAS, 262, 764

Aragon-Salamanca A., Baugh C. M., Kauffmann G., 1998, MNRAS, 297, 427

Arp H. C., Madore B., 1987, A catalogue of southern peculiar galaxies and associations

Ascasibar Y., Markevitch M., 2006, ApJ, 650, 102

Assef R. J., et al., 2013, ApJ, 772, 26

Bacon R., et al., 2010, in Ground-based and Airborne Instrumentation for Astronomy III. p. 773508, doi:10.1117/12.856027

Baldwin J. A., Phillips M. M., Terlevich R., 1981, PASP, 93, 5

Bauer F. E., Condon J. J., Thuan T. X., Broderick J. J., 2000, ApJS, 129, 547

Bayliss M. B., Hennawi J. F., Gladders M. D., Koester B. P., Sharon K., Dahle H., Oguri M., 2011, ApJS, 193, 8

Beers T. C., Geller M. J., Huchra J. P., 1982, ApJ, 257, 23

Belfiore F., et al., 2016, MNRAS, 461, 3111

Bellstedt S., et al., 2016, MNRAS, 460, 2862

Bertin E., Arnouts S., 1996, A&AS, 117, 393

Best P., von der Linden A., Kauffmann G., Heckman T., Kaiser C., 2007, MNRAS, 379, 894

Binney J., Tremaine S., 1987, Galactic dynamics

Birkinshaw M., 1999, Phys. Rep., 310, 97

Bîrzan L., Rafferty D. A., McNamara B. R., Wise M. W., Nulsen P. E. J., 2004, ApJ, 607, 800

Boehringer H., Voges W., Fabian A. C., Edge A. C., Neumann D. M., 1993, MNRAS, 264, L25

Böhringer H., et al., 2000, ApJS, 129, 435

Böhringer H., et al., 2004, A&A, 425, 367

Bower R. G., Lucey J. R., Ellis R. S., 1992, MNRAS, 254, 601

Bower R. G., Benson A. J., Malbon R., Helly J. C., Frenk C. S., Baugh C. M., Cole S., Lacey C. G., 2006, MNRAS, 370, 645

Boylan-Kolchin M., Ma C.-P., Quataert E., 2008, MNRAS, 383, 93

Bregman J. N., Fabian A. C., Miller E. D., Irwin J. A., 2006, ApJ, 642, 746

Brough S., Tran K.-V., Sharp R. G., von der Linden A., Couch W. J., 2011, MNRAS, 414, L80

Brough S., et al., 2017, preprint, (arXiv:1704.01169)

Bruzual G., Charlot S., 2003, MNRAS, 344, 1000

Burke C., Collins C. A., 2013, MNRAS, 434, 2856

Burke C., Hilton M., Collins C., 2015, MNRAS, 449, 2353

Burns J. O., 1990, AJ, 99, 14

Burns J. O., Gregory S. A., Holman G. D., 1981, ApJ, 250, 450

Burns J. O., Hallman E. J., Gantner B., Motl P. M., Norman M. L., 2008, ApJ, 675, 1125

Byram E. T., Chubb T. A., Friedman H., 1966, Science, 152, 66

Canning R. E. A., et al., 2012, MNRAS, 420, 2956

Cappellari M., Copin Y., 2003, MNRAS, 342, 345

Cappellari M., Emsellem E., 2004, PASP, 116, 138

Cappellari M., et al., 2006, MNRAS, 366, 1126

Cardelli J. A., Clayton G. C., Mathis J. S., 1989, ApJ, 345, 245

Cardiel N., Gorgas J., Aragon-Salamanca A., 1998, MNRAS, 298, 977

Cavagnolo K. W., Donahue M., Voit G. M., Sun M., 2008, ApJ, 683, L107

Colless M., et al., 2001, MNRAS, 328, 1039

Collins C. A., et al., 2009, Nature, 458, 603

Condon J. J., Cotton W. D., Greisen E. W., Yin Q. F., Perley R. A., Taylor G. B., Broderick J. J., 1998, AJ, 115, 1693

Conroy C., Wechsler R. H., Kravtsov A. V., 2007, ApJ, 668, 826

Conselice C. J., 2009, MNRAS, 399, L16

Cooke E. A., et al., 2016a, ApJ, 816, 83

Cooke K. C., O'Dea C. P., Baum S. A., Tremblay G. R., Cox I. G., Gladders M., 2016b, ApJ, 833, 224

Cooper A. P., et al., 2011, ApJ, 743, L21

Cooper A. P., Gao L., Guo Q., Frenk C. S., Jenkins A., Springel V., White S. D. M., 2015, MNRAS, 451, 2703

Cowie L. L., Hu E. M., 1986, ApJ, 305, L39

Cowie L. L., Hu E. M., Jenkins E. B., York D. G., 1983, ApJ, 272, 29

Crawford C. S., Allen S. W., Ebeling H., Edge A. C., Fabian A. C., 1999, MNRAS, 306, 857

Crawford C. S., Sanders J. S., Fabian A. C., 2005, MNRAS, 361, 17

Croom S. M., et al., 2012, MNRAS, 421, 872

De Lucia G., Blaizot J., 2007, MNRAS, 375, 2

Dickey J. M., Lockman F. J., 1990, ARA&A, 28, 215

Donahue M., et al., 2010, ApJ, 715, 881

Donahue M., de Messières G. E., O'Connell R. W., Voit G. M., Hoffer A., McNamara B. R., Nulsen P. E. J., 2011, ApJ, 732, 40

Dubinski J., 1998, ApJ, 502, 141

Dubinski J., Mihos J. C., Hernquist L., 1999, ApJ, 526, 607

Dunn R. J. H., Fabian A. C., 2006, MNRAS, 373, 959

Dutson K. L., White R. J., Edge A. C., Hinton J. A., Hogan M. T., 2013, MNRAS, 429, 2069

Dutson K. L., Edge A. C., Hinton J. A., Hogan M. T., Gurwell M. A., Alston W. N., 2014, MNRAS, 442, 2048

Ebeling H., Voges W., Bohringer H., Edge A. C., Huchra J. P., Briel U. G., 1996, MNRAS, 281, 799

Ebeling H., Edge A. C., Bohringer H., Allen S. W., Crawford C. S., Fabian A. C., Voges W., Huchra J. P., 1998, MNRAS, 301, 881

Ebeling H., Edge A. C., Allen S. W., Crawford C. S., Fabian A. C., Huchra J. P., 2000, MNRAS, 318, 333

Ebeling H., Edge A. C., Henry J. P., 2001, ApJ, 553, 668

Ebeling H., Barrett E., Donovan D., Ma C.-J., Edge A. C., van Speybroeck L., 2007, ApJ, 661, L33

Ebeling H., Edge A. C., Mantz A., Barrett E., Henry J. P., Ma C. J., van Speybroeck L., 2010, MNRAS, 407, 83

Edge A. C., 1991, MNRAS, 250, 103

Edge A. C., 2001, MNRAS, 328, 762

Edge A. C., 2004, Clusters of Galaxies: Probes of Cosmological Structure and Galaxy Evolution, p. 58

Edge A. C., Stewart G. C., 1991, MNRAS, 252, 428

Edge A. C., Ivison R. J., Smail I., Blain A. W., Kneib J.-P., 1999, MNRAS, 306, 599

Edge A. C., Wilman R. J., Johnstone R. M., Crawford C. S., Fabian A. C., Allen S. W., 2002, MNRAS, 337, 49

Edge A. C., Ebeling H., Bremer M., Röttgering H., van Haarlem M. P., Rengelink R., Courtney N. J. D., 2003, MNRAS, 339, 913

Edge A. C., et al., 2010, A&A, 518, L46

Edwards L. O. V., Patton D. R., 2012, MNRAS, 425, 287

Edwards L. O. V., Robert C., Mollá M., McGee S. L., 2009, MNRAS, 396, 1953

Edwards L. O. V., Alpert H. S., Trierweiler I. L., Abraham T., Beizer V. G., 2016, MNRAS, 461, 230

Egami E., et al., 2006a, ApJ, 647, 922

Egami E., Rieke G. H., Fadda D., Hines D. C., 2006b, ApJ, 652, L21

Emsellem E., et al., 2007, MNRAS, 379, 401

Fabian A., 1994, ARA&A, 32, 277

Fabian A. C., 2012, ARA&A, 50, 455

Fabian A. C., Nulsen P. E. J., 1977, MNRAS, 180, 479

Fabian A. C., Sanders J. S., 2009, in Heinz S., Wilcots E., eds, American Institute of Physics Conference Series Vol. 1201, American Institute of Physics Conference Series. pp 275–281 (arXiv:0909.2577), doi:10.1063/1.3293055

Fabian A. C., Johnstone R. M., Sanders J. S., Conselice C. J., Crawford C. S., Gallagher III J. S., Zweibel E., 2008, Nature, 454, 968

Fabian A. C., Sanders J. S., Williams R. J. R., Lazarian A., Ferland G. J., Johnstone R. M., 2011, MNRAS, 417, 172

Fabian A. C., Walker S. A., Pinto C., Russell H. R., Edge A. C., 2015, MNRAS, 451, 3061

Fabian A. C., et al., 2016, MNRAS, 461, 922

Falomo R., Pesce J. E., Treves A., 1993, AJ, 105, 2031

Falomo R., Pian E., Treves A., 2014, A&ARv, 22, 73

Feretti L., Giovannini G., Govoni F., Murgia M., 2012, A&ARv, 20, 54

Ferland G. J., Fabian A. C., Hatch N. A., Johnstone R. M., Porter R. L., van Hoof P. A. M., Williams R. J. R., 2009, MNRAS, 392, 1475

Fogarty K., Postman M., Connor T., Donahue M., Moustakas J., 2015, ApJ, 813, 117

Forman W., Jones C., Cominsky L., Julien P., Murray S., Peters G., Tananbaum H., Giacconi R., 1978, ApJS, 38, 357

Fraser-McKelvie A., Brown M. J. I., Pimbblet K. A., 2014, MNRAS, 444, L63

Giacintucci S., Venturi T., Murgia M., Dallacasa D., Athreya R., Bardelli S., Mazzotta P., Saikia D. J., 2007, A&A, 476, 99

Giles P. A., Maughan B. J., Birkinshaw M., Worrall D. M., Lancaster K., 2012, MNRAS, 419, 503

Gitti M., 2013, MNRAS, 436, L84

Gitti M., Brunetti G., Feretti L., Setti G., 2004, A&A, 417, 1

Gladders M. D., Yee H. K. C., 2000, AJ, 120, 2148

Gliozzi M., Brinkmann W., Laurent-Muehleisen S. A., Takalo L. O., Sillanpää A., 1999, A&A, 352, 437

Graham A., Lauer T. R., Colless M., Postman M., 1996, ApJ, 465, 534

Green T. S., et al., 2016, MNRAS, 461, 560

Green T. S., et al., 2017, MNRAS, 465, 4872

Groenewald D. N., Skelton R. E., Gilbank D. G., Loubser S. I., 2017, MNRAS, 467, 4101

Hall P. B., Ellingson E., Green R. F., 1997, AJ, 113, 1179

Hamer S. L., Edge A. C., Swinbank A. M., Wilman R. J., Russell H. R., Fabian A. C., Sanders J. S., Salomé P., 2012, MNRAS, 421, 3409

Hamer S. L., et al., 2014, MNRAS, 437, 862

Hamer S. L., et al., 2016, MNRAS,

Harrison C., 2014, PhD thesis, Durham University ¡EMAIL¿c.m.harrison@durham.ac.uk¡/EMAIL¿

Hatch N. A., Crawford C. S., Fabian A. C., 2007, MNRAS, 380, 33

Heckman T. M., 1980, A&A, 87, 152

Heckman T. M., 1981, ApJ, 250, L59

Heckman T. M., Baum S. A., van Breugel W. J. M., McCarthy P., 1989, ApJ, 338, 48

Hernquist L., Spergel D. N., 1992, ApJ, 399, L117

Hicks A. K., Mushotzky R., Donahue M., 2010, ApJ, 719, 1844

Hlavacek-Larrondo J., Fabian A. C., Edge A. C., Ebeling H., Sanders J. S., Hogan M. T., Taylor G. B., 2012, MNRAS, 421, 1360

Hlavacek-Larrondo J., Fabian A. C., Edge A. C., Ebeling H., Allen S. W., Sanders J. S., Taylor G. B., 2013, MNRAS, 431, 1638

Hlavacek-Larrondo J., et al., 2015, ApJ, 805, 35

Hoffer A. S., Donahue M., Hicks A., Barthelemy R. S., 2012, ApJS, 199, 23

Hogan M. T., et al., 2015a, MNRAS, 453, 1201

Hogan M. T., et al., 2015b, MNRAS, 453, 1223

Hu E. M., Cowie L. L., Wang Z., 1985, ApJS, 59, 447

Hudson D. S., Mittal R., Reiprich T. H., Nulsen P. E. J., Andernach H., Sarazin C. L., 2010, A&A, 513, A37

Ignesti A., Gitti M., Brunetti G., Feretti L., Giovannini G., 2017, preprint, (arXiv:1705.01787)

Inagaki T., Lin Y.-T., Huang H.-J., Hsieh B.-C., Sugiyama N., 2015, MNRAS, 446, 1107

Isobe T., Feigelson E. D., Akritas M. G., Babu G. J., 1990, ApJ, 364, 104

Iwasawa K., Allen S. W., Fabian A. C., Edge A. C., Ettori S., 1999, MNRAS, 306, 467

Jaffe W., Bremer M. N., 1997, MNRAS, 284, L1

Jaffe W., Bremer M. N., Baker K., 2005, MNRAS, 360, 748

Jeltema T. E., Mulchaey J. S., Lubin L. M., Fassnacht C. D., 2007, ApJ, 658, 865

Jimmy Tran K.-V., Brough S., Gebhardt K., von der Linden A., Couch W. J., Sharp R., 2013, ApJ, 778, 171

Johnston D. E., et al., 2007, preprint, (arXiv:0709.1159)

Johnstone R. M., Fabian A. C., Nulsen P. E. J., 1987, MNRAS, 224, 75

Jones D. H., et al., 2004, MNRAS, 355, 747

Jorstad S. G., et al., 2005, AJ, 130, 1418

Kale R., Gitti M., 2017, MNRAS, 466, L19

Kaviraj S., Devriendt J. E. G., Ferreras I., Yi S. K., 2005, MNRAS, 360, 60

Kewley L. J., Dopita M. A., Sutherland R. S., Heisler C. A., Trevena J., 2001, ApJ, 556, 121

Kewley L. J., Groves B., Kauffmann G., Heckman T., 2006, MNRAS, 372, 961

Kitzbichler M. G., White S. D. M., 2008, MNRAS, 391, 1489

Kodama T., Arimoto N., 1997, AAP, 320, 41

Kodama T., Arimoto N., Barger A. J., Arag'on-Salamanca A., 1998, A&A, 334, 99

Kodama T., Tanaka I., Kajisawa M., Kurk J., Venemans B., De Breuck C., Vernet J., Lidman C., 2007, MNRAS, 377, 1717

Kollatschny W., Kotulla R., Pietsch W., Bischoff K., Zetzl M., 2008, A&A, 484, 897

Kron R. G., 1980, ApJS, 43, 305

Laporte C. F. P., White S. D. M., Naab T., Gao L., 2013, MNRAS, 435, 901

Lauer T. R., 1988, ApJ, 325, 49

Lauer T. R., Postman M., Strauss M. A., Graves G. J., Chisari N. E., 2014, ApJ, 797, 82

Li Y., Bryan G. L., 2014, ApJ, 789, 153

Lidman C., et al., 2012, MNRAS, 427, 550

Lidman C., et al., 2013, MNRAS, 433, 825

Lietzen H., Nilsson K., Takalo L. O., Heinämäki P., Nurmi P., Keinänen P., Wagner S., 2008, A&A, 482, 771

Lin Y.-T., Mohr J. J., 2004, ApJ, 617, 879

Lin Y.-T., Mohr J. J., Stanford S. A., 2003, ApJ, 591, 749

Lin Y.-T., Brodwin M., Gonzalez A. H., Bode P., Eisenhardt P. R. M., Stanford S. A., Vikhlinin A., 2013, ApJ, 771, 61

Liu F. S., Mao S., Deng Z. G., Xia X. Y., Wen Z. L., 2009, MNRAS, 396, 2003

Liu F. S., Mao S., Meng X. M., 2012, MNRAS, 423, 422

Liu F. S., Lei F. J., Meng X. M., Jiang D. F., 2015, MNRAS, 447, 1491

Lloyd-Davies E. J., Ponman T. J., Cannon D. B., 2000, MNRAS, 315, 689

López-Cruz O., Barkhouse W. A., Yee H. K. C., 2004, ApJ, 614, 679

Loubser S. I., Babul A., Hoekstra H., Mahdavi A., Donahue M., Bildfell C., Voit G. M., 2016, MNRAS, 456, 1565

Mahony E. K., Croom S. M., Boyle B. J., Edge A. C., Mauch T., Sadler E. M., 2010, MNRAS, 401, 1151

Markevitch M., Vikhlinin A., 2007, Phys. Rep., 443, 1

Martel H., Robichaud F., Barai P., 2014, ApJ, 786, 79

Martin D. C., et al., 2005, ApJ, 619, L1

Martini P., Kelson D. D., Kim E., Mulchaey J. S., Athey A. A., 2006, ApJ, 644, 116

Massaro E., Giommi P., Leto C., Marchegiani P., Maselli A., Perri M., Piranomonte S., Sclavi S., 2009, A&A, 495, 691

Massaro E., Nesci R., Piranomonte S., 2012, MNRAS, 422, 2322

Massaro E., Maselli A., Leto C., Marchegiani P., Perri M., Giommi P., Piranomonte S., 2015, Ap&SS, 357, 75

McDonald M., 2011, ApJ, 742, L35

McDonald M., Veilleux S., Rupke D. S. N., Mushotzky R., 2010, ApJ, 721, 1262

McDonald M., et al., 2012a, Nature, 488, 349

McDonald M., Veilleux S., Rupke D. S. N., 2012b, ApJ, 746, 153

McDonald M., Wei L. H., Veilleux S., 2012c, ApJ, 755, L24

McDonald M., Benson B., Veilleux S., Bautz M. W., Reichardt C. L., 2013, ApJ, 765, L37

McDonald M., Roediger J., Veilleux S., Ehlert S., 2014, ApJ, 791, L30

McHardy I. M., Luppino G. A., George I. M., Abraham R. G., Cooke B. A., 1992, MNRAS, 256, 655

McIntosh D. H., Guo Y., Hertzberg J., Katz N., Mo H. J., van den Bosch F. C., Yang X., 2008, MNRAS, 388, 1537

McNamara B. R., Nulsen P. E. J., 2007, ARA&A, 45, 117

McNamara B. R., Nulsen P. E. J., 2012, New Journal of Physics, 14, 055023

McNamara B. R., Wise M., Sarazin C. L., Jannuzi B. T., Elston R., 1996, ApJ, 466, L9

McNamara B. R., et al., 2000, ApJ, 534, L135

Mehrtens N., et al., 2012, MNRAS, 423, 1024

Mei S., et al., 2006, ApJ, 644, 759

Mei S., et al., 2009, ApJ, 690, 42

Menci N., Rosati P., Gobat R., Strazzullo V., Rettura A., Mei S., Demarco R., 2008, ApJ, 685, 863

Merrifield M. R., Kent S. M., 1991, AJ, 101, 783

Merritt D., 1985, ApJ, 289, 18

Milosavljević M., Merritt D., 2001, ApJ, 563, 34

Mittal R., et al., 2012, MNRAS, 426, 2957

Mittal R., Whelan J. T., Combes F., 2015, MNRAS, 450, 2564

Mulchaey J. S., Lubin L. M., Fassnacht C., Rosati P., Jeltema T. E., 2006, ApJ, 646, 133

Murante G., Giovalli M., Gerhard O., Arnaboldi M., Borgani S., Dolag K., 2007, MNRAS, 377, 2

Nilsson K., Takalo L. O., Pursimo T., Sillanpää A., Heidt J., Wagner S. J., Laurent-Muehleisen S. A., Brinkmann W., 1999, A&A, 343, 81

Nipoti C., 2017, MNRAS, 467, 661

O'Dea C. P., Dent W. A., Balonek T. J., 1984, ApJ, 278, 89

O'Dea C. P., et al., 2008, ApJ, 681, 1035

Oliva-Altamirano P., et al., 2014, MNRAS, 440, 762

Oliva-Altamirano P., et al., 2017, AJ, 153, 89

Ostriker J. P., Hausman M. A., 1977, ApJ, 217, L125

Peng C. Y., Ho L. C., Impey C. D., Rix H.-W., 2002, AJ, 124, 266

Peng C. Y., Ho L. C., Impey C. D., Rix H.-W., 2010, AJ, 139, 2097

Pesce J. E., Fabian A. C., Edge A. C., Johnstone R. M., 1990, MNRAS, 244, 58

Pfrommer C., Chang P., Broderick A. E., 2012, ApJ, 752, 24

Pierre M., Soucail G., Boehringer H., Sauvageot J. L., 1994, A&A, 289, L37

Pizzolato F., Soker N., 2005, ApJ, 632, 821

Ponman T. J., Cannon D. B., Navarro J. F., 1999, Nature, 397, 135

Prasad D., Sharma P., Babul A., 2015, ApJ, 811, 108

Puchwein E., Springel V., Sijacki D., Dolag K., 2010, MNRAS, 406, 936

Quillen A. C., et al., 2008, ApJS, 176, 39

Quinn P. J., 1984, ApJ, 279, 596

Rafferty D. A., McNamara B. R., Nulsen P. E. J., Wise M. W., 2006, ApJ, 652, 216

Rafferty D. A., McNamara B. R., Nulsen P. E. J., 2008, ApJ, 687, 899

Rampazzo R., Sulentic J. W., 1992, A&A, 259, 43

Rasia E., et al., 2015, ApJ, 813, L17

Rasmussen J., Mulchaey J. S., Bai L., Ponman T. J., Raychaudhury S., Dariush A., 2010, ApJ, 717, 958

Rawle T. D., et al., 2012, ApJ, 747, 29

Rector T. A., Stocke J. T., Perlman E. S., 1999, ApJ, 516, 145

Richard J., et al., 2010, MNRAS, 404, 325

Rines K., Finn R., Vikhlinin A., 2007, ApJ, 665, L9

Romer A. K., Viana P. T. P., Liddle A. R., Mann R. G., 2001, ApJ, 547, 594

Russell H. R., Fabian A. C., Sanders J. S., Johnstone R. M., Blundell K. M., Brandt W. N., Crawford C. S., 2010, MNRAS, 402, 1561

Russell H. R., McNamara B. R., Edge A. C., Hogan M. T., Main R. A., Vantyghem A. N., 2013, MNRAS, 432, 530

Russell H. R., et al., 2016, MNRAS, 458, 3134

Russell H. R., et al., 2017, ApJ, 836, 130

Rykoff E. S., et al., 2014, ApJ, 785, 104

Salomé P., Combes F., 2003, A&A, 412, 657

Salomé P., Combes F., 2004, A&A, 415, L1

Salomé P., et al., 2006, A&A, 454, 437

Samuele R., McNamara B. R., Vikhlinin A., Mullis C. R., 2011, ApJ, 731, 31

Sánchez-Blázquez P., et al., 2006, MNRAS, 371, 703

Sanderson A. J. R., Edge A. C., Smith G. P., 2009, MNRAS, 398, 1698

Santos J. S., Rosati P., Tozzi P., Böhringer H., Ettori S., Bignamini A., 2008, A&A, 483, 35

Schaye J., et al., 2015, MNRAS, 446, 521

Schlafly E. F., Finkbeiner D. P., 2011, ApJ, 737, 103

Schwope A., et al., 2000, Astronomische Nachrichten, 321, 1

Seigar M. S., Lynam P. D., Chorney N. E., 2003, MNRAS, 344, 110

Seigar M. S., Graham A. W., Jerjen H., 2007, MNRAS, 378, 1575

Shankar F., et al., 2015, ApJ, 802, 73

Shanks T., et al., 2015, MNRAS, 451, 4238

Siemiginowska A., Burke D. J., Aldcroft T. L., Worrall D. M., Allen S., Bechtold J., Clarke T., Cheung C. C., 2010, ApJ, 722, 102

Smith G. P., et al., 2010, MNRAS, 409, 169

Soto K. T., Lilly S. J., Bacon R., Richard J., Conseil S., 2016, MNRAS, 458, 3210

Springel V., et al., 2005, Nature, 435, 629

Stanford S., Eisenhardt P., Dickinson M., 1998, ApJ, 492, 461

Stanford S. A., et al., 2012, ApJ, 753, 164

Stanford S. A., Gonzalez A. H., Brodwin M., Gettings D. P., Eisenhardt P. R. M., Stern D., Wylezalek D., 2014, ApJS, 213, 25

Stein W. A., Odell S. L., Strittmatter P. A., 1976, ARA&A, 14, 173

Stocke J. T., Morris S. L., Gioia I. M., Maccacaro T., Schild R., Wolter A., Fleming T. A., Henry J. P., 1991, ApJS, 76, 813

Stott J. P., Edge A. C., Smith G. P., Swinbank A. M., Ebeling H., 2008, MNRAS, 384, 1502

Stott J. P., Pimbblet K. A., Edge A. C., Smith G. P., Wardlow J. L., 2009, MNRAS, 394, 2098

Stott J. P., et al., 2010, ApJ, 718, 23

Stott J. P., et al., 2012, MNRAS, 422, 2213

Sunyaev R. A., Zeldovich Y. B., 1972, Comments on Astrophysics and Space Physics, 4, 173

Thomas D., Maraston C., Bender R., Mendes de Oliveira C., 2005, ApJ, 621, 673

Tonini C., Bernyk M., Croton D., Maraston C., Thomas D., 2012, ApJ, 759, 43

Tonry J. L., et al., 2012, ApJ, 750, 99

Tran K.-V. H., Moustakas J., Gonzalez A. H., Bai L., Zaritsky D., Kautsch S. J., 2008, ApJ, 683, L17

Tremblay G. R., et al., 2012, MNRAS, 424, 1042

Tremblay G. R., et al., 2014, ApJ, 790, L26

Tremblay G. R., et al., 2016, Nature, 534, 218

Urry C. M., Padovani P., 1995, PASP, 107, 803

Valentijn E. A., Bijleveld W., 1983, A&A, 125, 223

Veale M., Ma C.-P., Greene J. E., Thomas J., Blakeslee J., McConnell N., Walsh J., Ito J., 2017, preprint, (arXiv:1703.08573)

Véron-Cetty M.-P., Woltjer L., Staveley-Smith L., Ekers R. D., 2000, A&A, 362, 426

Vikhlinin A., Burenin R., Forman W. R., Jones C., Hornstrup A., Murray S. S., Quintana H., 2007, in Böhringer H., Pratt G. W., Finoguenov A., Schuecker P., eds, Heating versus Cooling in Galaxies and Clusters of Galaxies. p. 48 (arXiv:astro-ph/0611438), doi:10.1007/978-3-540-73484-0˙9

Vogelsberger M., et al., 2014, MNRAS, 444, 1518

Voges W., et al., 1999, A&A, 349, 389

Voit G. M., Donahue M., 2015, ApJ, 799, L1

Voit G. M., Donahue M., Slavin J. D., 1994, ApJS, 95, 87

Voit G. M., Bryan G. L., Balogh M. L., Bower R. G., 2002, ApJ, 576, 601

Voit G. M., Kay S. T., Bryan G. L., 2005, MNRAS, 364, 909

Voit G. M., Cavagnolo K. W., Donahue M., Rafferty D. A., McNamara B. R., Nulsen P. E. J., 2008, ApJ, 681, L5

Walker S. A., Fabian A. C., Russell H. R., Sanders J. S., 2014, MNRAS, 442, 2809

Wang J., Overzier R., Kauffmann G., von der Linden A., Kong X., 2010, MNRAS, 401, 433

Werner N., Durret F., Ohashi T., Schindler S., Wiersma R. P. C., 2008, Space Sci. Rev., 134, 337

Werner N., et al., 2014, MNRAS, 439, 2291

Werner N., et al., 2016, MNRAS, 460, 2752

Whiley I. M., et al., 2008, MNRAS, 387, 1253

White S. D. M., 1976, MNRAS, 174, 19

White S. D. M., Rees M. J., 1978, MNRAS, 183, 341

White D. A., Jones C., Forman W., 1997, MNRAS, 292, 419

Williams R. J., Quadri R. F., Franx M., 2011, ApJ, 738, L25

Wilman R. J., Edge A. C., Swinbank A. M., 2006, MNRAS, 371, 93

Wong K.-W., Sarazin C. L., Blanton E. L., Reiprich T. H., 2008, ApJ, 682, 155

Wright E. L., et al., 2010, AJ, 140, 1868

York D. G., et al., 2000, AJ, 120, 1579

Zenn A. R., Ebeling H., 2010, A&A, 524, A30

Zhao D., Aragón-Salamanca A., Conselice C. J., 2015, MNRAS, 448, 2530

Zhao D., Conselice C. J., Aragón-Salamanca A., Almaini O., Hartley W. G., Lani C., Mortlock A., Old L., 2017, MNRAS, 464, 1393

Zirm A. W., et al., 2008, ApJ, 680, 224

ZuHone J. A., Markevitch M., Johnson R. E., 2010, ApJ, 717, 908

ZuHone J. A., Markevitch M., Lee D., 2011, ApJ, 743, 16

Zwicky F., 1933, Helvetica Physica Acta, 6, 110

Zwicky F., Herzog E., Wild P., Karpowicz M., Kowal C. T., 1961, Catalogue of galaxies and of clusters of galaxies, Vol. I

de Jong J. T. A., Verdoes Kleijn G. A., Kuijken K. H., Valentijn E. A., 2013, Experimental Astronomy, 35, 25

van Dokkum P. G., van der Marel R. P., 2007, ApJ, 655, 30

van den Bosch F. C., Lewis G. F., Lake G., Stadel J., 1999, ApJ, 515, 50